Generalised 2D Ballooning Theory in Tokamaks: Obtaining the Global Properties of Linear Microinstabilities From the Local Ballooning Equations

Peshwaz Abdulkareem Abdoul

PhD

UNIVERSITY OF YORK

PHYSICS

JULY 2015

Abstract

This thesis involves the development of a technique to improve our understanding of the impact of global effects on linear microinstabilities. The technique combines local ballooning solutions with higher order theory to reconstruct the global eigenmode structure and associated global eigenvalue. In this work, the theory of 2D ballooning eigenmodes has been extended beyond the two limits of highly unstable isolated modes, which often sit on the outboard mid-plane, and less unstable general modes that peak on the top or bottom of the tokamak. Our generalised solutions can account for global modes with arbitrary poloidal positions which, in turn, enables us to explore experimentally relevant regimes with arbitrary equilibria.

Furthermore, using a generally applicable gyrokinetic plasma model, the global mode structures of the ion temperature gradient (ITG) driven microinstability have been reconstructed directly from the local gyrokinetic code, GS2. Using CYCLONE base case parameters with the circular Miller equilibrium model we benchmark our calculation against direct global gyrokinetic simulations. Introducing a radially varying profile for the mode drive that peaks about a reference rational surface $x_s = 0$, while holding other profiles constant, leads to a highly unstable isolated mode. The effect of the other equilibrium profiles is found to be stabilising. However, rotational flow shear introduced via a Doppler shift in the real local frequency, i.e $\omega_0 \rightarrow \omega_0 + nq'\gamma_E x_s$, where n is the toroidal mode number and γ_E represents the strength of the flow shear, can cancel the influence of the other profile variations and, for a critical value of flow shear, a highly unstable isolated mode can be captured again.

Finally, for an equilibrium that exhibits an isolated mode, we have also investigated the effect of the flux surface shaping through elongation $\bar{\kappa}$ and triangularity $\bar{\delta}$. Our simulations indicate that, depending on the value of $\bar{\kappa}$ and $\bar{\delta}$, the effect of shaping can be both stabilising and destabilising.

Contents

List of Figures

List of Tables

Acknowledgments

I would like to thank my academic supervisor Prof. Howard Wilson for his support, guidance and useful discussion throughout the period of my PhD study. I thank both Dr. David Dickinson and Dr. Colin Roach for their great support, particularly, for providing information and guidance on installation and compilation of the GS2 source code. I am tremendously grateful to Dr. David Dickinson for proof-reading this work and his helpful corrections and suggestions without which this work would not have been possible.

Furthermore, I should also mention the role of my sponsor, the Ministry of Higher Education in Kurdistan region of Iraq, for their financial support that allowed me to study for a PhD at University of York, for which I am extremely grateful. It is also important to mention that this work has also received funding from the European Union's Horizon 2020 research and innovation programme under grant agreement number 633053 and from the RCUK Energy Programme [grant number EP/I501045]. The views and opinions expressed herein do not necessarily reflect those of the European Commission. The local gyrokinetic simulation results presented in this thesis would not have been possible without using the available supercomputing resources such as HECToR and ARCHER in the UK (provided by the Plasma HEC Consortium EPSRC grant number EP/L000237/1) and HELIOS in Japan (funded under the Broader Approach collaboration between Euratom and Japan).

I would also like to extend my sincere gratitude to the following, who have helped me in ways that they may never fully be aware of: Hazhar A Rasull − for preparing the tables in the appendix A. Appreciation is also extended to the brothers at York Mosque, sheikh Abid, sheikh zubair, sheikh Yusuf, Yusuf Al-Portugali, Nasir Abu-Fahd, Hakim, Faisal, Tariq, Hameed, Yasir Al-Qwrayshi, Uncle Edris, Hashim Al-Suri and all others who made my stay in York an extremely pleasant one, providing fun, laughter and joy as well as the occasional intellectual debate!. From Thursday social circles consisting of a friendly cup of tea and biscuits, to Friday gatherings of over three hundred people, all ready to give you hug and a handshake.

The spiritual experience gained and the lessons learnt will stay with me forever. I would also like to thanks all my friends and colleagues at YPI (York Plasma Institute), Muhamad Shahzad, Reem Alraddadi, Apiwat Wijaikhum, Ben Moody, Dr Ben Dudson, Ozgur Gulfa, Andrew Allen, Lee Morgan, Sofia Henneberg, Brendan Shanahan, Jarrod Leddy, Omkar Myatra, Arkaprava Bokshi and all others for the help and support during all these four years of my PhD study.

Finally, I would like to thank my friends, Ranjdar, Sharif, Bestoon, Hayman, Dana and my family, especially my parents Abdulkareem Abdoul and Farida Awl, for their endless patience and support during the doctoral studies; to them I have dedicated this work. Above all, utmost appreciation to Almighty God for the divine intervention in this academic endeavour.

Declaration

I certify that the results and ideas presented in this thesis are purely based on my own research (except where stated) and are in accordance with university academic rules and ethical conduct. I declare that this work includes no material which has been accepted or submitted for a degree or award at any other UK or foreign universities, and I believe that it does not contain any previously published results or written material by another person, unless stated in the text. Although the results that are presented in this thesis could result in additional Journal publications, only the following paper has been published so far

- P. A. Abdoul, D. Dickinson, C. M. Roach and H. R. Wilson, "**Using a local gyrokinetic code to study global ion temperature gradient modes in tokamaks**". *Plasma Phys. Control. Fusion* 57 (6):065004, 10 April 2015.

Chapter 1

Introduction

The main purpose behind the fusion energy programme is to provide a safe, reliable and clean source of energy. Fusion is a nuclear process where light nuclei combine to produce heavier nuclei, releasing a large amount of energy. One of the main challenges for fusion is the issue of confinement. There are two main approaches to confining hot plasma in the laboratory; inertial and magnetic confinement. Here we will concentrate on magnetic confinement fusion (MCF). Owing to its high reaction rate and the fact that it takes place at a relatively low temperature, the deuterium-tritium ($D-T$) reaction is currently the most favourable reaction for energy production in laboratories. The main goal of MCF is to confine hot fusion plasma for a sufficiently long enough time to achieve an energy gain. The condition to achieve this goal has been obtained by Lawson in the 1950's [1]. For the $D-T$ reaction at the optimal temperature, in the range $10-20$ keV, the ignition condition reads [2]:

$$n_p T \tau_E > 3 \times 10^{21} m^{-3}\,\text{keVs}, \tag{1.1}$$

where n_p, T and τ_E are the plasma density, temperature and confinement time, respectively. It should be noted that, for a typical $D-T$ tokamak plasma, $n \approx 10^{20} m^{-3}$ and $T \approx 10$ keV, it follows from Eq. (1.1) that to achieve ignition the plasma needs to have a confinement time of $\sim$ few seconds. This confinement time is controlled by diffusion of heat and particles across flux surfaces. There are different mechanisms

for this transport, but the main contribution is typically due to turbulent transport. This transport impacts the minimum size of fusion reactors, ITER and DEMO for example [3], which in turn is a key factor in achieving the important goal of ignition. Low frequency, fine scale microinstabilities, driven by gradients in the equilibrium plasma parameters like density and temperature are believed to be the main source for the turbulent transport. The so-called "drift" modes are known to be the dominant type of microinstability in typical MCF experiments [2, 4] and hence, it is crucial to understand these modes and find a way to reduce their effects. In spite of the fact that our understanding of turbulent transport from experimental, computational and theoretical points of view has been greatly improved over the past few decades, there are still unsolved problems in this area. Among the most interesting subjects, which have attracted the attention of the MCF community, are the impact of global effects, such as plasma profile variations. Previous theoretical and numerical studies have shown that flow shear can suppress the drift waves or even stabilise them completely [5–11]. However, the flow shear, combined with the effect of the radial plasma profile variations, can also provide destabilising effects [12, 13]. This thesis is mainly devoted to improving our understanding of the global effects on linear microinstabilities. However, the linear aspect of the microinstabilities alone is not sufficient and cannot provide a complete picture of the physical mechanisms involved in turbulent transport. For example, the saturation of microinstabilities at a finite amplitude is a non-linear phenomenon. Nevertheless, linear physics plays a significant role in the development of many simplified, yet valuable plasma models, e.g. quasilinear turbulent transport models in tokamaks [14]. It is, therefore, of considerable importance to understand the stability and structure of linear instabilities. There exist many different models to investigate microinstabilities numerically, but here we mainly rely on the gyrokinetic equation [15–17]. Its solution can involve several different approaches, which we now discuss.

For an axisymmetric tokamak plasma, the gyrokinetic equation describing linear microinstabilities is usually reduced to a 2D eigenmode equation in radius, r, and poloidal angle, θ. A full solution to this 2D problem corresponds to a global solution

which provides the global mode structure, $\tilde{\phi}(r,\theta)$ with associated global eigenvalue, Ω. However, for high toroidal mode numbers, $n \gg 1$, the distance between neighbouring rational surfaces, Δ_r, becomes very small compared to the equilibrium scale length, L. Exploiting the small parameter $\Delta_r/L \ll 1$, one can expand, using a WKB perturbation technique, to reduce the 2D global eigenmode into a sequence of an infinite number of solutions. The leading order solutions correspond to the local or ballooning theory [18–21]. At this order adjacent rational flux surfaces experience approximately the same equilibrium quantities and the problem exhibits a so-called translational invariant (or ballooning) symmetry. Local codes, like the gyrokinetic GS2 code [21, 22], take advantage of this ballooning symmetry to transform the intrinsic 2D problem to 1D in the extended ballooning coordinate, η, along the magnetic field lines. Local codes only provide the local mode structure, $\xi(r,p,\theta)$ with associated local eigenvalue, $\Omega_0(r,p)$, where, both r and ballooning angle, p, are free parameters at this order. However, taking into account the higher order terms in the Δ_r/L expansion, the eigenfunction's dependence on r and p is constrained and one can reconstruct both $\tilde{\phi}(r,\theta)$ and Ω. Exploiting the higher order ballooning theory to investigate the global properties, for a simplified fluid model of ion temperature gradient (ITG) modes, has been previously employed and used in Ref [5]. This thesis extends this to demonstrate that the formalism can be applied to study more realistic gyrokinetic plasma models.

An important result from previously studied higher order ballooning theory calculations is that for a very special set of plasma equilibrium profiles a highly unstable isolated mode can exist at a particular rational surface on which $\Omega_0(r,p)$ is stationary [19]. This type of mode was originally studied in the context of ideal MHD theory [23, 24] and often sits on the outboard mid-plane, where $\theta = 0$ [5]. The associated global complex mode frequency, Ω, is related to $\Omega_0(r,p)$ according to $\Omega = \mathrm{Max}[\Omega_0(r,p)] + O(1/n)$, which includes an $O(1/n)$ correction to the local value evaluated at the maximally unstable r and p. A second class of mode, known as the "general mode", has also been predicted from the higher order ballooning theory [18, 19, 25, 26]. These modes are usually peaked at the top or bottom of the plasma

and have a reduced growth rate compared to the isolated mode. More usually in realistic experimental situations, the global modes can sit anywhere in the poloidal plane [13, 27, 28]. To account for these modes, in this thesis the analytical solutions have been extended beyond these two limits, such that both isolated and general modes can be considered as two special limits of our new generalised solution. We also point out that local gyrokinetic simulations alone cannot distinguish between isolated and non-isolated modes, but, taking into account the radial variation of equilibrium profiles, both type of modes can be captured in global gyrokinetic simulations. For example, global simulations of linear electrostatic ITG modes in both ASDEX Upgrade (AUG) plasmas [29] and the CYCLONE base case [12, 13], are found to be poloidaly shifted with respect to the outboard mid-plane. The methodology and analytical theory presented in this work can provide greater insight into the mechanisms underlying the symmetry breaking associated with the generalised modes. Such poloidal symmetry breaking is important and could be very helpful in generating flow shear in tokamaks [27, 30–32], especially in a machine like ITER for which the external torque is small.

Furthermore, shaping of the magnetic flux surfaces, specified by the elongation $\bar{\kappa}$ and triangularity $\bar{\delta}$, can provide stabilising effects on the microinstabilities. However, this is a topic of current research and has not yet been well understood. For example, in the TCV experiment with L-mode confinement, the electron heat transport decreases with negative triangularity [33]. This trend is reversed in the H-mode confinement in AUG and JET tokamaks, where increasing positive triangularity improves the confinement [34, 35]. On the other hand, the elongation has both stabilising and destabilising effects on the linear ITG modes [36–38], depending on plasma parameters. In addition, non-linear gyrokinetic simulations have also reported the stabilising effects of the elongation on the edge turbulent electron transport in tokamaks [39] and on the electron and ion heat fluxes [38]. In this thesis, considering the highly unstable isolated modes, the combined effect of both $\bar{\kappa}$ and $\bar{\delta}$ on the linear electrostatic ITG modes in tokamak plasmas has been investigated and both stabilising and destabilising trends have been observed. Finally, we note that

while non-linear simulations are necessary for a complete understanding of turbulence and flows in plasmas, linear theory provides a picture of the important physical mechanisms. The technique we present here is an alternative approach to full global simulations that uses an efficient formalism to shed light on the key linear physics.

This work is organised as follows. In Chapter 2 we discuss the basics of magnetic confinement fusion and shed light on different mechanisms that lead to cross-field transport of both particle and energy towards the outside of the confinement region. In Chapter 3, different models, often used to investigate drift waves, are introduced and used to gain some insight into the physics of both the electron drift wave and ion temperature gradient mode. This Chapter ends with the gyrokinetic model and briefly presents the local and global approaches used to solve the gyrokinetic equations. Chapter 4 is devoted to discussing ballooning theory, together with the theoretical formalism on which this thesis is based. This formalism describes how to obtain the global mode structure from solutions to the local equation by combining them with the higher order ballooning theory. In Chapter 5, in addition to previously available analytical solutions, we present new generalised analytic solutions. Chapter 6 is dedicated to applying the local gyrokinetic code, GS2, along with the higher order ballooning theory, to investigate the effects of profile variations and flux surface shaping on the global properties of ITG modes in tokamaks and benchmark our results against global gyrokinetic simulations. Finally, Chapter 7 summarises our conclusions, and plans for future work.

Chapter 2

Magnetic Confinement Fusion

The worldwide demand for a new and clean source of energy is increasing at an alarming rate. Fusion energy is among the best candidates for this role. Despite the fact that significant progress has been made from both theoretical and experimental points of view over the last few decades, there are still challenges that scientists have to face on their way to achieve their ultimate goal. The scientific research in fusion laboratories is divided into two main categories: Inertial and magnetic confinement fusion. In this chapter we will discuss different magnetic confinement geometries together with the various transport mechanisms responsible for the loss of particles and energy.

2.1 The Global Energy Crisis

Energy is a fundamental quantity that exists throughout the entire universe. Energy can be simply defined as ability to do work; no energy means no work, therefore the world of economy completely depends on energy. According to the first law of thermodynamics, energy, can neither be created nor destroyed, but can be transformed from one form to another. This law, however, does not account for the fact that all the natural processes take place with a preferred direction, for example heat readily goes from warm bodies to cold ones, but the reverse cannot happen spontaneously.

This leads to a so-called second law of thermodynamics. It states that a complete conversion of heat energy to work is impossible, or equivalently there is no machine that could work with 100% efficiency. Formulation and understanding of these laws of thermodynamics, especially recognising heat as a form of energy, marked a new era and start of technological development, driving the industrial revolution, and, to some extent, revolutionising the history of mankind on the planet [40]. Since then we have started using different forms of energy resource, at an ever accelerating rate. For example car engines convert chemical energy into kinetic energy; potential energy stored in water behind dams can be transformed into electrical energy, etc. In general the energy resources available on our planet, can be divided into the following main forms [41]:

1. Non-renewable sources: "Fossil fuels", like coal, oil, gas, etc.
2. Renewable sources: Solar, wind, tides, waves, geothermal, etc.
3. Nuclear sources: Fission and Fusion.

Burning fossil fuels usually releases carbon and sulphur dioxide into the atmosphere, polluting the environment and causing so called global warming [42] and acid rain, respectively. These type of resources are not renewable and will finally get exhausted. In contrast, renewable energy is sustainable and, therefore, it will never become fully exhausted. They do not contribute to global warming or greenhouse effects. However, it is difficult to produce the same amount of electrical energy compared to that generated by conventional fossil fuel generators. In addition, the weather is a major source for renewable energy and therefore it cannot be predictable and consistent. As a result the current renewable energy technology is far more expensive compared to conventional fossil fuel power generation. For these reasons, most developed countries still depend mainly on "fossil fuels", especially oil, gas and coal, for their energy needs. Furthermore, due to the current size and dramatic growth of the world population, the consumption of the current energy resources together with the demand for more energy production are increasing at an alarming rate. The

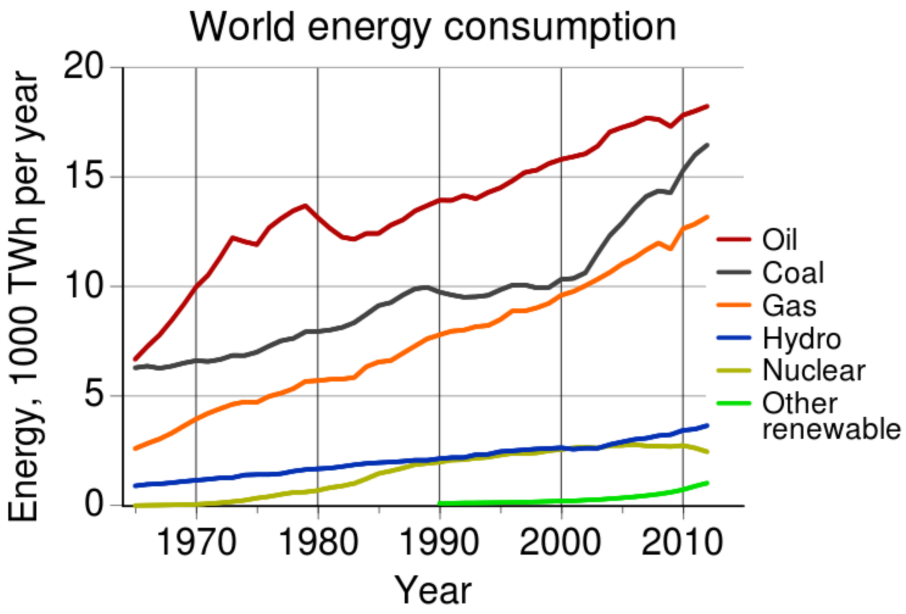

Figure 2.1: The global energy consumption, in unit of KTWh per year, for different energy resources [43]. Each colour corresponds to a particular energy resource. Note that the most consumed energy resources are mainly due to "fossil fuel" and especially coal, gas or oil.

energy crisis, once we run out of our current energy resources, will soon, regardless of our origins and political views, become an unavoidable challenge for each and every single country in the entire globe. Figure 2.1 shows the global energy consumption, in terms of kilo-tera Watt hours per year, for various energy sources. It delivers a simple message, which we all know - the end of our current energy resources may lead to the collapse of our industrial civilization.

If we are serious and concerned about the accumulation of atmospheric carbon dioxide, climate change, the end of "fossil fuels" resources, and want to fulfil the energy needs of our industrial civilization as well as meet the aspirations of developing countries, we must then encourage and accelerate the development of alternative sources of energy. Renewable energy sources, e.g solar and wind, should be advanced, but unfortunately they can only partially contribute to the energy needs of a growing economic and industrial civilization. Both fission and fusion nuclear reactions could provide reliable and clean sources of energy that we can exploit to address the energy crisis. Although, due to the confinement problem, we have not yet been able to build a commercial fusion reactor. Nevertheless, as we will discuss in the following section,

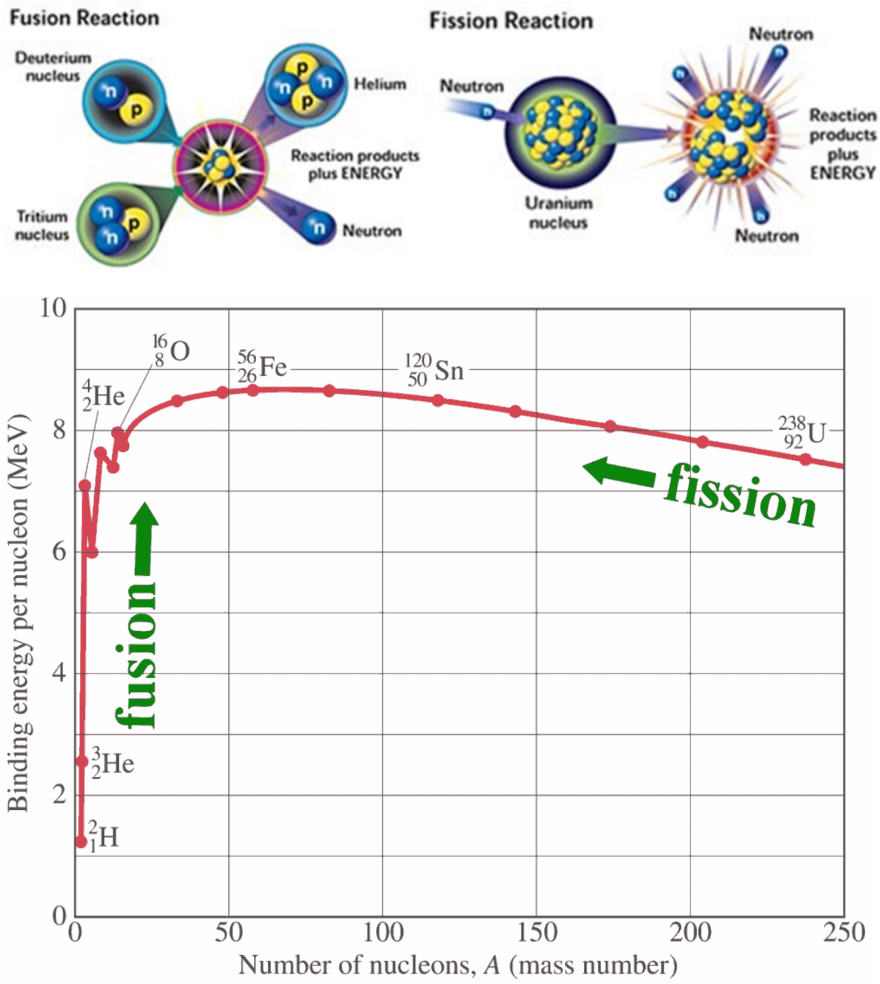

Figure 2.2: The average binding energy per nucleon (MeV) as a function of atomic mass number, A [44, 45]. Iron $^{56}_{26}Fe$ is the most stable nucleus. The larger nuclei, like $^{238}_{92}U$, split into smaller ones and release energy via nuclear fission. Lighter nuclei, like hydrogen isotopes deuterium $^{2}_{1}H$ and tritium $^{3}_{2}H$, can combine together to make a heavier helium, $^{4}_{2}He$, nucleus with a neutron, and releasing a huge amount of energy through the process of nuclear fusion.

there are some crucial points that make fusion an attractive option.

2.2 Nuclear Fusion vs Nuclear Fission

Nuclear fission and fusion are two complementary processes, in which huge amounts of energy are released. Fission can be defined as the process of splitting a large atomic nucleus into smaller nuclei. Fusion on the other hand takes place by fusing two or more small atomic nuclei to produce bigger ones. In both cases we end up with a little bit less mass than we started with. That missing mass, M, is converted to energy according to Einstein's famous energy-mass relation, $E_n = Mc^2$. Figure 2.2 shows the binding energy for some nuclei as a function of mass number, A. The

higher the binding energy per nucleon the more stable the correspond nucleus is. The medium size iron, ${}^{56}_{26}Fe$, nucleus is the most stable. It is clear from the figure that the nuclei can go toward iron by releasing some of their binding energy.

Using fission to produce energy in power stations is free of carbon dioxide, but this does not mean it is a completely clean source of energy. There are long-lived, undesirable radioactive waste products associated with nuclear fission. In addition, fission reactors require active safety systems to avoid accidents like Chernobyl and Fukushima. In contrast, fusion is a better source of energy. It is free of carbon dioxide and does not produce any long lived radioactive waste. It is safe, has compact power units and has effectively inexhaustible fuel [46, 47]. Therefore, fusion is a promising and sustainable solution to address the future energy crisis. But, unfortunately fusion is very hard to achieve. We have pursued economic fusion power for more than a half century and despite the fact that we have made remarkable progresses, we do not yet have an operational fusion reactor. The fusion reaction is the fundamental source of energy that powers the stars throughout the entire universe. It is the same reaction that continuously provides us with an enormous amount of energy from the sun. The strong gravitation force in the sun creates a very high pressure in the core and raises its temperature to about 15 million degrees Celsius. This creates the conditions required to fuse hydrogen nuclei together, producing helium and releasing energy. A different approach to fusion on earth must be adopted. This is to heat a relatively low density fusion fuel to the optimum temperature of about 150 million degrees Celsius. The possible candidate reactions for fusion energy on earth are the following [2, 48, 49]:

$$\begin{aligned} {}^{2}_{1}H + {}^{2}_{1}H \longrightarrow {}^{3}_{2}He + {}^{1}_{0}n + 3.27\ MeV(50\%) \\ \text{or } {}^{3}_{1}H + {}^{1}_{1}p + 4.03\ MeV(50\%) \end{aligned} \tag{2.1}$$

$${}^{2}_{1}H + {}^{3}_{2}He \longrightarrow {}^{4}_{2}He + {}^{1}_{1}p + 18.35\ MeV \tag{2.2}$$

$${}^{2}_{1}H + {}^{3}_{1}H \longrightarrow {}^{4}_{2}He + {}^{1}_{0}n + 17.59\ MeV \tag{2.3}$$

where ${}^{1}_{1}p$ and ${}^{1}_{0}n$ refer to proton and neutron, respectively. Currently, the most favorable and efficient reaction in laboratories is the fusion between two hydrogen isotopes Deuterium, D or ${}^{2}_{1}H$, and tritium, T or ${}^{3}_{1}H$. As can be seen in Figure 2.3, this reaction has a higher reaction rate and occurs at a relatively lower temperature, compared to other reactions like Deuterium-Deuterium, $D-D$, and Deuterium-Helium3, $D-He^3$. Deuterium is a safe, widely available and virtually inexhaustible fusion fuel. It can be recovered easily from all forms of water. Tritium, on the other hand, is a fast-decaying radioactive isotope of Hydrogen, which decays to helium3, ${}^{3}_{2}He$, an electron, ${}^{0}_{-1}e$, and an electron-neutrino, ${}^{0}_{0}\nu_e$, according to the following β-decay:

$$ {}^{3}_{1}H \longrightarrow {}^{3}_{2}He + {}^{0}_{-1}e + {}^{0}_{0}\nu_e \tag{2.4} $$

It has a half-life of about 12 years and only occurs in very small quantities in nature. However, tritium can be produced via interaction of the neutrons that escape from the $D-T$ reaction in Eq. (2.3) with lithium contained in a breeding blanket of the fusion reactor:

$$ {}^{1}_{0}n + {}^{6}L_i \longrightarrow {}^{4}_{2}He + {}^{3}_{1}H + 4.8\ MeV \tag{2.5} $$

$$ {}^{1}_{0}n + {}^{7}L_i \longrightarrow {}^{4}_{2}He + {}^{3}_{1}H + {}^{1}_{0}n - 2.5\ MeV \tag{2.6} $$

It should be noted that, due to the production of a secondary neutron, reaction 2.6 is practically more preferable. It does not consume neutrons and can be used as a self-sufficient reaction for tritium production in the blanket wall of fusion reactors.

In order to achieve nuclear fusion in laboratories, we first need to overcome the electrostatic or Coulomb repulsion between the positively charged protons inside the nuclei. To do that both nuclei are accelerated to a very large speed. We know that, at thermal equilibrium, the average speed of the constituent particles of any medium is directly proportional to the square root of the temperature of that medium. Thus, for nuclear fusion to take place, for example for the $D-T$ reaction, a very high temperature of about 100 million degrees Celsius is required. It is clear that at this temperature the atoms are stripped of their electrons; a new state is produced that

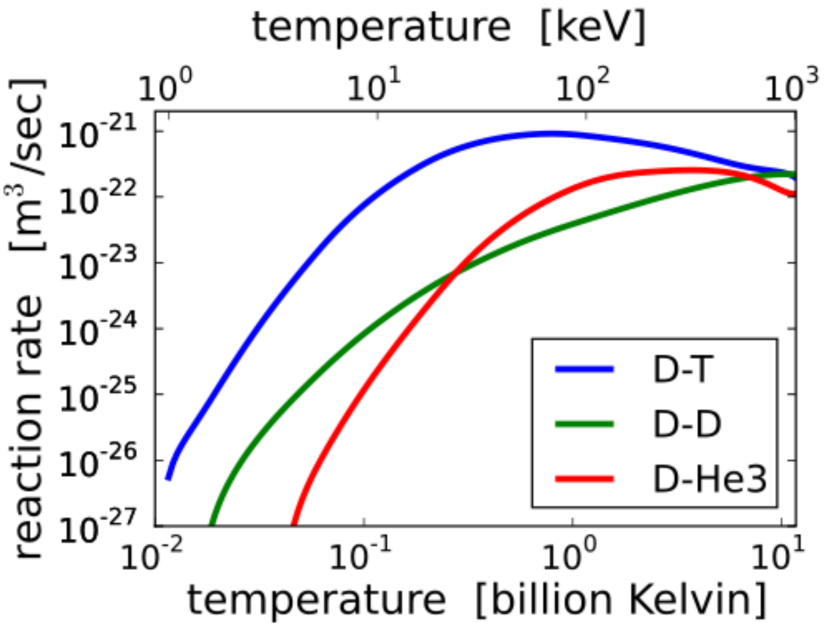

Figure 2.3: Reaction rate for three different fusion reactions between hydrogen isotopes as a function of temperature [50]. Note that, the $D-T$ curve peaks at relatively lower temperature with higher reaction rate compared to the other reactions.

contains both negatively and positively charged particles, which is called plasma.

In general there are two main obstacles that make fusion energy costly and challenging to achieve:

1. Achieving the high temperature at which the fusion reaction takes place

2. Containing the hot plasma (fusion medium)

Obtaining the high temperatures is challenging but feasible. There are three main heating mechanisms that can be employed on fusion reactors [51–53]. These are, ohmic heating, electromagnetic waves (Electron Cyclotron Resonance Heating ECRH and Ion Cyclotron Resonance Heating ICRH), and finally neutral beam injection NBI. Each of these methods can be used simultaneously in a complementary manner to achieve the desired temperature. However, unfortunately, any contact between the material wall of the container and the hot plasma can cause damage to the container and introduces impurities into the plasma that extinguish the fusion reaction. In the following we discuss different magnetic geometries that can be used to hold the hot

plasma away from the material wall.

2.3 Plasma inside Electromagnetic Fields

Plasma is a collection of positively and negatively charged particles. Therefore, it can support electric currents and interact with electromagnetic fields. The equation of motion for a charged particle under the influence of electric $\underline{E}(\underline{r},t)$ and magnetic $\underline{B}(\underline{r},t)$ fields, with charge q_j, mass M_j and velocity $\underline{v}$, is governed by the Lorentz equation:

$$\ddot{\underline{r}} = \dot{\underline{v}} = \frac{q_j}{M_j}\left(\underline{E}(\underline{r},t) + \underline{v} \times \underline{B}(\underline{r},t)\right) \tag{2.7}$$

where $\underline{r}$ refers to the particle's position vector. Here, the subscript $j = e, i$ corresponds to the electron, e, and ion, i, species, respectively. In the following we shall use this equation to investigate the behaviour of a test charge particle in given external electromagnetic fields. This provides important insights into the physics of magnetic confinement fusion. Let us start with the simplest possible case, which is to assume that $\underline{E} = 0$ and $\underline{B}$ is constant. It then follows from Eq. (2.7) that the component of the Lorentz force parallel to the background magnetic field is zero; therefore, the particle moves at constant speed along the magnetic field lines. The perpendicular velocity component, however, restricts the particle motion to a helical path about the magnetic field lines with a particular frequency ω_{cj} (called the cyclotron frequency) and radius ρ_{cj} (called the gyro or Larmor radius):

$$\underline{\omega}_{cj} = \frac{q_j B}{M_j}\hat{\underline{b}} \tag{2.8}$$

$$\underline{\rho}_{cj} = \frac{M_j}{q_j B}\left(\underline{v} \times \hat{\underline{b}}\right) \tag{2.9}$$

where $\hat{\underline{b}}$ is a unit vector along the magnetic field lines and $B = |\underline{B}|$. However, taking into account the effect of other forces, such as $\underline{F} = q_j\underline{E}$ in Eq. (2.7), in general, leads to the so-called drift of the charged particles across the magnetic field lines. Decomposing the particle position $\underline{r}$ into the gyroradius vector $\underline{\rho}_{cj}$ and the guiding

centre position $\underline{R}_c$, then solving Eq. (2.7) for $\underline{R}_c$ we have [54–57]:

$$\dot{\underline{R}}_c = v_{||}\hat{\underline{b}} + \frac{\underline{F}_\perp \times \underline{B}}{q_j B^2} \tag{2.10}$$

The first term on the right hand side leads to a parallel flow without any acceleration. The second term, however, describes a perpendicular particle drift that, in general, depends on both mass and charge of the particles. If the force is independent of charge, this leads to opposing drifts for unlike charged particles and in turn a net current inside the plasma. However, for a constant electric field we have $\underline{F} = q_j \underline{E}$ and the perpendicular drift is reduced to

$$\underline{v}_{E\times B} = \frac{\underline{E}_\perp \times \underline{B}}{B^2} \tag{2.11}$$

This is called the $\underline{E} \times \underline{B}$ drift. It does not depend on mass or the charge of the particles. Therefore, it has the same direction and magnitude for both ions and electrons, such that it generates a net plasma flow but not a current. Based on this simple picture of charged particle interactions with the electromagnetic fields, it can be easily seen that magnetic fields in a particular shape or geometry, can be used to confine hot fusion plasmas and avoid contact with the wall of the container. It should be noted that the plasma confinement inside a bounded volume can be achieved only inside inhomogeneous magnetic fields. In the following, different magnetic geometries to confine plasmas and the associated drifts that come about due to magnetic field inhomogeneities, are considered.

2.3.1 Linear Confinement: Particle Trapping

In a slowly varying magnetic field, such that the gyroradius is small compared to the magnetic field inhomogeneity scale length, the so-called magnetic moment,

$$\mu_j = \frac{M_j v_\perp^2}{2B} \tag{2.12}$$

is a conserved quantity of the particle motion. This plays an important role in one of the first schemes for plasma confinement, namely the magnetic mirror [55]. A magnetic mirror occurs in an inhomogeneous field whose magnitude varies parallel

to the field direction. Such a magnetic field configuration is depicted in Figure 2.4 (a). The physical consequence for such a field is a parallel force which is given by

$$\underline{F}_{||} = -\mu_j \underline{\nabla}_{||} B \tag{2.13}$$

This force does not change the particle total energy, E_n, so that

$$E_n = \frac{M_j v^2}{2} = \frac{M_j v_{||}^2}{2} + \frac{M_j v_{\perp}^2}{2} \tag{2.14}$$

is also a conserved quantity, but this conservation mean $v_{||}$ is converted to $v_{\perp}$ and it can reflect particles when $v_{||}$ is reduced to 0. It is possible for a charged particle, that is introduced into the central region of the mirror, to be reflected at the ends where the magnetic field is stronger. If we assume that B_ℓ and B_h are the magnetic fields at the centre and the throats of the mirror, respectively, from Eq. (2.14) we have

$$v_{||h} = \pm\sqrt{v_{||\ell}^2 + v_{\perp\ell}^2 - v_{\perp h}^2} \tag{2.15}$$

where, $v_{||}$ and $v_{\perp}$, respectively, refer to the parallel and perpendicular components of the velocity vector $\underline{v}$ with respect to the magnetic field B. Eq. (2.15) indicates that in regions where $v_{||\ell}^2 + v_{\perp\ell}^2 > v_{\perp h}^2$ the charged particles can drift in either directions parallel or anti-parallel with respect to the magnetic field lines. In contrast, in regions where $v_{||\ell}^2 + v_{\perp\ell}^2 < v_{\perp h}^2$ the particle velocity is imaginary and, hence, the particles must reverse their directions. Thus, from Eq. (2.15) we have confinement when

$$v_{||\ell}^2 + v_{\perp\ell}^2 \leq v_{\perp h}^2 \tag{2.16}$$

since $v_{||h}^2 = 0$ at or before the mirror throat, and the particle is reflected back towards the centre. Here, the location where $v_{||h}^2 = 0$ corresponds to the mirror (or bounce) point. Turning now to Eq. (2.12), conservation of the magnetic moment yields

$$v_{\perp h}^2 = v_{\perp\ell}^2 \frac{B_h}{B_\ell} \tag{2.17}$$

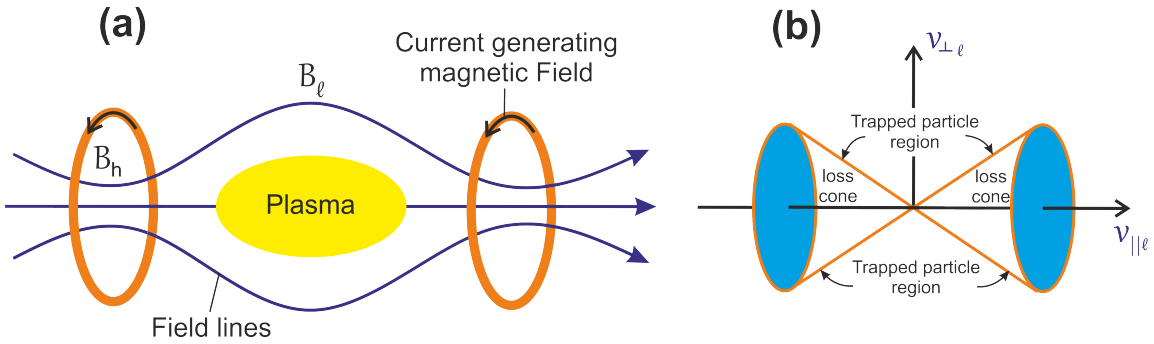

Figure 2.4: (a) The mirror magnetic configuration and (b) the associated loss cone distribution

Upon substituting this equation into Eq. (2.16), it follows that particles are only confined by the magnetic mirror when the following condition is satisfied.

$$v_{||\ell} \leq v_{\perp \ell} \sqrt{\frac{B_h}{B_\ell} - 1} \tag{2.18}$$

This defines a cone in velocity space such as that shown in Figure 2.4 (b). Those particles that fall into the loss cone are not trapped and can escape from both ends of the mirror. If the interactions between particles is disregarded the rest of the charged particles would be trapped. However, certain types of plasma instabilities, as well as Coulomb collisions between the charged particles, can scatter the initially trapped particles into the loss cone region and in turn all of the plasma eventually escapes. Therefore, magnetic mirror machines are not particularly successful devices for plasma confinement. A solution to this problem is to connect both ends to form a closed toroidal magnetic geometry, which is the subject of the following subsection.

2.3.2 Toroidal Confinement

The problem of end losses in magnetic mirror configurations can be overcome by connecting both ends to form a closed geometry in so-called toroidal systems. In such configurations, the magnetic field lines are curved and the magnetic field is stronger on the inboard side compared to the outboard side such that the magnetic gradient points towards the axis of the torus (see Figure 2.5). The curvature of the field lines together with the magnetic field gradient leads to a particle drift across

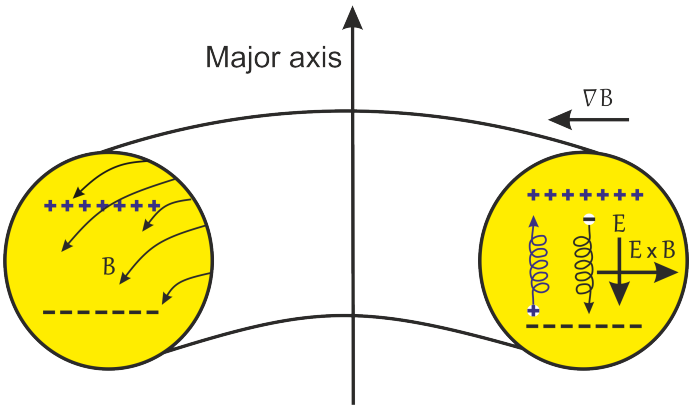

Figure 2.5: Particle drift inside a pure toroidal magnetic field

the magnetic field lines according to the following formula [55]:

$$\underline{v}_{cr} + \underline{v}_{\nabla B} = \frac{M_j}{q_j B^3}\left(v_{||}^2 + \frac{1}{2}v_{\perp}^2\right)\underline{B} \times \underline{\nabla} B \tag{2.19}$$

It should be noted that this gives rise to drifts that are in opposite directions for oppositely charged particles. The ions and electrons drift upward and downward, respectively, such that a space charge electric field attempts to build inside the system. This creates a vertical electric field which in turn, according to the $\underline{E} \times \underline{B}$ of Eq. (2.11), pushes all of the particles toward the outside of the confinement region. Therefore, confinement in pure toroidal fields is not sufficient for fusion.

The way around the problem of cross-field drifts is to introduce a poloidal component to the magnetic field. The resultant magnetic field is now twisted around the minor axis to follow helical paths and map out surfaces called magnetic flux surfaces. A charged particle that follows these helical field lines has no net cross-field drift and in turn averages out the vertical electric field that otherwise causes loss of confinement. The poloidal field component can be created in two different ways; either through a set of external helical coils such as in stellarators [58, 59], or by inducing a toroidal electric current through the plasma which leads to a so-called tokamak [2, 58, 60]. They both have advantages and disadvantages over each other. For example, due to the absence of toroidally induced currents, steady state operation is readily possible in stellarators and current-driven instabilities can be reduced. On the other hand, the magnetic topology in stellarators are inherently three dimensional and technical complications in the construction of coil systems is among the

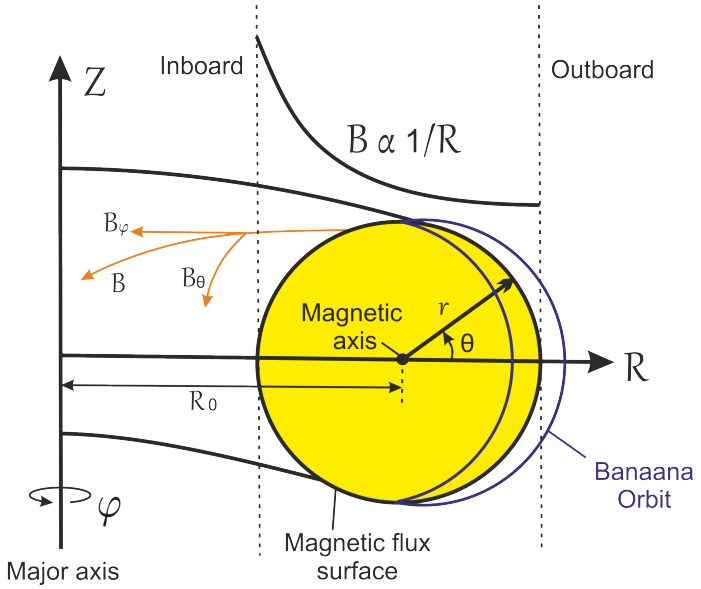

Figure 2.6: Magnetic configuration and field strength for a tokamak in a cylindrical polar coordinate system (R, Z, φ), introducing some key geometrical variables.

disadvantages of stellarators compared to the axisymmetric tokamaks. Stellarators are beyond the scope of this thesis, but more details on stellarators can be found in Refs [58, 59]. Currently, tokamaks are the main approach in which most effort has been invested. For example the next generation of fusion devices, such as ITER, are planned based on the tokamak principles, although there is a large stellarator, Wendelstein 7-X, approaching completion in Germany [61, and the references therein].

In tokamaks, the pitch angle of the magnetic field lines is defined by a quantity called the safety factor q. A useful description of their magnetic topology, as shown in Figure 2.6, is provided by the cylindrical polar coordinates (R, Z, φ), in which the pitch angle can be represented by:

$$\frac{d\ell_\varphi}{d\ell_\theta} = \frac{Rd\varphi}{rd\theta} = \frac{B_\varphi}{B_\theta} \tag{2.20}$$

where, $d\underline{\ell} = d\ell_\theta \underline{\hat{e}}_\theta + d\ell_\varphi \underline{\hat{e}}_\varphi$ is an incremental distance along the magnetic field line and $\underline{\hat{e}}_\theta$ and $\underline{\hat{e}}_\varphi$ are the poloidal and toroidal unit vectors, respectively. We can now rearrange Eq. (2.20) to get:

$$\frac{d\varphi}{d\theta} = \frac{rB_\varphi}{RB_\theta} = q(r) \tag{2.21}$$

Upon integrating we find

$$\theta = \frac{1}{q(r)}\varphi + \bar{\theta} \tag{2.22}$$

where $\bar{\theta}$ represents the constant of integration. From Eq. (2.22), it is obvious that for a single toroidal turn, i.e. $\varphi = 2\pi$, a field line undergoes $1/q$ poloidal turns. Based on the above definition for the safety factor, two different types of magnetic flux surfaces can be identified, namely rational and irrational flux surfaces. On the rational surfaces, the safety factor has rational values, i.e. $q = m/n$, and the field lines are closed upon themselves after m toroidal and n poloidal turns. Contrary to this, field lines on irrational surfaces never close upon themselves and eventually cover the whole toroidal magnetic flux surface. The safety factor, in general, varies from one flux surface to the next, such that its radial variation is characterized by the magnetic shear:

$$\hat{s} = \frac{r}{q}\frac{dq}{dr} \tag{2.23}$$

We now turn to discuss the particle drifts. As shown in Figure 2.6 the magnetic field is stronger in the inboard side compared to the outboard side, which leads to a magnetic field variation approximately of the form

$$B \propto \frac{1}{R} \tag{2.24}$$

where R is the major radius coordinate which is related to the minor radius r and the major radius R_0 of a toroidal flux surface according to

$$R = R_0(1 + \epsilon\cos\theta) \tag{2.25}$$

with, $\epsilon = r/R_0$ is called the inverse aspect ratio. Substituting Eq. (2.25) into Eq. (2.24), assuming that $\epsilon \ll 1$, a binomial expansion to leading order in ϵ gives

$$B \approx \bar{B}\left(\frac{1 - \epsilon\cos\theta}{1 - \epsilon}\right) \tag{2.26}$$

where, the normalisation is chosen such that $\bar{B}$ corresponds to the minimum value of the field strength on the outboard mid-plane ($\theta = 0$). Similar to the magnetic mirror discussed in the previous subsection, a particle that enters at $\theta = 0$ on the low field

side of the tokamak can be reflected when moving towards the inboard side of the tokamak where the field is stronger. Substituting Eq. (2.26) into Eq. (2.17), assuming that $\bar{B} = B_\ell$ at $\theta = 0$, and then substituting Eq. (2.17) back into Eq. (2.14), we finally have

$$\frac{v_{||}^2}{v^2} = 1 - \frac{v_{\perp\ell}^2}{v^2}\left(\frac{1-\epsilon\cos\theta}{1-\epsilon}\right) \tag{2.27}$$

where $v_{\perp\ell}$ is the perpendicular particle speed at $\theta = 0$. We can further simplify this equation by binomial expansion of $1/(1-\epsilon)$ to leading order in ϵ:

$$\frac{v_{||}^2}{v^2} = 1 - \frac{v_{\perp\ell}^2}{v^2}\left[1 + \epsilon(1-\cos\theta)\right] \tag{2.28}$$

It follows from this equation that, a particle is said to be trapped if $v_{||}^2 \leq 0$ at $\theta = \pi$. This in turn leads to the following condition for the trapped particles;

$$\frac{v_{\perp\ell}^2}{v^2}\left[1 + 2\epsilon\right] \geq 1 \tag{2.29}$$

At this point we apply conservation of energy to write $v^2 = v_{||\ell}^2 + v_{\perp\ell}^2$. Substituting this into Eq. (2.29) we get

$$\frac{v_{||\ell}}{v_{\perp\ell}} \leq \sqrt{2\epsilon} \tag{2.30}$$

From this equation we can also determine the fraction of the trapped particles f_t as follows

$$f_t = \sqrt{2\epsilon} \tag{2.31}$$

Finally, it should be noted that trapped particles cannot complete a full turn all the way around the torus, but rather oscillate back and forth between the mirror (or bounce) points. Furthermore, due to the magnetic gradient and curvature drifts, these particles do not stay on the flux surface, but drift across the flux surface such that, as can be seen in Figure 2.6, the poloidal cross-section of their orbit is called a banana orbit. The study of the consequence of these special orbits leads to the neoclassical theory [62, 63], which is important in explaining the baseline energy and particle cross field transport.

2.4 Plasma Cross-field Transport

Confinement in toroidal devices is not perfect. There are different mechanisms by which energy and particles can transport across the magnetic flux surfaces and out of the confinement region. Transport in toroidal systems can be divided into three major types; classical, neoclassical and anomalous (or turbulent) transport [2, 52, 62–64]. In classical theory, the collisions between the charged particles via the long range Coulomb force is considered to be the mechanism for energy and particle transport. To quantify the Coulomb collision effects, we consider a so-called Lorentz model, in which we assume the motion of light "electrons" through a "background" of infinitely massive ions. Without going into the calculation, the collisional frequency ν_{ei} is calculated and written as follow [55]:

$$\nu_{ei} = \frac{\pi n_e e^4}{(4\pi\epsilon_0)^2\sqrt{M_e}\sqrt{(k_B T_e)^3}} \ln\Lambda \tag{2.32}$$

where, n_e, M_e, T_e and k_B are the electron density, electron mass, electron temperature and Boltzmann constant, respectively. Finally, the "Coulomb logarithm" contains, the factor, Λ, where

$$\Lambda = 12\pi n_e \lambda_D^3 \tag{2.33}$$

This is attributed to the so called Debye shielding that cuts off the electric field of the interacting particles over a distance that is long compared to the Debye length $\lambda_D = \sqrt{\frac{\epsilon_0 k_B T_e}{n_e e^2}}$. The above discussion of Coulomb collisions is sufficient for our purpose, but for a more realistic model, in which the background ions are also allowed to move, Refs [63, 65] provide more details. Moreover, for a high temperature fusion plasma charged particles do not usually suffer large angle scatterings between two particle collisions. Instead, a charged particle is gradually deflected by the long range Coulomb-force collectively generated by the background charged particles. These collisions lead to the transport of electrons and ions across the magnetic field lines. If we now treat this cross-field transport of an electron as a random walk process,

we then see that after $\bar{N}$ steps the electron has moved [66, 67]

$$d = \sqrt{\bar{N}}\rho_{ce} = \sqrt{\frac{t}{\tau_{ei}}}\rho_{ce} \quad = \sqrt{\frac{\rho_{ce}^2}{\tau_{ei}}t} = \sqrt{D_{c\ell}t} \tag{2.34}$$

where, $\tau_{ei} = 1/\nu_{ei}$ and t are the time between collisions after one and after $\bar{N}$ collisions, respectively. The classical diffusion coefficient $D_{c\ell}$ is given by

$$D_{c\ell} = \frac{\rho_{ce}^2}{\tau_{ei}} \tag{2.35}$$

Here, the electron Larmor radius ρ_{ce} is considered to be the diffusion step size. Based on this simple theory, an order of magnitude estimate can then be performed to calculate how far an electron can travel across the field lines in one second. To do that, we start by recalling from Eq. (2.9) and assume that $v = v_{th} \sim \sqrt{\frac{k_B T_e}{M_e}}$, where v_{th} is the thermal speed of the electron. For $n_p = 10^{20} m^{-3}$, $B = 1$ Tesla and $T_e = 10KeV$, after one second a typical electron can travel a distance $d \sim 1 - 2cm$. We also know that due to the so-called ambipolar nature of the diffusion in plasmas, ions move the same distance as electrons[1]. It should be also noted that the particles carry energy as they are transported. Due to their large mass compared to electrons, ion-ion collisions are considered as the main classical mechanism for the energy cross-field transport. Considering the ion-ion collisions in the above calculations, it can be easily calculated that, in one second energy can be transported by approximately $10 - 20$ cm. Based on this simple picture of the particle collisions, it then follows from Eq. (1.1) that, using the above values for n_p and T, a fusion reactor of few $\times 10$ cm in diameter can achieve ignition, which led to an early design for a fusion reactor [68].

However, the level of transport that has been measured in laboratory devices was found to be larger by orders of magnitude than predicted by classical theory. We can understand this if we first consider the effect of the toroidal magnetic geometry in confining a group of particles (trapped particles) to the low magnetic field regions on the outboard side of the tokamak plasmas. The study of these particles leads to neoclassical theory. As we have seen in the previous section, the projection of

[1]Note that, collisions between identical particles do not contribute to particle transport.

the trapped particle trajectories onto the poloidal cross section forms a banana like orbit. Here, the radial step size for the particle diffusion is the width of the banana orbits δ_b [59, 69],

$$\delta_b \sim \frac{q}{\sqrt{\epsilon}}\rho_c \tag{2.36}$$

which is larger than the Larmor radius ρ_c. The corresponding diffusion coefficient D_b in the low collisionality (or banana) regime is estimated to be

$$D_b \sim q^2 \epsilon^{-\frac{3}{2}} \frac{\rho_c^2}{\tau} \tag{2.37}$$

Note that we have dropped the subscript e, such that the above two equations can be used for both electron and ion species. It follows from Eq. (2.37) that, the level of particle transport is larger by a factor of $q^2\epsilon^{-\frac{3}{2}}$ than that presented in Eq. (2.35) which is based on the classical theory. This in turn implies that, in order to satisfy Eq. (1.1), we need to build larger fusion reactors compared to those based solely on the predictions of classical theory.

Finally, even neoclassical theory cannot account for the high transport losses observed in toroidal devices [70, 71]. The major contribution to this transport is due to turbulent fluctuations in plasma parameters such as density, temperature, magnetic and electrostatic field. The associated transport is called anomalous (or turbulent) transport. The main source for this transport is believed to be due to the microinstabilities [2, 72]. These are fine scale instabilities that involve the growth of small-scale waves, such that they do not generate a bulk motion of the plasmas, but degrade the plasma confinement by enhancing the level of the fluctuations which in turn increases the diffusion of heat and particles across the magnetic field lines. Therefore, it is of great importance to understand the driving mechanisms underlying the microinstabilities and find a way to suppress or eliminate them completely. This would allow the development of more efficient fusion reactors. The research described in this thesis aims to advance our understanding of microinstabilities in tokamak plasmas, which is a key ingredient in understanding turbulent transport.

Chapter 3

Theoretical Background: Microinstabilities

The main source of turbulent transport is believed to be due to fine scale instabilities, namely microinstabilities [2, 72]. It is also well known that the drift-waves [4, 72, 73] driven unstable by free energy associated with temperature and density gradients are often the dominant tokamak microinstabilities. To investigate the structure and stability of drift waves one needs to couple Maxwell's equations for the evolution of the electromagnetic fields to the evolution of charge and current densities, for which a plasma model is required. There exist many different plasma models. In the following section the general kinetic equation is briefly discussed, from which different plasma models such as two fluid and gyrokinetic models can be derived, as discussed in subsequent subsections.

3.1 Kinetic Equation

Kinetic theory can be used to investigate neutral gas and plasma by describing their constituent particle motions. Due to the presence of a large number of particles, it is impossible (except for simple systems) to follow single particle trajectories, instead a statistical description in terms of the particle distribution function, $f_j(\underline{r}, \underline{v}, t)$ is

typically used. Recall from the previous chapter that the subscript $j = e, i$ corresponds to the electron, e, and ion, i, species. The three coordinates $\underline{r}$, $\underline{v}$, and t refer to space, velocity and time, respectively. The distribution function contains information about the probability to find a particle in a single point of phase space at a given instant of time. The evolution of f_j, is governed by the following equation:

$$\frac{\partial f_j}{\partial t} + \underline{v} \cdot \underline{\nabla}_r f_j + \underline{a} \cdot \underline{\nabla}_v f_j = C(f_j) \tag{3.1}$$

where, $\underline{\nabla}_r$ and $\underline{\nabla}_v$ are gradient operators in spatial and velocity spaces, respectively. This equation is the general kinetic equation that includes physics on all time and spatial scales of interest to most problems. The left hand side of this equation describes physics processes that vary smoothly in $(\underline{r}, \underline{v})$ space and is not sensitive to the discrete-particle nature of the plasma, while the term $C(f_j)$ on the right hand side represents the collisional effects. There are different models commonly adopted for the collision operator, but none are exact. However, for fully ionized plasmas where only binary Coulomb collisions are important, the most useful version of the collisional operator is obtained as follow:

$$C(f_j) = -\sum_{\alpha} \frac{\partial}{\partial v_\alpha}(\langle \triangle v_\alpha \rangle f_j) + \frac{1}{2} \sum_{\alpha,\beta} \frac{\partial^2}{\partial v_\alpha \partial v_\beta}(\langle \triangle v_\alpha \triangle v_\beta \rangle f_j) \tag{3.2}$$

This is the Fokker-Planck collision operator. Here, $\langle \triangle v_\alpha \rangle$ is known as the coefficient of the dynamic friction and $\langle \triangle v_\alpha \triangle v_\beta \rangle$ is called the diffusion tensor. In a plasma, the motion of the constituent charged particles is governed by the electromagnetic fields, such that the acceleration, $\underline{a} = d\underline{v}/dt$, is driven by the Lorentz force Eq. (2.7):

$$\underline{a} = \frac{q_j}{M_j}(\underline{E}(\underline{r}, t) + \underline{v} \times \underline{B}(\underline{r}, t)),$$

Substituting this into equation Eq. (3.1) yields the following equation:

$$\frac{\partial f_j}{\partial t} + \underline{v} \cdot \frac{\partial f_j}{\partial \underline{r}} + \frac{q_j}{M_j}(\underline{E}(\underline{r}, t) + \underline{v} \times \underline{B}(\underline{r}, t)) \cdot \frac{\partial f_j}{\partial \underline{v}} = C(f_j) \tag{3.3}$$

This equation describes the evolution of f_j in the six dimensional phase space, which depends on the electric field $\underline{E}$ and magnetic field $\underline{B}$, self-consistently modified by

the plasma particles, and are described by the following set of Maxwell's equations

$$\begin{aligned}
\underline{\nabla} \cdot \underline{E}(\underline{r}, t) &= \frac{\rho(\underline{r}, t)}{\epsilon_0} && (3.4)\\
\underline{\nabla} \cdot \underline{B}(\underline{r}, t) &= 0 && (3.5)\\
\underline{\nabla} \times \underline{E}(\underline{r}, t) &= -\frac{\partial \underline{B}(\underline{r}, t)}{\partial t} && (3.6)\\
\underline{\nabla} \times \underline{B}(\underline{r}, t) &= \mu_0 \underline{J}(\underline{r}, t) + \frac{\partial \underline{E}(\underline{r}, t)}{c^2 \partial t} && (3.7)
\end{aligned}$$

Here, ϵ_0 and μ_0 are the electric and magnetic permeabilities of free space, respectively. The electric charge density, ρ, and current density, $\underline{J}$, which are the sources for the electromagnetic fields, are determined from the distribution functions

$$\begin{aligned}
\rho(\underline{r}, t) &= \sum_j q_j \int f_j(\underline{r}, \underline{v}, t) dv \\
\underline{J}(\underline{r}, t) &= \sum_j q_j \int \underline{v} f_j(\underline{r}, \underline{v}, t) dv
\end{aligned} \qquad (3.8)$$

where, $dv = dv_x dv_y dv_z$ represents a volume element in velocity space.

Whilst, Eq. (3.3) describes a set of particles in a six dimensional phase space with velocity $\underline{v}$ and location $\underline{r}$, it is very hard to solve in most circumstances. Therefore, more tractable, reduced plasma models have been derived from the kinetic equation by employing various approximations and this is the subject of the following sections.

3.2 Two Fluid Model: Basic Mechanisms of the Drift Waves

Drift waves exist, in general, in a magnetised plasma with inhomogeneous equilibrium profiles [4, 72, 73]. They are characterised by their long parallel wave lengths compared to the perpendicular wavelengths with respect to the equilibrium magnetic field, i.e $\lambda_{||}/\lambda_{\perp} \gg 1$. To understand the basics of drift waves we employ a simplified version of the two fluid model, in which the electrons and ions are treated as two separate fluids. According to this model, neglecting collisional effects, $C(f_j) = 0$, the continuity and momentum equations are [55]:

$$\frac{\partial n_j}{\partial t} + \underline{\nabla} \cdot (n_j \underline{V}_j) = 0 \qquad (3.9)$$

and

$$M_j n_j \left[\frac{\partial \underline{V}_j}{\partial t} + (\underline{V}_j \cdot \underline{\nabla})\underline{V}_j\right] = -\underline{\nabla} P_j + q_j n_j \left(\underline{E} + \underline{V}_j \times \underline{B}\right) \tag{3.10}$$

These equations are simply the first two velocity moments of the kinetic equation (Eq. (3.3)). Here, M_j, n_j, $\underline{V}_j$ and P_j, correspond to the mass, density, fluid velocity and scalar pressure of a given species, respectively [1]. In the following subsections, using this model, the basic physics underlying electron drift waves and ion temperature gradient (ITG) microinstabilities are discussed.

3.2.1 Electron Drift Waves

In the following, for simplicity, we consider a slab of plasma and employ an orthogonal (x, y, z) coordinate system inside a shear-less uniform magnetic field (see for example Figure 3.2). Here, the coordinate system is chosen such that the equilibrium magnetic field is parallel to z and we have a density gradient along x. Now suppose that we are only interested in those waves which are slow compared to the electron thermal speed, $v_{th,e}$, parallel to the magnetic field lines, i.e. $\Omega/k_z \ll v_{th,e}$, where Ω and k_z are the wave characteristic frequency and wave vector parallel to the equilibrium magnetic, respectively. This also implies that the electrons stream rapidly along the magnetic field lines compared to the ions and establish an equilibrium parallel to the magnetic field lines by generating a parallel electric field $\underline{E}_{||}$ to balance the electron pressure gradient. The momentum equation for the electrons (from Eq. (3.10)) is then

$$ne\underline{E}_{||} + \underline{\nabla}_{||} P_e = 0 \tag{3.11}$$

We further assume that the waves are slow compared to the Alfven speed V_A, i.e. $\Omega/k_z \ll V_A$, there is no equilibrium flow and the equilibrium quantities are constant along the magnetic field lines. To proceed we shall decompose the physical quantities according to

$$G = G_0 + \tilde{G} \tag{3.12}$$

[1] The pressure P_j, in general, is a tensor quantity, but for simplicity, in this section, is assumed to be scalar.

where, G_0 and $\tilde{G}$ refer to the equilibrium and perturbed fluctuating quantities for a given plasma parameter, such that $\tilde{G}/G_0 \ll 1$. Linearising Eq. (3.11), limiting ourselves to electrostatic perturbations, i.e. $\underline{B} = \underline{B}_0$ and $\underline{E} = \tilde{\underline{E}} = -\underline{\nabla}\tilde{\phi}$, leads to the following relation between the perturbed electron density $\tilde{n}_e$ and the electrostatic potential $\tilde{\phi}$

$$\frac{\tilde{n}_e}{n_e} = \frac{e\tilde{\phi}}{T_e} \tag{3.13}$$

where, n_e and T_e are the electron equilibrium density and temperature, respectively. Eq. (3.13) is called the adiabatic or Boltzmann response. To obtain the wave dispersion relation, we now turn to the ion dynamics. We assume a perturbation of the following form:

$$\tilde{G} \sim e^{ik_y y + ik_z z - i\Omega t} \tag{3.14}$$

where, k_y is the perpendicular component of the wave vector with respect to the equilibrium magnetic field $\underline{B}_0$. Using this equation, we can transform the time and gradient operators into the Fourier space as, $-i\Omega$ and $i\underline{k} = i(k_y\hat{\underline{e}}_y + k_z\hat{\underline{e}}_z)$, respectively. Here, $\hat{\underline{e}}_y$ and $\hat{\underline{e}}_z$ are unit vectors along the y and z coordinates, respectively. Now employing a cold ion approximation, i.e. $T_i \sim 0$ (or equivalently $P_i \sim 0$), and linearising the continuity and momentum equations for ions in turn leads to the following equations:

$$-i\Omega\tilde{n}_i + in_i\underline{k}\cdot\underline{\tilde{V}}_i + \tilde{V}_{ix}\frac{dn_i}{dx} = 0 \tag{3.15}$$

and

$$-i\Omega\underline{\tilde{V}}_i = \frac{q_i}{M_i}\left(-i\underline{k}\tilde{\phi} + \underline{\tilde{V}}_i \times \underline{B}_0\right) \tag{3.16}$$

Decomposing Eq. (3.16) into its x, y and z components we have

$$\left(1 - \frac{\Omega^2}{\omega_{ci}^2}\right)\tilde{V}_{ix} = -\frac{ik_y}{B_0}\tilde{\phi}, \tag{3.17}$$

$$\tilde{V}_{iy} = -\frac{i\Omega}{\omega_{ci}}\tilde{V}_{ix} \tag{3.18}$$

and

$$\tilde{V}_{iz} = \frac{\omega_{ci} k_z}{\Omega B_0} \tilde{\phi}, \tag{3.19}$$

respectively, where $\omega_{ci} = q_i B_0 / M_i$ is the ion cyclotron frequency. For the modes with small characteristic frequency compared to the cyclotron frequency, i.e. $\Omega/\omega_{ci} \ll 1$, Eq. (3.17) and Eq. (3.18) are, respectively, reduced to

$$\tilde{V}_{ix} \approx -\frac{i k_y}{B_0} \tilde{\phi} \tag{3.20}$$

and

$$\tilde{V}_{iy} \approx 0 \tag{3.21}$$

This indicates that the ion dynamics in the perpendicular direction are dominated by the x component. Using this approximation, we can calculate $\underline{k} \cdot \underline{\tilde{V}}_i$ to obtain

$$\underline{k} \cdot \underline{\tilde{V}}_i = \frac{q_i k_z^2}{M_i \Omega} \tilde{\phi} \tag{3.22}$$

After substituting both Eq. (3.20) and Eq. (3.22) back into Eq. (3.15), we obtain

$$\frac{\tilde{n}_i}{n_i} = \left[\frac{k_y V_{\star e}}{\Omega} + \frac{k_z^2 V_s^2}{\Omega^2} \right] \frac{e\tilde{\phi}}{T_e} \tag{3.23}$$

where,

$$V_{\star e} = -\frac{T_e}{e B_0} \frac{1}{n_i} \frac{dn_i}{dx} \tag{3.24}$$

and

$$V_s = \sqrt{\frac{T_e}{M_i}} \tag{3.25}$$

are the electron diamagnetic drift speed and the ion sound speed, respectively. Finally, using the electron adiabatic response from Eq. (3.13) together with the quasineutrality condition $\frac{\tilde{n}_i}{n_i} = \frac{\tilde{n}_e}{n_e}$, Eq. (3.23) leads to the following dispersion relation

$$\Omega^2 - \Omega \omega_{\star e}^n - k_z^2 V_s^2 = 0 \tag{3.26}$$

where, $\omega^n_{\star e} = k_y V_{\star e}$ is the electron diamagnetic drift frequency. Eq. (3.26) has the following general solutions

$$\Omega = \frac{\omega^n_{\star e}}{2} \pm \frac{1}{2}\sqrt{(\omega^n_{\star e})^2 + 4k_z^2 V_s^2} \tag{3.27}$$

Let us now analyse this equation and describe the solutions in two special limits; assuming constant density, corresponding to $\omega^n_{\star e} = 0$, we have

$$\Omega = \pm k_z V_s \tag{3.28}$$

This is the usual ion sound wave that propagates parallel to the magnetic field lines. On the other hand if we assume that $k_z \to 0$, we then obtain

$$\Omega = 0 \text{ or } \omega^n_{\star e} \tag{3.29}$$

The solution $\Omega = \omega^n_{\star e}$ corresponds to a wave which propagates in the direction of the electron diamagnetic drift and, for this reason, is called the electron drift wave. Assuming $V_s/V_{\star e} = 1.0$, Figure 3.1 presents the full solution to Eq. (3.27); namely the plot of $\Omega/\omega^n_{\star e}$ as a function of k_z/k_y. The physics associated with electron drift waves in a slab geometry in the limit of $k_z/k_y \ll 1$ is shown in Figure 3.2. The rapid flow of electrons along the magnetic field lines leads to the accumulation of positive and negative charges in the region of positive and negative density perturbations, respectively. The resulting charge separation creates a perturbed electric field $\underline{E}_y$ in the y direction, which in turn leads to a cross field $\underline{E}_y \times \underline{B}_z$ drift. For instantaneously responding electrons (or adiabatic electrons) in the above example, the density and drift velocity perturbations are out of phase by 90°. For this simplified example, as can be seen from Eq. (3.27), the drift wave neither damps nor grows. However, it can become unstable by taking into account various kinetic corrections that can provide destabilising effects. For instance electron dissipation either through collisions or in a collisionless plasma through a so-called inverse Landau damping can drive the wave unstable.

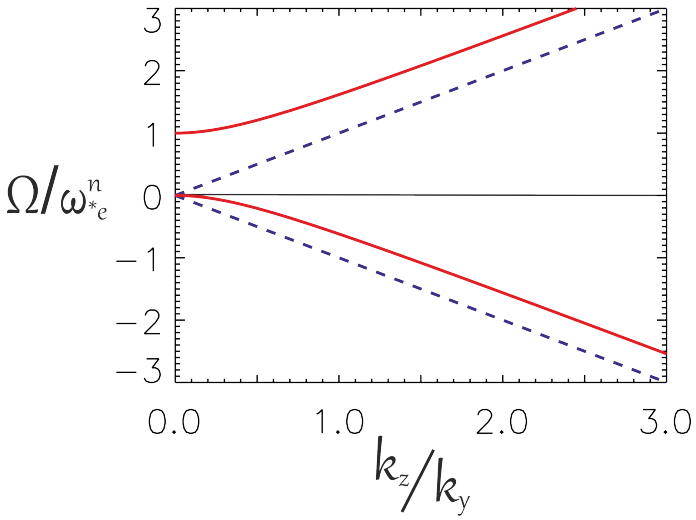

Figure 3.1: Shows the plot of $\Omega/\omega^n_{\star e}$ as function of k_z/k_y taken from Eq. (3.26). Note that we have assumed that $V_s/V_{\star e} = 1.0$ and the two dashed lines corresponds to constant density limits, i.e $\omega^n_{\star e} = 0$.

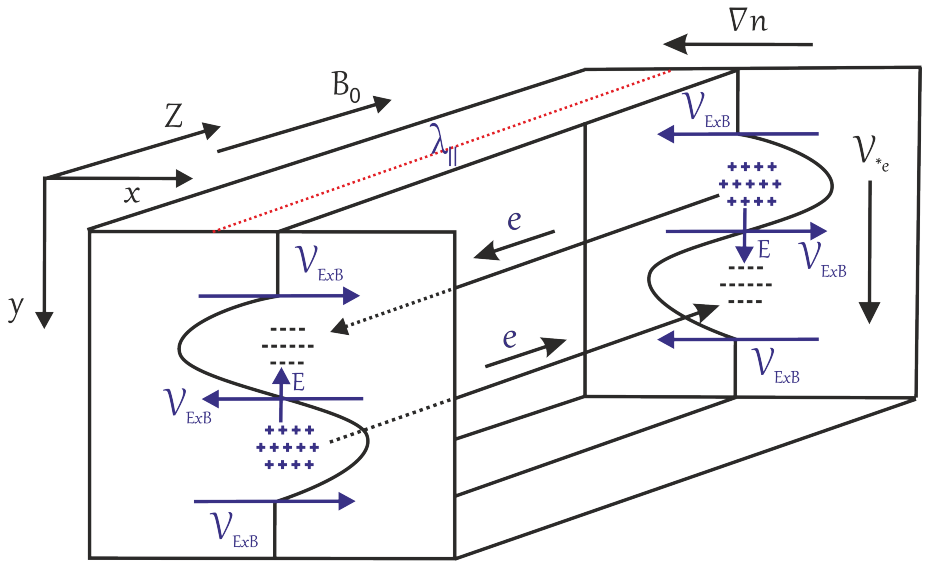

Figure 3.2: Drift Waves in a slab geometry. The equilibrium magnetic field $\underline{B}_0$ is parallel to z, the density gradient $\underline{\nabla} n$ is assumed to be along radial direction, x, and y represents the second perpendicular direction.

3.2.2 The ITG modes

This instability is driven by the ion temperature gradient and is often believed to be responsible for the turbulent transport in the core of tokamaks [26, 74, 75]. In the following, to understand the basic physics underlying the ITG mode the two fluid model is adopted. Here, we shall relax the cold ion assumption of the previous subsection and allow for significant ion temperatures such that the ion pressure is not zero, i.e. $P_i \neq 0$. Furthermore, for the ITG modes one requires $dT_i/dx \neq 0$ and

to describe the pressure fluctuations we assume the adiabatic equation of state:

$$\frac{d}{dt}(P_i n_i^{-\Gamma}) = 0 \tag{3.30}$$

where, Γ is the ratio of specific heats. Using the ion continuity equation, to eliminate the density in the above equation, we get:

$$\frac{\partial P_i}{\partial t} + (\underline{V}_i \cdot \underline{\nabla})\, P_i + \Gamma P_i \underline{\nabla} \cdot \underline{V}_i = 0 \tag{3.31}$$

Now assuming a perturbation of the form previously presented in Eq. (3.14), we linearise the ion continuity equation to obtain:

$$-i\Omega\tilde{n}_i + in_i\underline{k} \cdot \underline{\tilde{V}}_i + \tilde{V}_{ix}\frac{dn_i}{dx} = 0 \tag{3.32}$$

The velocity fluctuation can be calculated from the linearised ion momentum equation,

$$-iM_i n_i \Omega \underline{\tilde{V}}_i = -i\underline{k}\tilde{P}_i - in_i q_i \underline{k}\tilde{\phi} + n_i q_i \underline{\tilde{V}}_i \times \underline{B}_0 \tag{3.33}$$

Taking the parallel and perpendicular components, respectively, leads to

$$\underline{\tilde{V}}_{i||} = \underline{\tilde{V}}_{iz} = \left(\frac{k_z}{M_i\Omega}\right)\left[q_i\tilde{\phi} + \frac{\tilde{P}_i}{n_i}\right]\underline{\hat{e}}_z \tag{3.34}$$

and

$$\tilde{V}_{ix} = -\frac{\omega_{ci}}{i\Omega}\tilde{V}_{iy} \tag{3.35}$$

such that

$$\underline{\tilde{V}}_{i\perp} = \underline{\tilde{V}}_{ix} + \underline{\tilde{V}}_{iy} = \tilde{V}_{ix}\left(-\frac{i\Omega}{\omega_{ci}}\underline{\hat{e}}_y + \underline{\hat{e}}_x\right) \tag{3.36}$$

Note that we are only interested in low frequency waves, such that $\Omega/\omega_{ci} \ll 1$. This implies that $\underline{\tilde{V}}_{i\perp}$ is dominated by the radial component along x, which then leads to

$$\underline{\tilde{V}}_i \approx \tilde{V}_{ix}\underline{\hat{e}}_x + \tilde{V}_{iz}\underline{\hat{e}}_z = \tilde{V}_{ix}\underline{\hat{e}}_x + \left(\frac{k_z}{M_i\Omega}\right)\left[q_i\tilde{\phi} + \frac{\tilde{P}_i}{n_i}\right]\underline{\hat{e}}_z \tag{3.37}$$

Finally, we take the y component of Eq. (3.33) to get

$$\tilde{V}_{iy} = \frac{k_y}{M_i\Omega}\left[q_i\tilde{\phi} + \frac{\tilde{P}_i}{n_i}\right] - \frac{i\omega_{ci}}{\Omega}\tilde{V}_{ix} \tag{3.38}$$

By substituting $\tilde{V}_{ix}$ from Eq. (3.35) into this equation, to the lowest order in Ω/ω_{ci} we have

$$\tilde{V}_{ix} \approx -\frac{ik_y}{q_i B_0}\left[q_i\tilde{\phi} + \frac{\tilde{P}_i}{n_i}\right] \tag{3.39}$$

The first term on the right hand side corresponds to the familiar $\underline{E} \times \underline{B}$ drift whilst the second term is the diamagnetic drift from the pressure gradient. It is worth mentioning that, in the above calculations we have assumed a scalar pressure, however, if we consider a more rigorous approach in which we treat the pressure as a tensor quantity, the diamagnetic component can then be cancelled [76, 77], which is known as gyroviscous cancellation. Eq. (3.39) in turn reduces to

$$\tilde{V}_{ix} \approx -\frac{ik_y}{B_0}\tilde{\phi} \tag{3.40}$$

Taking the scalar product of Eq. (3.37) with the wave vector $\underline{k} = k_y\underline{\hat{e}}_y + k_z\underline{\hat{e}}_z$ we get

$$\underline{k}\cdot\underline{\tilde{V}}_i = \left(\frac{k_z^2}{M_i\Omega}\right)\left[q_i\tilde{\phi} + \frac{\tilde{P}_i}{n_i}\right] = \left(\frac{\omega_s^2}{\Omega T_e}\right)\left[q_i\tilde{\phi} + \frac{\tilde{P}_i}{n_i}\right] \tag{3.41}$$

where, $\omega_s = k_z V_s$ is the ion sound frequency and V_s is defined in Eq. (3.25). Upon substituting Eq. (3.40) and Eq. (3.41) back into Eq. (3.32), using the electron adiabatic response from Eq. (3.13) and the quasineutrality condition $\frac{\tilde{n}_i}{n_i} = \frac{\tilde{n}_e}{n_e}$ to write $\tilde{n}_i$ in terms of $\tilde{\phi}$ we finally have

$$\left[\Omega^2 - \Omega\omega_{\star e}^n - \omega_s^2\right] q_i n_i\tilde{\phi} = \omega_s^2\tilde{P}_i \tag{3.42}$$

Note that we have one equation with two different fluctuating quantities, therefore, we need one more equation to solve for the final dispersion relation. We can obtain the second equation if we apply an identical procedure to the ion pressure in Eq. (3.31), which yields

$$\left[\Omega^2 - \frac{\Gamma\omega_s^2}{\bar{T}}\right]\tilde{P}_i = \left[\frac{\Gamma\omega_s^2}{\bar{T}} - \Omega\omega_\star^P\right] q_i n_i\tilde{\phi} \tag{3.43}$$

where $\bar{T} = T_e/T_i$ is the species temperature ratio and the pressure diamagnetic frequency is defined as:

$$\omega_\star^P = \frac{k_y T_i}{q_i B_0 P_i}\frac{dP_i}{dx} \tag{3.44}$$

Finally, by substituting Eq. (3.42) into Eq. (3.43) we obtain the dispersion relation:

$$\Omega^3 - \Omega^2\omega^n_{\star e} - \Omega\omega_s^2\left(1+\frac{\Gamma}{\bar{T}}\right) + \omega_s^2\left(\omega^P_\star + \frac{\Gamma}{\bar{T}}\omega^n_{\star e}\right) = 0 \tag{3.45}$$

This is a cubic equation that can support growing solutions corresponding to positive imaginary roots. However, in order to investigate the effect of temperature and density gradients, separately, is more convenient to write the above equation in terms of $\omega^T_{\star i}$ and $\omega^n_{\star e}$, where the ion temperature diamagnetic frequency

$$\omega^T_{\star i} = \frac{k_y}{q_i B_0}\frac{dT_i}{dx} \tag{3.46}$$

and note that $\omega^P_\star = \omega^T_{\star e} - \omega^n_{\star e}/\bar{T}$, such that Eq. (3.45) reduces to the following one:

$$\Omega^3 - \Omega^2\omega^n_{\star e} - \Omega\omega_s^2\left(1+\frac{\Gamma}{\bar{T}}\right) + \omega_s^2\left(\omega^T_{\star i} + \left(\frac{\Gamma-1}{\bar{T}}\right)\omega^n_{\star e}\right) = 0 \tag{3.47}$$

Let us now analyse this equation, starting by considering cold ions such that $1/\bar{T} \to 0$, $dT_i/dx = 0$ and assuming $\omega_s \to 0$ such that $\Omega = \omega^n_{\star e}$. This is the electron drift wave dispersion relation which we previously obtained in Eq. (3.29). It should be noted that a general cubic equation $a_1x^3 + a_2x^2 + a_3x + a_4 = 0$, where a_1, a_2, a_3 and a_4 are in general assumed to be real numbers, has at least one complex root if $\Theta < 0$ with $\Theta = 18a_1a_2a_3a_4 - 4a_2^3a_4 + a_2^2a_3^2 - 4a_1a_3^3 - 27a_1^2a_4^2$. In the limit of $dn_i/dx = 0$ and assuming that $\Gamma = \bar{T} = 1$, this leads to ITG instability if $\omega^T_{\star i} > 1.18\omega_s$. This indicates that it is possible to support a small temperature gradient for which an ITG mode is stable, however, it becomes unstable once a critical temperature gradient is exceeded. Taking into account the effect of the density gradient influences the critical value of the temperature gradient. Figure 3.3 shows the boundary between stable and unstable regions as function of $\omega^n_{\star e}/\omega_s$ and $\omega^T_{\star i}/\omega_s$.

In conclusion, we have used a simplified two fluid model in a shear-less slab geometry inside a uniform magnetic field, to obtain a dispersion relation describing various types of waves with their associated instabilities. However, this neglected some important effects. For example, magnetic shear in slab geometry has a stabilising effect [78], but this shear damping can be suppressed in a more realistic toroidal geometry [79], and taking into account plasma flows can also have important ef-

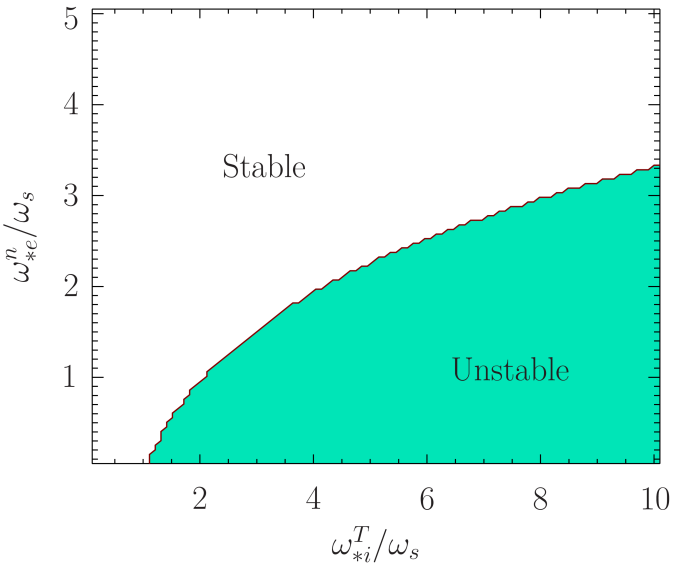

Figure 3.3: The dispersion relation for a two fluid ITG mode in slab geometry as a function of $\omega^n_{\star e}/\omega_s$ and $\omega^T_{\star i}/\omega_s$ under the assumption $\Gamma = 1$ and $\bar{T} = 1$. Note that this plot has been reproduced from [81] with permission.

fects [12, 13, 80]. In addition, to investigate turbulent transport we need to take into account the saturation mechanisms associated with non-linear effects. These together with other kinetic effects like Landau damping and finite ion Larmor radius can modify the stability picture for drift waves. For this reason, a more general and realistic kinetic model, from which the two fluid model is obtained as a limit, should be considered to capture all these important effects. The following section is devoted to a description of the gyrokinetic model.

3.3 The Gyrokinetic Model

The drift mode examples described in the previous section for a slab geometry only cover the very basics of the actual physical process. To capture all the important characteristics that are involved in the physics of the drift waves, one has to solve the full non-linear kinetic equation Eq. (3.3) together with the Maxwell's equations for the electromagnetic fields. Unfortunately, due to the number of variables involved, as well as the large range of time scales associated with different plasma processes, slow ion drift and fast electron gyromotion for instance, which have to be resolved simultaneously, it is not possible to solve this set of equations with current computational resources, except in a few special cases. Therefore, to overcome this problem in the

plasma conditions of interest, this system of equations can be reduced to develop a so-called gyrokinetic model. A full gyrokinetic model incorporates features such as non-linear and non-uniform plasma effects in an arbitrary magnetic geometry [82]. Historically, the first gyrokinetic formalism was originally developed to only treat the linear aspects of the electrostatic perturbations [15, 16]. Electromagnetic effects have since been added [83, 84]. Finally, the model has been further extended to include the study of turbulent transport by taking into account the non-linear terms [17]. In this section we follow the approach presented in Ref [17]. Without going through the mathematical details, we briefly outline the derivation of the collisionless gyrokinetic equation [2].

We start from Eq. (3.3) and ignore the collision term, i.e. $C(f_j) = 0$. Omitting the species label j for convenience, we write the Vlasov equation

$$\frac{\partial f}{\partial t} + \underline{v} \cdot \frac{\partial f}{\partial \underline{r}} + \frac{q}{M}(\underline{E} + \underline{v} \times \underline{B}) \cdot \frac{\partial f}{\partial \underline{v}} = 0 \tag{3.48}$$

In gyrokinetic models, the calculations are usually carried out in the guiding centre phase space $(\underline{R}_c, \underline{U})$ rather than the particle phase space $(\underline{r}, \underline{v})$. These two sets of coordinate systems are related by the following relations:

$$\begin{aligned} \underline{R}_c &= \underline{r} + \frac{\underline{v}_\perp \times \hat{\underline{b}}}{\omega_c} \\ \underline{U} &= \underline{U}(E_n, \mu, \vartheta), \end{aligned} \tag{3.49}$$

where, $E_n = Mv^2/2 + q\phi_0$ and $\mu = Mv_\perp^2/2B_0$ are the particle energy and guiding centre magnetic moments, respectively. The gyroangle, ϑ, together with E_n and μ represent the three velocity coordinates. The parallel, $\underline{v}_{||}$, and perpendicular, $\underline{v}_\perp$, velocity components are defined as:

$$\begin{aligned} \underline{v}_{||} &= v_{||}\hat{\underline{b}} \\ \underline{v}_\perp &= v_\perp(\hat{\underline{e}}_1 \cos\vartheta + \hat{\underline{e}}_2 \sin\vartheta) = v_\perp \hat{\underline{e}}_\perp \end{aligned} \tag{3.50}$$

where, $\hat{\underline{e}}_1$, $\hat{\underline{e}}_2$ and $\hat{\underline{b}} = \underline{B}_0/B_0$, are three orthogonal unit vectors such that $\hat{\underline{e}}_1 \times \hat{\underline{e}}_2 = \hat{\underline{b}}$. The motivation for the above transformation is that for low frequency waves

[2] The collisionless kinetic equation is called the Vlasov equation. Note that, for simplicity we neglect the effect of collisions throughout this section, but a generic and undefined form of the collision operator can be later reintroduced into the final equation.

compared to the cyclotron frequency, i.e. $\Omega/\omega_c \ll 1$, we can decompose the particle movement into three components; the extremely rapid particle gyromotion in a plane perpendicular to $\hat{\underline{b}}$, the fast parallel motion and slow perpendicular guiding centre drift with respect to $\underline{B}_0$. Taking advantage of this approximation, we can average variables over the fast cyclotron motion. This averaging eliminates the coordinate ϑ from the equations, which basically describes the instantaneous position of the particles on a gyro-ring, and in turn reduces the dimensionality of the problem from $6D$ to $5D$, which in turn describes the evolution of an ensemble of rings of charge.

Furthermore, to obtain the gyrokinetic equations, we firstly employ the above approximation to derive a hierarchical set of equations by expanding the distribution function as $f = F_0 + \tilde{f} + ...$ if the following gyrokinetic ordering assumptions are fulfilled:

$$\begin{aligned} &\frac{\Omega}{\omega_c} \sim \frac{\rho_c}{L} \sim \frac{\tilde{f}}{F_0} \sim \frac{q\tilde{\phi}}{T} \sim \frac{\tilde{B}_{||}}{B_0} \sim \frac{\tilde{A}_{||}}{\rho_c B_0} \equiv \lambda \ll 1 \\ &k_{||} L \sim k_\perp \rho_c \sim O(1) \end{aligned} \tag{3.51}$$

where F_0 is the equilibrium distribution function and $\tilde{f}$ is the perturbed part of the distribution function, $\tilde{\phi}$, $\tilde{A}_{||}$ and $\tilde{B}_{||}$ are the perturbed parts of the electrostatic potential, parallel magnetic vector potential and the parallel magnetic field, respectively, such that $\underline{\tilde{B}}_\perp = \hat{\underline{b}} \times \nabla_\perp \tilde{A}_{||}$, L represents the equilibrium scale length of the density, temperature or magnetic field and $k_\perp$ and $k_{||}$ are the characteristic perpendicular and parallel wave vectors with respect to $\underline{B}_0$. The above gyrokinetic ordering greatly simplifies the problem, but still keeps intact the relevant physics, especially the essential properties of the drift waves, for example small gyroradius compared to the long equilibrium scale lengths, perturbations with small amplitudes, and finally the anisotropic nature of the perturbations of interest, i.e. slow variation along the equilibrium magnetic field lines compared to the rapid variation in the perpendicular direction.

Solving the hierarchical equations in the expansion up to $O(\lambda^2)$, and after analysis and manipulation one can obtain the electromagnetic non-linear gyrokinetic

equation which describes the evolution of the gyroangle independent part of the distribution function $\tilde{f}$ such that [17]

$$\tilde{f} = \frac{q\tilde{\phi}}{m}\frac{\partial F_0}{\partial E_n} + \tilde{h}, \tag{3.52}$$

where, the first term on right hand side corresponds to adiabatic response while the second term, $\tilde{h}$, represents the non-adiabatic response. The gyrokinetic equation is written as follows:

$$\frac{\partial \tilde{h}}{\partial t} + U_{||}\hat{\underline{b}} \cdot \underline{\nabla}\tilde{h} + \underline{U}_D \cdot \underline{\nabla}_\perp \tilde{h} = -\left[\frac{q}{m}\frac{\partial F_0}{\partial E_n}\frac{\partial}{\partial t} + \frac{\underline{\nabla} F_0}{B_0} \cdot \hat{\underline{b}} \times \underline{\nabla}_\perp + R_{nl}\right] \langle \tilde{\mathcal{L}} \rangle_\vartheta \tag{3.53}$$

where,

$$\langle \tilde{\mathcal{L}} \rangle_\vartheta = \frac{1}{2\pi}\oint \tilde{\mathcal{L}} d\vartheta \tag{3.54}$$

represents the average over a period in ϑ. In the following we explain different terms in Eq. (3.53).

Using the gyrokinetic ordering expansion, the solutions for the equilibrium distribution function F_0, provides

$$F_0 = F_0(E_n, \underline{R}_c) \tag{3.55}$$

where, F_0 does not depend on the gyrophase angle ϑ and $\hat{\underline{b}} \cdot \underline{\nabla} F_0 = 0$. Note that we have further assumed that F_0 does not depend on μ, i.e. $\partial F_0/\partial\mu = 0$. This is reasonable for the objective of this work as we shall not consider the interaction of the plasma with the external sources. The parameter $\tilde{\mathcal{L}}$ represents the self consistent electromagnetic field perturbations and is defined as follows:

$$\tilde{\mathcal{L}} = \tilde{\phi} - \underline{v} \cdot \underline{\tilde{A}} \tag{3.56}$$

The convective derivative terms are due to the fast motion parallel to the magnetic field lines described by the $U_{||}\hat{\underline{b}} \cdot \underline{\nabla}$ term and the particle drifts across the magnetic field lines are described by the $\underline{U}_D$ term (including the familiar $\underline{E} \times \underline{B}_0$ drift together with the combined magnetic curvature and $\underline{\nabla} B_0$ drifts). The term R_{nl} contains the

non-linear interactions that couple perpendicular modes and is given by

$$R_{nl} = \frac{\underline{\nabla}_\perp \tilde{h}}{B_0} \cdot \hat{\underline{b}} \times \underline{\nabla}_\perp \tag{3.57}$$

This non-linear term leads to additional complications to the solutions of Eq. (3.53) compared to its linear formalism, but provides important effects, such as the saturation of the microinstabilities, which is required for quantitative calculations of both particle and heat transport. However, this thesis is devoted to improving our understanding of the impact of the global effects on linear microinstabilities. Therefore, in what follows, we shall neglect R_{nl}. Note also that we shall limit ourselves to the electrostatic approximation for which the small fluctuations of the magnetic field are neglected, such that from Eq. (3.56) we have $\tilde{\mathcal{L}} = \tilde{\phi}$.

Finally, it should be noted that, there are two methods of solving the gyrokinetic equations numerically, namely the global and the local approximations. In the former, the radial variations of the equilibrium profiles are taken into account, such that the simulations cover many flux surfaces over a substantial radial extent. In contrast to this, if the characteristic radial size of the instability, is much smaller than the equilibrium scale length L, one can then simplify the gyrokinetic equation and exploit the so-called "ballooning transformation" [19, 20, 24] to remove the radial dimension from the problem (or more precisely, treat it as a parameter). This leads to the local gyrokinetic approximation. In this approximation, the problem exploits translational symmetry such that the equilibrium parameters are approximately constant over the radial extent of the instability. In axisymmetric tokamak plasmas, the toroidal angle φ is an ignorable coordinate, and, hence, the spatial component of the global gyrokinetic model that describes the drift waves is usually reduced to a 2D eigenvalue problem in radius, r, and poloidal angle, θ. Applying the ballooning transformation reduces this intrinsic 2D global problem to 1D in the extended ballooning coordinate, η, which is aligned with magnetic field lines. Local gyrokinetic codes solve the gyrokinetic equations along flux tubes lying on a single flux surface and are not capable of providing the radial mode structures directly. Instead they provide the local mode structure along the magnetic field lines together with their

local eigenvalues $\Omega_0(r,p)$, where p can be interpreted as the poloidal location about which the mode peaks, and is a free parameter at this order. However, as we shall see, the global eigenmode structure can be reconstructed purely from solutions of the local gyrokinetic equations by proceeding to consider the higher order theory [5, 13]. In this approach, the solutions from a local gyrokinetic code, for instance GS2 [21, 22], are combined with the higher order theory to reconstruct the global properties, and this is the subject of the rest of this thesis.

Chapter 4

Ballooning Theory

Ballooning theory [24, 85–87] is a very powerful technique to investigate high toroidal mode number, n, instabilities. For this type of mode, the distance between the rational surfaces become very small compared to the equilibrium scale length. Therefore, one can exploit this separation between these two scale lengths and employ the so-called WKB expansion method to transform the calculations and develop an infinite series of solutions. The lowest order in $1/n$ corresponds to the local ballooning solutions that provide both the local mode structures along field lines with their associated local mode frequencies. However, taking into account the higher order terms provides constraints to the local solutions which determine the global (radial) mode structures with their global mode frequencies. In this thesis we reconstruct the global properties for the microinstabilities in tokamak plasmas from the solutions to the local ballooning equations combined with the higher order theory. This chapter introduces the mathematical theory underlying the ballooning transformation and its extension to higher orders.

4.1 Useful Geometrical Identities and Operators

The magnetic topology of tokamaks is usually assumed to be toroidally symmetric. Plasma equilibrium properties are typically approximately constant along the mag-

netic field lines on each magnetic flux surface. A general divergence free equilibrium magnetic field, $\underline{B}$, in an orthogonal coordinate system (ψ, θ, φ), is given by [88]:

$$\underline{B} = I(\psi)\underline{\nabla}\varphi - \underline{\nabla}\psi \times \underline{\nabla}\varphi = B_\varphi \hat{\underline{e}}_\varphi + B_\theta \hat{\underline{e}}_\theta \tag{4.1}$$

where ψ is the poloidal flux within a magnetic surface and represents the radial direction, $I(\psi)$ is a prescribed function which is constant on a magnetic flux surface, θ is an angle like variable in the poloidal direction, and φ the toroidal angle. The Jacobian, J, for this magnetic coordinate system is written as:

$$J = [\underline{\nabla}\psi \cdot \underline{\nabla}\theta \times \underline{\nabla}\varphi]^{-1} \tag{4.2}$$

and the gradient operator $\underline{\nabla}$ is given by

$$\underline{\nabla} = \underline{\nabla}\psi \frac{\partial}{\partial \psi} + \underline{\nabla}\theta \frac{\partial}{\partial \theta} + \underline{\nabla}\varphi \frac{\partial}{\partial \varphi} \tag{4.3}$$

with,

$$\underline{\nabla}\psi = |\underline{\nabla}\psi|\, \hat{\underline{e}}_\psi \tag{4.4}$$

$$\underline{\nabla}\theta = |\underline{\nabla}\theta|\, \hat{\underline{e}}_\theta \tag{4.5}$$

$$\underline{\nabla}\varphi = |\underline{\nabla}\varphi|\, \hat{\underline{e}}_\varphi \tag{4.6}$$

where, $\hat{\underline{e}}_\psi$, $\hat{\underline{e}}_\theta$ and $\hat{\underline{e}}_\varphi$ are the orthogonal unit vectors in the radial, poloidal and toroidal direction, respectively. The three coefficients $|\underline{\nabla}\psi|$, $|\underline{\nabla}\theta|$ and $|\underline{\nabla}\varphi|$ can be determined, as follows. Firstly, we introduce a cylindrical coordinate system which is based on the major axis of the torus, to write

$$|\underline{\nabla}\varphi| = \frac{1}{R} \tag{4.7}$$

After substituting Eq. (4.6) and Eq. (4.7) into Eq. (4.1) and taking the toroidal component of the equilibrium magnetic field, i.e $\underline{B} \cdot \hat{\underline{e}}_\varphi$, we get

$$I(\psi) = RB_\varphi \tag{4.8}$$

We then consider the poloidal component of the magnetic field, i.e. $B_\theta = \underline{B} \cdot \underline{\hat{e}}_\theta$, and after using Eq. (4.4) and Eq. (4.5), from Eq. (4.1) we have

$$|\underline{\nabla}\psi|\,|\underline{\nabla}\varphi|\,\underline{\hat{e}}_\psi \times \underline{\hat{e}}_\varphi = -B_\theta \underline{\hat{e}}_\theta \tag{4.9}$$

Knowing that $\underline{\hat{e}}_\psi \times \underline{\hat{e}}_\varphi = -\underline{\hat{e}}_\theta$, after we substitute $|\underline{\nabla}\varphi|$ from Eq. (4.7), we finally get

$$|\underline{\nabla}\psi| = RB_\theta \tag{4.10}$$

Furthermore, after we substitute $|\underline{\nabla}\varphi|$ and $|\underline{\nabla}\psi|$ from both Eq. (4.7) and Eq. (4.10), respectively, back into Eq. (4.2), and knowing that $\underline{\hat{e}}_\psi \cdot \left(\underline{\hat{e}}_\theta \times \underline{\hat{e}}_\varphi\right) = 1$, we finally get:

$$|\underline{\nabla}\theta| = \frac{1}{JB_\theta} \tag{4.11}$$

Upon substituting Eq. (4.7), Eq. (4.10) and Eq. (4.11) back into Eq. (4.3), the gradient operator $\underline{\nabla}$ is then rewritten as follows:

$$\underline{\nabla} = \underline{\hat{e}}_\psi RB_\theta \frac{\partial}{\partial\psi} + \underline{\hat{e}}_\theta \frac{1}{JB_\theta}\frac{\partial}{\partial\theta} + \underline{\hat{e}}_\varphi \frac{1}{R}\frac{\partial}{\partial\varphi} \tag{4.12}$$

This is a very useful geometric operator that will be used in the subsequent sections. Finally, the line and volume elements are given by

$$(d\ell)^2 = \frac{(d\psi)^2}{(RB_\theta)^2} + (JB_\theta)^2(d\theta)^2 + R^2(d\varphi)^2 \tag{4.13}$$

and

$$dV = Jd\psi d\theta d\varphi \tag{4.14}$$

respectively. In the following section, we shall discuss how the instabilities are localised about the rational surfaces as well as how the coupling between poloidal harmonics leads to unstable modes inside non-uniform sheared magnetic fields.

4.2 Toroidal Coupling

For an axisymmetric toroidal plasma, the toroidal symmetry means that the toroidal dependence of linear fluctuations can be written as $\exp[in\varphi]$, where n is the toroidal mode number. Throughout this section we will consider a single independent toroidal mode number. The linear fluctuating quantities, e.g. electrostatic potential

$\tilde{\phi}(\psi, \theta, \varphi)$, are periodic in θ and φ such that

$$\tilde{\phi}(\psi, \theta, \varphi) = \tilde{\phi}(\psi, \theta + 2\pi, \varphi + 2\pi) = \tilde{\phi}(\psi, \theta, \varphi + 2\pi) = \tilde{\phi}(\psi, \theta + 2\pi, \varphi). \quad (4.15)$$

which then allows us to Fourier expand $\tilde{\phi}(\psi, \theta, \varphi)$ into its individual Fourier modes as follows:

$$\tilde{\phi}(\psi, \theta, \varphi) = \exp[in\varphi]\tilde{\phi}(\psi, \theta) = \exp[in\varphi] \sum_m \tilde{\phi}_m(\psi) \exp[-im\theta] \quad (4.16)$$

where m is the poloidal mode number. Here, both n and m are integers so that the periodicity condition in Eq. (4.15) is satisfied. Note that one aspect of toroidal geometry is that equilibrium parameters depend on poloidal angle, θ, and this leads to coupling of poloidal Fourier harmonics labelled by m.

In the axisymmetric tokamaks the most unstable modes are associated with perturbations that have a long wave length along magnetic field lines but short wave length across them, i.e $k_{||}/k_{\perp} \ll 1$. This can be understood as follows. For large $k_{||}$, the phase velocity of the wave, $v_{ph} = \omega/k_{||}$, becomes small such that a larger number of slower particles can be in resonance with the wave. This in turn leads to stabilisation through Landau damping (for a more complete description of Landau damping see Refs [55, 89, 90]). Therefore, perturbations tend to minimise $k_{||}$ while the perpendicular wave length is typically comparable to the ion Larmor radius, or less.

Furthermore, because the magnetic field line pitch varies across surfaces, the most unstable modes are localized about the rational flux surfaces where $k_{||}$ is small. To understand this, we write $\tilde{\phi}(\psi, \theta, \varphi) \sim \exp[i\underline{k} \cdot \underline{r}]$, where $\underline{r}$ is a position vector, and taking its gradient along the magnetic field lines we have

$$\underline{B} \cdot \underline{\nabla}\tilde{\phi}(\psi, \theta, \varphi) = ik_{||}B\tilde{\phi}(\psi, \theta, \varphi), \quad (4.17)$$

Using Eq. (4.12) for the gradient operator $\underline{\nabla}$, after substituting $\tilde{\phi}(\psi, \theta, \varphi)$ from

Eq. (4.16) into Eq. (4.17) we get

$$\begin{aligned} ik_{||}B\tilde{\phi}(\psi,\theta,\varphi) &= \sum_m \tilde{\phi}_m(\psi)\left[\frac{1}{J}\frac{\partial}{\partial\theta}\exp\left[in\varphi - im\theta\right] + \frac{B_\varphi}{R}\frac{\partial}{\partial\varphi}\exp\left[in\varphi - im\theta\right]\right] \\ &= \left[\frac{-im}{J} + \frac{inB_\varphi}{R}\right]\tilde{\phi}(\psi,\theta,\varphi) \end{aligned} \tag{4.18}$$

Now we can rearrange this equation to get

$$k_{||} = \frac{n}{JB}\left[\hat{q}(\psi,\theta) - \frac{m}{n}\right] \tag{4.19}$$

where the local quantity

$$\hat{q}(\psi,\theta) = \frac{JB_\varphi}{R} \tag{4.20}$$

is related to the "safety factor" $q(\psi)$ by

$$q(\psi) = \frac{1}{2\pi}\oint \hat{q}(\psi,\theta)d\theta \tag{4.21}$$

In the cylindrical limit, corresponding to $\epsilon = 0$ in Eq. (2.26), $\underline{B}$ does not vary with θ, such that $\hat{q}$ is constant on a magnetic flux surface. Thus, on the rational flux surface we can write $\hat{q} = m/n$ which leads to $k_{||} = 0$. As one moves away from the rational surface where $\psi = \psi_0$, we have

$$k_{||} \approx \frac{n}{JB}\frac{\partial\hat{q}}{\partial\psi}\left[\psi - \psi_0\right] \tag{4.22}$$

Thus $k_{||}$ becomes very large as one moves far from the rational surface. However, in a toroidal plasma, because different m are coupled, the mode switches from one m to the next as one moves across rational surfaces. This leads to a so-called "twisted slice" [91] such that the mode structure twists to stay aligned with the field lines even out to quite large distances. Thus in toroidal geometry, many Fourier modes, m, are coupled, but each is highly localised about its rational surface. To understand the essential features of toroidal coupling, we may consider a simplified high aspect ratio toroidal plasma for which the magnetic field is defined by Eq. (2.26):

$$B \sim (1 - \epsilon\cos\theta)$$

The $\cos\theta$ term incorporates the variation of the magnetic field around the flux surfaces. After multiplying Eq. (4.16) by $\cos\theta = \frac{\exp\left[i\theta\right]+\exp\left[-i\theta\right]}{2}$, and integrating over a

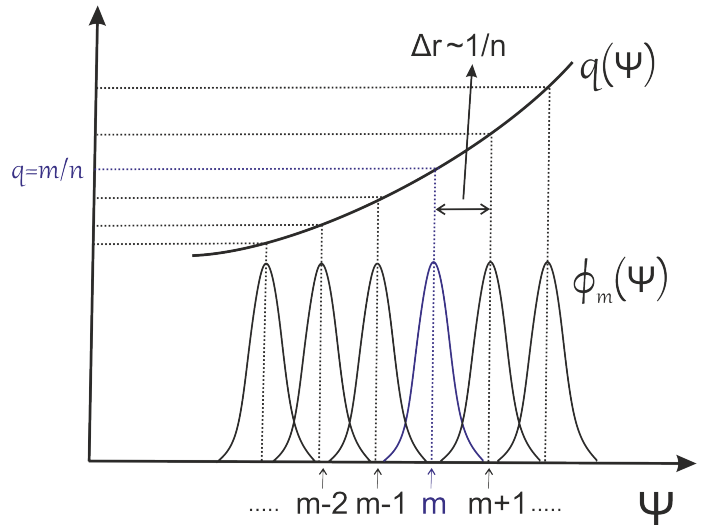

Figure 4.1: Radial separation between rational surfaces about which individual Fourier harmonics of instabilities are localised

period in θ, we get

$$\begin{aligned}\frac{1}{2\pi}\oint \cos\theta\tilde{\phi}(\psi,\theta,\varphi)d\theta &= \frac{1}{2\pi}\sum_m \tilde{\phi}_m(\psi)\oint\left[\frac{e^{i\theta}+e^{-i\theta}}{2}\right]e^{in\varphi-im\theta}d\theta \\ &= \frac{1}{4\pi}\oint\sum_m \tilde{\phi}_m(\psi)\left[e^{-i(m-1)\theta}+e^{-i(m+1)\theta}\right]e^{in\varphi}d\theta \\ &= \frac{1}{2}\left[\tilde{\varphi}_{+1}(\psi)+\tilde{\varphi}_{-1}(\psi)\right]\exp\left[in\varphi\right]\end{aligned} \tag{4.23}$$

Thus, poloidal variation in the equilibrium provide a coupling between the poloidal harmonics and results in two dimensional unstable modes that extend both poloidally and radially across multiple rational surfaces [79].

4.3 High Toroidal Mode Number Instabilities: Shear vs Periodicity

As discussed in the previous section, the poloidal Fourier harmonics are radially localised around the rational surfaces with $k_{||} = 0$. The radial separation between two neighbouring rational flux surfaces can be related to the toroidal mode number, n, through the following formula:

$$\Delta r = \frac{1}{nq'} \tag{4.24}$$

where q' is the derivative of the safety factor with respect to ψ. For high n the rational surfaces are closely packed (see Figure 4.1) and there exist two separate scale lengths: the distance between rational surfaces, Δr, and the equilibrium scale length, L. They satisfy the following gyrokinetic ordering:

$$\frac{\Delta r}{L} \sim O(\frac{1}{n}) \ll 1 \tag{4.25}$$

It is this separation between scale lengths that can be exploited to represent the perturbations in axisymmetric toroidal plasmas in an Eikonal form, which reads:

$$\tilde{\phi}(\psi, \theta, \varphi) = \hat{F}(\psi, \theta) \exp\left[in\hat{S}(\psi, \theta, \varphi)\right] \tag{4.26}$$

where, $\hat{F}(x, \theta)$ incorporates slow variation whilst the exponential incorporates the rapid variation across the magnetic field lines. This representation, however, conflicts with the periodicity requirement in θ. To see this, we start by substituting Eq. (4.26) into Eq. (4.17) to get:

$$\begin{aligned} iBk_{||}\tilde{\phi}(\psi, \theta, \varphi) = \Big(\underline{B} \cdot \underline{\nabla}\hat{F}(\psi, \theta) + in\hat{F}(\psi, \theta)\underline{B} \cdot \underline{\nabla}\hat{S}(\psi, \theta, \varphi)\Big) \\ \times \exp\left[in\hat{S}(\psi, \theta, \varphi)\right] \end{aligned} \tag{4.27}$$

In the limit $n \gg 1$, the first term inside the bracket remains finite and small compared to the second term. As we are interested in the most unstable modes which are elongated along the magnetic field lines with small $k_{||}$, Eq. (4.27) requires

$$\underline{B} \cdot \underline{\nabla}\hat{S}(\psi, \theta, \varphi) = 0 \tag{4.28}$$

This implies that $\hat{S}(\psi, \theta, \varphi)$ is constant along the magnetic field lines such that the perpendicular wave vector is approximately given by $k_\perp \sim n\underline{\nabla}\hat{S}(\psi, \theta, \varphi)$. We also know that for axisymmetric tokamaks the φ dependence can be separated as a single Fourier mode $\sim \exp[in\varphi]$. This in turn allows us to write $\hat{S}(\psi, \theta, \varphi)$ in the form:

$$\hat{S}(\psi, \theta, \varphi) = \varphi + \hat{Y}(\psi, \theta) \tag{4.29}$$

Upon substituting this equation back into Eq. (4.28) and using Eq. (4.12) for the gradient operator $\underline{\nabla}$, we find that:

$$\hat{Y}(\psi, \theta) = -\int^{\theta} \hat{q}(\psi, \theta) d\theta \tag{4.30}$$

where $\hat{q}$ is defined in Eq. (4.20). Finally, using $\hat{Y}(\psi,\theta)$ from Eq. (4.30), and substituting Eq. (4.29) back into Eq. (4.26), we get:

$$\tilde{\phi}(\psi,\theta,\varphi) = \hat{F}(\psi,\theta)\exp\left[in\left(\varphi - \int^{\theta}\hat{q}(\psi,\theta)d\theta\right)\right] \tag{4.31}$$

For $\tilde{\phi}(\psi,\theta,\varphi)$ to be periodic, assuming that $\hat{F}(\psi,\theta)$ is periodic, we require $\exp\left[in\hat{Y}(\psi,\theta)\right]$ to be periodic, which in turn requires

$$n\hat{Y}(\psi,\theta+2\pi) = n\hat{Y}(\psi,\theta) + 2\pi m \tag{4.32}$$

or equivalently

$$n\oint \hat{q}(\psi,\theta)d\theta = 2\pi m \tag{4.33}$$

Using the definition of the safety factor from Eq. (4.21), Eq. (4.33) also implies

$$\frac{1}{2\pi}\oint \hat{q}(\psi,\theta)d\theta = q(\psi) = \frac{m}{n} \tag{4.34}$$

This indicates that on a magnetic flux surface, for which $q(\psi)$ is a rational number, namely on a rational flux surface, the eikonal form in Eq. (4.31) satisfies the periodicity condition. Everywhere else, it does not. Let us now examine the periodicity condition for a small distance away from the rational surface of interest at $\psi = \psi_0$. We employ a Taylor series expansion about $\psi = \psi_0$ to get:

$$n\hat{Y}(\psi,\theta) \approx n\int^{\theta}\hat{q}(\psi_0,\theta)d\theta + n(\psi-\psi_0)\int^{\theta}\left.\frac{\partial\hat{q}(\psi,\theta)}{\partial\psi}\right|_{\psi=\psi_0}d\theta \tag{4.35}$$

Using the periodicity constraint of Eq. (4.32), this reduces to [92]

$$n\left(\hat{Y}(\psi,\theta+2\pi) - \hat{Y}(\psi,\theta)\right) \approx 2\pi n q(\psi) = 2\pi m + 2\pi n(\psi-\psi_0)\left.\frac{dq(\psi)}{d\psi}\right|_{\psi=\psi_0} \tag{4.36}$$

where $q(\psi) = m/n$. It is then quite clear that for $n \gg 1$ even when $\psi - \psi_0 \ll 1$, so long as magnetic shear is not zero, i.e. $dq/d\psi|_{\psi=\psi_0} \neq 0$, the perturbation $\tilde{\phi}(\psi,\theta,\varphi)$ using the eikonal form of Eq. (4.31) is not periodic under the transformation $\theta \to \theta + 2\pi$. To reconcile this conflict between the magnetic shear and periodicity, one should transform the problem from the periodic domain into an infinite one along the magnetic field lines. This is called the ballooning transformation, which we now introduce.

4.4 Ballooning Transformation and Translational Invariance

The aforementioned conflict between periodicity and magnetic shear can be resolved by transforming the solutions from the periodic domain, $0 < \theta < 2\pi$, into an infinite one $-\infty < \eta < +\infty$ via the ballooning transformation [24]. This transformation includes the Fourier transformation of the coefficient $\tilde{\phi}_m(\psi)$ in Eq. (4.16) as follows:

$$\tilde{\phi}_m(\psi) = \frac{1}{2\pi} \int_{-\infty}^{+\infty} \exp\left[-im\eta\right] \hat{f}(\psi, \eta) d\eta \tag{4.37}$$

where, η is the extended ballooning angle along the magnetic field lines. Note that the periodicity condition is replaced by the boundary condition at infinity such that $\hat{f}(\psi, \eta)$ goes to zero as $\eta \to \pm\infty$. One can understand the meaning of this boundary condition as follows. If $\hat{f}(\psi, \eta)$ does not go to zero as $|\eta| \to \infty$ then the integral will not converge and so $\tilde{\phi}_m(\psi)$ would be undefined or infinite. Now substituting Eq. (4.37) into Eq. (4.16) to get[1]:

$$\begin{aligned} \tilde{\phi}(\psi, \theta) &= \sum_m \exp\left[-im\theta\right] \frac{1}{2\pi} \int_{-\infty}^{+\infty} \exp\left[-im\eta\right] \hat{f}(\psi, \eta) d\eta \\ &= \int_{-\infty}^{+\infty} \frac{1}{2\pi} \sum_m \exp\left[-im(\theta + \eta)\right] \hat{f}(\psi, \eta) d\eta \end{aligned} \tag{4.38}$$

We then have Poisson's summation formula identity, which reads

$$\frac{1}{2\pi} \sum_m \exp\left[-im(\theta + \eta)\right] = \sum_N \delta(\theta + \eta - 2\pi N) \tag{4.39}$$

where, δ is the Dirac delta function and N is an integer. Substituting this identity back into Eq. (4.38) we get

$$\begin{aligned} \tilde{\phi}(\psi, \theta) &= \int_{-\infty}^{+\infty} \sum_N \delta(\theta + \eta - 2\pi N) \hat{f}(\psi, \eta) d\eta \\ &= \sum_N \hat{f}(\psi, \theta - 2\pi N). \end{aligned} \tag{4.40}$$

[1]Note also that, as we have mentioned earlier, the φ dependence has been dropped. This is because the toroidal behaviour is described solely by the toroidal mode number, n, and can be recovered by multiplying the solution by $\exp\left[in\varphi\right]$. Therefore in what follows we only focus on the two dimensional problem in ψ-θ space.

It can be seen from this equation that, by summing infinite copies of a non periodic function $\hat{f}$, a periodic function $\tilde{\phi}$ can be reconstructed. Furthermore, using the ballooning transformation of Eq. (4.38) allows us to map the original two dimensional eigenvalue problem in $\psi - \theta$ space, described by

$$\mathcal{L}(\psi, \theta)\tilde{\phi}(\psi, \theta) = \Omega\tilde{\phi}(\psi, \theta) \tag{4.41}$$

to the following one in $\psi - \eta$ space:

$$\mathcal{L}(\psi, \eta)\hat{f}(\psi, \eta) = \Omega\hat{f}(\psi, \eta) \tag{4.42}$$

It is important to note that, Eq. (4.42) generates the same periodic solution of Eq. (4.41) with the same eigenvalue Ω. The advantage of the ballooning transformation is that the requirement for periodicity is guaranteed allowing an eikonal representation of the following form to be adopted

$$\hat{f}(\psi, \eta) = \hat{A}(\psi, \eta) \exp\left[-inq'(\psi\eta - \hat{S}(\psi))\right] \tag{4.43}$$

where $\hat{A}(\psi, \eta)$ is slowly varying, $\hat{S}(\psi)$ (defined in Eq. (4.29)) is constant along the magnetic field lines and varies slowly with ψ, but such that $\exp\left[inq'\hat{S}(\psi)\right]$ varies rapidly across the magnetic field lines. This incorporates the important characteristic $k_{||}/k_{\perp} \ll 1$.

For high n instabilities, the eigenvalue problem can be solved by expanding in the small parameter $\Delta r/L \sim 1/n$. To lowest order, the poloidal Fourier modes $\tilde{\phi}_m$, $\tilde{\phi}_{m-1}$, $\tilde{\phi}_{m+1}$, ..., experience the same equilibrium parameters, because (a) they are centred on their mode rational surfaces, and (b) the distance between rational surfaces goes to zero as $n \to \infty$. Thus, we may expect them to have the same mode structure and write (see also figure 4.1):

$$\tilde{\phi}_m(\psi) \approx \tilde{\phi}_{m-1}(\psi) \approx \tilde{\phi}_{m+1}(\psi) \approx .... \tag{4.44}$$

This indicates that the problem possesses translational invariance and therefore it is appropriate to seek a solution of the following form:

$$\tilde{\phi}_m(\psi) = \tilde{\phi}_0(nq - m) \exp\left[imp\right] \tag{4.45}$$

Here q is assumed to provide a suitable radial coordinate and p is a free parameter called the ballooning phase angle which contains the relative phases of each poloidal mode. By substituting this back into equation Eq. (4.16), one can derive

$$\tilde{\phi}(\psi,\theta) = \sum_m \tilde{\phi}_0(nq-m)\exp\left[-im(\theta-p)\right] \tag{4.46}$$

It is obvious from *Eq.* (4.46) that the perturbation $\tilde{\phi}(\psi,\theta)$ peaks at $\theta = p$ where there is constructive interference between the Fourier modes. Now the transformation from periodic domain, $0 < \theta < 2\pi$, into an infinite domain, $-\infty < \eta < +\infty$ can be carried out by Fourier transforming $\tilde{\phi}_0(nq-m)$;

$$\tilde{\phi}_0(nq-m) = \frac{1}{2\pi}\int_{-\infty}^{+\infty} \xi(\eta)\exp\left[-i(nq-m)\eta\right]d\eta, \tag{4.47}$$

and substituting Eq. (4.47) back into Eq. (4.46) to yield

$$\tilde{\phi}(\psi,\theta) = \frac{1}{2\pi}\sum_m \exp\left[-im(\theta-p)\right]\int_{-\infty}^{+\infty} \xi(\eta)\exp\left[-i(nq-m)\eta\right]d\eta \tag{4.48}$$

Finally, using this equation, one can transform the original two dimensional problem of Eq. (4.41) in $\psi-\theta$ space into the following one dimensional one in η space

$$\mathcal{L}_0(\eta;\psi,p)\xi(\eta) = \Omega_0(\psi,p)\xi(\eta) \tag{4.49}$$

This is a local eigenvalue equation obtained for the lowest order expansion in $1/n$. Here, $\mathcal{L}_0$ is a differential operator in η, with ψ and p as parameters. From this equation we can get both the local mode structure, $\xi(\eta)$, and the associated local eigenvalue $\Omega_0(\psi,p)$. Here both radius ψ and ballooning angle p are free parameters, but their choice is constrained in the higher order theory. In the next section we discuss the higher order treatment which determines ψ and p and shows how to reconstruct the global solution from the local model.

4.5 From Local to Global Ballooning Analysis: The Formalism

In this section the theoretical formalism on which this thesis is based is presented. The methodology we implement here has been previously used, for example in

Ref [81]. This section builds on Ref [25, 26, 81] and improves the technique and method to provide a rigorous mathematical framework. Our procedure is quite general and can be used with any local code, gyrokinetic or MHD local code. In this thesis we have particularly focused on gyrokinetic models. In particular, we have employed the local gyrokinetic code, GS2 [21, 22], to solve the leading order linearised gyrokinetic equation [15, 17] numerically. From GS2 we can obtain both the local mode structure along a given magnetic field line $\xi(x_s, p, \eta)$, in the infinite domain in η, together with associated local eigenvalue, $\Omega_0(x_s, p)$. Here, $x_s = (r - r_0)/a$ is the normalised radial distance from the reference surface r_0 and a is the minor radius of the last closed flux surface[2]. It should be noted that the independent variable x_s in the argument of ξ incorporates the slow variations of the equilibrium profiles and, together with p, are free parameters in this order. To reconstruct the linear global mode properties from these local modes, rather than using the ballooning transformation, we employ the related Fourier-Ballooning (FB) representation [87]:

$$\tilde{\phi}(x_s, \theta, t) = \int_{-\infty}^{\infty} \xi(x_s, p, \theta, t) \exp\left[-inq\theta\right] \exp\left[inq' x_s p\right] A(p) dp \tag{4.50}$$

where $\tilde{\phi}(x_s, \theta, t)$ corresponds to the global mode structure for fluctuations in the electrostatic potential, and we have Taylor expanded

$$q(x_s) \approx q_0 + q' x_s = q_0 + \left.\frac{dq}{dx_s}\right|_{x_s=0} x_s \tag{4.51}$$

Here q_0 and q' refer to the safety factor and its radial derivative at $x_s = 0$, respectively. Note that, unlike the conventional ballooning transformation, in Eq. (4.50) we have the periodic poloidal angle θ instead of the infinite domain in η. However, the mapping from η to θ is possible and can be performed via the following symmetry property

$$\xi(x_s, p + 2\ell\pi, \theta + 2\ell\pi) = \xi(x_s, p, \theta) \tag{4.52}$$

where ℓ is an integer. It is worth mentioning that the time dependence in both the linear global modes, $\tilde{\phi}(x_s, \theta, t)$ and $\xi(x_s, p, \theta, t)$ can be separated from the spatial

[2]Note that in what follows, for the rest of this thesis, we shall replace ψ with x_s to represent the radial distance from a reference rational surface at $x_s = 0$

dependence, which then allows us to write

$$\tilde{\phi}(x_s, \theta, t) = \tilde{\phi}(x_s, \theta) \exp\left[-i\Omega t\right] \tag{4.53}$$

and

$$\xi(x_s, p, \theta, t) = \xi(x_s, p, \theta) \exp\left[-i\Omega_0(x_s, p)t\right] \tag{4.54}$$

where Ω and $\Omega_0(x_s, p)$ are the global and local complex linear eigenmode frequencies, respectively. Furthermore, we note from Eq. (4.50) that, to find the global mode structure, $\tilde{\phi}(x_s, \theta, t)$, one needs to first calculate the envelope $A(p)$, for which we need to employ the higher order theory which we now turn to discuss. We start by taking the time derivative of Eq. (4.53) which provides a global eigenmode satisfying

$$\frac{\partial \tilde{\phi}(x_s, \theta, t)}{\partial t} = -i\Omega \tilde{\phi}(x_s, \theta, t) \tag{4.55}$$

where $\Omega = \omega + i\gamma$, with ω and γ the global frequency and growth rate, respectively. Substituting Eq. (4.50) into Eq. (4.55) we obtain

$$-i\Omega \tilde{\phi}(x_s, \theta, t) = \int_{-\infty}^{\infty} \left[\frac{\partial \xi(x_s, p, \theta, t)}{\partial t}\right] \exp\left[-inq\theta\right] \exp\left[inq' x_s p\right] A(p) dp \tag{4.56}$$

where $\partial \xi(x_s, p, \theta, t)/\partial t$ can be evaluated from Eq. (4.54), which provides

$$\frac{\partial \xi(x_s, p, \theta, t)}{\partial t} = -i\Omega_0(x_s, p)\xi(x_s, p, \theta, t) \tag{4.57}$$

Substituting Eq. (4.57) into Eq. (4.56), using Eq. (4.50) for $\tilde{\phi}$, we have

$$\int_{-\infty}^{\infty} \left[\Omega - \Omega_0(x_s, p)\right] \xi(x_s, p, \theta, t) \exp\left[-inq\theta\right] \exp\left[inq' x_s p\right] A(p) dp = 0 \tag{4.58}$$

In the limit of $n \gg 1$, exploited by the local codes, we expect the radial extent of the reconstructed global modes to be very small compared to the equilibrium scale lengths. Therefore, we may Taylor expand Ω_0 to second order in x_s about $x_s = 0$ to write:

$$\Omega_0(x_s, p) = f(p) + S(p)x_s + R(p)x_s^2 \tag{4.59}$$

where the three functions $f(p) = \Omega_0(x_s = 0, p)$, $S(p) = \frac{\partial \Omega_0(x_s, p)}{\partial x_s}|_{x_s=0}$ and $R(p) = \frac{1}{2}\frac{\partial^2 \Omega_0(x_s, p)}{\partial x_s^2}|_{x_s=0}$ are, in general, complex and periodic in p. Substituting Eq. (4.59)

into Eq. (4.58), we get

$$\int_{-\infty}^{\infty} \left[\Omega - \left(f(p) + S(p)x_s + R(p)x_s^2\right)\right] A(p)\xi(x_s, p, \theta, t) \exp\left[-inq\theta\right] \exp\left[inq'x_s p\right] dp = 0. \tag{4.60}$$

We note that $nq'p$ is a radial wave number, and assuming $A(p)$ varies much more rapidly than ξ with p, we can use Eq. (4.50), integrating by parts, to derive the following relation

$$(x_s)^\ell A(p) \to \left(\frac{i}{nq'}\right)^\ell \frac{d^\ell A(p)}{dp^\ell} \tag{4.61}$$

for any positive integer ℓ, which in turn transforms Eq. (4.60) into the following:

$$\int_{-\infty}^{\infty} \left[\Omega A(p) - \left(f(p) + \frac{iS(p)}{nq'}\frac{d}{dp} - \frac{R(p)}{(nq')^2}\frac{d^2}{dp^2}\right) A(p)\right] \times \xi(x_s, p, \theta, t) \exp\left[-inq\theta\right] \exp\left[inq'x_s p\right] dp = 0. \tag{4.62}$$

The integration in Eq. (4.62) must vanish for all values of θ, and this in turn leads to the following second order linear differential equation for $A(p)$:

$$\frac{R(p)}{(nq')^2}\frac{d^2A(p)}{dp^2} - \frac{iS(p)}{nq'}\frac{dA(p)}{dp} + \left[\Omega - f(p)\right] A(p) = 0 \tag{4.63}$$

Knowing that $\tilde{\phi}(x_s, \theta, t)$ is periodic in θ, from Eq. (4.50) this requires that $A(p)$ must also be periodic in p. Therefore, we solve Eq. (4.63), imposing periodic boundary conditions, to evaluate both $A(p)$ with its associated eigenvalue Ω. This solution of $A(p)$, can be used along with $\xi(x_s, p, \theta, t)$ from a local code, for example GS2, to reconstruct the full global mode structure, $\tilde{\phi}(x_s, \theta, t)$, from Eq. (4.50).

Finally, it is important to mention that, in what follows, in the rest of this thesis, the explicit t dependence will be dropped and, in turn, $\tilde{\phi}(x_s, \theta)$ and $\xi(x_s, p, \theta)$ will be used to represent the spatial dependence. The following section is devoted to providing a technique to solve Eq. (4.63) numerically.

4.6 Numerical Solutions

We solve the eigenvalue problem of Eq. (4.63) numerically using finite differences to transform the governing differential equation into a system of simultaneous linear

algebraic equations. We first approximate the derivatives A' and A'' at each node j via 2nd order central differences

$$A' = \frac{A_{j+1} - A_{j-1}}{2\Delta p} \tag{4.64}$$

$$A'' = \frac{A_{j+1} - 2A_j + A_{j-1}}{(\Delta p)^2} \tag{4.65}$$

where the step size $\Delta p = p_{j+1} - p_j$ is the (uniform) distance between two consecutive mesh points. Substituting these back into Eq. (4.63), we obtain

$$\alpha_j A_{j+1} + \beta_j A_j + \mu_j A_{j-1} = \bar{\Gamma} A_j \tag{4.66}$$

where the coefficients α_j, β_j and μ_j, in general, depend on p and represent the coefficients of the equation acting respectively at the $j+1$, j and $j-1$ mesh points. They are defined as follows:

$$\begin{aligned} \alpha_j &= R_j - \frac{inq'\Delta p}{2} S_j \\ \beta_j &= -2R_j - (nq'\Delta p)^2 f_j \\ \mu_j &= R_j + \frac{inq'\Delta p}{2} S_j \end{aligned} \tag{4.67}$$

Equation (4.66) defines a system of simultaneous linear algebraic equations with $\bar{m}$ unknown eigenvalues $\bar{\Gamma} = -(nq'\Delta p)^2\Omega$ with their associated eigenfunctions A. Here, $\bar{m}$ is the total number of p-mesh points. It can be written in matrix form as follows:

$$\begin{pmatrix} \beta_1 & \alpha_1 & 0 & 0 & \cdots & \mu_1 \\ \mu_2 & \beta_2 & \alpha_2 & 0 & \cdots & 0 \\ 0 & \mu_3 & \beta_3 & \alpha_3 & \cdots & \vdots \\ \vdots & \vdots & \ddots & \ddots & \ddots & 0 \\ 0 & 0 & 0 & \mu_{\bar{m}-1} & \beta_{\bar{m}-1} & \alpha_{\bar{m}-1} \\ \alpha_{\bar{m}} & 0 & \cdots & 0 & \mu_{\bar{m}} & \beta_{\bar{m}} \end{pmatrix} \begin{pmatrix} A_1 \\ A_2 \\ A_3 \\ \vdots \\ A_{\bar{m}-1} \\ A_{\bar{m}} \end{pmatrix} = \bar{\Gamma} \begin{pmatrix} A_1 \\ A_2 \\ A_3 \\ \vdots \\ A_{\bar{m}-1} \\ A_{\bar{m}} \end{pmatrix} \tag{4.68}$$

Note that we have applied the periodic boundary condition at both ends of the intervals, i.e. $\mu_1 A_{\bar{m}} = \mu_1 A_0$ and $\alpha_{\bar{m}} A_{\bar{m}+1} = \alpha_{\bar{m}} A_1$. This in turn has replaced the zeros in the last element of the first row with μ_1 and the first element of the last row with $\alpha_{\bar{m}}$, respectively. To solve this equation we firstly write it down in a short

matrix notation

$$\sum_{j=1}^{\bar{m}} \left(Q_{ij} - \bar{\Gamma} I_{ij}\right) A_j = 0 \tag{4.69}$$

For all i in the range $1 \leq i \leq \bar{m}$. Here I is the identity matrix and Q_{ij} represents the elements of a square, complex, non-symmetric, almost tridiagonal, matrix. This system is suitable to be solved via the so called QR algorithm. For this reason, to compute all eigenvalues Γ and non trivial eigenvectors $A \neq 0$ for Q, we have employed the LA_EIGENPROBLEM IDL built in function. This function uses the QR algorithm [93] and is based on the LAPACK library that provides routines for solving systems of simultaneous linear equations.

4.7 Isolated and General Modes: Two Special Analytic Limits

Equation (4.63) has been already solved analytically in two limits [5, 18, 19, 25]: either $S(p) = 0$ or $R(p) = 0$. These lead to two different eigenmode classes, referred to as "isolated modes" when $S(p) = 0$ and "general modes" when $S(p) \neq 0$, but $R(p) = 0$.

4.7.1 Pure Isolated Modes

This class of eigenmode was originally studied in the context of ideal MHD [23, 24]. They can only be observed for a special set of the equilibrium parameters, where $\Omega_0(x_s, p)$ is stationary at $x_s = 0$, i.e. $S(p) = \partial\Omega_0/\partial x_s|_{x_s=0} = 0$. As we discuss in the following, this leads to a highly unstable mode that usually sits on the outboard mid-plane, radially centred about $x_s = 0$ [5, 19].

For isolated modes, where $S(p) = 0$, Eq. (4.63) reduces to

$$\frac{R(p)}{(nq')^2}\frac{d^2A}{dp^2} + \left[\Omega - f(p)\right] A = 0 \tag{4.70}$$

This equation is still hard to solve exactly. However as we are only interested in the $nq' \gg 1$ limit, the solutions for $A(p)$ are highly localised in p. Therefore, assuming

an up-down symmetric equilibrium, we may apply the Taylor series expansion to expand about $p = 0$ and replace $R(p)$ and $f(p)$ with $R(0)+\frac{R''(0)}{2}p^2$ and $f(0)+\frac{f''(0)}{2}p^2$, respectively. This leads to a Hermite equation which has a ground state solution, called the fundamental mode, of the form

$$A(p) = e^{-\chi p^2} \tag{4.71}$$

where, χ is a constant that can be determined after we substitute Eq. (4.71) into Eq. (4.70) and collect coefficients:

$$\begin{aligned}\left(\frac{2R''(0)\chi^2}{n^2q'^2}\right)p^4 + \left(\frac{\chi^2 R(0)}{n^2q'^2} - \frac{\chi R''(0)}{n^2q'^2} - \frac{f''(0)}{2}\right)p^2 \\ + \left(\Omega - f(0) - \frac{2\chi R(0)}{n^2q'^2}\right)p^0 = 0\end{aligned} \tag{4.72}$$

Considering powers of p separately (neglecting p^4 which is small); from the coefficient in front of p^0 we obtain the global complex mode frequency in terms of a, which reads;

$$\Omega = f(0) + \frac{2\chi R(0)}{n^2q'^2} \tag{4.73}$$

From the coefficient in front of p^2, a non-trivial solution for χ can be easily obtained

$$\chi = \frac{R''(0)}{8R(0)} \pm nq' \frac{\sqrt{\left(\frac{R''(0)}{nq'}\right)^2 + 8R(0)f''(0)}}{8R(0)} \underset{n\to\infty}{\approx} \pm nq'\sqrt{\frac{f''(0)}{8R(0)}} \tag{4.74}$$

Note that the sign of the square root is chosen such that $A(p)$ is localized in p space. Moreover, as a necessary localization condition the real component of χ, namely χ_r, should be finite and positive, i.e. $\chi_r > 0$. In the limit of $nq' \to \infty$, the eigenvalue Ω approaches the local complex mode frequency evaluated at the stationary point, here assumed to be $x_s = 0$, and $p = 0$, i.e. $\Omega = \mathrm{Max}[\Omega_0(x_s, p)] = f(0)$. Thus one selects the maximally unstable value of x_s and p.

Now to reconstruct the global mode structure and calculate its radial width, we substitute $A(p) = \exp(-\chi p^2)$ into Eq. (4.50), completing the square in p, to obtain

$$\begin{aligned}\tilde{\phi}(x_s, \theta) = \exp\left[-inq\theta - \frac{n^2q'^2x_s^2}{4\chi}\right]\int_{-\infty}^{+\infty}\xi(x_s, p, \theta) \\ \times \exp\left[-\chi\left(p - \frac{inq'x_s}{2\chi}\right)^2\right]dp\end{aligned} \tag{4.75}$$

Assuming that the local mode structure $\xi(x_s, p, \theta)$ varies slowly with p compared to $A(p)$ and applying the so-called stationary phase approximation, from Eq. (4.75) we obtain:

$$\begin{aligned}\tilde{\phi}(x_s,\theta) \approx \xi(x_s, p=0, \theta) \exp\left[-inq\theta - \frac{n^2 q'^2 x_s^2}{4\chi}\right] \\ \times \int_{-\infty}^{+\infty} \exp\left[-\chi\left(p - \frac{inq'x_s}{2\chi}\right)^2\right] dp\end{aligned} \tag{4.76}$$

Here, $\xi(x_s, p=0, \theta)$ determines the poloidal extent of the global mode and $p=0$ corresponds to where $A(p)$ peaks in p space. Finally, the integration on the right side is a Gaussian integral with a complex shift $\frac{inq'x_s}{2\chi}$. We can change variables, $p \to \acute{p} + \frac{inq'x_s}{2\chi}$, such that the integral transforms to the normal Gaussian and the result is [94, pp. 121 and 95, pp. 413-414][3]

$$\int_{-\infty}^{+\infty} \exp\left[-\chi\left(p - \frac{inq'x_s}{2\chi}\right)^2\right] dp = \int_{-\infty+\frac{inq'x_s}{2\chi}}^{+\infty+\frac{inq'x_s}{2\chi}} \exp\left[-\chi\left(\acute{p}\right)^2\right] d\acute{p} = \sqrt{\frac{\pi}{\chi}} \tag{4.77}$$

This leads to an analytic approximation for the reconstructed global mode structure;

$$\tilde{\phi}(x_s,\theta) \approx \xi(x_s, p=0, \theta) \exp\left[-inq\theta\right] \exp\left[-\frac{n^2 q'^2 x_s^2}{4\chi}\right] \tag{4.78}$$

It is important to note that for purely imaginary χ, the function $A(p)$ is not localized in p; hence the solution for $\tilde{\phi}$ is oscillatory in that situation. However, in general, for complex χ, we evaluate the magnitude of $\tilde{\phi}$ to get:

$$|\tilde{\phi}(x_s,\theta)| \sim \exp\left[-n^2 |q'^2 \chi_r| \frac{x_s^2}{4|\chi|^2}\right] \tag{4.79}$$

From this equation it is obvious that the mode peaks about $x_s = 0$, and extends over a small radial region with width:

$$\Delta_x = \frac{4\sqrt{log(2)}|\chi|}{n|q'|\sqrt{|\chi_r|}} \underset{n\to\infty}{\approx} \frac{4\sqrt{log(2)}}{\sqrt{n\,|q'|}} \frac{\left|\frac{f''(0)}{8R(0)}\right|}{\sqrt{\left|\left(\sqrt{\frac{f''(0)}{8R(0)}}\right)_r\right|}} \tag{4.80}$$

Note that, this provides a narrow mode width $\Delta_x \propto 1/\sqrt{n}$.

[3]Eq. (4.77) is a well known complex Gaussian integral that does not have poles, for a long time people did not know how to calculate it using contour integration. It was only around the middle of last century several contour integral solutions were proposed. Here, we do not show how to calculate Eq. (4.77), but its calculation detail can be found for example in references [94, pp. 121 and 95, pp. 413-414] or online documents [96, 97].

To validate our calculations, we reproduce the results presented in [5, 81]. Firstly, Fourier expand in p, retaining only two Fourier modes, to write $R(p) = R_0$ and $f(p) = f_0 + f_1 \cos(p)$. Where, R_0, f_0 and f_1 are, in general, complex and are the coefficients of the Fourier expansion. This corresponds to $R(0) = R_0$, $R''(0) = 0$, $f(0) = f_0$ and $f''(0) = -f_1$, respectively. In this limit, the corresponding equations for $A(p)$ (from Eq. (4.71)), Ω (from Eq. (4.73)), $\tilde{\phi}$ (from Eq. (4.78)), and Δ_x (from Eq. (4.80)) are, respectively, reduced to the following forms:

$$A(p) = \exp\left[-inq'\beta p^2\right] \tag{4.81}$$

$$\Omega = \frac{2iR_0}{nq'}\beta + f_0 + f_1 \tag{4.82}$$

$$\tilde{\phi}(x_s, \theta) \approx \xi(x_s, p = 0, \theta) \exp\left[-inq\theta\right] \exp\left[inq'\frac{x_s^2}{4\beta}\right] \tag{4.83}$$

$$\Delta_x = 4\sqrt{log(2)}\sqrt{\frac{|\beta|^2}{n|q'\beta_i|}}, \tag{4.84}$$

where, $\beta = \pm\sqrt{\frac{f_1}{8R_0}}$ and its sign is chosen such that $A(p)$ is localised in p.

4.7.2 General Modes

This class of eigenmode can be obtained if we assume that $R(p) = 0$ [18, 25]. For this case Eq. (4.63) is simplified to:

$$\frac{iS(p)}{nq'}\frac{dA}{dp} - [\Omega - f(p)]A = 0 \tag{4.85}$$

This is a first order linear differential equation and its exact solution is easily obtained:

$$A(p) = \exp\left[-inq'\int^p \left(\frac{\Omega - f(p)}{S(p)}\right) dp\right] \tag{4.86}$$

The condition that $A(p)$ is periodic in p leads to the constraint

$$\oint \left[\frac{\Omega - f(p)}{S(p)}\right] dp = \frac{2\ell\pi}{nq'} \tag{4.87}$$

with ℓ integer. This equation describes the existence of a set of separate eigenmode solutions, each corresponding to a different value of ℓ. For $\ell = 0$ the eigenvalue Ω can be calculated as

$$\Omega = \frac{\oint \left[\frac{f(p)}{S(p)}\right] dp}{\oint \left[S(p)\right]^{-1} dp} \tag{4.88}$$

Having obtained the solutions for $A(p)$ and Ω, we may now reconstruct the global mode structure from the Fourier Ballooning representation of Eq. (4.50). For convenience, we Fourier expand to approximate $S(p) = S_0$ and $f(p) = f_0 + f_1 \cos(p)$, where only two Fourier modes have been retained. This simplification reduces Eq. (4.88) to:

$$\Omega = f_0 \tag{4.89}$$

This represents the average of the local complex mode frequency over 2π in p, evaluated at $x_s = 0$, i.e $\Omega = \langle \Omega_0(x_s = 0, p) \rangle_p$. This provides an exact analytic solution for $A(p)$ from Eq. (4.86)

$$A(p) = \exp\left[inq'\delta \sin(p)\right] \tag{4.90}$$

where $\delta = \frac{f_1}{S_0}$, and δ must be complex for $A(p)$ to be localised in p. Furthermore, for this model, the envelope $A(p)$ peaks at $p = \pm\frac{\pi}{2}$, with $+$ and $-$ signs corresponding to the top (for $\delta_i < 0$) and bottom (for $\delta_i > 0$) of the tokamak plasmas, respectively. The appropriate choice of solution depends on the sign of $q'\delta$. Substituting $A(p)$ from Eq. (4.90) back into Eq. (4.50), knowing the fact that $A(p)$ has the fastest variation in p compared to $\xi(x_s, p, \theta)$, and again using the stationary phase approximation for the integral in Eq. (4.50), one can obtain an analytic approximation for the reconstructed global mode structure [19]:

$$\tilde{\phi}(x_s, \theta) \sim \exp\left[inq'\left(x_s cos^{-1}\left(\frac{x_s}{\delta}\right) \pm \delta\left(1 - \frac{x_s^2}{\delta^2}\right)^{\frac{1}{2}}\right)\right] \exp\left[-inq\theta\right] \tag{4.91}$$

The sign is chosen such that $\tilde{\phi}$ decays for large x_s. The mode is again radially localised about $x_s = 0$, corresponding to a pure general mode, and its radial width

can be calculated if we expand Eq. (4.91) for small x_s to get

$$\left|\tilde{\phi}\right| \sim \exp\left[\frac{-n\left|q'\delta_i\right|}{2\left|\delta\right|^2}x_s^2\right] \tag{4.92}$$

This is a Gaussian with radial mode width, Δ_x;

$$\Delta_x = 2\sqrt{2\log 2}\sqrt{\frac{\left|\delta\right|^2}{n\left|q'\delta_i\right|}} \tag{4.93}$$

We therefore again find that the mode width $\Delta_x \propto 1/\sqrt{n}$.

In the next chapter, we extend the analytic solution of Eq. (4.63) to account for more general cases. This allows us to investigate more realistic situations for which an eigenmode can sit somewhere between the outboard mid-plane and the top or bottom of the tokamak plasma.

Chapter 5

Extended Analytical Solutions

In the previous chapter we described two previously published analytic solutions of Eq. (4.63). Those solutions correspond to the highly unstable "isolated" modes and relatively less unstable "general" modes that, respectively, peak on the outboard mid-plane and the top (or bottom) of the tokamak plasmas [5, 18, 19, 25]. For more realistic experimental profiles, it is more likely that the eigenmode will, in general, sit at an arbitrary poloidal position and undergo radial shifts with respect to the reference surface at $x_s = 0$. In this chapter, to account for these modes we have extended the analytical solutions, such that those previously considered limits can be considered as two special limits from our new solutions. In addition, we have used these analytic approaches to investigate the influence of rotational flow shear on the stability and structures of the global ballooning eigenmode in tokamak plasmas. We have also shed light on the mechanisms underlying poloidal and radial symmetry breaking. Note also that we introduce the terminology "pure" and "shifted" global modes to define the mode peaking at $x_s = 0$ and away from this point, respectively.

5.1 Fundamental Modes with Small Poloidal Shifts

As a first step we consider an eigenmode that undergoes a small poloidal shift with respect to the outboard mid-plane[1]. Isolated modes can be considered as a special limit of these new solutions. However, these new analytical solutions cannot account for the general modes.

5.1.1 The Envelope A(p) and Global Eigenvalue Ω

We start with Eq. (4.63) and seek localised modes with the following solution for $A(p)$:

$$A(p) = \exp\left[-\chi p^2\right] \exp\left[bp\right] \tag{5.1}$$

where χ and b are, in general, complex numbers. As we shall see in the following, the first exponential term on the right hand side represents a mode that sits on the outboard mid-plane at $\theta = 0$, while the second term incorporates the effect of $S(p)$, and can introduce both a radial shift away from $x_s = 0$ and a poloidal shift with respect to the outboard mid-plane. Recalling that $nq' \gg 1$, and we are only considering solutions that undergo small poloidal shifts with respect to the outboard mid-plane, we Taylor expand about $p = 0$ and replace $R(p)$, $S(p)$ and $f(p)$ with $R(0) + \frac{R''(0)}{2}p^2$, $S(0) + \frac{S''(0)}{2}p^2$ and $f(0) + \frac{f''(0)}{2}p^2$, respectively. We restrict ourselves to up-down symmetric equilibria so first derivatives are zero at $p = 0$. After substituting $A(p)$ from Eq. (5.1), collecting coefficients with like powers of p, Eq. (4.63) reduces to the following algebraic equations:

$$p^2 : \frac{4\chi^2 R(0)}{n^2 q'^2} + \frac{(b^2 - 2\chi)R''(0)}{2n^2 q'^2} - \frac{ibS''(0)}{2nq'} - \frac{f''(0)}{2} = 0 \tag{5.2}$$

[1]In this section only fundamental modes with small poloidal shifts are investigated, but the technique that we present here enable us to take into account the finite corrections due to the p dependence of the $R(p)$ coefficient in Eq. (4.63). For this reason we have separated these solutions from the generalised solutions that are presented in section 5.4 in which the non-fundamental modes, with arbitrary poloidal shifts, are also included, but $R(p)$ is assumed to be constant.

$$p^1 : -\frac{4\chi b R(0)}{n^2 q'^2} + \frac{2i\chi S(0)}{nq'} = 0 \tag{5.3}$$

$$p^0 : \Omega - f(0) + \frac{(b^2 - 2\chi)R(0)}{n^2 q'^2} - \frac{ibS(0)}{nq'} = 0 \tag{5.4}$$

From these equations we can determine the unknown parameters, namely χ, b and Ω. Note that we still assume solutions localised in the vicinity of $p = 0$, and therefore neglect the terms in p^3 and p^4. Solving the first two equations, corresponding to the coefficients of p^1 and p^2, simultaneously, we obtain χ, b as follows:

$$b = inq' \frac{S(0)}{2R(0)} = -inq' x_0 = nq' \left(x_{0,i} - ix_{0,r}\right) \tag{5.5}$$

where $x_0 = -S(0)/2R(0)$ is a complex number and the subscripts r and i refer to the real and imaginary components, respectively. We will see later in this section that x_0 is related to the physical radial shift of the mode. In addition

$$\chi = \frac{R''(0)}{8R(0)} \pm nq' \frac{\sqrt{8R(0)f''(0) + (\frac{R''(0)}{nq'})^2 + 8x_0 R(0)S''(0) + 8x_0^2 R(0)R''(0)}}{8R(0)} \tag{5.6}$$

and finally, from Eq. (5.4), using Eq. (5.5) to write b in terms of x_0, we obtain the following solution for the global eigenvalue Ω[2]:

$$\Omega = f(0) - x_0^2 R(0) + \frac{2\chi}{(nq')^2} R(0) \tag{5.7}$$

Furthermore, using Eq. (5.1), taking the first derivative of $A(p)$ at $p = p_0$ and equating it to zero, i.e. $dA/dp|_{p=p_0} = 0$, we see that $A(p)$ peaks on

$$p = p_0 = \frac{b}{2\chi} \tag{5.8}$$

where p_0 is called the ballooning phase angle and is, in general, complex [98, 99] (our p_0 corresponds to θ_0 in [98] and λ in [99]). Decomposing p_0 into its real and

[2]Note that section 5.3 is devoted to investigating how Ω and other global parameters, such as mode radial width Δ_x etc., scale with n. For example how the finite n correction due to p dependence of $R(p)$ affects this scaling. Therefore, in this section we merely derive the general formula and do not discuss how the global parameters scale with n.

imaginary components, i.e. $p_0 = p_{0,r} + ip_{0,i}$, we get:

$$\begin{aligned} p_{0,r} &= \frac{b_r\chi_r + b_i\chi_i}{2|\chi|^2} \\ p_{0,i} &= \frac{b_i\chi_r - b_r\chi_i}{2|\chi|^2} \end{aligned} \tag{5.9}$$

If we now substitute $\chi = \chi_r + i\chi_i$ and $b = b_r + ib_i$ into Eq. (5.1) we may decompose $A(p)$ into its magnitude and oscillatory parts to get;

$$A(p) = A_0 \exp\left[-\chi_r(p - p_m)^2\right] \exp\left[-i\chi_i(p - p_p)^2\right] \tag{5.10}$$

where the constant $A_0 = \exp[\chi_r p_m^2 + i\chi_i p_p^2]$ is complex and determines the arbitrary amplitude and phase of $A(p)$. Note that, the parameters p_m and p_p are both real and are defined as follows:

$$\begin{aligned} p_m &= \frac{b_r}{2\chi_r} = nq'\frac{x_{0,i}}{2\chi_r} \\ p_p &= \frac{b_i}{2\chi_i} = -nq'\frac{x_{0,r}}{2\chi_i} \end{aligned} \tag{5.11}$$

Here, Eq. (5.5) is used to relate b_r and b_i to $x_{0,i}$ and $x_{0,r}$, respectively. The first exponential on the right hand side of Eq. (5.10) is proportional to the magnitude of $A(p)$, i.e. $|A(p)|$, while the second exponential is oscillatory and can be thought of as $A(p)/|A(p)|$. The function $|A(p)|$ peaks and is symmetric about a line that goes through $p = p_m$, but $A(p)/|A(p)|$ is symmetric about an axis that goes through $p = p_p$. The resultant $A(p)$ can only be symmetric if and only if these two lines of symmetry coincide, which happens when $p_m = p_p$. We shall see later in section 5.2 that this symmetry breaking leads to a physical radial shift in the reconstructed global mode structure with respect to $x_s = 0$.

Having obtained solutions for the envelope $A(p)$ with its associated eigenvalue Ω we are now ready to derive an analytic formula for the global mode structure $\tilde{\phi}(x_s, \theta)$ which is the subject of the following subsection.

5.1.2 The Global Eigenmode Structures $\tilde{\phi}(x_s, \theta)$

To reconstruct the global mode structure and calculate its radial width, we shall follow the same procedure and steps that have been used in the previous chapter

(see section 4.7.1). We first substitute $A(p) = \exp\left(-\chi p^2 + bp\right)$ from Eq. (5.1) into the Fourier ballooning representation in Eq. (4.50), and knowing that $\xi(x_s, \theta, p)$ varies slowly with p compared to $A(p)$, we can then apply the stationary phase approximation to the integral in Eq. (4.50). To lowest order we derive:

$$\tilde{\phi}(x_s, \theta) \approx \xi(x_s, p = p_m, \theta) \exp\left[-inq\theta + \chi x_1^2\right] \int_{-\infty}^{+\infty} \exp\left[-\chi\left(p - x_1\right)^2\right] dp \quad (5.12)$$

where, $x_1 = \left[inq'/2\chi\right](x_s - x_0)$ and $\xi(x_s, p = p_m, \theta)$ determines the poloidal extension of the global mode. The parameter p_m is defined in Eq. (5.11) and determines where $|A(p)|$ peaks in p space, which in turn leads to a global mode that peaks at $\theta = p_m$. The result of the integration on the right side is equal to $\sqrt{\pi/\chi}$[3]. This provides an analytic formula for the reconstructed global mode structure, which is represented by the following equation:

$$\tilde{\phi}(x_s, \theta) \approx \xi(x_s, p = p_m, \theta) \exp\left[-inq\theta\right] \exp\left[\chi x_1^2\right] \quad (5.13)$$

Note that, from the last exponential term on the right hand side we can see that the global mode radially peaks at $x_s = x_0$. This indicates that the parameter x_0, previously defined in Eq. (5.5), can be thought of as a radial shift of the reconstructed global mode in the complex plane. It is important to note that for purely imaginary χ, the function $A(p)$ is not localised in p; hence the solution for $\tilde{\phi}$ is oscillatory. In general, for a complex χ, we find

$$|\tilde{\phi}(x_s, \theta)| \sim \exp\left[-n^2 |q'^2 \chi_r| \frac{\left(x_s - x_m\right)^2}{4|\chi|^2}\right] \quad (5.14)$$

where

$$x_m = x_{0,r} + \frac{\chi_i}{\chi_r} x_{0,i} = \frac{1}{nq'}\left[-b_i + \frac{\chi_i}{\chi_r} b_r\right] = -\frac{1}{2}\left[\left(\frac{S(0)}{R(0)}\right)_r + \frac{\chi_i}{\chi_r}\left(\frac{S(0)}{R(0)}\right)_i\right] \quad (5.15)$$

is real and represents a physical radial shift away from $x_s = 0$. As we can see, x_m is a consequence of a finite value of the part of $\Omega_0(x_s, p)$ that is linear in x_s, $S(0)$. Note, therefore, that our Taylor expansion of $\Omega_0(x_s, p)$ about $x_s = 0$ requires us to restrict consideration to those equilibria for which this shift is small.

Finally, the mode's radial width is determined from the full width at half max-

[3]For more details see subsection 4.7.1 − second to the last paragraph.

imum (FWHM) of the Gaussian Eq. (5.14)

$$\Delta_x = \frac{4\sqrt{log(2)}|\chi|}{n|q'|\sqrt{|\chi_r|}}, \tag{5.16}$$

Having obtained solutions for the global mode structure $\tilde{\phi}(x_s, \theta)$ and its eigenvalue Ω, we are able to recapture the so-called isolated type of modes in the limit $S(p) \to 0$. More generally, the isolated mode is recovered when x_0 is purely real−in that case the term involving $S(p)$ can be transformed away by simply transforming $x_s \to x_s + x_0$. This is the origin of the radial shift, but otherwise the mode structure is unaffected. When x_0 is complex, however, both the radial and poloidal structure are affected, as we now discuss in more detail.

5.2 Radial and Poloidal Symmetry Breaking

In the analytical calculation that has been developed in section 5.1, two different classes of symmetry breaking can be identified; radial symmetry breaking associated with the radial shift with respect to $x_s = 0$, i.e. $\tilde{\phi}(x_s, \theta) \neq \tilde{\phi}(-x_s, \theta)$, and poloidal symmetry breaking associated with the mode's poloidal shift with respect to the outboard mid-plane, i.e $\tilde{\phi}(x_s, \theta) \neq \tilde{\phi}(x_s, -\theta)$. To understand the mechanisms underlying this symmetry breaking we start by anticipating a symmetric $A(p)$, assuming that $p_m = p_p$, from Eq. (5.11) we get the following constraint:

$$b_i\chi_r = b_r\chi_i \tag{5.17}$$

or equivalently,

$$x_{0,r} = -\frac{\chi_i}{\chi_r}x_{0,i} \tag{5.18}$$

Upon substituting Eq. (5.17) and Eq. (5.18) into Eq. (5.9) and Eq. (5.15), respectively, we have

$$p_{0,i} = x_m = 0 \tag{5.19}$$

It is quite clear that the function $A(p)$ is symmetric only when $p_{0,i} = 0$ which then provides a radially centred reconstructed global mode that peaks about a reference

flux surface $x_s = 0$[4]. In this case, $p_{0,r} = \frac{b_r}{2\chi_r} = p_m$, or $p_{0,r} = \frac{b_i}{2\chi_i} = p_p$ and this in turn implies that the two lines of symmetry always coincide at $p = p_{0,r}$. However, a symmetric $A(p)$, does not, in general, imply a poloidally symmetric reconstructed global mode. Only Isolated modes preserve poloidal symmetry with respect to the outboard mid-plane at $\theta = p_m = 0$. This can be seen from Eq. (5.11), which states that if $p_m = 0$, then

$$b_r = x_{0,i} = 0 \tag{5.20}$$

Thus, $p_m = 0$ requires $x_{0,i} = 0$, which therefore means x_0 is real[5]. Recalling that $x_s = x_0$ corresponds to the position where $\partial\Omega_0(x_s, p)/\partial x_s = 0$, then transforming $x_s \to x_s + x_0$ recovers the isolated mode. Substituting $x_{0,i} = 0$ into Eq. (5.15) we have

$$x_m = x_{0,r} \tag{5.21}$$

and from Eq. (5.14) we see that the mode is localised at the position where $\partial\Omega_0(x_s, p)/\partial x_s = 0$.

5.2.1 Shifted Isolated Modes: Regular Radial Symmetry Breaking

To illustrate the radial symmetry breaking that is associated with the shifted isolated modes, we shall examine a simple problem. We start with Fourier expansion and write $R(p) = R_0$, $S(p) = S_0$ and $f(p) = f_0 + f_1 \cos p$, respectively, and consider the following model coefficients given in [81]:

$$\begin{aligned} f_0 &= -0.1183 + 0.2571i \\ f_1 &= 0.1257 + 0.0831i \\ R_0 &= 12.61 - 15.90i \\ S_0 &= 0 \end{aligned} \tag{5.22}$$

[4] $p_{0,i} \neq 0 \to A(p) \neq A(-p) \to$ radial shift $x_m \neq 0 \to$ radial symmetry breaking $\tilde{\phi}(x_s, \theta) \neq \tilde{\phi}(-x_s, \theta)$.

[5] $x_{0,i} \neq 0 \to$ poloidal shift $p_m \neq 0 \to$ poloidal symmetry breaking $\tilde{\phi}(x_s, \theta) \neq \tilde{\phi}(x_s, -\theta)$.

These coefficients are obtained from a simplified fluid model for a so-called ITG mode in a circular tokamak and lead to $R(0) = R_0$, $S(0) = S_0 = 0$, $f(0) = f_0$, $R''(0) = 0$, $S''(0) = 0$ and $f''(0) = -f_1$, respectively. Here, we have assumed $n = 50$ and $q' = 10$, respectively, and as $S_0 = 0$ we find a pure type of isolated mode that peaks at $x_s = 0$. Let us now consider a different $S_0 = 0.4000 - i0.5044$. From Eq. (5.5) we see that x_0 is then purely real. Specifically; $x_0 = x_{0,r} + ix_{0,i} = -0.01586 + i0$. This corresponds to a local mode frequency $\Omega_0(x_s, p) = \omega_0(x_s, p) + i\gamma_0(x_s, p)$ that exhibits a stationary point at $x_s = x_{0,r} = -0.01586$ and therefore is susceptible to an isolated mode that sits on the outboard mid-plane at $\theta = 0$. The calculated values for both Ω (from Eq. (5.7)) and Δ_x (from Eq. (5.16)) are $0.00384 + i0.34176$ and 0.03162, respectively. Solving equation Eq. (4.63) numerically provides the function $A(p)$ and its eigenvalue $\Omega = 0.00384 + i0.34175$. Using this $A(p)$, numerical integration of equation Eq. (4.50) provides the reconstructed global mode structure $\tilde{\phi}(x_s, \theta)$ with radial width $\Delta_x = 0.0315$. The local real frequency $\omega_0(x_s, p = 0)$ and the local growth rate $\gamma_0(x_s, p = 0)$ are both shown in Figure 5.1(top row). In the middle row, the envelope $A(p)$ (obtained from Eq. (5.1) with $\chi = 10.2962 - i11.2263$ and $b = 0.0000 + i7.9302$), its magnitude $|A(p)|$ and the oscillatory component $A(p)/|A(p)|$ are shown. Finally, the bottom row of the same figure, presents the associated magnitude of the reconstructed eigenmode structure $|\tilde{\phi}(x_s, \theta = 0)|$, obtained from Eq. (5.14)), as function of x_s. The solid lines and plus symbols correspond to the solutions, derived from the analytic (Eq. (5.1)) and numerical (solution of Eq. (4.63)) forms for $A(p)$, respectively. As we can see perfect agreement between the analytical and numerical solutions is found. Moreover, for the model parameters considered here, the calculated ballooning phase angle, $p_0 = -0.0611 + i0.0560$, has a non zero imaginary component. Consequently, the symmetric axis of $|A(p)|$, which is located at $p_m = 0$, is shifted with respect to the symmetric axis of $A(p)/|A(p)|$, which is located at $p_p = -0.1124$. This in turn, as expected for an isolated mode, leads to an envelope $A(p)$ that still peaks at $p_m = 0$, but it is not symmetric under the transformation $p \to -p$. It is this symmetry breaking that eventually leads to the radial shift in the global mode with respect to $x_s = 0$. The global mode sits at the

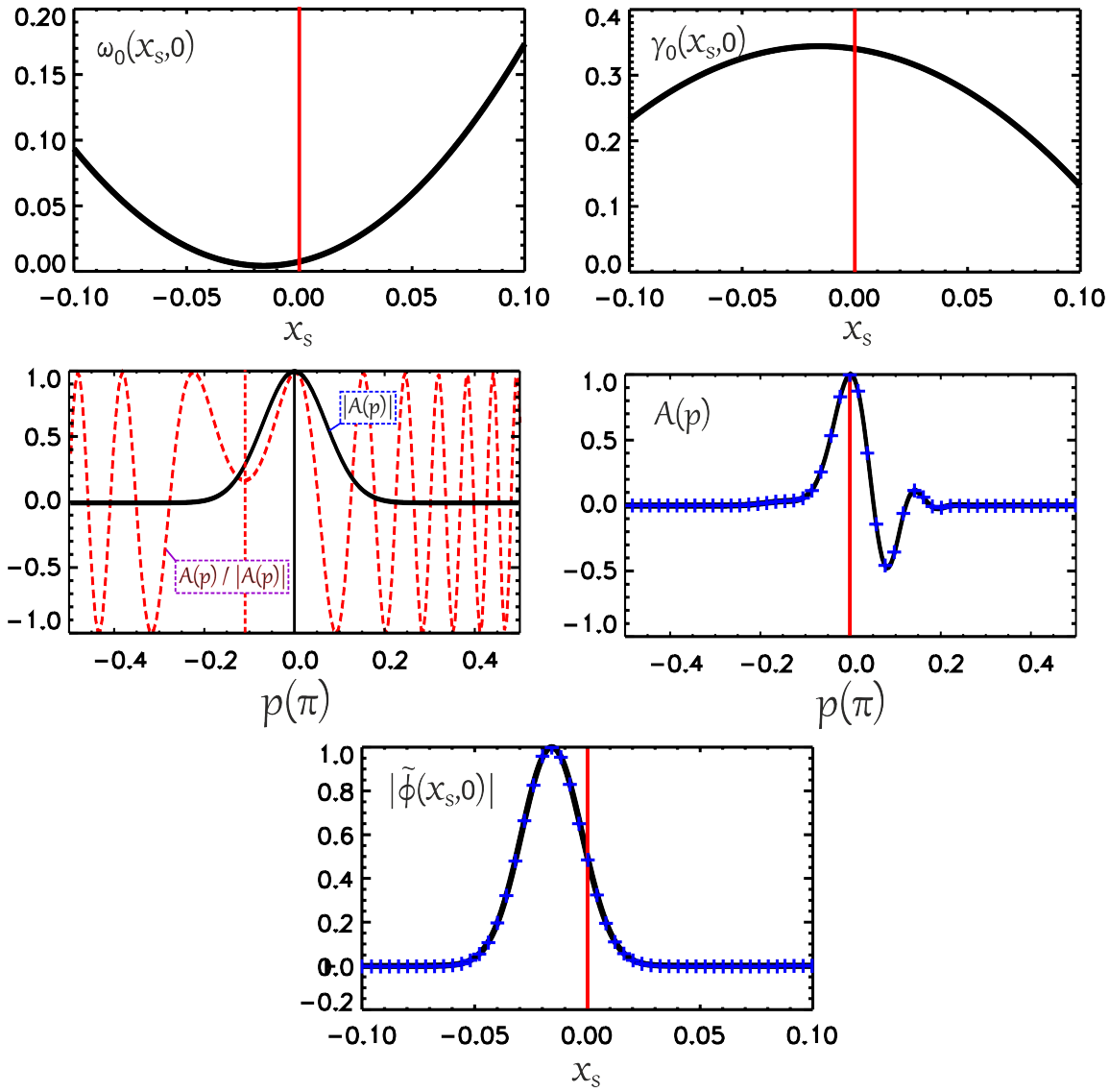

Figure 5.1: An isolated mode in nonshifted radial coordinate system x_s. The top row from left to right presents the radial variation of both local frequency $\omega_0(x_s, p = 0)$ and local growth rate $\gamma_0(x_s, p = 0)$, respectively. The middle row shows the envelope $A(p)$ [right] with both its magnitude $|A(p)|$ and oscillatory $A(p)/|A(p)|$ components [left]. Finally, the bottom row presents the magnitude of the reconstructed global mode structure $|\tilde{\phi}(x_s, \theta = 0)|$. The analytic solutions are represented by solid lines while the plus symbols correspond to the numerical solutions. Note that the local frequency $\Omega_0(x_s, p)$ is stationary at $x_s = x_m = -0.01586$. This provides a non zero imaginary component for the ballooning phase angle, i.e. $p_{0,i} \neq 0$, which also implies that the line of symmetry for $A(p)/|A(p)|$ is shifted with respect to the line of symmetry of $|A(p)|$. This introduces asymmetry in the resultant $A(p)$ about $p = 0$, which in turn leads to a radially shifted global eigenmode that, for the example considered here, peaks about $x_s = x_m = -0.01586$.

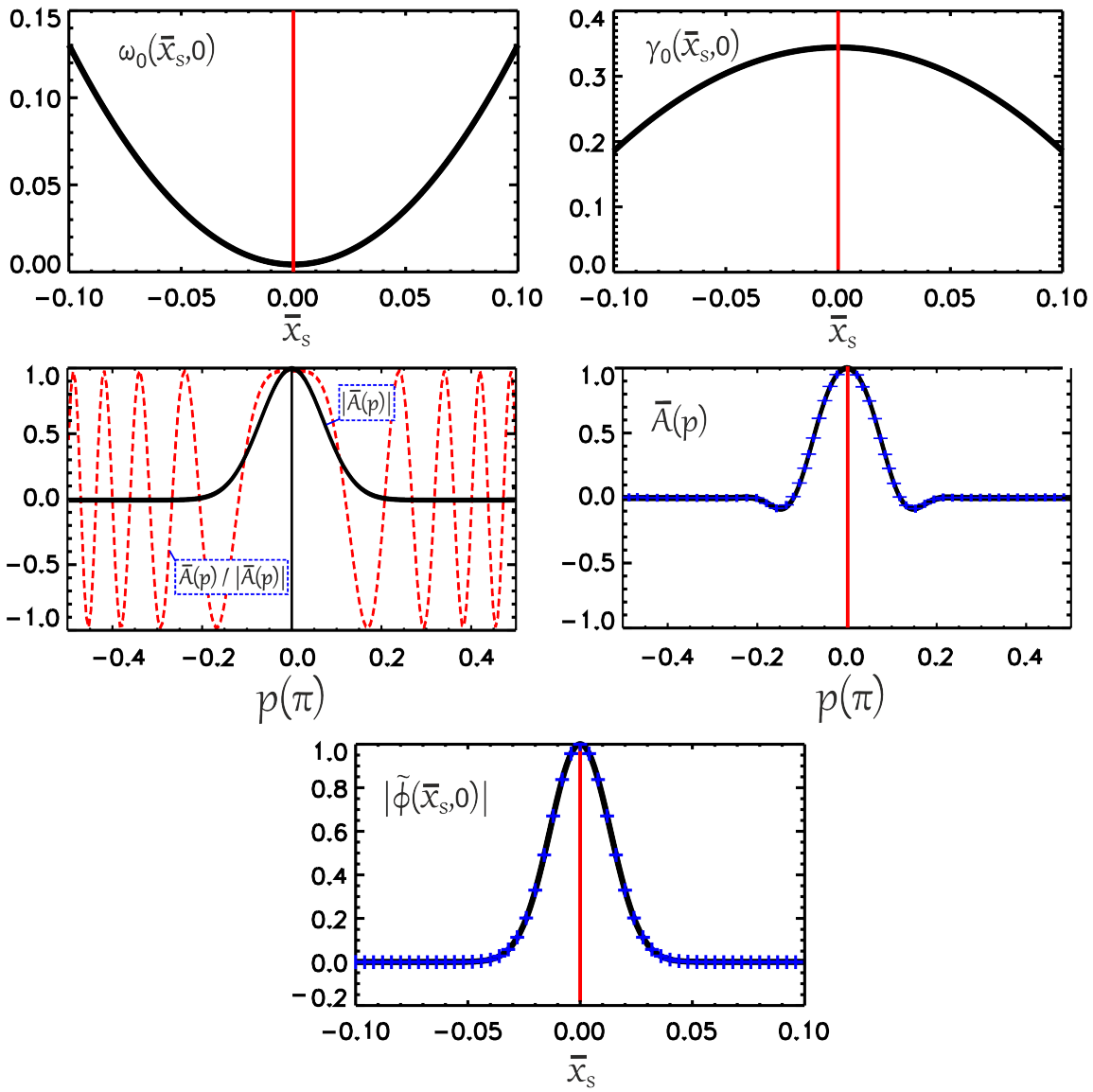

Figure 5.2: A pure isolated mode in shifted radial coordinate system $\bar{x}_s$. The top row from left to right presents the radial variation of both local frequency $\omega_0(\bar{x}_s, p = 0)$ and local growth rate $\gamma_0(\bar{x}_s, p = 0)$, respectively. The middle row shows the envelope $\bar{A}(p)$ [right] with both its magnitude, $|\bar{A}(p)|$, and oscillatory, $\bar{A}(p)/|\bar{A}(p)|$, components [left]. Finally, the bottom row presents the magnitude of the reconstructed global mode structure $|\tilde{\phi}(\bar{x}_s, \theta = 0)|$. The analytic solutions are represented by solid lines while the plus symbols correspond to the numerical solutions. Note that, the local frequency $\Omega_0(\bar{x}_s, p = 0)$ is stationary at $\bar{x}_s = 0$. This provides a real ballooning phase angle, i.e. $p_{0,i} = 0$, which also implies that, the two lines of symmetry that, respectively, corresponds to the functions $A(p)/|A(p)|$ and $|A(p)|$ should coincide. The resultant $A(p)$ is then symmetric about $p = 0$, which in turn leads to a radially centred global eigenmode that peaks about $\bar{x}_s = 0$.

point where $\Omega_0(x_s, p)$ is stationary, i.e. $x_s = x_m = x_{0,r} = -0.01586$.

From the above analysis we can deduce the fact that so long as $x_{0,i} = 0$, the symmetry breaking can always be regulated by transforming the radial coordinate into a new one, $\bar{x}_s$, such that the complex mode frequency is stationary at $\bar{x}_s = 0$. Figure 5.2 shows the solution obtained by repeating the above analysis, but in the radial coordinate $\bar{x}_s = x_s + x_0$, so that the local complex mode frequency is stationary at $\bar{x}_s = 0$. This is the case considered in subsection 4.7.1. Although the form for $A(p)$ differs to that found in Figure 5.1, the physical potential $\tilde{\phi}(x_s, \theta)$ is identical and we recover the same global eigenmode, $\Omega = 0.00384 + i0.34175$.

5.2.2 Poloidal Symmetry Breaking: An Example

We now turn to the more general case, where $x_{0,i} \neq 0$, in which case the global mode sits slightly away from the outboard mid-plane. The poloidal shift, in general, can be caused by shear in the equilibrium profiles [13, 27], which can have very important physical consequences. For example it can lead to flow generation in axisymmetric tokamaks [27, 30–32] which is important for a machine like ITER for which the external torque is small. To illustrate the poloidal symmetry breaking that is associated with these classes of eigenmode solutions, we consider the model parameters from Eq. (5.22) with an additional effect from a purely real linear term $S_0 = 0.6$. This set of model coefficients leads to $x_{0,i} \neq 0$. This corresponds to a local complex mode frequency $\Omega_0(x_s, p)$ that does not exhibit a stationary point on the real axis which in turn, according to Eq. (5.11) leads to $p_m \neq 0$ and provides a global mode that poloidally shifts with respect to the outboard mid plane. Figure 5.3 presents the local complex mode frequency $\Omega_0(x_s, p = 0) = \omega_0(x_s, p = 0) + i\gamma_0(x_s, p = 0)$, the envelope function $A(p)$ and the associated reconstructed global mode structure $\tilde{\phi}(x_s, \theta)$. Note that we have assumed the local mode structure $\xi(x_s, \theta, p)$ to vary with θ and p according to $e^{-(\theta-p)^2}$. The global parameters for this model are; $b = -5.7913 + i4.5930$ (from Eq. (5.5)), $\chi = 10.2962 - i11.2263$ (from Eq. (5.6)), the global mode frequency $\Omega = 0.00425 + i0.3343$ (from Eq. (5.7)), complex ballooning

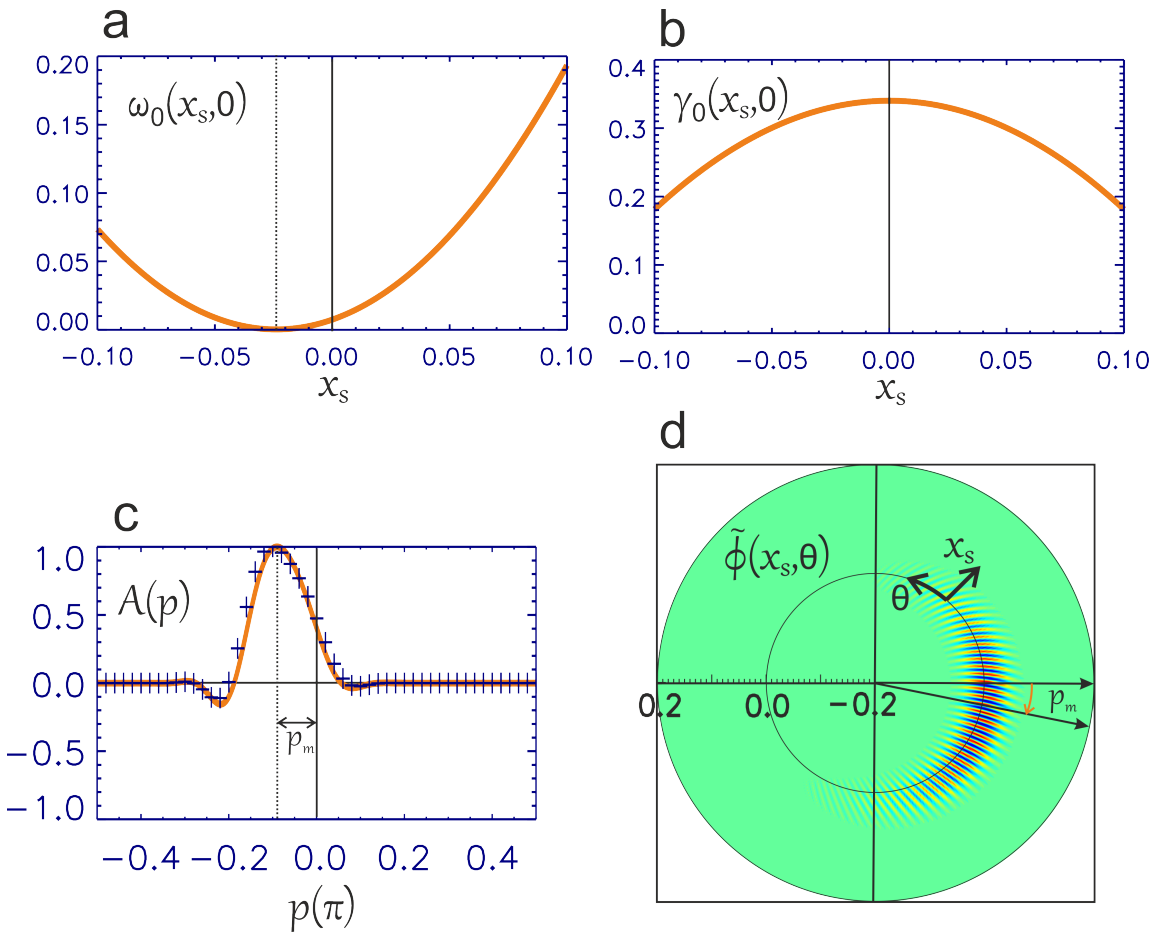

Figure 5.3: The local complex mode frequency $\Omega_0(x_s, p = 0) = \omega_0(x_s, p = 0) + i\gamma_0(x_s, p = 0)$ (a,b), the function $A(p)$ (c) and poloidal cross-section for the global mode structure $\tilde{\phi}(x_s, \theta)$ (d). Note that, the local mode structure is assumed to be Gaussian with respect to θ and p, namely $\xi(x_s, p, \theta) \sim e^{-(\theta-p)^2}$. The model coefficients are taken from Eq. (5.22) with $S_0 = 0.6 + i0$ in addition. For the function $A(p)$, the analytic solution is represented by a solid line, while plus symbols refer to the numerical solution of Eq. (4.63). Note that, $\Omega_0(x_s, p = 0)$ does not have a stationary point on the real axis. This, in turn, leads to a non-isolated type of mode that shifts slightly downward with respect to the outboard mid-plane.

phase angle $p_0 = -0.07626 - i0.01216$ (from Eq. (5.8)), mode poloidal position $p_m = -0.08952\pi$ (from Eq. (5.11)), complex radial parameter $x_0 = ib/nq' = -0.009186 - i0.01158$, mode radial position $x_m = 0.003443$ (from Eq. (5.15)) and finally the mode radial width $\Delta_x = 0.03162$ (from Eq. (5.16)). The corresponding values derived from a numerical solution of Eq. (4.63) are; $\Omega = 0.00425 + i0.3343$, $p_m = -0.09\pi$, $x_m = 0.0035$ and finally $\Delta_x = 0.0314$. Note that, excellent agreement between the analytical and numerical solutions is found.

Furthermore, we can see from Figure 5.3 that the local growth rate $\gamma_0(x_s, 0)$ still peaks at $x_s = 0$, which is expected because $S_{0,i} = 0$. However, the local frequency

$\omega_0(x_s, 0)$ has a minimum at $x_s \neq 0$. The calculated value for this radial position where $\partial\omega_0/\partial x_s|_{x_s=x_{\omega_0}} = 0$ is $x_{\omega_0} = -\frac{[S(0)]_r}{2[R(0)]_r} = -\frac{S_{0,r}}{2R_{0,r}} = -0.024$. Note that, the envelope function $A(p)$ is not symmetric (corresponds to $p_{0,i} \neq 0$) and also peaks at $p = p_m \neq 0$ (corresponds to $x_{0,i} \neq 0$). This in turn leads to a global mode that shifts slightly downward with respect to the outboard mid-plane and does not peak at the centre of the domain, i.e. $x_m \neq 0$. Both the radial and the poloidal symmetries are broken, i.e. $\tilde{\phi}(x_s, \theta) \neq \tilde{\phi}(-x_s, \theta)$ and $\tilde{\phi}(x_s, \theta) \neq \tilde{\phi}(x_s, -\theta)$, respectively[6].

5.3 Scaling with Toroidal Mode Number: Small Poloidal Shifts

Having derived the analytical equations for the fundamental modes with small poloidal shifts, we are now in a position to investigate how the global parameters scale with toroidal mode number n. We consider a general case and take into account the finite n correction due to the p dependence of the coefficient $R(p)$, i.e. where $R''(0) \neq 0$. However, in this section we will also look at a few limits. For example the limit with $R''(0) = 0$ as well as the effect of toroidal rotational flow on the scaling laws. In the limit of $nq' \gg 1$ we can assume that $(\frac{R''(0)}{nq'})^2$ is negligible[7], and this allow us to rewrite χ from Eq. (5.6) in the following form[8];

$$\chi \approx \chi_0 \pm nq'\chi_1 \tag{5.23}$$

where,

$$\begin{aligned} \chi_0 &= \frac{R''(0)}{8R(0)} \\ \chi_1 &= \frac{\sqrt{8R(0)f''(0) + 8x_0R(0)S''(0) + 8x_0^2R(0)R''(0)}}{8R(0)}, \end{aligned} \tag{5.24}$$

[6]Recall that the radial symmetry breaking considered with respect to $x_s = 0$, while the poloidal symmetry breaking corresponds to up-down asymmetry with respect to $\theta = 0$.

[7]Note that, taking into account the effect of $(\frac{R''(0)}{nq'})^2$ only contributes to the higher order terms in the the scaling of the global parameters with n. For example the correction would be of order $O(1/n^3)$ for both p_m and Ω, therefore we can neglect this term in the limit of $nq' \gg 1$.

[8]Note that, for convenient, we have introduced the extra terms χ_0 and χ_1 solely to simplify the calculations.

Substituting χ from Eq. (5.23) into Eq. (5.11) and employing the Binomial expansion with $nq' \gg 1$, we get

$$p_m = \frac{x_{0,i}}{2\chi_{1,r}} \left[1 - \frac{\chi_{0,r}}{nq'\chi_{1,r}} + O(\frac{1}{n^2 q'^2}) + ... \right] \tag{5.25}$$

Note that, if we are particularly interested in the first two terms on the right hand side then the fact that we have assumed $(\frac{R''(0)}{nq'})^2 = 0$ does not have any effect on the result. However it does contribute to the coefficients of the higher order terms. It is important to note that the global modes tend to finite poloidal positions in the limit of $nq' \to \infty$ (i.e. p_m is finite) and those positions depend on the equilibrium profiles through the $x_{0,i}$ and $\chi_{1,r}$ parameters. We now compare our predictions against previously published results, for example Ref [27]. According to [27, Eq.27] p_m (or θ_0 in their notation) scales with n according to $\theta_0 \sim 1/\sqrt[3]{n}$. However, our result indicates that the scaling presented in Ref [27] is not correct for small poloidal shifts. Therefore, it can not be considered as a universal scaling law. Similarly, the global mode frequency Ω (from Eq. (5.7)), scales as:

$$\Omega = f(0) - x_0^2 R(0) + \frac{2\chi_1 R(0)}{nq'} + \frac{2\chi_0 R(0)}{n^2 q'^2} \tag{5.26}$$

The mode radial position x_m (from Eq. (5.15)) is found to scale with n as follows:

$$x_m = x_{0,r} + x_{0,i} \left[\frac{\chi_{1,i}}{\chi_{1,r}} + \frac{\chi_{0,i}\chi_{1,r} - \chi_{0,r}\chi_{1,i}}{(\chi_{1,r})^2 nq'} - \frac{\chi_{0,r}\chi_{0,i}\chi_{1,r} - (\chi_{0,r})^2\chi_{1,i}}{(\chi_{1,r})^3 n^2 q'^2} \right] + O(\frac{1}{n^3 q'^3}) + ... \tag{5.27}$$

Finally, the mode's radial width Δ_x (from Eq. (5.16)) scales as:

$$\Delta_x = \frac{4|\chi_1|\sqrt{\log(2)}}{\sqrt{|nq'\chi_{1,r}|}} + \frac{2\sqrt{|\chi_{1,r}|\log(2)}}{|\chi_1|^3\sqrt{|nq'|^3}} \left[-\frac{|\chi_{0,r}||\chi_1|^2}{|\chi_{1,r}|^2} + \frac{2\chi_{0,r}\chi_{1,r} + \chi_{0,i}\chi_{1,i}}{|\chi_{1,r}|} \right] + O(\frac{1}{\sqrt{|nq'|^5}}) + ... \tag{5.28}$$

From the preceding discussion it appears that assuming $R''(0) \neq 0$ (or equivalently $R(p)$ varies with p) has the effect of finite n corrections of different orders for different global parameters. To the leading order, the corrections are of order $O(1/nq')$ for both p_m and x_m, but $O(1/n^2 q'^2)$ and $O(1/\sqrt{(nq')^3})$ corrections to Ω and Δ_x,

respectively[9].

If we now take the limit of $R''(0) = 0$ (or assuming that $R(p)$ is constant), from Eq. (5.24) we have

$$\begin{aligned} \chi_0 &= 0 \\ \chi_1 &= \frac{\sqrt{8R(0)f''(0) + 8x_0R(0)S''(0)}}{8R(0)}, \end{aligned} \tag{5.29}$$

such that the scalings with n for the above global parameters are, respectively, reduced to the following ones:

$$p_m = \frac{x_{0,i}}{2\chi_{1,r}}, \tag{5.30}$$

$$\Omega = f(0) - x_0^2 R(0) + \frac{2\chi_1 R(0)}{nq'}, \tag{5.31}$$

$$x_m = x_{0,r} + \left[\frac{\chi_{1,i}}{\chi_{1,r}}\right] x_{0,i}, \tag{5.32}$$

and finally,

$$\Delta_x = 4\sqrt{\log(2)} \left[\frac{|\chi_1|}{\sqrt{|nq'\chi_{1,r}|}}\right] \tag{5.33}$$

where, for $p_m = x_m = 0$, these last four equations recapture the ordering for a so-called conventional ballooning mode, namely a pure isolated mode, in which we have an $O(1/n)$ correction to Ω with respect to the maximum of the local complex mode frequency $\Omega_0(x_s, p)$, i.e. $\Omega = \mathrm{Max}[\Omega_0(x_s, p)] + O(1/n)$ and the radial mode width $\sim O(1/\sqrt{nq'})$.

Finally, let us take a second limit for which in addition to $R''(0) = 0$ we also assume that $S''(0) = 0$. This reduces χ_1 from Eq. (5.29) to

$$\chi_1 = \sqrt{\frac{f''(0)}{8R(0)}} \tag{5.34}$$

If we now consider a special case and assume that $S(0) = nq'\gamma_E$, where γ_E corresponds to a constant rotational flow shear. This additional nq' in $S(0)$ changes the

[9]It is important to mention that, the effect of p dependence of $R(p)$ (or equivalently where $R''(0) \neq 0$) on the magnitude of global parameters p_m, Ω, x_m and Δ_x is embodied in both χ_0 and χ_1 coefficients.

scaling of the global parameters with n. Substituting $S(0) = nq'\gamma_E$ into Eq. (5.5) we have:

$$x_0 = -\frac{nq'\gamma_E}{2R(0)} \sim O(nq')$$

this in turn leads to $p_m \sim O(nq')$ and $x_m \sim O(nq')$ from both Eq. (5.30) and Eq. (5.32), respectively, but the ordering for the mode radial width from Eq. (5.33) does not change and we still have $\Delta_x \sim O(1/\sqrt{nq'})$. Finally, from Eq. (5.31) Ω scales as follow:

$$\Omega = \omega + i\gamma = f(0) - \frac{n^2 q'^2 \gamma_E^2}{4R(0)} + \frac{\sqrt{8R(0)f''(0)}}{4nq'}, \tag{5.35}$$

where, ω and γ are the global frequency and global growth rate, respectively. Eq. (5.35) points to the fact that, in contrast to stationary plasmas for which the most unstable mode is associated with the largest n, in rotating plasmas the most unstable mode occurs at some intermediate n whose value depends on γ_E. This is in agreement with Ref [80] (see their Figure 4). Figure 5.4, using the parameters of Eq. (5.22) but with flow shear $S(0) = nq'\gamma_E$, shows how γ varies as a function of n at different values of γ_E. As we can see, the analytical solutions (solid lines) agree with the numerical solutions (symbols) for small values of flow shear, namely for $|nq'\gamma_E| < 12$.

In conclusion, our analytical treatment can only provide accurate results for a mode that sits close to the outboard mid-plane. Parameter regimes with large poloidal shifts cannot be covered in the context of this analytical treatment. In addition, we have only addressed the fundamental modes and for large poloidal shifts, the scaling laws governing the variation of the global parameters with n might be quite different from what we have presented so far. For these reasons, the following section is devoted to extending the analytical works beyond those limits that have been addressed so far. This new approach can account for large poloidal shifts and the stability of other harmonics in addition to the fundamental modes.

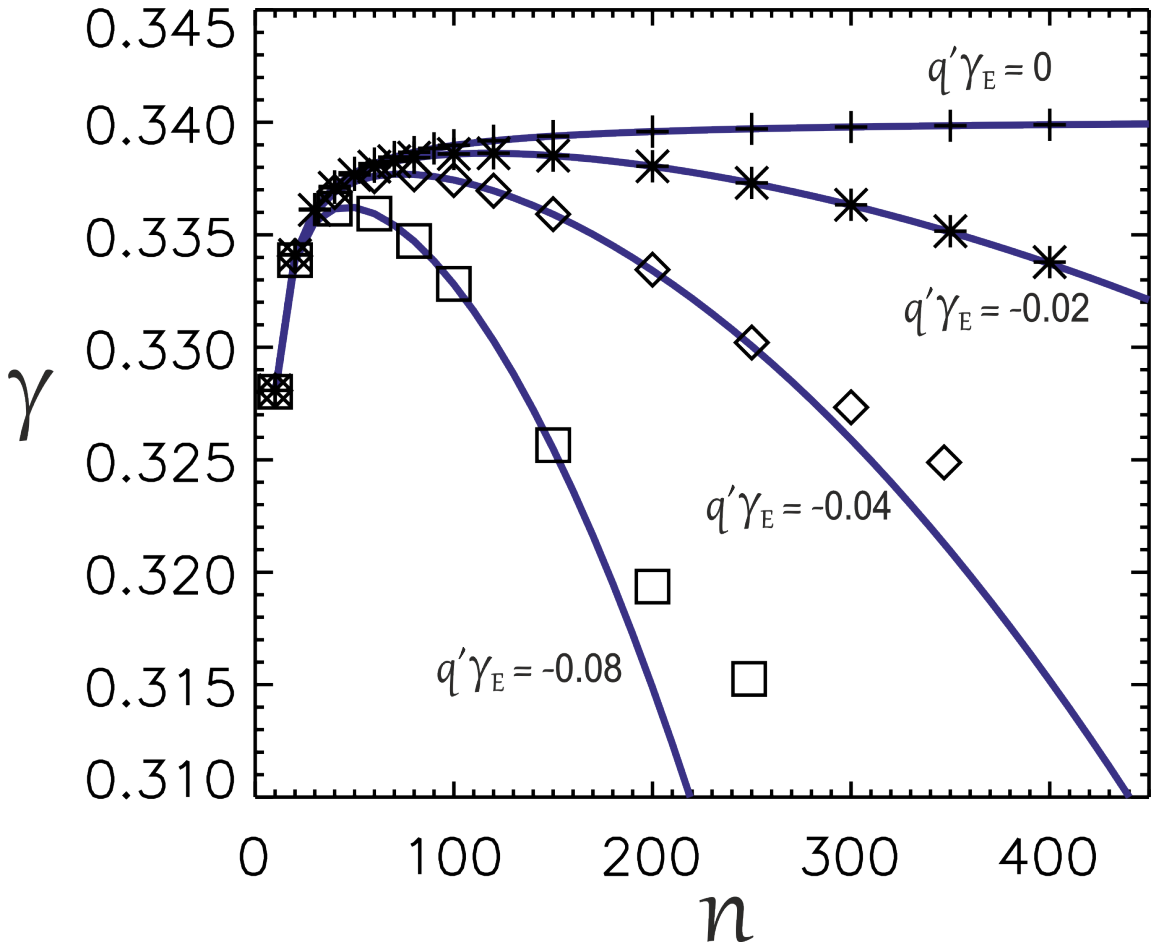

Figure 5.4: Growth rate, γ, as function of toroidal mode number, n, for different values of rotational flow, $q'\gamma_E$, where $q' = 10$. The analytic solutions (obtained from equation Eq. (5.35)) are represented by solid lines, while the symbols correspond to the numerical solutions. The model coefficients are taken from Eq. (5.22) with additional effect from $S(0) = S_0 = nq'\gamma_E$. Note that only for $\gamma_E = 0$ does the most unstable mode correspond to the largest n.

5.4 Generalised Analytic Solutions

The analytical solutions that we have developed so far are not suitable to describe all experimentally relevant situations. For example, with realistic experimental equilibria it is possible that one might find a mode that sits somewhere between the outboard mid plane and the top (or bottom) of the plasma or even sits on the inboard side in the good curvature region [28][10]. Thus, in order to be able to describe these types of modes analytically, in this section we have generalised our analytical solutions beyond those limits that have been discussed so far.

Furthermore, in the previous sections, we have only focused on the highly localised fundamental harmonic eigenmodes, but these may not be the only important modes of the system. Therefore, the results that we derive in this section can also be used to investigate the non-fundamental modes.

5.4.1 Calculating the Envelope A(p) and its Eigenvalue Ω

We start our new analytic solutions by keeping both $S(p)$ and $f(p)$ as two general complex function of p whilst assuming that $R(p) = R$, where R is a constant. This assumption avoids the introduction of singularities and poles into the problem and in turn we can rewrite Eq. (4.63) as follows:

$$\frac{R}{(nq')^2}\frac{d^2A}{dp^2} - \frac{iS(p)}{nq'}\frac{dA}{dp} + [\Omega - f(p)]A = 0 \tag{5.36}$$

This equation is a linear second order differential equation of a general form. It can always be reduced to a normal/standard form if we make the following substitution:

$$A(p) = g(p)\exp\left[\frac{inq'}{2R}\int_p S(p)dp\right] \tag{5.37}$$

[10]In the literature, a mode that sits on the outboard mid-plane is either known as isolated mode or conventional ballooning mode or ballooning mode of a first kind (BMI). On the other hand, a mode that sits on the top or bottom of the plasma is called general mode or ballooning mode of a second kind (BMII). Furthermore, a mode that sits at an arbitrary poloidal angle on the outboard side (bad curvature region) is called unconventional ballooning mode. Finally, anti-ballooning mode refers to a mode that balloons on the inboard side in the good curvature region.

which reduces Eq. (5.36) to

$$\frac{d^2g(p)}{dp^2} + \left[\frac{(nq')^2}{R}\left(\Omega - f(p)\right) + \frac{inq'}{2R}S'(p) + \left(\frac{nq'}{2R}\right)^2 S^2(p)\right] g(p) = 0 \tag{5.38}$$

This equation is, in general, complicated to solve analytically. But, recalling that $nq' \gg 1$, the solutions are highly localised in p about $p = p_0$, for example. We can then Taylor expand in p to give:

$$\begin{aligned}
f(p) &\approx f(p_0) + f'(p_0)(p-p_0) + \frac{f''(p_0)}{2!}(p-p_0)^2 \\
S(p) &\approx S(p_0) + S'(p_0)(p-p_0) + \frac{S''(p_0)}{2!}(p-p_0)^2 \\
S'(p) &\approx S'(p_0) + S''(p_0)(p-p_0) + \frac{S'''(p_0)}{2!}(p-p_0)^2 \\
S^2(p) &\approx S^2(p_0) + 2S(p_0)S'(p_0)(p-p_0) + \left(S'^2(p_0) + S(p_0)S''(p_0)\right)(p-p_0)^2
\end{aligned} \tag{5.39}$$

where, we have retained up to the second order terms in $p-p_0$ and recall from section 5.1 that p_0 is the complex ballooning phase angle. Substituting the above back into Eq. (5.38), rearranging and collecting terms in powers of $p - p_0$, we get

$$\begin{aligned}
&\frac{d^2g(p)}{dp^2} - \left(\frac{(nq')^2 f''(p_0)\mathcal{L}_{c2}}{2R}\right)\left(p - p_0 + \frac{f'(p_0)\mathcal{L}_{c1}}{f''(p_0)\mathcal{L}_{c2}}\right)^2 g(p) \\
&\qquad + \left(\frac{(nq')^2}{R}\right)\left[\Omega - f(p_0) + \frac{f'^2(p_0)\mathcal{L}_{c1}^2}{2f''(p_0)\mathcal{L}_{c2}} + \frac{(\frac{S(p_0)}{2})^2}{R} + \frac{iS'(p_0)}{2nq'}\right] g(p) = 0
\end{aligned} \tag{5.40}$$

Here, the variation of $S(p)$ with p is incorporated through $S'(p_0)$ and the "coupling parameters" $\mathcal{L}_{c1}$ and $\mathcal{L}_{c1}$, which are:

$$\begin{aligned}
\mathcal{L}_{c1} &= 1 - \frac{iS''(p_0)}{2nq'f'(p_0)} - \frac{1}{2Rf'(p_0)}\left[S(p_0)S'(p_0)\right] \\
\mathcal{L}_{c2} &= 1 - \frac{iS'''(p_0)}{2nq'f''(p_0)} - \frac{1}{2Rf''(p_0)}\left[S'^2(p_0) + S(p_0)S''(p_0)\right]
\end{aligned} \tag{5.41}$$

It follows that, for constant $S(p)$ we have $\mathcal{L}_{c1} = \mathcal{L}_{c2} = 1$.

For the sake of further simplification we introduce the following transformation:

$$p - p_0 + \frac{f'(p_0)\mathcal{L}_{c1}}{f''(p_0)\mathcal{L}_{c2}} = \varepsilon y \tag{5.42}$$

where ε is an arbitrary parameter. We substitute this equation into Eq. (5.40) to

obtain

$$\frac{d^2g(y)}{dy^2} - \left(\frac{\varepsilon^4(nq')^2 f''(p_0)\mathcal{L}_{c2}}{2R}\right) y^2 g(y) + \left(\frac{\varepsilon^2(nq')^2}{R}\right)\left[\Omega - f(p_0) + \frac{f'^2(p_0)\mathcal{L}_{c1}^2}{2f''(p_0)\mathcal{L}_{c2}} + \frac{(\frac{S(p_0)}{2})^2}{R} + \frac{iS'(p_0)}{2nq'}\right] g(y) = 0 \tag{5.43}$$

We can then choose ε, such that $\varepsilon^4 \frac{(nq')^2 f''(p_0)\mathcal{L}_{c2}}{2R} = 1$ or similarly $\varepsilon^2 = \frac{1}{nq'}\sqrt{\frac{2R}{f''(p_0)\mathcal{L}_{c2}}}$. This gives;

$$y^2 = nq'\sqrt{\frac{f''(p_0)\mathcal{L}_{c2}}{2R}}\left(p - p_0 + \frac{f'(p_0)\mathcal{L}_{c1}}{f''(p_0)\mathcal{L}_{c2}}\right)^2 \tag{5.44}$$

and substituting this into Eq. (5.43) we get

$$\frac{d^2g(y)}{dy^2} + \left(\bar{\mu} - y^2\right) g(y) = 0 \tag{5.45}$$

where

$$\bar{\mu} = nq'\sqrt{\frac{2}{Rf''(p_0)\mathcal{L}_{c2}}}\left[\Omega - f(p_0) + \frac{f'^2(p_0)\mathcal{L}_{c1}^2}{2f''(p_0)\mathcal{L}_{c2}} + \frac{(\frac{S(p_0)}{2})^2}{R} + \frac{iS'(p_0)}{2nq'}\right] \tag{5.46}$$

and Eq. (5.45) is known as the Weber-Hermite differential equation and is closely related to the Hermite differential equation. If we substitute,

$$g(y) = H(y)\exp\left[\frac{-y^2}{2}\right] \tag{5.47}$$

into Eq. (5.45), after some algebra we obtain the following differential equation:

$$\frac{d^2H(y)}{dy^2} - 2y\frac{dH(y)}{dy} + (\bar{\mu} - 1)H(y) = 0 \tag{5.48}$$

This is a general Hermite equation of index $\bar{\mu}$. In order to solve Eq. (5.45), we must first seek the solutions for Eq. (5.48). It is important to note that $\bar{\mu}$ is in general complex. As we are looking for physical solutions, solutions to Eq. (5.48) must lead to localised $A(p)$, which implies that we are looking for solutions which do not grow faster than $\exp(\frac{y^2}{2})$ as $y \to \infty$. This condition can be satisfied only if, $\bar{\mu} = 2N + 1$, where N is a non negative integer [100, 101]. Therefore, using Eq. (5.44) to transform from y space back into p space, the solution for Eq. (5.45) is readily given as

$$g_N(p) = H_N(p)\exp\left[inq'\sigma\left(p - p_0 + \frac{f'(p_0)\mathcal{L}_{c1}}{f''(p_0)\mathcal{L}_{c2}}\right)^2\right] \tag{5.49}$$

This is the Weber-Hermite function of order N, where

$$\sigma = \pm i\sqrt{\frac{f''(p_0)\mathcal{L}_{c2}}{8R}} \tag{5.50}$$

and the Hermite polynomials $H_N(p)$ are given by

$$\begin{aligned} H_N(p) = (-1)^N \left(\frac{i}{2nq'\sigma}\right)^{\frac{N}{2}} \exp\left[-2inq'\sigma\left(p - p_0 + \frac{f'(p_0)\mathcal{L}_{c1}}{f''(p_0)\mathcal{L}_{c2}}\right)^2\right] \\ \times \left(\frac{d^N}{dp^N}\right) \exp\left[2inq'\sigma\left(p - p_0 + \frac{f'(p_0)\mathcal{L}_{c1}}{f''(p_0)\mathcal{L}_{c2}}\right)^2\right] \end{aligned} \tag{5.51}$$

Substituting Eq. (5.49) back into Eq. (5.37) we derive the final solution for the envelope function $A_N(p)$;

$$A_N(p) = H_N(p) \exp\left[inq'\sigma\left(p - p_0 + \frac{f'(p_0)\mathcal{L}_{c1}}{f''(p_0)\mathcal{L}_{c2}}\right)^2\right] \exp\left[\frac{inq'}{2R}\Psi(p)\right] \tag{5.52}$$

where the sign of σ is chosen such that $A_N(p)$ is localised. Here, $\Psi(p) = \int_p S(p)dp$ which also implies that $S(p) = \Psi'(p)$. Taylor expanding $\Psi(p)$ to the second order about $p = p_0$, leads to:

$$\begin{aligned} \frac{inq'}{2R}\Psi(p) &\approx \frac{inq'\Psi(p_0)}{2R} + \frac{inq'\Psi'(p_0)}{2R}(p - p_0) + \frac{inq'\Psi''(p_0)}{4R}(p - p_0)^2 \\ &= inq'\alpha + inq'\lambda(p - p_0) + inq'\nu(p - p_0)^2 \end{aligned} \tag{5.53}$$

with

$$\begin{aligned} \alpha &= \frac{\Psi(p_0)}{2R} \\ \lambda &= \frac{\Psi'(p_0)}{2R} \equiv \frac{S(p_0)}{2R} \\ \nu &= \frac{\Psi''(p_0)}{4R} \equiv \frac{S'(p_0)}{4R} \end{aligned} \tag{5.54}$$

Substituting Eq. (5.53) into Eq. (5.52) we get;

$$\begin{aligned} A_N(p) = H_N(p) \exp\left[inq'\sigma\left(p - p_0 + \frac{f'(p_0)\mathcal{L}_{c1}}{f''(p_0)\mathcal{L}_{c2}}\right)^2\right] \\ \times \exp\left[inq'\alpha + inq'\lambda(p - p_0) + inq'\nu(p - p_0)^2\right] \end{aligned} \tag{5.55}$$

To understand how p_0 is related to R, $S(p)$ and $f(p)$, we shall take the first derivative

of $A_N(p)$ at $p = p_0$ and equating it to zero, i.e $\frac{dA_N(p)}{dp}|_{p=p_0} = 0$. This leads to:

$$\frac{f'(p_0)\mathcal{L}_{c1}}{\sqrt{2f''(p_0)\mathcal{L}_{c2}}} = \left(\frac{\sqrt{R}}{nq'}\right)\left(\frac{H'_N(p_0)}{H_N(p_0)}\right) + \frac{\frac{iS(p_0)}{2}}{\sqrt{R}},$$

or equivalently:

$$\left(\frac{f'(p_0)\mathcal{L}_{c1}}{\sqrt{2f''(p_0)\mathcal{L}_{c2}}}\right)^2 = \left(\frac{R}{n^2q'^2}\right)\left(\frac{H'_N(p_0)}{H_N(p_0)}\right)^2 - \frac{S(p_0)^2}{4R} + \frac{iS(p_0)}{nq'}\left(\frac{H'_N(p_0)}{H_N(p_0)}\right) \quad (5.56)$$

and

$$\frac{2\sigma f'(p_0)\mathcal{L}_{c1}}{f''(p_0)\mathcal{L}_{c2}} = \left(\frac{i}{\sqrt{R}}\right)\left(\frac{f'(p_0)\mathcal{L}_{c1}}{\sqrt{2f''(p_0)\mathcal{L}_{c2}}}\right) = -\frac{S(p_0)}{2R} + \frac{i}{nq'}\left(\frac{H'_N(p_0)}{H_N(p_0)}\right)$$

For given $S(p)$ this equation controls how the envelope $A(p)$ moves in p space. Eq. (5.56) is at the heart of our calculations, from which subsequent constraints emerge. We may use either of these relations throughout this section whenever they are needed. Furthermore, except for the very special case of the shifted isolated modes (i.e. when x_0 is real), for non zero $S(p)$ the reconstructed global mode sits away from the outboard mid-plane, which in turn leads to poloidal symmetry breaking with respect to the outboard mid plane. It is important to note that, from this equation, we can understand how, and under what circumstances, the ballooning phase angle p_0 shifts into the complex plane which, as discussed in section 5.2, pushes the global mode away from $x_s = 0$.

Finally, we substitute $\bar{\mu} = 2N + 1$ into Eq. (5.46) and using Eq. (5.56) to eliminate $\frac{f'^2(p_0)\mathcal{L}_{c1}^2}{2f''(p_0)\mathcal{L}_{c2}}$ we derive;

$$\Omega_N = f(p_0) - \frac{i}{nq'}\left[2R\sigma(2N+1) + \left(\frac{S'(p_0)}{2} + \frac{H'_N(p_0)}{H_N(p_0)}S(p_0)\right)\right] - \frac{R}{(nq')^2}\left(\frac{H'_N(p_0)}{H_N(p_0)}\right)^2 \quad (5.57)$$

Recalling the analytical treatment of section 5.1, we have assumed that the fundamental mode (i.e. $N = 0$) is the most unstable mode of the system. However, from Eq. (5.57), it is important to note that the fundamental mode may not always be the most unstable mode of the system. This finding is consistent with results that

were presented in Ref [28][11].

In experiments we do not usually measure p_0, but rather a poloidal position about which the magnitude of $A(p)$ peaks in real p space, i.e at $p = p_m$, where p_m is real and measures the physical poloidal position of the reconstructed global modes. To extract information about p_m, and to know how it is related to p_0, we shall first rewrite Eq. (5.55) by collecting terms with like powers of p, to get

$$A_N(p) = H_N(p) \underbrace{\exp\left[inq'\left(\sigma+\nu\right)p^2\right]}_{I} \underbrace{\exp\left[inq'\Pi p\right]}_{II} \underbrace{\exp\left[inq'\tau\right]}_{III}, \tag{5.58}$$

where

$$\begin{aligned} \Pi &= \sigma\frac{2f'(p_0)\mathcal{L}_{c1}}{f''(p_0)\mathcal{L}_{c2}} + \lambda - 2p_0\left(\sigma+\nu\right) \\ \tau &= \alpha - \lambda p_0 + \nu p_0^2 + \sigma\left(p_0 - \frac{f'(p_0)\mathcal{L}_{c1}}{f''(p_0)\mathcal{L}_{c2}}\right)^2 \end{aligned} \tag{5.59}$$

Note that, the first term (I) is the envelope that gives rise to the localisation of the mode in p space. This term alone describes a pure isolated mode, if we assume $S(p) = 0$. The second term (II), is responsible for both radial and poloidal asymmetries under the influence of $S(p)$. Finally, the third term (III) does not depend on p, but depends on p_0. Therefore, it can be simply considered as a normalization factor that scales the phase of $A(p)$.

Decomposing Eq. (5.58) into real and imaginary components and completing the square in p, we get

$$\begin{aligned} \bar{A}_N(p) = H_N(p) &\underbrace{\exp\left[-nq'\left(\sigma+\nu\right)_i\left(p + \frac{\Pi_i}{2\left(\sigma+\nu\right)_i}\right)^2\right]}_{The\ envelope} \\ &\times \underbrace{\exp\left[inq'\left(\sigma+\nu\right)_r\left(p + \frac{\Pi_r}{2\left(\sigma+\nu\right)_r}\right)^2\right]}_{Oscillatory\ part} \end{aligned} \tag{5.60}$$

[11] In Ref [28] they found that for weak gradient (L-mode) parameter regime the most unstable mode is the fundamental mode which corresponds to an isolated mode that sits on the outboard mid-plane. However, for a parameter regime that corresponds to strong gradient (H-mode) the mode sits at an arbitrary poloidal position and the most unstable solutions are not usually the fundamental modes.

where we have normalised $A_N(p)$ such that

$$A_N(p) = \bar{A}_N(p) \exp\left[nq'\left(i\tau + \left(\frac{\Pi_i}{2}\right)^2 (\sigma+\nu)_i^{(-1)} - i\left(\frac{\Pi_r}{2}\right)^2 (\sigma+\nu)_r^{(-1)}\right)\right]$$

Here, the second exponential term on the right hand side of Eq. (5.60) is an oscillatory function, but the first term (*the envelope*) gives rise to the localisation in p space about $p = p_m$ which is calculated as follow:

$$p_m = -\frac{\Pi_i}{2\,(\sigma+\nu)_i} = -\frac{\left(\sigma\frac{2f'(p_0)\mathcal{L}_{c1}}{f''(p_0)\mathcal{L}_{c2}} + \lambda - 2p_0\,(\sigma+\nu)\right)_i}{2\,(\sigma+\nu)_i} \tag{5.61}$$

We then divide p_0 into its real and imaginary components and rearrange to get:

$$p_m = \left(p_{0,r} + \frac{(\sigma+\nu)_r}{(\sigma+\nu)_i} p_{0,i}\right) - \left(\frac{\left(\frac{\sigma f'(p_0)\mathcal{L}_{c1}}{f''(p_0)\mathcal{L}_{c2}}\right)_i}{(\sigma+\nu)_i} + \frac{\lambda_i}{2\,(\sigma+\nu)_i}\right) \tag{5.62}$$

We can now use the constraint of Eq. (5.56), knowing that $\lambda = \frac{S(p_0)}{2R}$, to eliminate $\left(\frac{\sigma f'(p_0)\mathcal{L}_{c1}}{f''(p_0)\mathcal{L}_{c2}}\right)_i$, and then to obtain the final equation for p_m, which reads

$$p_m \;=\; p_{0,r} + \frac{(\sigma+\nu)_r}{(\sigma+\nu)_i} p_{0,i} - \left(\frac{1}{2nq'}\right)\frac{\left(\frac{H'_N(p_0)}{H_N(p_0)}\right)_r}{(\sigma+\nu)_i} \tag{5.63}$$

One can use this equation to understand how both real and imaginary components of p_0 contribute to the physical poloidal position of the global mode under the influence of terms associated with $S(p)$. In addition, the last term on the right hand side of Eq. (5.63) contributes an $O(\frac{1}{nq'})$ correction for harmonics with $N > 0$. Finally, comparing the envelope part of Eq. (5.60) with a Gaussian function, allow us to calculate the width of $A(p)$ in p space, Δ_p, which is defined to be the full width at half maximum (FWHM) of the Gaussian, and has the following form:

$$\Delta_p \sim (n|q'(\sigma+\nu)_i|)^{-\frac{1}{2}} \tag{5.64}$$

As n increases Δ_p decreases, such that for $nq' \gg 1$ $|A(p)|$ is highly localised about $p = p_m$.

5.4.2 The two Dimensional Eigenmode Structures $\tilde{\phi}(x_s, \theta)$

We have solved the eigenmode problem of Eq. (5.36) for both $A(p)$ and the associated eigenvalue Ω under the assumption $R(p) = R$, where R is constant. We are now in a position to provide an analytic description for the global eigenmode, $\tilde{\phi}(x_s, \theta)$. We start by substituting Eq. (5.58) into (4.50), to obtain

$$\begin{aligned}\tilde{\phi}(x_s, \theta) = \exp\left[-inq\theta + inq'\tau\right] \int_{-\infty}^{+\infty} \xi(x_s, p, \theta) H_N(p) \\ \times \exp\left[inq'\left(\sigma + \nu\right)\left(p^2 + \frac{x_s + \Pi}{\sigma + \nu} p\right)\right] dp\end{aligned} \tag{5.65}$$

We have factored out those terms that do not depend on p. Knowing that $\xi(x_s, p, \theta)$ is a slowly varying function of p compared to $A(p)$, the stationary phase method to the lowest order is employed to simplify Eq. (5.65) to obtain the following result[12]:

$$\begin{aligned}\tilde{\phi}(x_s, \theta) \approx \xi(x_s, p = p_m, \theta) H_N(p_m) \exp\left[-inq\theta + inq'\tau\right] \\ \times \int_{-\infty}^{+\infty} \exp\left[inq'\left(\sigma + \nu\right)\left(p^2 + \frac{x_s + \Pi}{\sigma + \nu} p\right)\right] dp\end{aligned} \tag{5.66}$$

In order to evaluate the integral, we first complete the square in p, to obtain

$$\begin{aligned}\int_{-\infty}^{+\infty} \exp\left[inq'\left(\sigma + \nu\right)\left(p^2 + \frac{x_s + \Pi}{\sigma + \nu} p\right)\right] dp = \exp\left[\frac{-inq'\kappa^2}{4(\sigma + \nu)}\right] \\ \times \int_{-\infty}^{+\infty} \exp\left[inq'\left(\sigma + \nu\right)\left(p + \frac{\kappa}{2(\sigma + \nu)}\right)^2\right] dp\end{aligned} \tag{5.67}$$

where,

$$\kappa = x_s + \Pi = x_s + \lambda - 2p_0(\sigma + \nu) + \frac{2\sigma f'(p_0)\mathcal{L}_{c1}}{f''(p_0)\mathcal{L}_{c2}} \tag{5.68}$$

The integral is a Gaussian which can be solved analytically and it is equal to $\sqrt{[i\pi]/[nq'(\sigma + \nu)]}$[13]. Hence, Eq. (5.67) reduces to the following:

$$\int_{-\infty}^{+\infty} \exp\left[inq'\left(\sigma + \nu\right)\left(p^2 + \frac{x_s + \Pi}{\sigma + \nu} p\right)\right] dp = \sqrt{\frac{i\pi}{nq'(\sigma + \nu)}} \exp\left[\frac{-inq'\kappa^2}{4(\sigma + \nu)}\right] \tag{5.69}$$

This equation yields the expected result that the Fourier transformation of a Gaussian in p space is also a Gaussian in the κ or x_s space. Substituting Eq. (5.69) into

[12] We can see from Eq. (5.60) that for $nq' \gg 1$ the envelope part of $A_N(p)$ is highly localised about $p = p_m$. We have expand both $\xi(x_s, p, \theta)$ and $H_N(p)$ about $p = p_m$ and to the lowest order we write $\xi(x_s, p, \theta) \approx \xi(x_s, p = p_m, \theta)$ and $H_N(p) \approx H_N(p_m)$, respectively.

[13] For more details see subsection 4.7.1 − second to the last paragraph.

Eq. (5.66), we derive the final form for the 2D eigenmode $\tilde{\phi}(x_s, \theta)$ in tokamaks:

$$\tilde{\phi}(x_s, \theta) \approx \xi(x_s, p = p_m, \theta) H_N(p_m) \exp\left[inq'\left(\tau - \frac{\kappa^2}{4(\sigma+\nu)}\right)\right] \exp\left[-inq\theta\right] \quad (5.70)$$

From Eq. (5.70) it can be seen that the exponential term on the right hand side peaks at $\kappa = 0$ or equivalently at $x_s = x_0$, where the radial parameter x_0 is complex and is defined as follows:

$$x_0 = -\Pi = 2p_0(\sigma+\nu) - \lambda - \frac{2\sigma f'(p_0)\mathcal{L}_{c1}}{f''(p_0)\mathcal{L}_{c2}} \quad (5.71)$$

By using Eq. (5.56) to eliminate $\frac{\sigma f'(p_0)\mathcal{L}_{c1}}{f''(p_0)\mathcal{L}_{c2}}$, we can reduce Eq. (5.71) to:

$$x_0 = -\Pi = 2p_0\left(\sigma+\nu\right) - \left(\frac{i}{nq'}\right)\left(\frac{H'_N(p_0)}{H_N(p_0)}\right) \quad (5.72)$$

The real and imaginary components of x_0 are:

$$\begin{aligned} x_{0,r} = -\Pi_r &= 2p_{0,r}\left(\sigma+\nu\right)_r - 2p_{0,i}\left(\sigma+\nu\right)_i + \left(\frac{1}{nq'}\right)\left(\frac{H'_N(p_0)}{H_N(p_0)}\right)_i \\ x_{0,i} = -\Pi_i &= 2p_{0,r}\left(\sigma+\nu\right)_i + 2p_{0,i}\left(\sigma+\nu\right)_r - \left(\frac{1}{nq'}\right)\left(\frac{H'_N(p_0)}{H_N(p_0)}\right)_r \end{aligned} \quad (5.73)$$

The correction for the higher order harmonics with $N > 0$, is of order $\sim O(\frac{1}{nq'})$.

Having obtained a formula for x_0, we may note the similarity to Eq. (5.63) to provide

$$p_m = \frac{x_{0,i}}{2(\sigma+\nu)_i} \quad (5.74)$$

This shows that the mode's poloidal shift is a direct consequence of $x_{0,i}$[14]. For a given equilibrium, if the complex mode frequency $\Omega_0(x_s, p)$ does not have a stationary point on the real axis, x_0 enters into the complex plane, which forces the mode to shift in the poloidal plane away from the outboard mid-plane. This has an impact on both its structure and stability. Furthermore, Eq. (5.74) also sheds light on another important point. It predicts that different harmonics with $N \geq 0$ are initially peaked on the outboard mid-plane for $x_{0,i} = 0$. However, as can be seen from Eq. (5.73), they exihibit slightly different poloidal shifts seperated by order $O(1/nq')$ for equilibria with $x_{0,i} \neq 0$.

[14]Note that, the magnitude of $A(p)$ is highly localised about $p = p_m$. This leads to a reconstructed global mode $\tilde{\phi}(x_s, \theta)$ that peaks at $\theta = p_m$.

It is important to mention again that the reconstructed global mode, in general, undergoes a radial shift with respect to $x_s = 0$. To quantify this radial shift we decompose $\tilde{\phi}(x_s, \theta)$ in Eq. (5.70) into its amplitude and oscillatory parts. The magnitude of $\tilde{\phi}(x_s, \theta)$ is

$$|\tilde{\phi}| \sim \exp\left[\frac{-n|q'(\sigma+\nu)_i|}{4|\sigma+\nu|^2}\,(x_s - x_m)^2\right] \tag{5.75}$$

We can clearly see that the localisation condition demands that $(\sigma+\nu)_i$ must not be zero. Here, the parameter x_m represents the radial shift in real space and is defined as:

$$x_m = -\Pi_r + \frac{(\sigma+\nu)_r}{(\sigma+\nu)_i}\Pi_i \tag{5.76}$$

Using Eq. (5.73), x_m can be related to x_0 as follow:

$$x_m = x_{0,r} - \frac{(\sigma+\nu)_r}{(\sigma+\nu)_i}x_{0,i} \tag{5.77}$$

This equation describes how the reconstructed global mode shifts radially in real space. It is worth mentioning that this shift is not simply the real part of the complex shift x_0, but rather a combination of both its real and imaginary components. Upon substituting both $x_{0,r}$ and $x_{0,i}$ from Eq. (5.73), Eq. (5.77) can be rewritten as:

$$\begin{aligned} x_m = -2p_{0,i}(\sigma+\nu)_i\left[1 + \left(\frac{(\sigma+\nu)_r}{(\sigma+\nu)_i}\right)^2\right] \\ +\frac{1}{nq'}\left[\left(\frac{H'_N(p_0)}{H_N(p_0)}\right)_i + \frac{(\sigma+\nu)_r}{(\sigma+\nu)_i}\left(\frac{H'_N(p_0)}{H_N(p_0)}\right)_r\right] \end{aligned} \tag{5.78}$$

This equation sheds light on the mechanism behind the radial shift away from $x_s = x_m = 0$. By considering only the fundamental harmonic with $N = 0$, Eq. (5.78) tells us that the mode's radial shift is a direct consequence of the imaginary component of $p_{0,i}$. This is consistent with the analysis of section 5.2. From Eq. (5.78) we can highlight another crucial point. Even though the fundamental mode is radially centred with $p_{0,i} = 0$, it is possible that the other harmonics still undergo an $O(1/nq')$ radial shift. In what follows and throughout the rest of this thesis we shall focus on the theory of fundamental modes.

The global mode extends over a region with a radial width Δ_x that can be

obtained from Eq. (5.75):

$$\Delta_x = 4\sqrt{\log(2)}\sqrt{\frac{|\sigma+\nu|^2}{n|q'(\sigma+\nu)_i|}}, \tag{5.79}$$

where Δ_x scales inversely with the square root of nq'.

Finally, we comment on the validity of our analytic solutions. It is important to remember that in obtaining Eq. (4.63) we have Taylor expanded the local complex mode frequency about $x_s = 0$; our solutions are only valid if the mode is confined radially near this point. But as we have shown in the above calculations it is possible for the mode to undergo large radial shifts (independent of n) that can lead to the breakdown of the theory. Therefore, it is crucial to understand how the radial shift is related to the coefficients that we obtained for the model fitted to the local complex mode frequency $\Omega_0(x_s, p)$. We seek a constraint that limits the mode's radial shift to a small region about $x_m = 0$. In general, we may allow small radial shifts of order of the mode radial width and write our constraint as follows;

$$0 \leq |x_m| \leq \Delta_x \tag{5.80}$$

In contrast to direct global solutions, this constraint provides a limitation to our analytical calculations and hence to the formalism on which this thesis is based. This will be further clarified after we apply our calculations to ITG modes in circular tokamaks in section 5.6.

5.5 Validation of Analytical Solutions: The Fundamental Modes

In this section, considering the fundamental modes for simplicity, the generalised analytical solutions are validated by considering two special limits, namely the isolated and general modes. The analytic solutions in this chapter can account for a mode that sits somewhere between the outboard mid-plane and the top or bottom of the tokamak plasma with different stability and structures compared to the isolated and general mode limits. In addition, we also consider the so-called anti-ballooning

modes that sit on the inboard side of the tokamaks [28]. In our terminology, we would like to distinguish these type of modes and call them generalised modes. We proceed with our analysis, assuming up-down symmetric equilibria, and Fourier expand the three functions $f(p)$, $S(p)$ and $R(p)$ to obtain

$$\begin{aligned} R(p) &= R_0 \\ S(p) &= S_0 \\ f(p) &= f_0 + f_1 \cos p \end{aligned} \tag{5.81}$$

where, for simplicity, only two Fourier modes are retained. Here, R_0, S_0 , f_0 and f_1 are the Fourier coefficients, which are evaluated at $p = p_0$. For this set of parameters, we have $R = R_0$, $S(p_0) = S_0$, $S'(p_0) = S''(p_0) = 0$, $f(p_0) = f_0 + f_1 \cos p_0$, $f'(p_0) = -f_1 \sin p_0$ and $f''(p_0) = -f_1 \cos p_0$, respectively. Using Eq. (5.81), the analytical solutions for p_0 (Eq. (5.56)), $A(p)$ (Eq. (5.55)), Ω (Eq. (5.57)) and $\tilde{\phi}(x_s, \theta)$ (Eq. (5.70)), become:

1. p_0 from Eq. (5.56):

The constraint that relates p_0 to the model parameter S_0, and tells how the generalised modes shift both radially and poloidally, is reduced to the following form:

$$\tan p_0 = \frac{-\lambda}{2\sigma}, \tag{5.82}$$

where

$$\begin{aligned} \lambda &= \frac{S_0}{2R_0} \\ \sigma &= -\beta\sqrt{\cos p_0} \\ \beta &= \sqrt{\frac{f_1}{8R_0}} \end{aligned} \tag{5.83}$$

Note that, the fact that $S(p) = S_0$ does not vary with p, forces $\mathcal{L}_{c1} = \mathcal{L}_{c2} = 1$.

2. $A(p)$ from Eq. (5.55)

$$A(p) = \exp\left[inq'\sigma\left(p - p_0 + \tan p_0\right)^2 + inq'\lambda p\right] \tag{5.84}$$

Using Eq. (5.82) this formula can be also rewritten in the following form:

$$A(p) = \exp\left[inq'\sigma\left(p - p_0\right)^2\right] \exp\left[\frac{inq'\lambda}{2}\left(2p_0 - \tan p_0\right)\right] \tag{5.85}$$

From Eq. (5.73) and Eq. (5.74),

$$p_m = \frac{x_{0,i}}{2\sigma_i} = -\frac{\Pi_i}{2\sigma_i} = p_{0,r} + \frac{\sigma_r}{\sigma_i} p_{0,i} \tag{5.86}$$

where, we have used $\nu = (\frac{1}{4R_0}\frac{dS(p)}{dp}|_{p=p_0}) = 0$, which is true as $S(p)$ is constant.

3. Ω from Eq. (5.57)

$$\Omega = \frac{i}{nq'}\left[2R_0\beta\sqrt{\cos p_0}\right] + f_0 + f_1 \cos p_0 \tag{5.87}$$

4. $\tilde{\phi}(x_s, \theta)$ from Eq. (5.70)

$$\tilde{\phi}(x_s, \theta) \approx \xi(x_s, p = p_m, \theta) \exp\left[inq'\left(\tau - \frac{\kappa^2}{4\sigma}\right)\right] \exp\left[-inq\theta\right] \tag{5.88}$$

where τ and κ are defined as

$$\begin{aligned} \tau &= \alpha - \lambda p_0 + \sigma\left(p_0 - \tan p_0\right)^2 \\ \kappa &= x_s + \Pi = x_s - 2\sigma p_0 \end{aligned} \tag{5.89}$$

The complex radial parameter x_0 (from Eq. (5.72)), can be now written as

$$x_0 = -\Pi = 2\sigma p_0 \tag{5.90}$$

Furthermore, the mode radial shift in real space, x_m, (from Eq. (5.77)), reduces to:

$$x_m = x_{0,r} - \frac{\sigma_r}{\sigma_i} x_{0,i} = -2\sigma_i p_{0,i}\left[1 + \left(\frac{\sigma_r}{\sigma_i}\right)^2\right] \tag{5.91}$$

Finally, the mode radial width, Δ_x from Eq. (5.79), is given by:

$$\Delta_x = 4\sqrt{\log(2)}\sqrt{\frac{|\sigma|^2}{n|q'\sigma_i|}} \tag{5.92}$$

Having obtained the important equations for the fundamental modes, we consider a few limits of these solutions. We start by solving Eq. (5.82) for p_0 to explore how it depends on the model coefficients of Eq. (5.81). To do that, we write Eq. (5.82)

in the form:

$$\sin^2 p_0 = \varrho^2 \cos p_0 \tag{5.93}$$

where

$$\varrho = \frac{\lambda}{2\beta} = \frac{S_0}{\sqrt{2 f_1 R_0}} \tag{5.94}$$

Here, Eq. (5.83) is used to write both λ and β in terms of the model coefficients. Using the trigonometric relation ($\sin^2 p_0 = 1 - \cos^2 p_0$), substituting Z for $\cos p_0$ for simplification, we rearrange Eq. (5.93) to get;

$$Z^2 + \varrho^2 Z - 1 = 0 \tag{5.95}$$

Solving this equation for Z leads to the following solutions:

$$\begin{gathered} Z = \frac{-\varrho^2 \pm \sqrt{\varrho^4 + 4}}{2} \\ \text{and,} \\ p_0 = \cos^{-1} Z \end{gathered} \tag{5.96}$$

where $\pm$ signs correspond to two different branches of the eigenmode solutions. If we now decompose both Z and p_0 into their real and imaginary components we get

$$\begin{aligned} Z_r &= \cos p_{0,r} \cosh p_{0,i} \\ Z_i &= -\sin p_{0,r} \sinh p_{0,i} \end{aligned} \tag{5.97}$$

This is the main equation that we use in the following to describe and understand the stability and structure of the global modes that belong to each of the above branches of eigenmode solutions. We now discuss the constraints on the model coefficients to avoid large radial shifts, which would otherwise invalidate the Taylor expansion of $\Omega_0(x_s, p)$ in x_s.

5.5.1 Radial Shift: Constraint on the Model Coefficients

To understand the radial shift, we decompose ϱ^2 (from Eq. (5.94)) into its real and imaginary components to get:

$$\begin{aligned}(\varrho^2)_r &= \frac{\left(S_{0,r}^2 - S_{0,i}^2\right)\left[f_{1,r}R_{0,r} - f_{1,i}R_{0,i}\right] - 2S_{0,r}S_{0,i}\left(f_{1,i}R_{0,r} + f_{1,r}R_{0,i}\right)}{2|f_1R_0|^2} \\ (\varrho^2)_i &= \frac{\left(S_{0,r}^2 - S_{0,i}^2\right)\left[f_{1,i}R_{0,r} + f_{1,r}R_{0,i}\right] + 2S_{0,r}S_{0,i}\left(f_{1,r}R_{0,r} - f_{1,i}R_{0,i}\right)}{2|f_1R_0|^2}\end{aligned} \tag{5.98}$$

Considering the case $(\varrho^2)_i = 0$ (or $\varrho^2 = (\varrho^2)_r$)[15], which also implies $Z_i = 0$ for all $S_0 \neq 0$[16], we obtain the following constraint on the model coefficients:

$$\left(S_{0,r}^2 - S_{0,i}^2\right)\left[f_{1,i}R_{0,r} + f_{1,r}R_{0,i}\right] = -2S_{0,r}S_{0,i}\left(f_{1,r}R_{0,r} - f_{1,i}R_{0,i}\right) \tag{5.99}$$

For a particular set of equilibrium parameters, this constraint provides a solution that leads to a radially centred global mode. While it is straight forward to keep S_0 as an arbitrary complex number, for convenience, in what follow we consider either S_0 real or imaginary.

5.5.2 Profile Shearing: A Linear Variation in the Local Frequency

We start with a pure isolated type of mode and investigate how it evolves under the effect of $S_0 = S_{0,r}$. This may arise as rotational flow shear is introduced, if we assume that $S_0 = nq'\gamma_E$, which corresponds to a Doppler shift in the local frequency $\omega_0(x_s, p)$. This introduces a radial shift in the local frequency $\omega_0(x_s, p)$ with respect to the local growth rate $\gamma_0(x_s, p)$, which, in turn, removes the stationary point from the local complex mode frequency $\Omega_0(x_s, p)$. This allows the mode to shift poloidally with respect to the outboard mid-plane[17]. For this particular choice of S_0, Eq. (5.99) reduces to the following equation;

$$f_{1,r}R_{0,i} + f_{1,i}R_{0,r} = 0 \tag{5.100}$$

[15] In what follow, for the rest of this section, whenever ϱ^2 appears it means $(\varrho^2)_r$

[16] For $S_0 = 0$, there is no constraint on the model coefficients. This special case corresponds to a pure isolated mode that peaks at $x_s = 0$.

[17] Recall from section 5.2 that, if Ω_0 is not stationary, implying that $x_{0,i}$ is not zero, the reconstructed global mode in turn shifts poloidally with respect to the outboard mid-plane.

This equation shows that one of the four coefficients should have opposite sign compared to the other ones. This in turn implies that, if the local frequency $\omega_0(x_s, p)$ has a maximum at $x_s = 0$, then the associated growth rate $\gamma_0(x_s, p)$ should be minimum here, or vice versa[18]. For a set of the model coefficients that satisfy this equation, Eq. (5.97) is simplified to:

$$\begin{aligned} Z_r &= \cos p_{0,r} \cosh p_{0,i} \\ Z_i &= -\sin p_{0,r} \sinh p_{0,i} = 0 \end{aligned} \tag{5.101}$$

We can then solve these two simultaneous equations for the two branches of Eq. (5.96). In the following we explore these two solutions separately.

5.5.2.1 Solutions on the Outboard Mid-plane

As we shall see, these solutions correspond to the branch in Eq. (5.96) with the + sign. If Eq. (5.100) is satisfied, from Eq. (5.96) we have:

$$\begin{aligned} Z_r^+ &= \frac{-\varrho^2 + \sqrt{\varrho^4 + 4}}{2} \\ Z_i^+ &= 0 \end{aligned} \tag{5.102}$$

The easiest starting point to understand how this class of eigenmode responds to the effect of $S_{0,r}$, is to consider the solutions in two limits, namely $|S_{0,r}| \ll 1$ and $|S_{0,r}| \gg 1$, to get

$$\begin{aligned} Z_r^+ &= \begin{cases} 1, & \text{if } |S_{0,r}| \ll 1. \\ 0, & \text{if } |S_{0,r}| \gg 1. \end{cases} \\ Z_i^+ &= 0 \end{aligned} \tag{5.103}$$

Substituting these back into Eq. (5.101) we obtain:

$$1 \geq Z_r^+ = \cos p_{0,r}^+ \cosh p_{0,i}^+ \geq 0 \tag{5.104}$$

[18]This finding is in agreement with Ref [5] (see their Fig.1 panels a and b). They found that the global mode peaks very close to $x_s = 0$ for all values of γ_E (see their Fig.2 and Fig.3). However, the set of equilibrium parameters that they have used do not exactly satisfy our Eq. (5.100), which in turn leads to a small radial shift for intermediate values of γ_E and this is discussed in section 5.6.

and

$$Z_i^+ = -\sin p_{0,r}^+ \sinh p_{0,i}^+ = 0 \tag{5.105}$$

Note that, we have further assumed that $\varrho^2 = (\varrho^2)_r > 0$, such that from Eq. (5.98) we have $f_{1,r}R_{0,r} > f_{1,i}R_{0,i}$. As we will see later, this is not considered to be a constraint, in the sense that we can also assume that $\varrho^2 = (\varrho^2)_r < 0$ and still get a solution that leads to a radially centred global mode[19]. Examining Eq. (5.105), we can see that either $\sinh p_{0,i}^+ = 0$ (or equivalently $p_{0,i}^+ = 0$) or $\sin p_{0,r}^+ = 0$ (or equivalently $p_{0,r}^+ = \pm\ell\pi$) for all values of $S_{0,r}$. Considering the solution with $p_{0,r}^+ = \pm\ell\pi$ from Eq. (5.104) we have $-1 \leq \cosh p_{0,i}^+ \leq 1$ which is never satisfied. Hence, the correct solution is $p_{0,i}^+ = 0$ and this provides the following global solutions:

$$\begin{aligned} p_{0,r}^+ &= \cos^{-1} Z_r^+ \\ p_{0,i}^+ &= 0 \end{aligned} \tag{5.106}$$

Substituting this into Eq. (5.86) we get:

$$p_m^+ = p_{0,r}^+ = \cos^{-1} Z_r^+ \tag{5.107}$$

Recalling from Eq. (5.103) that $0 \leq Z_r^+ \leq 1$, where the two limits 0 and 1 correspond to $|S_{0,r}| = \infty$ and $|S_{0,r}| = 0$, respectively, Eq. (5.107) shows that $p_m^+ = 0$ for $S_{0,r} = 0$ and then increases with $S_{0,r}$, according to $p_m^+ = \cos^{-1} Z_r^+$, and eventually, depending on the sign of $S_{0,r}$, approaches $\pm\frac{\pi}{2}$ asymptotically as $S_{0,r}$ goes to $\pm\infty$. Note that, these eigenmodes can only exist on the bad curvature regions and do not explore the good curvature regions on the inboard side of the tokamak. As $p_{0,i}^+ = 0$, these eigenmode solutions are classified as a pure type of generalised modes for which the function $A(p)$ is symmetric about $p = p_m^+$. This in turn, from Eq. (5.91), leads to the reconstructed global modes that are radially confined to the centre of the domain and peaks about a reference surface $x_s = x_m^+ = 0$.

In the following, we consider two limits of these classes of generalised modes,

[19]From Eq. (5.98) we can see that $\varrho^2 = (\varrho^2)_r < 0$ in two cases; either $S_0 = S_{0,r}$ for $f_{1,r}R_{0,r} < f_{1,i}R_{0,i}$ or $S_0 = iS_{0,i}$ for $f_{1,r}R_{0,r} > f_{1,i}R_{0,i}$. Switching between different signs of ϱ^2 simply switches the highly localised solutions about $x_s = 0$ between the outboard side and the inboard side of the tokamaks. Therefore, we keep $\varrho^2 = (\varrho^2)_r > 0$ here, but we shall see the solutions with $\varrho^2 = (\varrho^2)_r < 0$ that corresponds to $S_0 = iS_{0,i}$ later in section 5.5.3.

namely a pure isolated and general type of modes which are, respectively, obtained in the $S_{0,r} = 0$ and $S_{0,r} = \pm\infty$ limits.

A Pure Isolated Mode

This type of eigenmode is obtained in the limit of $S_0 = 0$ (or equivalently $Z_r^+ = 1$). Using Eq. (5.107), we have $p_{0,r}^+ = p_m^+ = 0$, and the correspond analytical solutions for Ω (from Eq. (5.87)), $A(p)$ (from Eq. (5.85)), $\tilde{\phi}(x_s, \theta)$ (from Eq. (5.88)) and Δ_x (from Eq. (5.92)), are respectively reduced to the following forms:

$$\begin{aligned}
\Omega^{(0)} &= \frac{2iR_0}{nq'}\beta + f_0 + f_1 \\
A^{(0)}(p) &= \exp\left[-inq'\beta p^2\right] \\
\tilde{\phi}^{(0)}(x_s, \theta) &\approx \xi(x_s, p = 0, \theta) \exp\left[\frac{inq'x_s^2}{4\beta}\right] \exp\left[-inq\theta\right] \\
\Delta_x^{(0)} &= 4\sqrt{\log(2)}\sqrt{\frac{|\beta|^2}{n|q'\beta_i|}},
\end{aligned}$$

where, the superscript (0) corresponds to $p = p_m = 0$. Note that these solutions are exactly what we have obtained for a pure isolated mode in section 4.7.1 that sits on the outboard mid-plane. Having recaptured the same solutions that were presented in last paragraph of subsection 4.7.1 for this isolated mode in the limit $S_0 = 0$ from the generalised analytical solutions, we gain confidence in the correctness of our calculations.

A Pure General Mode

Here, the behaviour of a pure generalised mode is investigated in the limit of $|S_0| \gg 1$ (or equivalently $Z_r^+ \ll 1$), which corresponds to a mode that sits near to the top or bottom of the tokamak plasmas. We now want to prove that whether the mode that sits at $p_m^+ \approx \pm\pi/2$ as S_0 goes to $\pm\infty$ has exactly the same eigenvalue and eigenfunction as a pure general mode. We start by expanding Z_r^+ in Eq. (5.102) for $\varrho^2 \gg 1$ (from Eq. (5.94) this also implies $|S_{0,r}| \gg 1$), and then substitute the result

into Eq. (5.107) and rearrange to get

$$\cos p_m^+ = Z_r^+ \approx \frac{1}{\varrho^2} = \frac{4\beta^2}{\lambda^2}, \tag{5.108}$$

where, Eq. (5.94) is used to write ϱ^2 in terms of β and λ. By substituting this equation into Eq. (5.87), the global mode frequency Ω reduces to:

$$\Omega = \frac{i2R_0\beta}{nq'\varrho} + f_0 + \frac{f_1}{\varrho^2} \tag{5.109}$$

In the limit $S_{0,r}$ goes to $\pm\infty$ (or equivalently ϱ^2 goes to $\pm\infty$) we obtain

$$\Omega \approx f_0 \tag{5.110}$$

This indicates that, our mode has the same eigenvalue as a pure general mode that we considered in 4.7.2 (see Eq. (4.89)). This is necessary but not sufficient to see whether it is exactly the same general mode. We proceed further and try to see whether they have exactly the same eigenfunctions as well. Using the expansion of Eq. (5.108) we may rewrite σ from Eq. (5.83) as follows:

$$\sigma \approx -\beta\sqrt{\cos p_m^+} = -\frac{2\beta^2}{\lambda} = -\frac{f_1}{2S_0}, \tag{5.111}$$

where Eq. (5.83) is used to write β and λ in terms of the coefficients S_0, R_0 and f_1. Finally, substituting Eq. (5.111) back into Eq. (5.85), and after multiplying and dividing by a constant factor $\exp[inq'\delta]$, the eigenfunction $A(p)$ takes the following form:

$$\begin{aligned} A(p) = \exp\left[inq'\delta\left(1 - \frac{(p-p_m^+)^2}{2}\right)\right] \exp\left[inq'(\lambda p_m^+ - \delta)\right] \\ \times \exp\left[-\frac{inq'}{2}\lambda\tan p_m^+\right], \end{aligned} \tag{5.112}$$

where $\delta = \frac{f_1}{S_0}$ and the last two exponential term on the right hand side are just constants that scale the phase and amplitude of $A(p)$. Knowing that p_m^+ goes to $\pm\pi/2$ as S_0 goes to $\pm\infty$, the term $(1 - \frac{(p-p_m^+)^2}{2})$ in the exponent of the first term can be in turn approximated by $(1 - \frac{(p-\pi/2)^2}{2})$ and this simply represents the expansion of $\sin p$ about $p = \frac{\pi}{2}$, such that Eq. (5.112) can be rewritten as

$$A(p) \approx \exp\left[inq'\delta\sin p\right] \exp\left[inq'(\lambda p_m^+ - \delta)\right] \exp\left[-\frac{inq'}{2}\lambda\tan p_m^+\right] \tag{5.113}$$

The first exponential term on the right hand side resembles that of a pure general mode obtained in section 4.7.2 (see Eq. (4.90)). However, in our generalised approach, the mode only asymptotically approaches the top or bottom of the plasma as $S_{0,r}$ is increased, and cannot exactly sit there. This can be easily seen for example from the last exponential term on the right hand side; as p_m^+ goes to $\pm\pi/2$ we have $\lambda \tan p_m^+$ goes to ∞, this leads to $A(p) \approx 0$ and in turn does not allow the mode to sit at $p_m^+ = \pm\pi/2$. Nevertheless, in what follows, to a very good approximation, we shall consider our pure generalised type of mode, to sit close to the top or bottom of the plasma as a pure general mode.

5.5.2.2 Solutions on the Inboard Mid-plane

This class of eigenmode solution is associated with the Z^- branch, for which, provided that Eq. (5.100) is satisfied, from Eq. (5.96) we get:

$$\begin{aligned} Z_r^- &= \frac{-\varrho^2 - \sqrt{\varrho^4 + 4}}{2} \\ Z_i^- &= 0 \end{aligned} \tag{5.114}$$

The solutions for the two limits $|S_{0,r}| \ll 1$ and $|S_{0,r}| \gg 1$ are as follow;

$$\begin{aligned} Z_r^- &= \begin{cases} -1, & \text{if } |S_{0,r}| \ll 1. \\ -\varrho^2, & \text{if } |S_{0,r}| \gg 1. \end{cases} \\ Z_i^- &= 0 \end{aligned} \tag{5.115}$$

Upon substituting these solutions back into Eq. (5.101) we get:

$$-\varrho^2 \leq Z_r^- = \cos p_{0,r}^- \cosh p_{0,i}^- \leq -1 \tag{5.116}$$

and

$$Z_i^- = \sin p_{0,r}^- \sinh p_{0,i}^- = 0 \tag{5.117}$$

The global solutions for these two simultaneous equations can be easily obtained. If we first examine Eq. (5.117) we can see that either $\sinh p_{0,i}^- = 0$ (or equivalently $p_{0,i}^- = 0$) or $\sin p_{0,r}^- = 0$ (or equivalently $p_{0,r}^- = \pm\ell\pi$, for any positive integer ℓ) for

all values of $S_{0,r}$. Considering the solution with $p^-_{0,i} = 0$ from Eq. (5.116) we have $-\varrho^2 \leq \cos p^-_{0,r} \leq -1$ which is not valid, because $\cos p^-_{0,r}$ can not have values smaller than -1 for any values of $p^-_{0,r}$. Therefore, we take $p^-_{0,r} = \pm\ell\pi$ as our solution. It should be noted also that for even values of ℓ we have $-\varrho^2 \leq \cosh p^-_{0,i} \leq -1$, but $\cosh p^-_{0,i} \geq 1$ for all values of $p^-_{0,i}$. Hence, only odd values of ℓ can lead to acceptable solutions which then provide the following global solutions:

$$p^-_{0,r} = \pm(2\ell+1)\pi \tag{5.118}$$

$$p^-_{0,i} = \cosh^{-1}(-Z^-_r) \tag{5.119}$$

such that ℓ can be either odd or even. Note that, the only solution that provides a mode that peaks at $x_s = 0$, corresponding to $p^-_{0,i} = 0$ (or $Z^-_r = -1$), is obtained for $S_{0,r} = 0$. This mode sits in the good curvature region at $p_m = p_{0,r} = \pm\pi$. This indicates that, in addition to a pure isolated mode that sits on the outboard side, there is yet another class of mode that sits on the inboard mid-plane of the tokamak plasma. Let us call this a pure anti-isolated mode. The global properties, Ω (from Eq. (5.87)), $A(p)$ (from Eq. (5.85)), $\tilde{\phi}(x_s,\theta)$ (from Eq. (5.88)) and Δ_x (from Eq. (5.92)), for this type of mode, assuming that $p_0 = \pm\pi$, are characterised by the following set of equations:

$$\begin{aligned}
\Omega^{(\pm)} &= \frac{-2R_0}{nq'}\beta + f_0 - f_1 \\
A^{(\pm)}(p) &= \exp\left[nq'\beta\,(p \pm \pi)^2\right] \\
\tilde{\phi}^{(\pm)}(x_s,\theta) &\approx \xi(x_s, p = \pm\pi, \theta)\exp\left[inq'\left(\tau + \frac{i\kappa^2}{4\beta}\right)\right]\exp\left[-inq\theta\right] \\
\Delta_x^{(\pm)} &= 4\sqrt{\log(2)}\sqrt{\frac{|\beta|^2}{n|q'\beta_r|}},
\end{aligned}$$

where $\tau = -i\beta\pi^2$, $\kappa = x_s + 2i\beta(\pm\pi)$ and $\pm$ signs correspond to $p^\pm_m = p^\pm_{0,r} = \pm\pi$. The complex radial parameter is obtained to be $x_0 = -2i\beta(\pm\pi)$, whose imaginary component provides a poloidal shift of $\pm\pi$ into the inboard side of the tokamak plasma with respect to the outboard mid-plane.

Let us now compare the stability of this pure anti-isolated mode with a pure

isolated mode that sits on the outboard mid-plane, using the model coefficients presented in Eq. (5.22) with $n = 50$ and $q' = 10$. For the mode that peaks on the outboard side, i.e $p_m^{(0)} = 0$, we have $\Omega^{(0)} = 0.0070 + 0.3477i$, $x_0^{(0)} = x_m^{(0)} = 0$ and $\Delta_x^{(0)} = 0.0316$. However, for the mode that sits on the inboard side, i.e. $p_m^{\pm} = \pm\pi$, we have $\Omega^{(\pm)} = -0.2464 + 0.1744i$, $x_0^{(\pm)} = 0.2588 - 0.2821i, x_m^{(\pm)} = 0$ and $\Delta_x^{(\pm)} = 0.0303$. It should be noted that the global mode frequency for both modes can be thought of as the local mode frequency evaluated at $x_s = 0$ and $p = p_m$, i.e. $\Omega = \Omega_0(0, p = p_m) + O(1/n)$. The correction factor for both cases is of order $O(\frac{1}{n})$. Moreover, the mode on the outboard side has a higher growth rate compared to the one that peaks on the inboard side. This is expected as the mode on the inboard side corresponds to the good curvature region, whilst the one on the outboard side corresponds to the bad curvature region.

In conclusion, in the situation that S_0 is real (eg. as provided by a toroidal flow shear), from Eq. (5.118) and Eq. (5.119) we can see that in general the global modes that correspond to $Z_r^{(-)}$ can be radially confined close to $x_s = 0$ only for $|S_{0,r}| \ll 1$. Otherwise, the global modes undergo large radial shifts with respect to $x_s = 0$. However, as we have seen in the above calculations, the solutions on the outboard side associated with $Z_r^{(+)}$ are acceptable solutions as they provide global modes that peak very close to $x_s = 0$ for all values of $S_{0,r}$. Furthermore, these solutions can be obtained only for a set of model coefficients for which Eq. (5.100) is satisfied. Finally, in the following a second case for which S_0 is assumed to be imaginary is considered.

5.5.3 Profile Shearing: A Linear Variation in the Local Growth Rate

In subsection 5.5.2, we assumed that $S_0 = S_{0,r}$, arising from toroidal flow shear for example, for which two different classes of eigenmode, corresponding to Z^+ and Z^- branches, have emerged. Here, the effect of $S_0 = iS_{0,i}$ is considered. This corresponds to a radial shift in $\gamma_0(x_s, p)$ with respect to $\omega_0(x_s, p)$. In what follows, we only consider a set of equilibrium parameters for which Eq. (5.100) is satisfied,

such that $(\varrho^2)_i = Z_i^{\pm} = 0$. Note that we are still assuming that $f_{1,r}R_{0,r} > f_{1,i}R_{0,i}$ in Eq. (5.98), such that ϱ^2 is negative now. As a consequence, the parameter ϱ^2 is now replaced with $-\varrho^2$ and from Eq. (5.96) we have

$$\begin{aligned} Z_r^+ &= \frac{\varrho^2 + \sqrt{\varrho^4 + 4}}{2} \\ Z_i^+ &= 0 \end{aligned} \tag{5.120}$$

and

$$\begin{aligned} Z_r^- &= \frac{\varrho^2 - \sqrt{\varrho^4 + 4}}{2} \\ Z_i^- &= 0 \end{aligned} \tag{5.121}$$

To obtain the global solutions for both Z^+ and Z^- branches, we apply the same procedure that we used in subsection 5.5.2 and without going through the calculations, we directly present the results. For Z^+ we have

$$\begin{aligned} p_{0,r}^+ &= \pm 2\pi\ell \\ p_{0,i}^+ &= \cosh^{-1}(Z_r^+) \end{aligned} \tag{5.122}$$

From Eq. (5.120) we can see that Z_r^+ depends on ϱ which is proportional to $S_{0,i}$. Hence, Eq. (5.122) shows that $p_{0,i}^+$ increases with $S_{0,i}$; this, eventually, leads to a mode that radially shifts away from $x_s = 0$. These solutions are equivalent to the Z^- branch that we considered in the previous subsection for S_0 real, but now on the outboard rather than on the inboard side of the tokamak plasmas.

Furthermore, the solutions that correspond to Z^- branch are as follows:

$$\begin{aligned} p_{0,r}^- &= \cos^{-1}(Z_r^-) \\ p_{0,i}^- &= 0 \end{aligned} \tag{5.123}$$

where, the fact that $p_{0,i}^- = 0$ indicates that $p_m^- = p_{0,r}^-$ and the mode is radially confined about $x_s = 0$ for all values of $S_{0,i}$. Moreover, for $S_{0,i} = 0$ (or $Z_r^- = -1$), the mode sits on the inboard side of the tokamak with $p_m^- = \pm\pi$. But as $|S_{0,i}| \to \pm\infty$ (or $Z_r^- \to 0$ according to Eq. (5.121)) we have $p_m \to \pm\pi/2$ and a pure general type of mode is captured. This indicates that the mode asymptotically approaches the top or bottom of the plasma as $S_{0,i}$ increases from 0 to $\pm\infty$. These solutions are

again equivalent to the Z_r^+ branch that has been previously considered for S_0 real, but now on the inboard side rather than the outboard side of the tokamak plasma.

Finally, acceptable solutions that lead to a radially centred global mode with $p_{0,i} = 0$, correspond to the Z^+ branch on the outboard side and Z^- branch on the inboard side of the tokamak for $S_0 = S_{0,r}$ and $S_0 = iS_{0,i}$, respectively. It is important to also mention that, these solutions will be reversed between these two cases if we now assume that $f_{1,r}R_{0,r} < f_{1,i}R_{0,i}$ instead of $f_{1,r}R_{0,r} > f_{1,i}R_{0,i}$ which in turn points to the fact that, as is explained earlier, this relation can not be considered as a constraint on the model coefficients[20]. Finally, from our analysis for the above two limits, we can readily generalise the solutions and allow S_0 to be any complex number. Note that, as long as Eq. (5.99) is satisfied, we can always obtain a solution that leads to a global mode that peaks at $x_s = 0$ for all values of S_0.

In conclusion, the analytical solutions can be used to analyse and understand the structure and stability of the global modes that sit at an arbitrary poloidal position with respect to the outboard mid-plane[21]. In the following section, our generalised solutions are used to investigate ITG modes in circular tokamaks, especially to explain the result of global numerical solutions presented in Ref [5].

5.6 Isolated to General Inter-mode Transition: ITG Modes in Circular Tokamaks

In the previous sections we have derived the analytic dispersion relation for the global complex mode frequency Ω with the associated global mode structures $\tilde{\phi}(x_s, \theta)$. In the following, we use the model coefficients from Eq. (5.22), assuming $n = 50$ and $q' = 10$, and benchmark our analytical solutions against the numerical ones. These

[20]Note that replacing $f_{1,r}R_{0,r} < f_{1,i}R_{0,i}$ with $f_{1,r}R_{0,r} > f_{1,i}R_{0,i}$ is equivalent to replacing $\varrho^2 = (\varrho^2)_r$ with $-\varrho^2 = -(\varrho^2)_r$. This switch between $\pm$ sign can transform for example Eq. (5.120) and Eq. (5.121), which correspond to $S_0 = iS_{0,i}$, back into Eq. (5.102) and Eq. (5.114), respectively, which correspond to $S_0 = S_{0,r}$. This indicates that, switching the sign of ϱ^2 switches between the solutions that correspond to S_0 real and S_0 imaginary, respectively.

[21]It is worth mentioning the limitations of our calculations again; $R(p)$ is assumed to be constant with p and to avoid big radial shifts we have put a constraint on the model coefficients (see subsection 5.5.1).

coefficients correspond to a simplified model of ITG modes in circular tokamaks which are taken from Ref [5]. This in turn allows us to also benchmark our analytical solutions against their global numerical simulations. In addition to the effect of rotational flow shear that is considered in Ref [5], we also look at a case where S_0 is imaginary. To do this, we introduce a linear radial variation into both local frequency and local growth rate as follows:

$$\begin{aligned}\Omega_0(x_s,p) &\rightarrow \Omega_0(x_s,p) + S_0 x_s \\ &= \left[\omega_0(x_s,p) + i\gamma_0(x_s,p)\right] + \left[nq'(1-\Upsilon)\gamma_E + i\Upsilon S_{0,i}\right] x_s \\ &= \left[\omega_0(x_s,p) + nq'(1-\Upsilon)\gamma_E x_s\right] + i\left[\gamma_0(x_s,p) + \Upsilon S_{0,i} x_s\right]\end{aligned} \tag{5.124}$$

where the parameter Υ controls the relative strength of the real and imaginary components of S_0. For $\Upsilon = 0$ we have $S_0 = nq'\gamma_E$, which introduces a linear radial variation term into $\omega_0(x_s,p)$. In contrast, $\Upsilon = 1$ leads to $S_0 = iS_{0,i}$, which corresponds to a linear radial variation in $\gamma_0(x_s,p)$. Note that, $\gamma_E = \frac{d\Omega_\varphi}{dq}$ is constant, with Ω_φ corresponding to the rotational flow shear. Flow shears, in general, are often invoked as the cause of transport barriers in magnetic confinement devices. Transport barriers, which are very important to improve plasma confinement, are generated through the suppression, or even a complete elimination, of the underlying microinstabilities and their associated particle and energy turbulent transport [6–11, 102]. There are various mechanisms by which flow shear can be produced; for example through Neutral Beam Injection (NBI) [11], through flows self-generated by turbulence [7], or through the so-called intrinsic rotation [7, 8]. It is worth mentioning that the direction of the flow shear is mainly toroidal, due to the fact that the poloidal flow is collisionally damped [103, 104]. The toroidal component can then be decomposed into perpendicular and parallel components with respect to the equilibrium magnetic field. The shear in the perpendicular flow has a stabilising effect, while the parallel component is destabilising and can lead to the parallel velocity gradient (PVG) instability [105, 106].

For a simplified drift wave model in circular tokamaks, it has been shown in both global gyrokinetic simulations [5] and using higher order ballooning analytic

calculations [6, 20] that rotation shear smoothly evolves isolated modes into general ones. This shows that the flow shear can indeed stablize the underlying linear mode that is believed to be the drive for the turbulence. However, there is an exceptional situation where the rotation shear precisely compensates the effect of the profile variations and for a critical value of flow shear it is possible to capture a highly unstable isolated mode again [12, 13].

Figure 5.5 presents the parameter Z and ballooning phase angle p_0 as a function of $S_0 = nq'\gamma_E$ ($\Upsilon = 0$ in Eq. (5.124)). The Z^+ (blue curves) and Z^- (black curves) branches respectively correspond to the eigenmode solutions on the outboard and inboard side of the plasma. We can see that, $Z^- = -1$ for $S_{0,r} = 0$, but both its real and imaginary components decrease as $|S_{0,r}|$ increases. In contrast, $Z^+ = 1$ for $S_{0,r} = 0$, and its real component decreases monotonically and tends to zero in the limit $|S_{0,r}| \gg 1$, while, its imaginary component, initially decreases and, for an intermediate value with $|S_{0,r}| \approx 3$, reaches its maximum deviation from zero, before it increases to zero for the other limit when $|S_{0,r}| \gg 1$. It is worth mentioning that, even though this set of model coefficients does not exactly satisfy the constraint of Eq. (5.100), nevertheless $Z_i^+ = 0$ in the two limits $S_{0,r} \ll 1$ and $|S_{0,r}| \gg 1$. To understand this, using $S_{0,i} = 0$, we can write ϱ^2 from Eq. (5.98) as;

$$\varrho^2 = (\varrho^2)_r + i(\varrho^2)_i = S_{0,r}^2(u + iw) \tag{5.125}$$

where,

$$\begin{aligned} u &= \frac{f_{1,r}R_{0,r} - f_{1,i}R_{0,i}}{2|f_1R_0|^2} \\ w &= \frac{f_{1,i}R_{0,r} + f_{1,r}R_{0,i}}{2|f_1R_0|^2} \end{aligned} \tag{5.126}$$

Upon substituting ϱ^2 from Eq. (5.125) back into Eq. (5.96) we can write Z as;

$$Z^{\pm} = \frac{-S_{0,r}^2}{2}(u + iw) \pm \frac{S_{0,r}^2 u}{2}\sqrt{(1 - \frac{w^2}{u^2}) + \frac{2iw}{u} + \frac{4}{u^2 S_{0,r}^4}} \tag{5.127}$$

where, $\pm$ signs correspond to Z^+ and Z^- branches, respectively. Note that, for the model considered here $w/u \approx 0.3$, such that in the limit $|S_{0,r}| \gg 1$, we can make the approximation $1 - \frac{w^2}{u^2} + \frac{4}{u^2 S_{0,r}^4} \approx 1$. After recognising w/u as our small parameter,

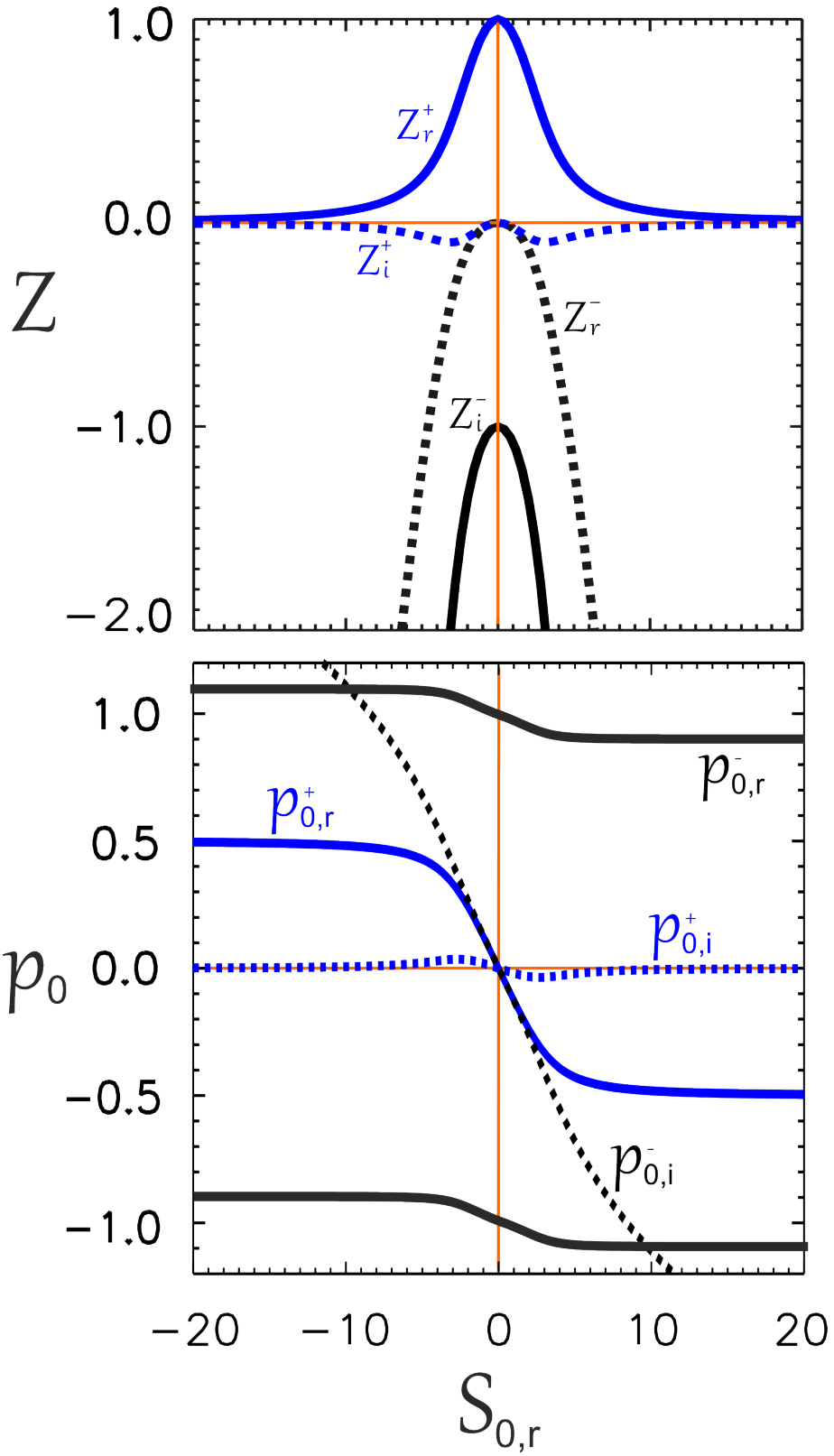

Figure 5.5: The parameter Z and ballooning phase angle p_0 as a function of $S_{0,r} = nq'\gamma_E$ with $n = 50$ and $q' = 10$, for the model coefficients presented in Eq. (5.22). Here, p_0 is measured in units of π. The blue curves correspond to the solutions associated with the Z^+ branch eigenmode solutions, while the solutions associated with Z^- branch are represented by black curves. Note that, the real and imaginary components for each branch corresponds to the solid and dotted lines, respectively.

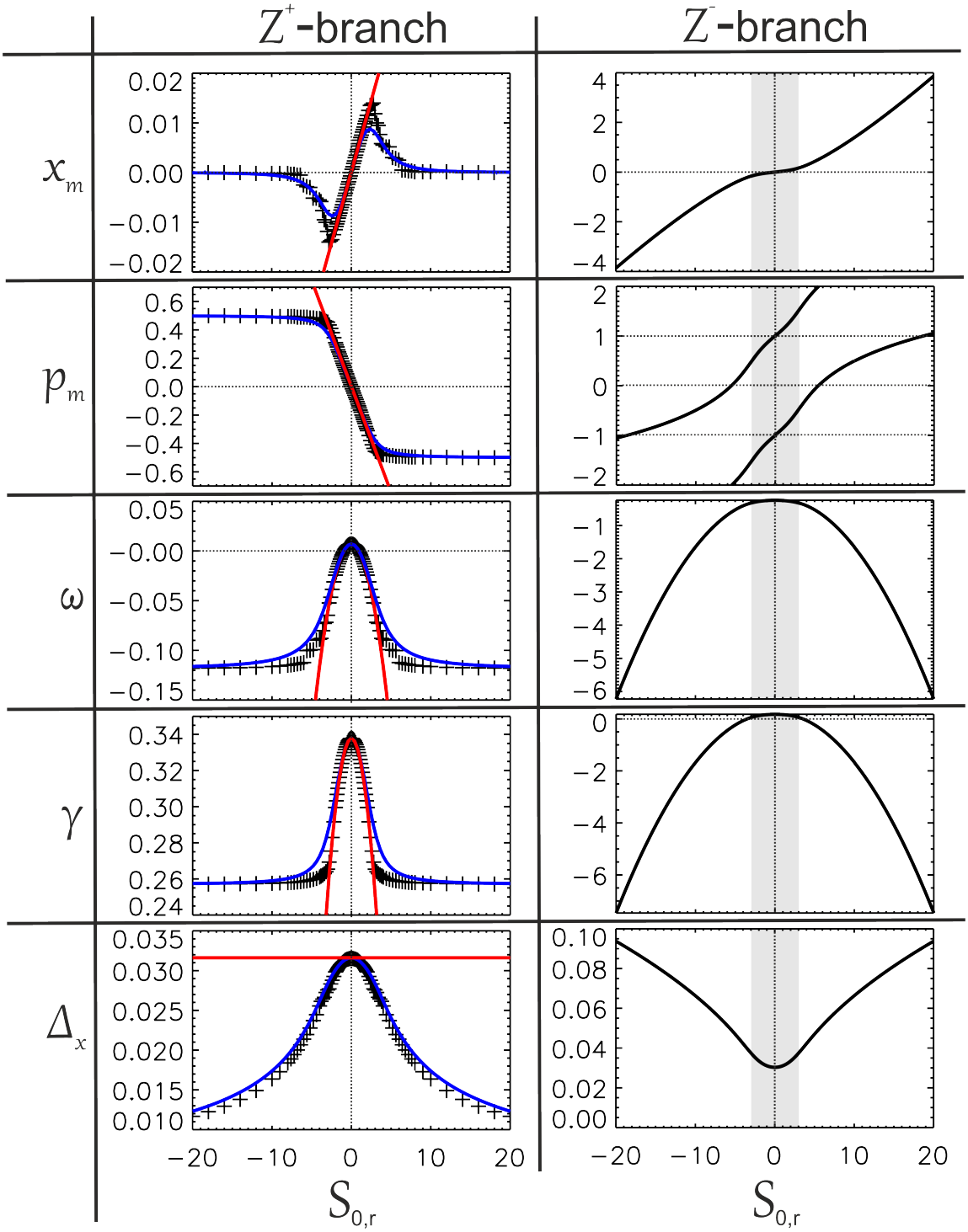

Figure 5.6: The global parameters as a function of $S_{0,r} = nq'\gamma_E$ with $n = 50$ and $q' = 10$, corresponding to the eigenmode branches (Z^+ and Z^-) of Figure 5.5. From top to bottom, the mode's radial shift x_m, the mode's poloidal position p_m (in units of π), the real frequency ω, the growth rate γ and finally the radial width Δ_x. Note that, for the Z^- branch only analytical solutions are presented. For the Z^+ branch, in addition to the generalised analytical solutions (blue lines), the associated full numerical solutions (crosses) and the analytical solutions previously developed in section 5.1 (see Eq. (5.7), Eq. (5.11), Eq. (5.15) and Eq. (5.16)) for small poloidal shifts (red lines) are also presented.

we apply the Binomial expansion to Eq. (5.127) to get:

$$Z^{\pm} \approx \frac{S_{0,r}^2}{2}\left(-u - iw \pm u \pm iw\right) \tag{5.128}$$

From this equation, we can see that, for Z^- branch the real and imaginary components decrease with out bound as $S_{0,r}$ goes to $\pm\infty$ according to $Z^- \approx S_{0,r}^2(-u-iw)$. In contrast, for Z^+ branch, both real and imaginary components tend to zero as $S_{0,r}$ goes to $\pm\infty$. The ballooning phase angle p_0^+ that corresponds to Z^+ is not real for all values of $S_{0,r}$, but it has a small imaginary component, $p_{0,i}^+ \neq 0$, whose value reaches its maximum deviation from zero at $|S_{0,r}| \approx 3$ and goes to zero at both the limits $S_{0,r} = 0$ and $|S_{0,r}| \gg 1$, respectively. However, the real component $p_{0,r}^+$ is zero at $S_{0,r} = 0$, but tends to $\pm\pi/2$ as $S_{0,r}$ goes to $\mp\infty$. On the other hand, for the Z^- branch, $p_{0,i}^- = 0$ at $S_{0,r} = 0$, but increases without bound as $S_{0,r}$ goes to $\pm\infty$. In contrast, $p_{0,r}^- = \pm\pi$ at $S_{0,r} = 0$ and tends to 1.1π and 0.9π as $S_{0,r}$ goes to $-\infty$ and $+\infty$, respectively.

Figure 5.6 presents the global parameters corresponding to branches Z^+ and Z^- of Figure 5.5, comparing full numerical solutions with our new analytic solution derived in this chapter. Note that, for the Z^- branch only those regions indicated by the shaded area corresponding to small radial shifts $x_m \leq \Delta_x$ are considered to be acceptable solutions. The solutions associated with Z^+ lead to a global mode that always stays very close to $x_s = 0$ for our chosen parameters (Eq. (5.22)). The maximum radial shift, corresponding to the maximum deviation of Z_i^+ (or equivalently $p_0^{i,+}$) into the complex plane, occurs at $|S_{0,r}| \approx 3$. This maximum value of the radial shift is still smaller than the radial mode width measured at the same value of $S_{0,r}$. Therefore, this set of eigenmode solutions, corresponding to the outboard mid plane, are acceptable for all values of $S_{0,r}$ from $-\infty$ to ∞. For this branch, the generalised analytical solutions are indicated by blue lines, while the crosses represent the full numerical solutions. In addition, for comparison, the analytical solutions that we developed in section 5.1 for small poloidal shifts are also presented and are indicated by red lines. As expected, the analytical solutions with small poloidal shifts are only valid for small values of flow shear, namely $|S_{0,r}| \leq 2$. In what follows for the rest

of this chapter, whenever analytical solutions are mentioned, this corresponds to the generalised analytical solutions of section 5.4.

We can see that, a pure isolated mode that initially sits on the outboard mid-plane at $p_m = 0$ (or $\theta = 0$) with $\Omega = f_0 + f_1 + O(1/n)$, shifts poloidally as flow shear increases from zero until it eventually reaches the top or bottom of the plasma as $S_{0,r}$ goes to $-\infty$ and $+\infty$, respectively. This is a pure type of general mode with $\Omega \approx f_0$, and as we expected, it is less unstable than the isolated mode. It is worth mentioning that overall very good agreement between the analytical and numerical solutions is found for all values of $S_{0,r}$. A slight discrepancy is observed for intermediate values of $S_{0,r}$ corresponding to those values for which the global mode undergoes maximum radial shifts. This might be attributed to the fact that the analytical solutions are obtained by employing Taylor series expansion in p and only the first two terms are retained.

Let us now consider $S_0 = iS_{0,i}$ ($\Upsilon = 1$ in Eq. (5.124)). This corresponds to a radial shift in $\gamma_0(x_s, p)$ with respect to $\omega_0(x_s, p)$. Figure 5.7 presents the parameter Z and the associated ballooning phase angle p_0. The curves that correspond to different branches of Z can be thought of as the mirror image of the similar solutions previously presented in Figure 5.5 for real $S_0 = nq'\gamma_E$, but here the solutions between the two branches are switched. Figure 5.8 presents the variation of the global parameters as functions of $S_{0,i}$. As we can see, the Z^- branch, that corresponds to the inboard side of the tokamak plasma, provides acceptable solutions, i.e. $x_m \leq \Delta_x$, for all values of $S_{0,i}$. In contrast, the solutions on the outboard side of the tokamak plasmas, which are associated with Z^+ branch, are acceptable only for small values of $S_{0,i}$ (indicated by the shaded regions in the figure). For the Z^+ branch, the effect of $S_0 = iS_{0,i}$ is destabilising and in turn increases the mode's radial width. However, for the Z^- branch, even though the effect is destabilising, the radial mode width nevertheless decreases. The mode that initially sits on the inboard side of the tokamak at $p_m = \pm\pi$ eventually approaches the top or bottom of the tokamak plasma, i.e. $\pm\pi/2$, as $S_{0,i} \to \mp\infty$. The mode that finally sits close to $\pm\pi/2$ is a pure type of general mode,

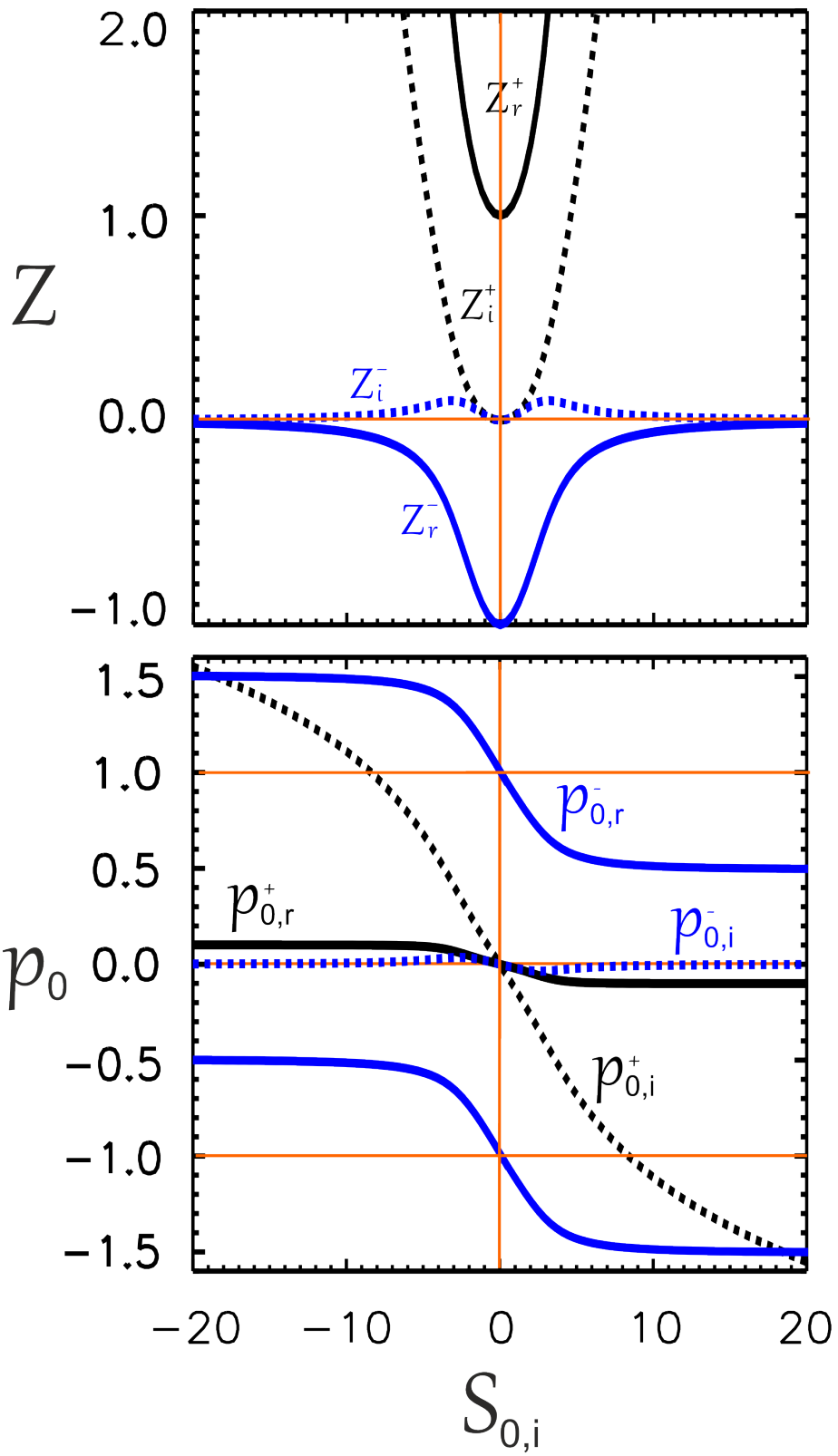

Figure 5.7: The parameter Z and ballooning phase angle p_0 as a function of $S_{0,i}$ (for $S_0 = iS_{0,i}$), for the model coefficients presented in Eq. (5.22). Here, p_0 is measured in units of π. The curves correspond to the solutions associated with the Z^- branch eigenmode solutions, while the solutions associated with Z^+ branch are represented by black curves. Note that, the real and imaginary components for each branch correspond to the solid and dotted lines, respectively.

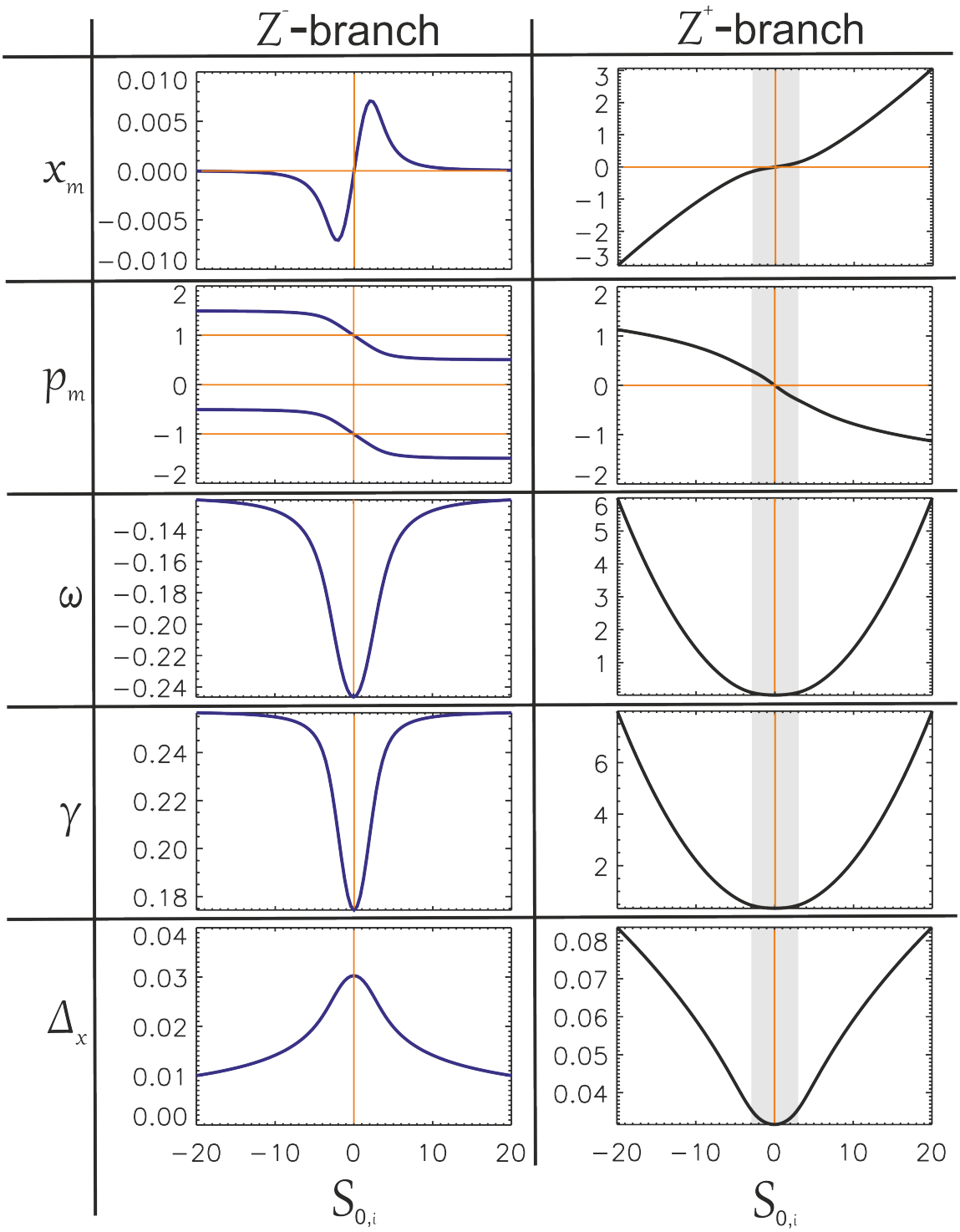

Figure 5.8: The global parameters as a function of $S_{0,i}$ (for $S_0 = iS_{0,i}$), correspond to the two branches Z^+ and Z^- of Figure 5.7. From top to bottom, the mode radial shift x_m, the mode poloidal position p_m (in units of π), the real frequency ω, the growth rate γ and finally the mode radial width Δ_x.

and is found to be the most unstable mode for the Z^+ branch.

In conclusion, we have discussed the effect of S_0 in two limits; either $S_0 = nq'\gamma_E$ or $S_0 = iS_{0,i}$. The former corresponds to rotational flow shear and leads to localised solutions about $x_s = 0$ for which the global modes only explore the bad curvature region on the outboard side of the tokamak plasmas. The latter provides localised solutions close to $x_s = 0$ that can only explore the good curvature region on the inboard side of the tokamak. Finally, before this chapter is closed, in the following we investigate how the global parameters, for examples p_m and Ω, scale with n, especially at large values of S_0.

5.7 Scaling with Toroidal Mode Number: High Flow Shear Limit

In our previous analytical calculations for small poloidal shifts, we showed how different parameters scale with toroidal mode number n (see section 5.3). But this treatment is only valid for small values of S_0 (see Figure 5.4). To extend this, in the light of the generalised analytical solutions, we investigate how the global parameters, scale with n in the limit $|S_0| \gg 1$. Anticipating that a pure general mode is captured at $p_m \approx \pm\pi/2$ as S_0 goes to $\pm\infty$, which also implies that $p_{0,i} = 0$ (or equivalently $Z_i = 0$) and $p_m = p_{0,r}$, we rewrite Eq. (5.108) to get;

$$p_m \approx \cos^{-1}(\frac{1}{\varrho^2}) \tag{5.129}$$

As S_0 goes to infinity, $1/\varrho^2$ goes to zero. In this limit Taylor expansion of p_m to the first order about $1/\varrho^2 = 0$, reduces Eq. (5.129) to

$$p_m \approx \pm\frac{\pi}{2} - \frac{1}{\varrho^2} = \pm\frac{\pi}{2} - \frac{2f_1R_0}{S_0^2} \tag{5.130}$$

where Eq. (5.94) is used to write ϱ in terms of the model coefficients. This equation does not depend on n, but if we consider a special case and assume that $S_0 = nq'\gamma_E$,

we can then calculate how p_m scales with n as follows

$$p_m \approx \pm\frac{\pi}{2} - \frac{1}{\varrho^2} = \pm\frac{\pi}{2} - \frac{1}{n^2 q'^2}\frac{2f_1 R_0}{\gamma_E^2} \tag{5.131}$$

This equation indicates that for non-zero flow shear, $|\gamma_E| > 0$, all the global modes sit close to the top or bottom of the plasma as n goes to ∞. Similarly, substituting $\sqrt{\frac{f_1}{8R_0}}$ for β and using ϱ^2 from Eq. (5.94), from Eq. (5.109) the global frequency scales with n according to

$$\Omega = f_0 + \left(\frac{f_1 R_0}{n^2 q'^2}\right)\left(\frac{i\gamma_E + 2f_1}{\gamma_E^2}\right) \tag{5.132}$$

This equation again indicates that, providing $\gamma_E \neq 0$, a pure general mode with $\Omega \approx f_0$ is captured as n goes to ∞.

Using the model coefficients in Eq. (5.22), Figure 5.9 presents how γ and p_m scale with n for different values of rotational flow shear. The generalised analytical solutions for both p_m and γ are indicated by black curves, and are respectively obtained from Eq. (5.86) and Eq. (5.87). The blue curves correspond to the solutions obtained for small poloidal shifts away from the outboard mid-plane for which both p_m and γ are calculated from Eq. (5.11) and Eq. (5.7), respectively. It can be seen that for $|nq'\gamma_E| < 12$ excellent agreement between both solutions is found. This limit was analysed in section 5.3. In this limit, assuming that $q'\gamma_E \neq 0$, p_m scales linearly with n, but γ scales according to Eq. (5.35). In the presence of flow, the most unstable modes are associated with intermediate values of n. However, for a pure isolated mode, $q'\gamma_E = 0$, the most unstable mode is associated with the largest n. This mode always sits on the outboard mid-plane, $p_m = 0$, for all values of n.

Furthermore, the solutions with small poloidal shifts are not correct for large values of $nq'\gamma_E$. Therefore, in this limit we only consider those solutions that have been obtained from the generalised analytical calculations. As we can see, for the curves that correspond to rotating plasmas, we find both p_m and γ tend to a constant value as n goes to infinity. This is consistent with the above calculations presented in Eq. (5.131) and Eq. (5.132) for both p_m and Ω, respectively.

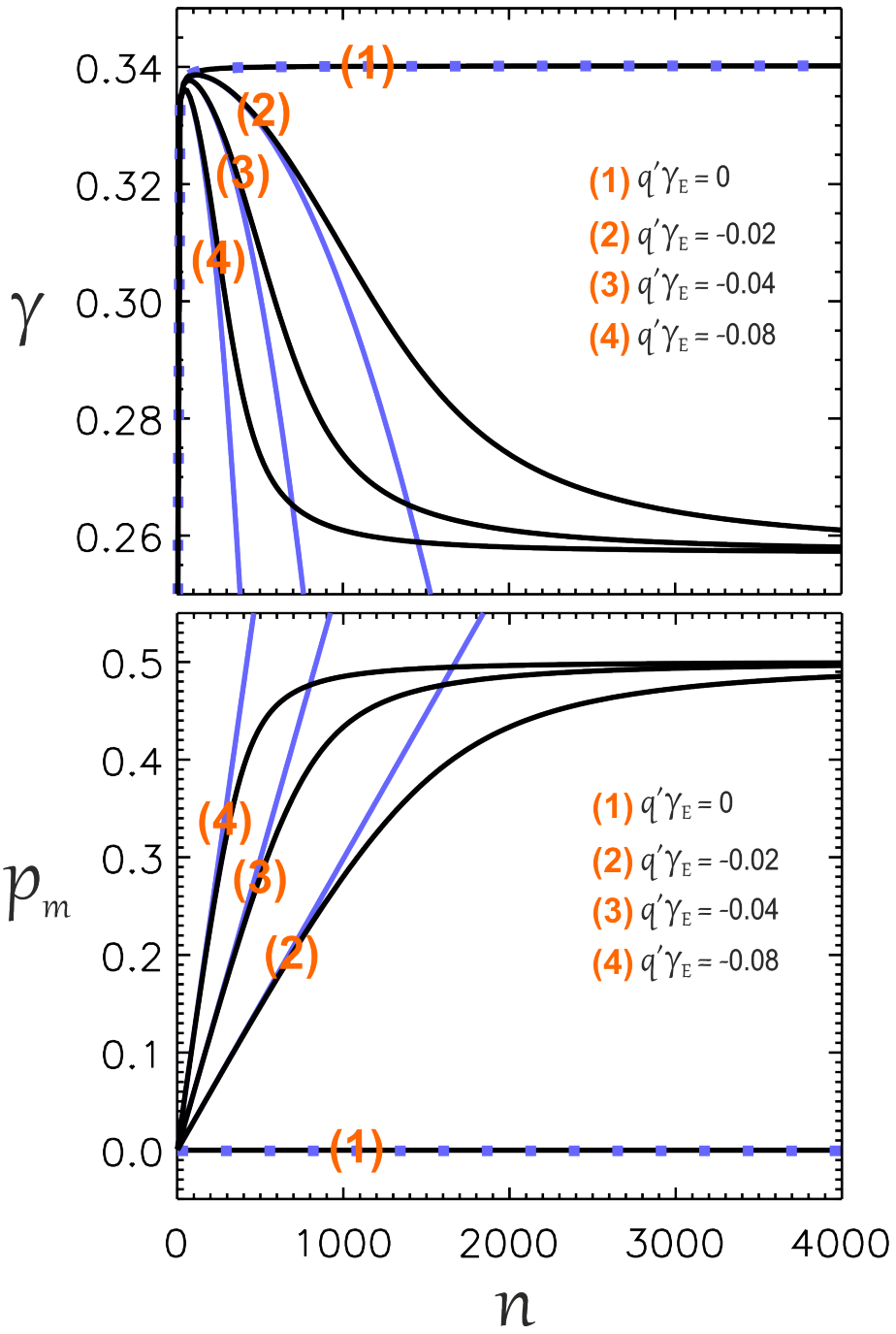

Figure 5.9: The growth rate γ and offset in the poloidal angle p_m as function of toroidal mode number n for different values of flow shear, namely $q'\gamma_E = 0.00, -0.02, -0.04$ and -0.08 where $q' = 10$. The solutions from the generalised analytical solutions are represented by black curves. For comparison, the analytical solutions for small poloidal shifts (blue curves) are also presented.

In conclusion, we can note that for small values of $nq'\gamma_E$ where the mode sits close to the outboard mid-plane the scaling of the global parameters with n are different compared to the large values of $nq'\gamma_E$ where the mode sits close to the top or bottom of the plasma. For example for small values of $nq'\gamma_E$, p_m scales linearly with n, but for large values of $nq'\gamma_E$ it tends towards $\pi/2$ with a correction that scales as $1/n^2$. This indicates that the scaling of different global parameters depends on the details of the profile shearing and in turn on the equilibrium profiles.

5.8 Summary and Conclusion

In this chapter analytical solutions for the two dimensional ballooning eigenmode in tokamak plasmas have been presented. The solutions have been extended beyond the two limits previously discussed in literature; "isolated" and "general" modes. The isolated mode sits on the outboard mid-plane and exists for a particular set of the equilibrium profiles such that the local complex mode frequency $\Omega_0(x_s, p)$ is stationary at some radius, $x_s = x_m$. On the contrary, the less unstable general mode, which balloons on the top or bottom of the plasmas, arises when $\Omega_0(x_s, p)$ does not exhibit a stationary point.

In realistic experimental cases, the global eigenmode can, in general, sit anywhere between the outboard mid-plane and the top or bottom of the tokamak plasma depending on the radial profiles of the equilibrium. Therefore, as a first step, the theory of isolated modes has been extended to account for the radial shift with respect to $x_s = 0$ as well as small poloidal shifts with respect to the outboard mid-plane. We found that the radial shift is a direct consequence of the imaginary component of the ballooning phase angle, i.e. where $p_{0,i} \neq 0$. A radial shift parameter x_0 has been identified. When x_0 is purely real a transformation of the radial coordinate recovers the isolated mode. However when x_0 has a non zero imaginary component this corresponds to situation where $\Omega_0(x_s, p)$ has no stationary point. This introduces a poloidal shift relative to the outboard midplane and, in turn, leads to poloidal symmetry breaking. Using these calculations, we have also discussed how different global

parameters, such as global frequency Ω and the offset in the poloidal angle p_m scale with the toroidal mode number n. Our first study considered small poloidal shifts and can only be applied to the fundamental modes which are not, in general, the only important modes of the system. To account for these points, in our second step, we have generalised the analytical solutions beyond these limits. For a simplified fluid model of an ITG mode in circular tokamaks [5], we have predicted that under the effect of rotational flow shear an isolated mode that initially sits on the outboard mid-plane can be smoothly converted to a general mode at the top or bottom of the plasmas. We have also found that the scaling of the global parameters, like Ω and p_m, with n depends on the details of the equilibrium profiles.

It should be noted that, for convenience, we have limited the applications here to only consider a simplified fluid model for ITG modes in circular tokamaks. However, the procedure and analytical solutions presented in this chapter are more general, and can be used to investigate, for instance, experimentally relevant simulations with more realistic plasma models. In the following chapter, we explore a full gyrokinetic model to demonstrate that the approach can be used with a state of art local gyrokinetic code, GS2.

Chapter 6

Numerical Simulations and Analysis

Using a simplified fluid model of ITG modes, it has been shown that global mode structures can be accurately constructed from local ballooning results for given radial profiles [5, 81]. The technique and theoretical formalisms underlying this approach have been discussed in section 4.5. The procedure is to combine numerical solutions from a local code with the higher order analytical theory [19] to reconstruct the global eigenmode properties. This chapter demonstrates that this approach can be used with a state of the art local gyrokinetic code (GS2) and in turn to extend the approach beyond the simplified fluid model of ITG modes that was presented in Ref [5]. As a first illustration of using this method with GS2, we have investigated a simple and familiar example of electrostatic ITG modes in the circular $s - \alpha$ equilibrium model [23, 107], assuming that the electron response is adiabatic. Then in section 6.2, we extend this to consider the circular Miller equilibrium model [108], and investigate the stability of ITG modes for the so-called CYCLONE base parameters which then helps us to understand the results from global simulations for this case, presented in Ref [12]. Finally, some initial investigations into the effects of shaping on the global mode properties are presented in section 6.3.

Table 6.1: The model parameters used with $s - \alpha$ equilibrium model.

Parameter	Value	Parameter	Value
$\hat{s}$	1.5	$r_0(m)$	0.306
q_0	1.4	β	0.0
R/L_T	17	nq'	$\approx$350
R/L_n	2.2	$\nu_{ii}R/v_{th}$	0.8
$k_y\rho_{ci}$	0.45	$\frac{T_i}{T_e}$	1.0
$a(m)$	0.612	$\rho_{ci}(m)$	0.0007
$R(m)$	1.70	$\rho_\star = \frac{\rho_{ci}}{a}$	0.0012

6.1 Demonstrating the Numerical Technique: Initial Results

In the previous chapter, we have shown that the radial shift of the reconstructed global mode with respect to $x_s = 0$ depends on the choice of equilibrium parameters and this shift is caused by the linear terms associated with the function $S(p)$. Therefore, in our first simulations we have chosen a set of parameters that avoids large radial shifts and can capture both isolated and general modes[1]. In this section we also demonstrate how to use a local gyrokinetic code, GS2, to obtain global results[2]. The equilibrium parameters are presented in Table 6.1, which is analysed for linear electrostatic ITG modes with adiabatic electrons, employing the so-called $s - \alpha$ model [23, 107], in which a large aspect ratio and circular magnetic flux surfaces have been assumed. These modes are strongly unstable for these parameters such that, as we shall see in the following, both isolated and general modes are unstable. Furthermore, modes are confined within the radial simulation domain.

Figure 6.1 shows the local real frequency, ω_0, and growth rate, γ_0, obtained from GS2 as functions of normalised binormal wave number, $k_y\rho_{ci}$, for the dominant modes with $p = x_s = 0$, together with the local mode structure ξ. The most unstable mode is found at $k_y\rho_{ci} = 0.45$, which corresponds to toroidal mode number $n = 50$. In the

[1]We shall see in section 6.2 that using different sets of equilibrium parameters can lead to a weakly unstable global mode which becomes stable before it gets to the top or bottom of the plasma. In addition, the general modes cannot be confined close to $x_s = 0$. Therefore, using this set of equilibrium parameters is a good initial step to investigate both isolated and general modes.

[2]The technique developed in this thesis is not limited to gyrokinetic simulations, but can be used in parallel with any local code, MHD local codes for example, to investigate global properties.

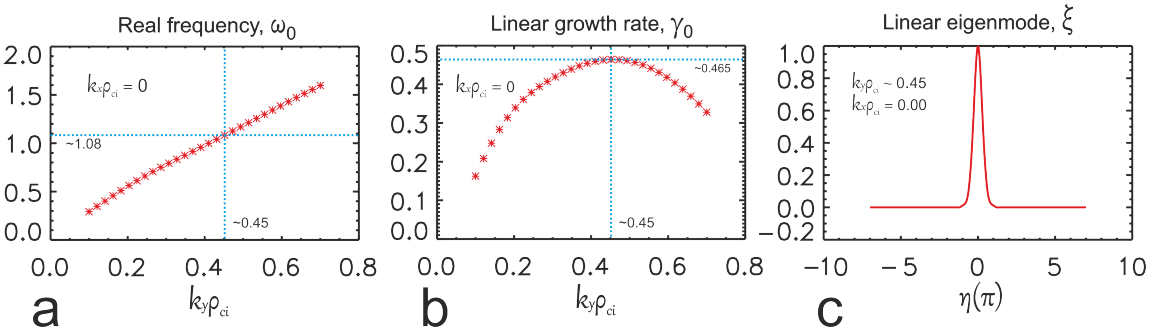

Figure 6.1: The variation of (a) real frequency, ω_0, (b) linear growth rate, γ_0, with $k_y\rho_{ci}$, for the dominant modes at $p = x_s = 0$; (c) shows the local mode structure, $\xi(x_s = 0, \eta, p = 0)$, for the most unstable mode with collisions at $k_y\rho_{ci} = 0.45$, as a function of ballooning coordinate η along the magnetic field line. Note that both ω_0 and γ_0 are measured in units of (v_{th}/R) and these local simulations have been carried out at mid-radius, i.e. $x_s = 0$ (or equivalently $r = r_0 = a/2$).

following we shall reconstruct the global properties for the most unstable mode.

6.1.1 Quadratic and Linear η_i Profiles

To proceed with the global calculations, we have introduced two different radial R/L_T profiles, namely linear and quadratic profiles, which are, respectively, defined by the following equations;

$$R/L_T = 17 - 150x_s \tag{6.1}$$

$$R/L_T = 17 - 1500x_s^2 \tag{6.2}$$

We assume all other equilibrium parameters to be independent of x_s. Here, x_s measures the distance from a reference rational surface at $x_s = 0$ and is normalised to the minor radius a. Note that the drive for the ITG mode is characterised by $\eta_i = L_n/L_T$, where L_T and L_n are temperature and density scale lengths, respectively. Here, we have held $R/L_n = 2.2$ constant such that $R/L_T = 2.2\eta_i$ can be considered as a drive for the mode. We have then scanned the local flux tube gyrokinetic code, GS2, many times over a range of x_s and ballooning phase angle, $-\pi \leq p \leq \pi$, to map out the local complex mode frequency $\Omega_0(x_s, p)$ and the associated local mode structure $\xi(x_s, p, \eta)$. Note that instead of $\xi(x_s, p, \eta)$ in Eq. (4.50) we require $\xi(x_s, p, \theta)$ where $-\pi \leq \theta \leq \pi$ and p is on the infinite domain. However, a mapping from the infinite η domain to the poloidal angle θ is possible because of the symmetry

property $\xi(x_s, p+2\pi\ell, \theta+2\pi\ell) = \xi(x_s, p, \theta)$ for any integer ℓ. For the profiles that we have considered in this chapter, we can model $\Omega_0(x_s, p)$ by using Taylor and Fourier expansion in x_s and p, respectively. Knowing that $\Omega_0(x_s, p)$ is periodic in p, we may Fourier expand the three coefficients $R(p)$, $S(p)$ and $f(p)$, respectively, to get

$$\begin{aligned} R(p) &= \sum_{k=0}^{N_k} R_k \cos(kp) \\ S(p) &= \sum_{k=0}^{N_k} S_k \cos(kp) \\ f(p) &= \sum_{k=0}^{N_k} f_k \cos(kp) \end{aligned} \tag{6.3}$$

such that

$$\begin{aligned} R(0) = \sum_{k=0}^{N_k} R_k,\ R''(0) = -\sum_{k=0}^{N_k} k^2 R_k \\ S(0) = \sum_{k=0}^{N_k} S_k,\ S''(0) = -\sum_{k=0}^{N_k} k^2 S_k \\ f(0) = \sum_{k=0}^{N_k} f_k,\ f''(0) = -\sum_{k=0}^{N_k} k^2 f_k \end{aligned} \tag{6.4}$$

where, N_k is the number of Fourier modes retained. Note that, for the up-down symmetric equilibrium profiles considered here, $\Omega_0(x_s, p)$ is symmetric about $p = 0$. Therefore, the coefficients with $\sin(kp)$ components all vanish and $f'(0) = S'(0) = R'(0) = 0$. Substituting Eq. (6.3) back into Eq. (4.59), the parametrisation for $\Omega_0(x_s, p)$ is reduced to:

$$\Omega_0(x_s, p) = \sum_{k=0}^{N_k} f_k \cos(kp) + \sum_{k=0}^{N_k} S_k \cos(kp) x_s + \sum_{k=0}^{N_k} R_k \cos(kp) x_s^2 \tag{6.5}$$

Figure 6.2 shows the contour for $\Omega_0(x_s, p)$ as function of x_s and p obtained from GS2 compared to the fit using the parametrisation given in Eq. (6.5). For the quadratic η_i profile (see panel (a) in Figure 6.2) $\Omega_0(x_s, p)$ is stationary at $x_s = p = 0$, i.e. both $\omega_0(x_s, p)$ and $\gamma_0(x_s, p)$ peak here. The coefficients resulting from the fit are presented in Table 6.2, the coefficients associated with $S(p)$ are 0. Using these coefficients we can first obtain the analytic solutions and then benchmark these

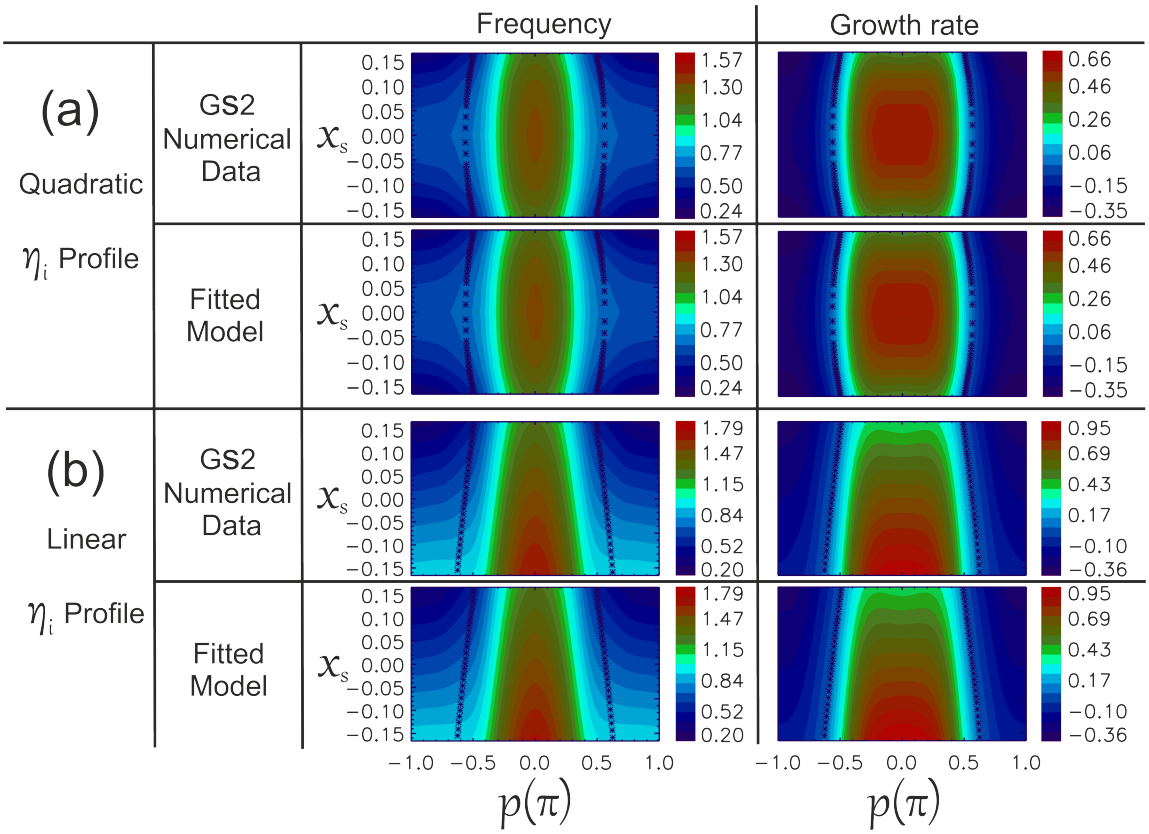

Figure 6.2: The local complex mode frequency $\Omega_0(x_s, p) = \omega_0(x_s, p) + i\gamma_0(x_s, p)$ determined by GS2 along with the fitted model for two different η_i profiles; (a) quadratic η_i profile and (b) linear η_i profile. Here, ω_0 and γ_0 are, respectively, the real frequency and growth rate and are measured in units of v_{th}/R. The $\star$ symbols correspond to the boundary of the marginal stability where $\gamma_0(x_s, p) = 0$.

against numerical ones[3]. From Eq. (5.5) we have $b = 0$ (or equivalently $x_0 = 0$), which leads to $p_0 = 0$ and $p_m = 0$ from Eq. (5.8) and Eq. (5.11), respectively, and, from Eq. (5.6), $\chi = 31.517 - i15.28$. As we shall see in the following, this corresponds to a pure isolated type of mode that preserves both radial and poloidal symmetries. Substituting χ and b into Eq. (5.1) and Eq. (5.7) provides the analytical solutions for both the envelope $A(p)$ and the associated global eigenvalue, $\Omega = 1.1044 + i0.4656$. Furthermore, from Eq. (5.13) and Eq. (5.16) we can calculate the global mode structure $\tilde{\phi}(x_s, \theta)$ and its radial width $\Delta_x = 0.0594$. The corresponding numerical solution provides $\Omega = 1.1044 + i0.4656$ and $\Delta_x = 0.0597$. Here, to evaluate the numerical value for Δ_x, we have substituted the numerical data for $A(p)$, obtained from the numerical solutions to Eq. (4.63), into the Fourier-ballooning representation

[3]In this chapter, due to the p dependence of the coefficient $R(p)$, we limit ourselves to the analytical solutions of section 5.1 which are developed under the assumption of small poloidal shifts with respect to the outboard mid-plane.

Table 6.2: The model coefficients, f_k and R_k, with eight Fourier modes for the quadratic $\eta_i(x_s)$ profile. The real and imaginary components contribute to the real frequency, ω_0, and linear growth rate, γ_0, respectively. Note that $S_k = 0$ for all values of k.

k	f_k	R_k
0	0.6419 + 0.1333 i	-6.6495 - 4.2772 i
1	0.3369 + 0.3710 i	1.6021 - 3.1212 i
2	0.1298 + 0.0154 i	-0.6344 - 0.7085 i
3	0.0200 - 0.0455 i	-0.1835 + 0.2488 i
4	-0.0150 - 0.0142 i	0.1210 + 0.0023 i
5	-0.0090 + 0.0039 i	-0.0458 - 0.0184 i
6	0.0012 + 0.0055 i	0.0510 + 0.0272 i
7	0.0035 - 0.0011 i	-0.0100 - 0.0663 i

in Eq. (4.50). We then performed a numerical integration to obtain $\tilde{\phi}(x_s, \theta)$. Finally, we have fitted a Gaussian function to the magnitude of $\tilde{\phi}$ on the outboard mid-plane, i.e. $|\tilde{\phi}(x_s, \theta = 0)|$. The radial mode width is then calculated from the full width at half maximum of the Gaussian.

Figure 6.3 presents both the envelope $A(p)$ and a colour contour plot of the associated global mode structure $\tilde{\phi}(x_s, \theta)$ in the poloidal plane. As we can see from panel (a), $|A(p)|$ peaks at $p = p_m = 0$ and shares the same line of symmetry with $A(p)/|A(p)|$, i.e. $p_m = p_p = 0$. The function $A(p)$ in turn is symmetric about $p = 0$ (see panel (b)). This leads to a reconstructed global mode that sits on the outboard mid-plane (panel (c)) and is radially peaked about $x_s = 0$ (see panel (d)). This is the pure isolated mode identified in section 4.7.1. Finally, from the above analysis and Figure 6.3 we found excellent agreement between the analytic and numerical solutions.

Let us now consider the linear R/L_T profile (or equivalently linear η_i profile) and examine how this affects the global properties of the reconstructed mode compared to the above quadratic profile. The model coefficients corresponding to this case are presented in Table 6.3. The numerical data for $\Omega_0(x_s, p)$ obtained from the local code GS2 together with the corresponding fit using the model from Eq. (6.5) are both depicted in Figure 6.2−b. As expected, for a linear $\eta_i(x_s)$ profile, we have $R_k = 0$ for all k. This corresponds to $\Omega_0(x_s, p)$ without stationary points. This in

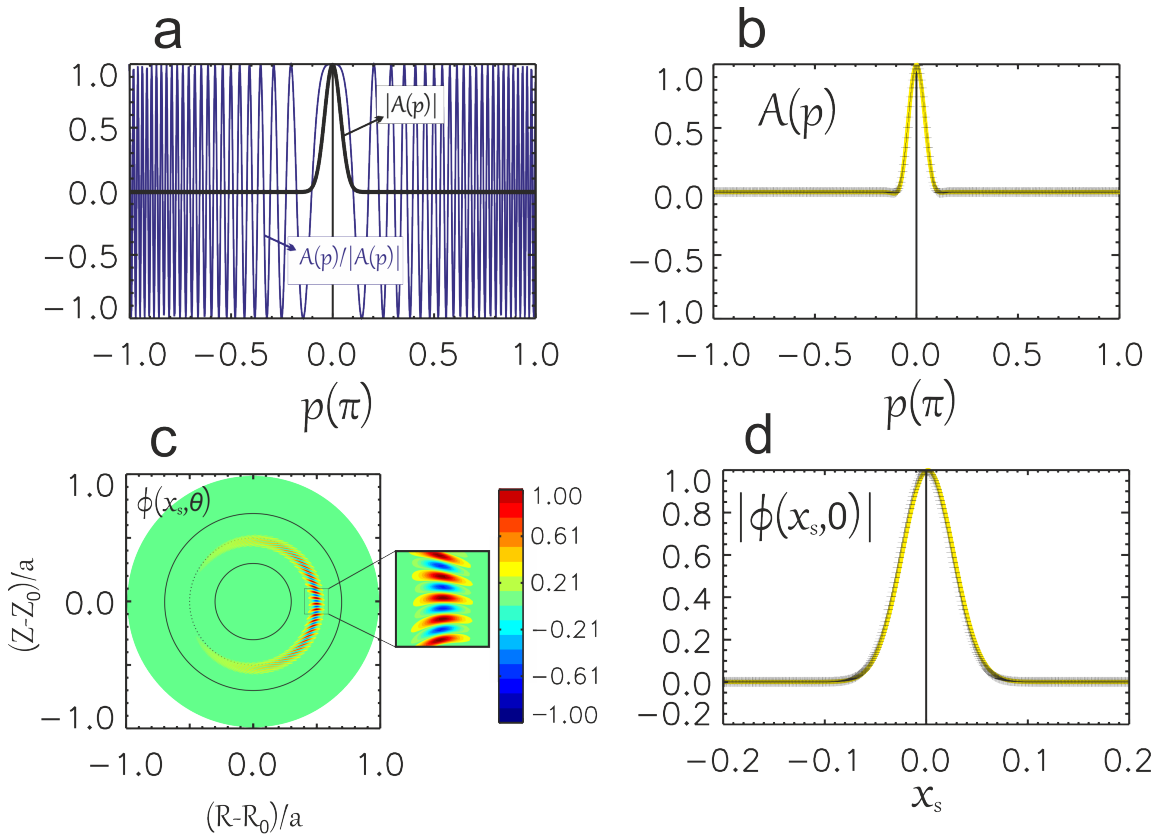

Figure 6.3: The envelope $A(p)$ and the associated reconstructed global mode structure $\tilde{\phi}(x_s, \theta)$ for a quadratic η_i profile. (a) presents $|A(p)|$ together with $A(p)/|A(p)|$ and (b) shows the resultant envelope $A(p)$. The colour contour plot of $\tilde{\phi}(x_s, \theta)$ in the poloidal cross-section is shown in (c) and finally (d) presents $|\tilde{\phi}(x_s, 0)|$ as function of x_s, which is evaluated on the outboard mid-plane at $\theta = p_m = 0$. Note that crosses correspond to the numerical solutions while the full curves represent the corresponding analytical solutions.

turn, according to section 5.2, leads to a radial parameter x_0 with non-zero imaginary component, generating a global mode which does not sit on the outboard mid-plane.

Using the coefficients from Table 6.3, numerical solutions of Eq. (4.86), Eq. (4.88) and Eq. (4.50) provide $A(p)$, $\Omega = 0.6891 + i0.0546$ and $\tilde{\phi}(x_s, \theta)$, respectively. Figure 6.4 shows the envelope $A(p)$ and the reconstructed global mode structure, $\tilde{\phi}(x_s, \theta)$, in the poloidal cross section. The mode sits close to the top of the plasma at $\theta = p_m = 0.59\pi$. As we can see $|A(p)|$ is symmetric about $p = p_m = 0.59\pi$, while the function $A(p)/|A(p)|$ is symmetric about $p = p_p = 0.43\pi$. This corresponds to $p_m - p_p = 0.16$, leading to an envelope $A(p)$ that peaks at $p = p_m = 0.59$ and is not symmetric about this point. It is this symmetry breaking that eventually leads to the

Table 6.3: The model coefficients, f_k and S_k, with eight Fourier modes for the linear $\eta_i(x_s)$ profile. The real and imaginary components contribute to the real frequency, ω_0, and linear growth rate, γ_0, respectively. Note that $R_k = 0$ for all values of k.

k	f_k	S_k
0	0.6342 + 0.1263 i	-1.7408 - 1.0909 i
1	0.3386 + 0.3649 i	0.4201 - 0.7844 i
2	0.1282 + 0.0134 i	-0.1546 - 0.1684 i
3	0.0197 - 0.0447 i	-0.0468 + 0.0580 i
4	-0.0146 - 0.0145 i	0.0295 + 0.0050 i
5	-0.0093 + 0.0042 i	-0.0089 - 0.0095 i
6	0.0018 + 0.0053 i	0.0064 + 0.0094 i
7	0.0030 - 0.0015 i	0.0028 - 0.0131 i

radial shift in the reconstructed global mode with respect to $x_s = 0$, and in turn to a so-called radial symmetry breaking with respect to $x_s = 0$, i.e. $\tilde{\phi}(x_s, \theta) \neq \tilde{\phi}(-x_s, \theta)$. For our example here, $\tilde{\phi}(x_s, \theta)$ sits at $x_s = x_m = -0.09$ and has the radial width $\Delta_x = 0.051$. It should be noted that, compared to the isolated mode corresponding to the quadratic η_i profile, the mode we have captured here is less unstable. We classify this mode as a shifted class of general modes. We have learnt from the previous chapter that the imaginary component of the ballooning phase angle, i.e. $p_{0,i}$, causes radial shifts, but, in addition to this radial shift, we also want to understand why the general mode of Figure 6.4 undergoes a poloidal shift relative to the top of the plasma. To investigate this we start by considering Eq. (4.86), differentiating $A(p)$ at $p = p_0$ and equating it to zero, i.e. $dA(p)/dp|_{p=p_0} = 0$, to obtain

$$\Omega - \sum_{k=0}^{N_k} f_k \cos(k p_0) = 0 \tag{6.6}$$

This is a constraint from which we can determine p_0 in terms of Ω, where Ω is calculated from Eq. (4.88). For simplicity, we now examine three simple cases for which we can solve Eq. (6.6) exactly. For the first example we assume that $f_k = 0$ for $k \geq 2$ and $S_k = 0$ for $k \geq 1$ such that from Eq. (4.89) we have $\Omega = f_0$. This in turn reduces Eq. (6.6) to

$$\cos(p_0) = 0 \tag{6.7}$$

This equation has solutions with $p_0 = \pm(2\ell + 1)\pi/2$. This corresponds to a mode that peaks at the top or bottom of the plasma and because $p_{0,i} = 0$, the mode

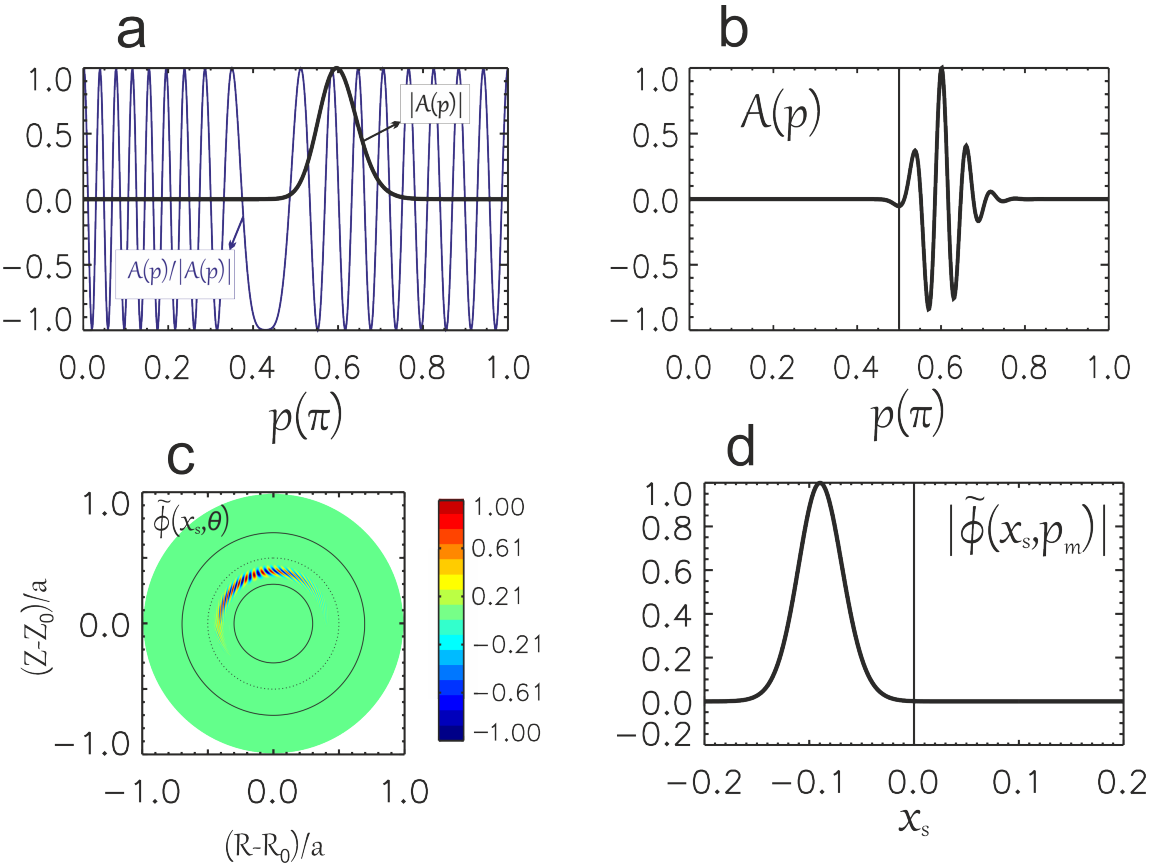

Figure 6.4: The numerical solutions for the envelope $A(p)$ and the associated reconstructed global mode structure $\tilde{\phi}(x_s, \theta)$ for a linear $\eta_i(x_s)$ profile. (a) presents $|A(p)|$ together with $A(p)/|A(p)|$ and (b) shows the resultant envelope $A(p)$. The poloidal cross-section of $\tilde{\phi}(x_s, \theta)$ is shown in (c) and finally (d) presents $|\tilde{\phi}(x_s, 0)|$ as a function of x_s, which is evaluated at $\theta = p_m = 0.59\pi$. Note that $A(p)$ is not symmetric under $p \to -p$ transformation. The global mode in turn is shifted with respect to $x_s = 0$.

peaks at $x_s = 0$. We call this a pure general mode [5, 18] (see also section 4.7.2 for more detail). However, in addition to f_0, f_1 and S_0, taking the effect of higher Fourier harmonics into account leads to a radial shift in the reconstructed global mode with respect to $x_s = 0$. To demonstrate this, we shall consider the effect of the S_1 and f_2 coefficients separately. The former corresponds to $f(p) = f_0 + f_1 \cos p$ and $S(p) = S_0 + S_1 \cos p$. Here, for this set of parameters, from Eq. (4.88) we have $\Omega \neq f_0$. Solving Eq. (6.6) for p_0 we have

$$p_0 = \cos^{-1}\left(\frac{\Omega - f_0}{f_1}\right) \tag{6.8}$$

However, the latter corresponds to $f(p) = f_0 + f_1 \cos p + f_2 \cos 2p$ and $S(p) = S_0$ for which $\Omega = f_0$ and Eq. (6.6) reduces to

$$f_1 \cos(p_0) - f_2 \cos(2p_0) = 0 \tag{6.9}$$

This equation has the following solutions:

$$p_0 = \cos^{-1}\left[-\left(\frac{f_1}{4f_2}\right) \pm \sqrt{\left(\frac{f_1}{4f_2}\right)^2 + \frac{1}{2}}\right] \tag{6.10}$$

From Eq. (6.8) and Eq. (6.10) we can see that, unlike the case of a pure general mode, p_0 can be complex, which causes a radial shift away from $x_s = 0$. Furthermore, for $p_{0,i} \neq 0$, we have $p_m \neq p_{0,r}$, but from the previous chapter we know that p_m is determined from a combination of both $p_{0,r}$ and $p_{0,i}$. This, in general, may lead to a general mode that shifts poloidally with respect to the top or bottom of the plasma, i.e. $p_m \neq \pm\pi/2$. From this argument we can conclude that due to the effect of higher Fourier harmonics, i.e. when $f_k \neq 0$ for $k > 1$ or $S_k \neq 0$ for $k > 0$, we have captured a shifted general type of mode in our simulations. As we can see from Figure 6.4 the mode shifts slightly towards the good curvature region into the inboard side of the plasma and some authors have recently classified these type of modes as anti-ballooning modes [28].

In the following section we extend our $s - \alpha$ study to consider the so-called CYCLONE base case parameters employing the circular Miller equilibrium model. This allows us to benchmark against global gyrokinetic simulations that have been used to study this case.

6.2 Effect of Equilibrium Profiles: CYCLONE Base Case

The variation of the equilibrium profiles can have important effects on the eigenmode structures and their stability. For example, linear global gyrokinetic simulations of both ASDEX Upgrade (AUG) and MAST plasmas point to the fact that the electrostatic ITG modes are shifted with respect to the outboard mid-plane [12, 29]. This shift corresponds to a poloidal symmetry breaking which can be very important in providing a mechanism for flow generation in tokamaks [27, 30–32] especially in next-step fusion machines like ITER for which the external torque is expected to

be small. Local gyrokinetic codes alone cannot determine when these shifted modes occur, rather than isolated modes that typically peak on the outboard mid-plane. However, using our technique, which combines the numerical results from a local gyrokinetic code, GS2, with the higher order ballooning theory, has enabled us to capture the global properties of the linear 2D eigenmode structures. This in turn has allowed us to understand the mechanisms underlying the poloidal symmetry breaking and provides more physical details behind the mode structures and their stability for interpreting the direct global gyrokinetic simulations.

In this section we investigate the effect of both rotational flow shear and the equilibrium profiles and, again, focus on electrostatic ITG modes with adiabatic electrons, but here we adopt the CYCLONE parameters [109, 110] for a Miller equilibrium with circular flux surfaces. This in turn has allowed us to benchmark our calculations against intriguing results from global gyrokinetic simulations that were presented in Ref [12] for the same equilibrium. It is worth mentioning that the $s-\alpha$ and the circular Miller equilibrium models are not equivalent [107], except for $\epsilon = 0$, where $\epsilon = r/R$ is the inverse aspect ratio.

The radial equilibrium profiles used in this section, namely safety factor q, magnetic shear $\hat{s}$, temperature T, density n_e, temperature a/L_T and density a/L_n gradients, are chosen to match Ref [12]. They are, respectively, defined according to the following equations:

$$q = 0.84 + 2.24(r/a)^2 \tag{6.11}$$

$$\hat{s} = 2\left(1 - \frac{0.84}{q}\right) \tag{6.12}$$

$$\frac{T}{T_{ref}} = \exp\left[-\Delta T\left(\frac{a}{L_T}\right)\tanh(\frac{x_s}{\Delta T})\right] \tag{6.13}$$

$$\frac{n_e}{n_{ref}} = \exp\left[-\Delta n\left(\frac{a}{L_n}\right)\tanh(\frac{x_s}{\Delta n})\right] \tag{6.14}$$

$$\frac{a}{L_T} = \left(\frac{a}{L_T}\right)_0\left(\cosh(\frac{x_s}{\Delta T})\right)^{-2} \tag{6.15}$$

Table 6.4: CYCLONE equilibrium parameters on our reference flux surface, where $r = a/2$.

Parameter	Value	Parameter	Value
$\hat{s}$	0.8	$r_0(m)$	0.313
q_0	1.4	β	0.0
a/L_T	2.54	nq'	144
a/L_n	0.81	$\nu_{ii}a/V_s$	0.28
$k_y\rho_{ci}$	0.58	$\frac{T_i}{T_e}$	1.0
$a(m)$	0.625	$\rho_{ci}(m)$	0.003384
$R(m)$	1.70	$\rho_\star = \frac{\rho_{ci}}{a}$	0.005415

$$\frac{a}{L_n} = \left(\frac{a}{L_n}\right)_0 \left(\cosh(\frac{x_s}{\Delta n})\right)^{-2} \tag{6.16}$$

where, $\Delta T = \Delta n = 0.208$, the values of T_{ref} and n_{ref} are chosen such that $T/T_{ref} = n/n_{ref} = 1$ on the reference surface at $x_s = 0$ (or $r = r_0$), where $x_s = (r - r_0)/a$. Here $(a/L_T)_0 = 2.54$ and $(a/L_n)_0 = 0.81$ corresponding to the values of the temperature and density gradients, respectively, evaluated at $x_s = 0$. The above radial profiles are all plotted in Figure 6.5. Note that the horizontal dashed lines represents the value of a particular quantity at $x_s = 0$ (i.e. where $r = a/2$).

Before considering the global calculations, we first describe the local ballooning analysis. The model parameters are given in Table 6.4. Figure 6.6 shows the local real frequency, ω_0, and growth rate, γ_0, obtained from GS2 as functions of normalised binormal wave number, $k_y\rho_{ci}$, for the dominant modes with $x_s = p = 0$, together with the local mode structure, ξ. The results for a normalised ion-ion collision frequency of $\nu_{ii}a/V_s = 0.28$ are found to be very similar to those for a collisionless plasma when $p = 0$. We use this finite collision frequency in the remaining calculations as it helps damp non-physical modes found by GS2 at values of p close to marginal stability, and yet gives local eigenmode result similar to the collisionless case. The most unstable mode is found at $k_y\rho_{ci} = 0.58$ which corresponds to toroidal mode number $n = 39$. Now we apply the technique presented in Section 4.5 to reconstruct the global structure for the most unstable mode.

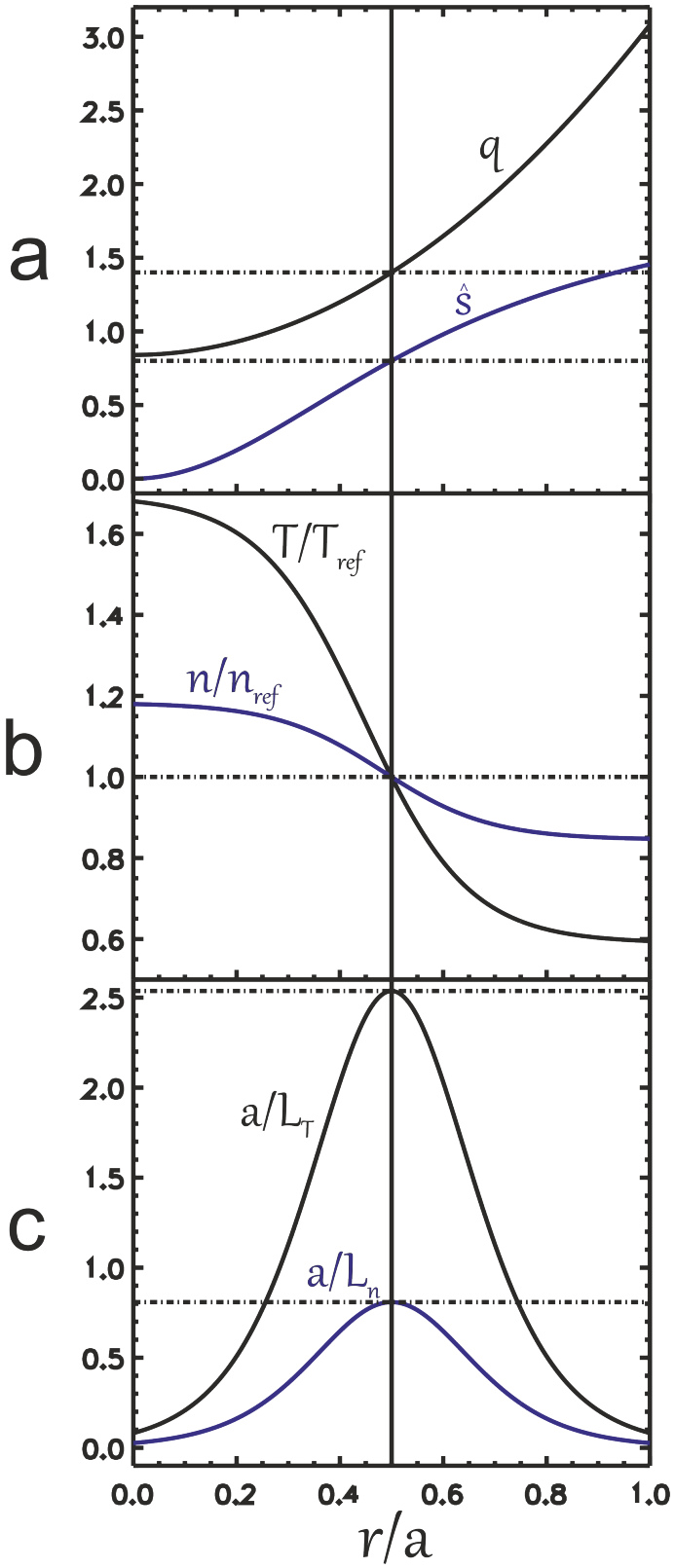

Figure 6.5: The radial profiles taken from Eq. (6.11) – Eq. (6.16): (a) Safety factor and magnetic shear and (b) temperature and density and finally (c) The temperature and density gradients.

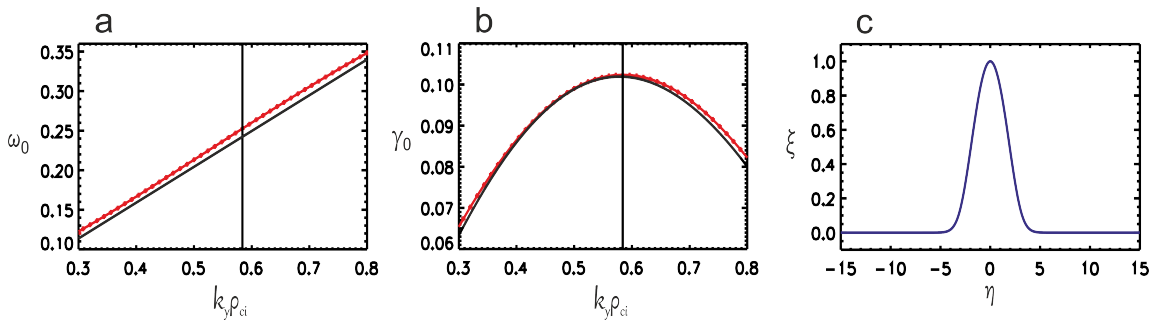

Figure 6.6: From left to right: The variation of (a) real frequency, ω_0, (b) linear growth rate, γ_0, with $k_y\rho_{ci}$, for the dominant modes at $x_s = p = 0$ for two values of the normalised ion collision frequency, $\nu_{ii}a/V_s = 0$ (solid line) and $\nu_{ii}a/V_s = 0.28$ (solid line with $*$ symbols); (c) shows the local mode structure, $\xi(x_s = 0, \eta, p = 0)$, for the most unstable mode with collisions at $k_y\rho_{ci} = 0.58$, as a function of ballooning coordinate η along the magnetic field line. Note that both ω_0 and γ_0 are measured in units of (V_s/a) and these local simulations have been carried out at mid-radius, i.e. $r = r_0 = a/2$.

Table 6.5: The model coefficients, f_k and R_k, with ten Fourier modes. The real and imaginary components contribute to the real frequency, ω_0, and growth rate, γ_0, respectively. Note that $S_k = 0$ for all k for this special case where only profiles in a/L_T and a/L_n are retained (and are symmetric about $x_s = 0$).

k	f_k	R_k
0	0.1177 - 0.0680 i	-1.5689 - 1.9352 i
1	0.1804 + 0.1221 i	1.3347 - 2.2466 i
2	0.0462 + 0.0461 i	0.0825 - 0.8734 i
3	0.0229 + 0.0231 i	-0.0015 - 0.2477 i
4	0.0068 + 0.0098 i	-0.1007 - 0.0227 i
5	0.0012 + 0.0078 i	-0.1090 + 0.1078 i
6	-0.0022 + 0.0045 i	-0.1134 + 0.1240 i
7	-0.0033 + 0.0023 i	-0.0861 + 0.0856 i
8	-0.0035 - 0.0000 i	-0.0461 + 0.0105 i
9	-0.0026 - 0.0018 i	0.0111 - 0.0525 i

6.2.1 Global Calculations with Flat η_i Profile

For our first investigation using the CYCLONE parameters, we have assumed radially varying a/L_T and a/L_n profiles from Eq. (6.15) and Eq. (6.16), respectively, which corresponds to a flat profile in $\eta_i = L_n/L_T$ (see also Figure 6.5c). The other equilibrium profiles are held constant (i.e. independent of x_s) at those values given in Table 6.4 (and are indicated by dashed lines in Figure 6.5−a and b)[4]. We then performed local gyrokinetic GS2 calculations for the range of interest in x_s and a full period in ballooning angle $-\pi \leq p \leq \pi$. This provides the local mode structure

[4]Their profile effects are considered in the next subsection.

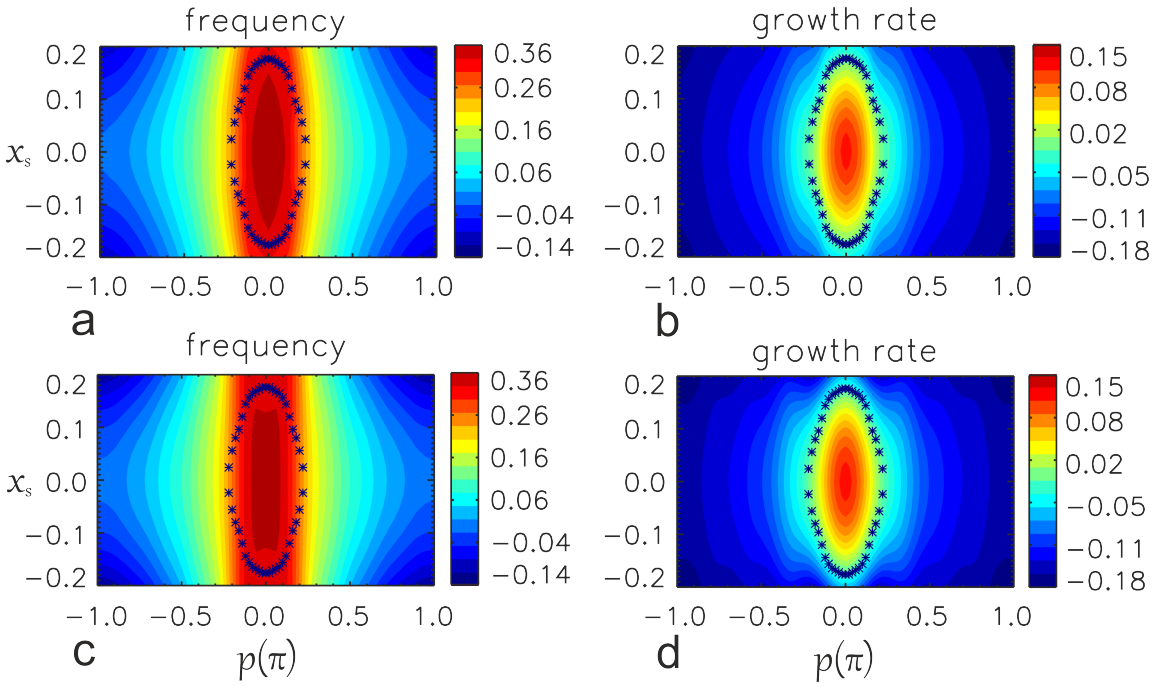

Figure 6.7: Contour plots of real and imaginary parts of the local complex mode frequency, measured in unit of (V_s/a), as functions of radius, x_s, and ballooning phase angle, p, for parabolic L_T and L_n radial profiles (see Figure 6.5c), while excluding other profile variations. (a) and (b) are, respectively, the frequency and growth rate obtained from the local gyrokinetic code, GS2. The corresponding frequency and growth rate from the fitted model, using Eq. (6.5), are presented in (c) and (d) respectively. The $\star$ symbols indicate the marginal stability contour where $\gamma_0(x_s, p) = 0$.

$\xi(x_s, p, \theta)$ with associated local complex mode frequency $\Omega_0(x_s, p)$. Figure 6.7 shows $\Omega_0(x_s, p)$ from GS2, compared to the fit using the parameterisation given in Eq. (6.5). The coefficients resulting from the fit are given in Table 6.5. As expected, because the linear drive profiles, namely a/L_T and a/L_n profiles, peak and are symmetric about $x_s = 0$, we have $S_k = 0$ for all k. Figure 6.7 shows that for this particular choice of the equilibrium profiles $\Omega_0(x_s, p)$ has a stationary point at $x_s = 0$, $p = 0$.

Using the values of f_k and R_k in Table 6.5 we solve Eq. (4.63) numerically to obtain $A(p)$ and the associated eigenvalue $\Omega = 0.3623 + 0.1353i$. Substituting this numerical solution for $A(p)$ together with $\xi(x_s, p, \theta)$ obtained from GS2, the numerical solution of Eq. (4.50) in turn provides the global mode structure, $\tilde{\phi}(x_s, \theta)$ with its radial width $\Delta_x = 0.1123$. The corresponding analytical solutions are $\chi = 22.9821 + i1.3012$ (from Eq. (4.74)) and after substituting this value back into Eq. (4.71) we obtain $A(p)$. We also obtain $\Omega = 0.3629 + i0.1352$ and $\Delta_x = 0.1110$ from Eq. (4.73) and Eq. (4.80), respectively. We note that excellent agreement is

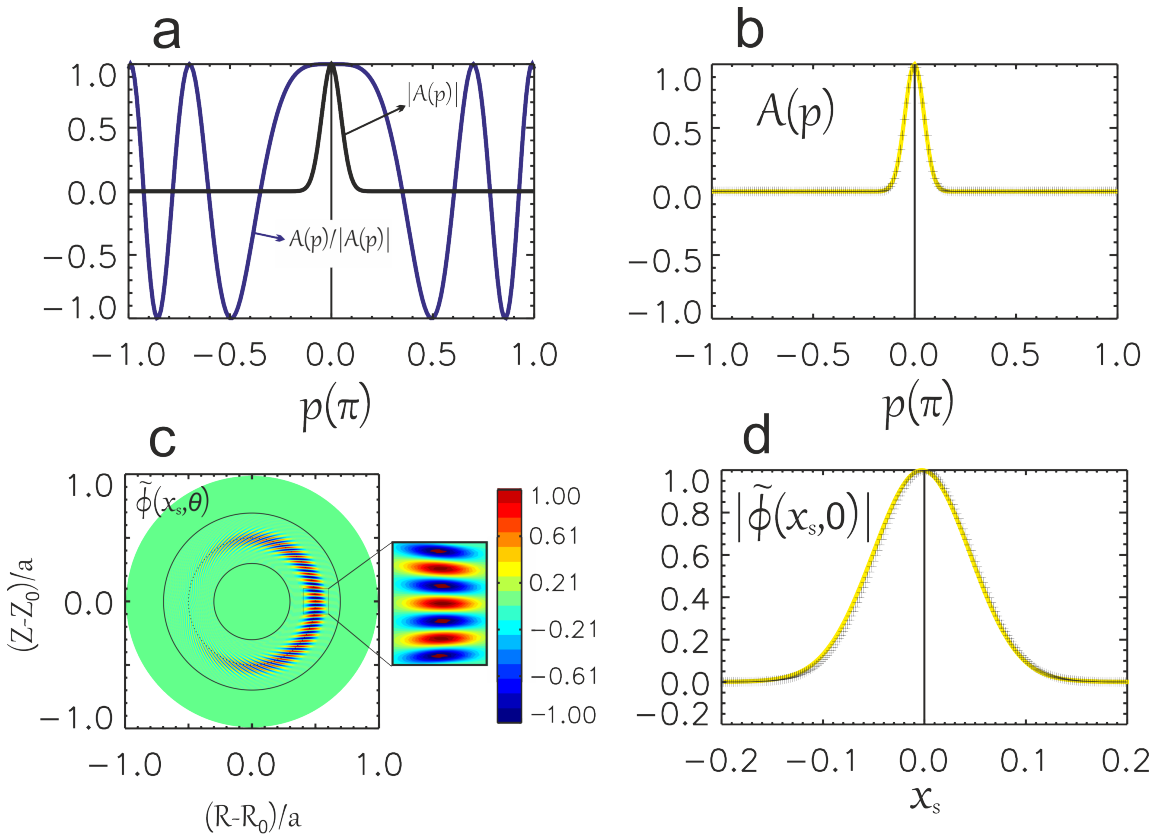

Figure 6.8: A pure isolated mode for which profile variations other than L_T and L_n are excluded: (a) and (b), respectively, present $|A(p)|$, $A(p)/|A(p)|$ and the envelope function, $A(p)$ as a function of ballooning phase angle, p, (c) shows the reconstructed global mode structure, $\tilde{\phi}(x_s, \theta)$, in the poloidal plane, where the two solid concentric circles indicate the radial domain of the calculation, and finally (d) presents $|\tilde{\phi}(x_s, \theta = 0)|$. Note that, the cross symbols and full curves correspond to the numerical and analytical solutions, respectively.

found between the numerical and analytical solutions. Figure 6.8 shows our solutions for $A(p)$ and the corresponding solution for $\tilde{\phi}(x_s, \theta)$ in the poloidal cross-section. We see that both $|A(p)|$ and $A(p)/|A(p)|$ are symmetric about $p = 0$. This leads to an envelope $A(p)$ which is symmetric under the transformation $p \to -p$ and is highly localised about $p = 0$, as is required for the procedure to be accurate (recall, we assumed $A(p)$ varies rapidly with p compared to $\xi(x_s, p, \theta)$ to derive Eq. (4.63)). As shown in Figure 6.8, this leads to a mode that balloons on the outboard mid-plane at $\theta = 0$ and radially peaks about $x_s = 0$. This is a pure isolated (or conventional ballooning) mode which has been previously identified in [5, 19, 20] (see also section 4.7.1 for more detail). However, radial variation of the other equilibrium profiles can introduce significant deviation from these pure isolated modes as we discuss in the following subsection.

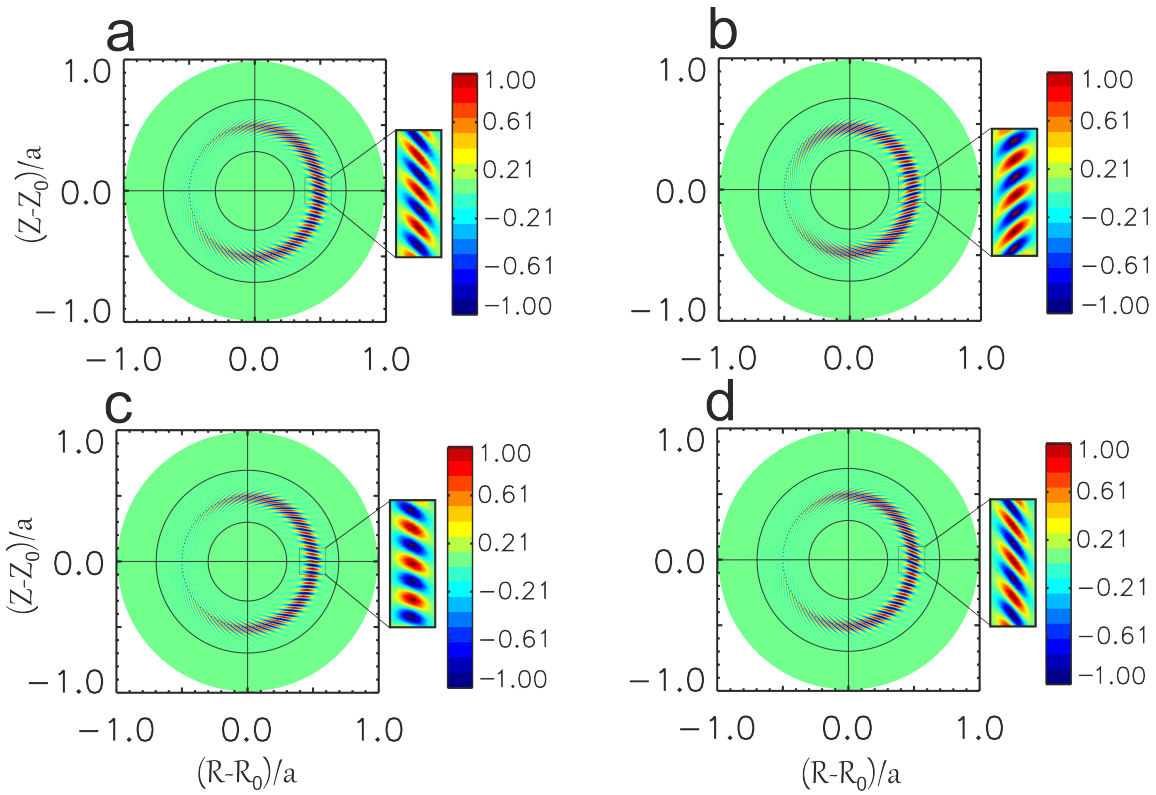

Figure 6.9: The reconstructed electrostatic potential global mode structure, $\tilde{\phi}(x_s, \theta)$, for $n = 39$, in the poloidal plane for different radial profile variations taken from Figure 6.5: (a) L_T, L_n and $r(x_s)$ vary, here both temperature T and density n_e are assumed to be constant, (b) L_T, L_n, q and $\hat{s}$ vary (c) L_T, L_n, $r(x_s)$, q and $\hat{s}$ vary and finally (d) full profile variation in which L_T, T, L_n, n_e, $r(x_s)$, q and $\hat{s}$ all vary.

6.2.2 Global Calculations with Profile Variations

It has been found in the linear global gyrokinetic simulations that the radial variation in the equilibrium profiles can tilt the global mode structures poloidally with respect to the outboard mid-plane [12, 27, 111] and this, in general, reduces the global growth rate of the mode compared to the highly unstable isolated modes. In this subsection, we repeat the analysis of the previous subsections and, in addition to both a/L_T and a/L_n equilibrium profiles, we take into account the influence of the other profile variations such as q, $\hat{s}$, T and n_e; these are defined in Eq. (6.11) − Eq. (6.14) (see also Figure 6.5). From our new methodological perspective, these equilibrium profiles vary over the radial scale of the instability and introduce additional linear radial variation in $\Omega_0(x_s, p)$, such that the S_k terms in Eq. (6.5) become significant. These extra linear terms impact $\omega_0(x_s, p)$ and $\gamma_0(x_s, p)$ differently and give rise to a shift in the relative positions where $\omega_0(x_s, p)$ and $\gamma_0(x_s, p)$ are maximum; this in

turn moves the stationary point of $\Omega_0(x_s, p)$ off the real x_s-axis. This leads to a constraint on the poloidal position of the reconstructed global mode such that the mode is now shifted poloidally with respect to the outboard mid-plane. This in turn influences both its structure and linear growth rate.

Figure 6.9 presents the reconstructed global mode structure in the poloidal cross-section, $\tilde{\phi}(x_s, \theta)$, for a number of cases where we introduce different profiles. Introducing the effect of variation in radius $r(x_s)$ itself, which impacts physics such as the trapped fraction, shifts the mode slightly downward with respect to the outboard mid-plane as shown in panel (a). In contrast to this, taking into account the impact of both q and $\hat{s}$ profile variations results in a mode that undergoes a small upward poloidal shift (see panel b). On the other hand, combining the influences from the above profile variations presented in both (a) and (b) leads to a mode that peaks very close to the outboard mide-plane (see panel c). This points to the fact that for this particular case the effect of different profiles are competing and almost cancel. Nevertheless, the result is slightly in favor of the $r(x_s)$ variation, leading to a slight net downward poloidal shift with respect to the outboard mid-plane. Finally, in panel (d), in addition to the profiles considered in (c), we include radial variations in the T and n_e profiles. The reconstructed global mode is then shifted poloidally downward with respect to the outboard mid-plane, breaking the up-down poloidal symmetry. This reduces the growth rate compared to the pure isolated mode considered in subsection 6.2.1. Furthermore, considering the full profile variation in case (d) we find $\Omega = 0.363 + i0.118$ and as we see the mode structure is tilted on the outboard mid-plane. This finding is in a good qualitative agreement with the full global simulations of linear ITG modes that published in Ref [12]. Note that the growth rate is reduced by 20% compared to the pure isolated mode case considered in section 6.2.1.

6.2.3 Calculations with Profile Variations and Sheared Toroidal Flow

In this subsection we investigate the influence of toroidal flow shear on the reconstructed mode structures and their stability. Here, due to this flow shear, different rational surfaces rotate at different speeds relative to each other, and this influences the toroidal coupling that provides the global mode structure [112]. We choose to work in a frame of reference rotating toroidally with the plasma such that there is no flow at $x_s = 0$, neglecting any centrifugal or Coriolis force effects. The dominate physics we retain is the Doppler shift in $\Omega_0(x_s, p)$, which can be obtained from Eq. (5.124) by assuming $\Upsilon = 0$ and rewrite it as follows[5]:

$$\Omega_0(x_s, p) \rightarrow \Omega_0(x_s, p) - nq'\gamma_E x_s = [\omega_0(x_s, p) - nq'\gamma_E x_s] + i\gamma_0(x_s, p), \qquad (6.17)$$

where the flow shear $\Omega'_\varphi = q'\gamma_E x_s$ is normalised to V_s/a and represents the toroidal rotational frequency of the magnetic flux surfaces with respect to the rational surface at $x_s = 0$. Note that $\gamma_E = d\Omega_\varphi/dq$ is constant and sets the flow shearing rate. For the set of equilibrium parameters that we have considered here, as the flow shear is increased the reconstructed global modes undergo increasing radial shifts away from $x_s = 0$. To keep the modes within our computational domain, we have limited ourselves to a small toroidal flow shear in the range $-0.02 \leq \gamma_E \leq +0.02$. Note also that, the poloidal flows are expected to be damped in tokamak plasmas [103, 104], and hence we have assumed the flow shear to be purely toroidal. Furthermore, if we compare Eq. (6.17) with Eq. (6.5), it is clear that flow shear only influences the S_k coefficients. This indicates that both flow shear and profile shearing can have similar impacts on the properties of the reconstructed global modes, which we will now quantify.

Figure 6.10 presents the variation of the growth rate as a function of flow shear for the different radially varying equilibrium profiles that we considered earlier in

[5]While this method can in principle handle an arbitrary experimental profile of toroidal rotation, for the simple example here we assume that the toroidal flow varies linearly in x_s.

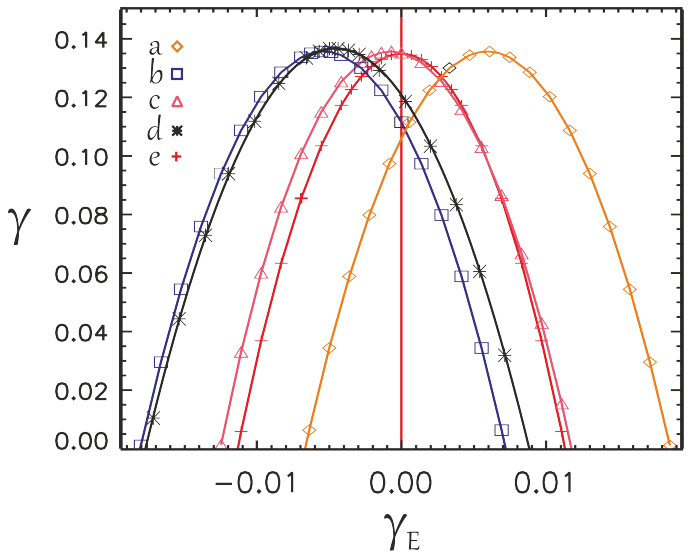

Figure 6.10: The linear growth rate, γ, as a function of flow shear, γ_E, calculated for the most unstable mode with $k_y\rho_{ci} = 0.58$. Note that both γ and γ_E are measured in units of (V_s/a), the toroidal mode number, $n = 39$ and $q' \approx 3.6$. For curve (e) the radial variations of the profiles other than L_T and L_n are excluded, while the other curves correspond to the profile variations of Figure 6.9(a-d) respectively.

figures 6.8 and 6.9. For the isolated mode of Figure 6.8, for which the effect of the equilibrium profiles other than a/L_T and a/L_n profiles are excluded, the growth rate spectrum is symmetric about $\gamma_E = 0$ and this corresponds to curve (e) of Figure 6.10. Considering this special case, at $\gamma_E = 0$ the mode is radially aligned on the outboard mid-plane (see panel (c) of Figure 6.8), but for $\gamma_E \neq 0$ depending on the sign of the flow shear the mode shifts poloidally downward or upward with respect to the outboard mid-plane, tilting the mode structure, and reducing its linear growth rate. Taking the effect of the other radially varying equilibrium profiles into account leads to an asymmetry in the spectrum of γ with respect to $\gamma_E = 0$. Moreover, there is a critical value for flow shear at which the growth rate is maximised, as illustrated in Figure 6.10 (for curves $a - d$). Note that this maximum value is independent of the profiles. To explain these results a new analytical theory is developed which we now discuss in the following.

For the above mentioned critical value of γ_E we expect an isolated mode to exist and when this happens both $\omega_0(x_s, p)$ and $\gamma_0(x_s, p)$ are stationary at the same radial position, let us assume at $x_s = x_0$, for which the S_k coefficients satisfy certain criteria, as we now turn to explain. From symmetry we anticipate that $\partial\omega_0/\partial p|_{p=0} =$

$\partial\gamma_0/\partial p|_{p=0} = 0$, so let us consider $p = 0$. Then introducing the effect of flow shear into our expression of $\Omega_0(x_s, p)$ in Eq. (4.59) we have

$$\Omega_0(x_s, 0) = f(0) + (S(0) - nq'\gamma_E)\, x_s + R(0)x_s^2 \tag{6.18}$$

Now we complete the square in x_s and rewrite Eq. (6.18) to obtain

$$\Omega_0(x_s, 0) = f(0) - x_0^2 R(0) + (x_s - x_0)^2 R(0), \tag{6.19}$$

where,

$$x_0 = \frac{nq'\gamma_E - S(0)}{2R(0)}, \tag{6.20}$$

For an isolated mode, we require $\Omega_0(x_s, p)$ to have a stationary point on the real x_s-axis, which in turn requires x_0 to be real. This provides the following constraint:

$$([S(0)]_r - nq'\gamma_E)\,[R(0)]_i = [S(0)]_i[R(0)]_r \tag{6.21}$$

as well as an expression for the radial position about which the mode is localised:

$$x_{0,r} = \frac{nq'\gamma_E - [S(0)]_r}{2[R(0)]_r} = -\frac{[S(0)]_i}{2[R(0)]_i} \tag{6.22}$$

where the subscripts r and i indicate the real and imaginary component respectively.

Let us now use our analytic results to interpret the numerical results of this section. First, let us consider the situation without flow shear, $\gamma_E = 0$. Eq. (6.21) then provides the condition for an isolated mode to exist:

$$[S(0)]_r = \frac{[S(0)]_i[R(0)]_r}{[R(0)]_i} \tag{6.23}$$

If the profiles are such that this expression is satisfied, then an isolated mode exists at the radial position $x_s = x_{0,r} = -[S(0)]_r/2[R(0)]_r = -[S(0)]_i/2[R(0)]_i$. This is (almost) the situation in case (c) of Figure 6.10 where the profiles combine such that Eq. (6.23) is satisfied. More generally, the isolated mode exists for a critical value of flow shear which, from Eq. (6.21) is given by

$$\gamma_E^m = \frac{1}{nq'}\left([S(0)]_r - \frac{[S(0)]_i[R(0)]_r}{[R(0)]_i}\right) \tag{6.24}$$

Thus, we expect the maximally unstable isolated mode to exist for this critical shear-

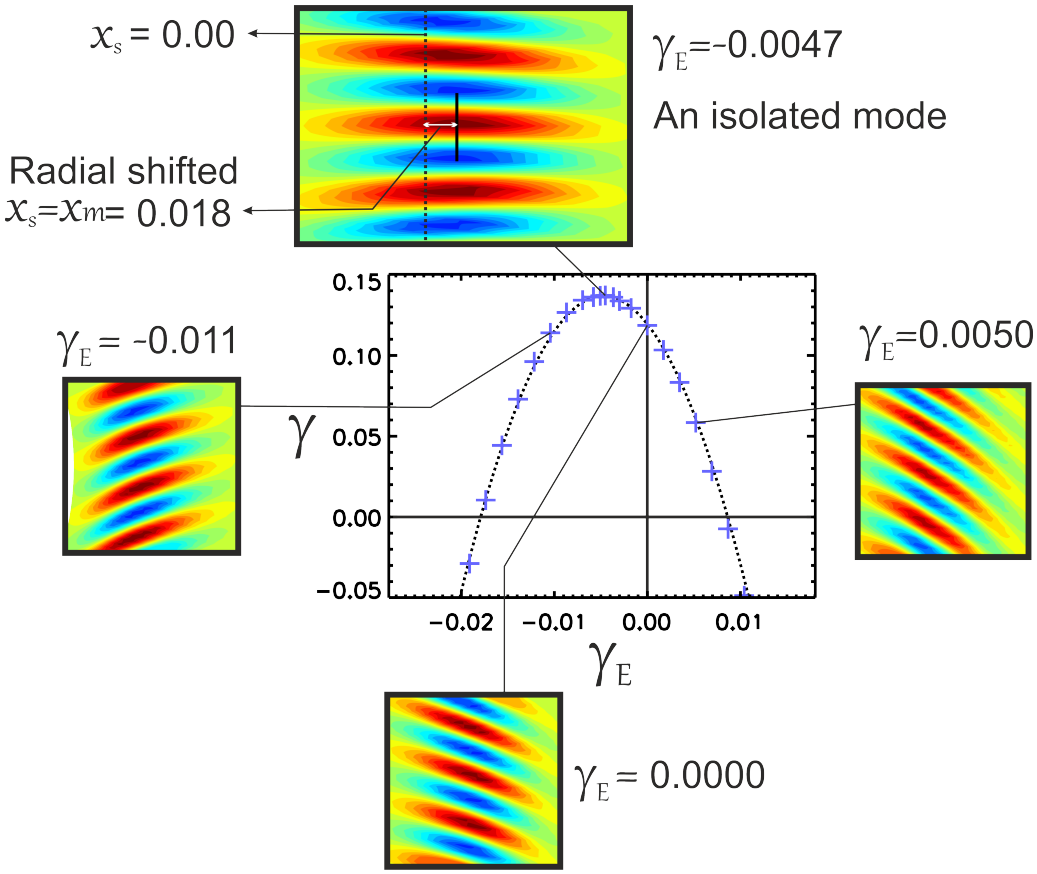

Figure 6.11: The numerical solutions (crosses) benchmarked against the analytical solutions (dotted line) for the global growth rate, γ, as a function of flow shear, γ_E, for the full equilibrium profile variation from Figure 6.10 curve (d) (see also Figure 6.9 panel d for the global mode structure that corresponds to $\gamma_E = 0$). The reconstructed global mode structure, $\tilde{\phi}$, in a small region of the poloidal cross-section at the outboard mid-plane are also presented at four different points that correspond to $\gamma_E = -0.0110, -0.0047, 0.0000$ and 0.0050, respectively. For $\gamma_E = 0$, the mode is already tilted, due to the profile variation effect, while a critical value of flow shear, occurs at $\gamma_E \approx -0.0047$, which cancels out the effect of profile variation and, once again, the mode structure is aligned radially (as for a conventional ballooning mode) and this is the maximally unstable flow shear.

ing rate, $\gamma_E = \gamma_E^m$, but centered on $x_s = x_{0,r}$ rather than $x_s = 0$. It is also obvious that γ_E^m scales inversely with n.

To compare our flow shear results with the global gyrokinetic simulations presented in Ref [12] and also to benchmark the numerical solutions against the analytical theory developed in the previous chapter, we shall now consider the full profile variation case in a little more detail (curve-d in Figure 6.10). The associated model coefficients are presented in Table 6.6 [Note, in the notation above, $f(0) = \sum_{k=0}^{N_k} f_k$; $S(0) = \sum_{k=0}^{N_k} S_k$ and $R(0) = \sum_{k=0}^{N_k} R_k$]. Figure 6.11 presents the global linear growth rate γ as function of γ_E. The numerical and analytical solutions correspond to the

Table 6.6: The model coefficients, f_k, S_k and R_k corresponding to the full profile variation case (Figure 6.11).

k	f_k	S_k	R_k
0	0.1226 - 0.0686 i	-0.6409 + 0.3054 i	-3.0422 - 2.5486 i
1	0.1728 + 0.1216 i	-0.1554 - 0.0292 i	6.8274 - 1.5667 i
2	0.0566 + 0.0453 i	-0.3002 - 0.0788 i	-4.3586 - 0.3931 i
3	0.0177 + 0.0240 i	0.2293 - 0.0363 i	3.0658 - 0.6156 i
4	0.0123 + 0.0101 i	-0.0553 + 0.0167 i	-3.6445 - 0.6267 i
5	-0.0042 + 0.0086 i	0.2126 - 0.0093 i	1.2683 - 0.5595 i
6	-0.0027 + 0.0046 i	0.0427 + 0.0300 i	-1.5755 - 0.3859 i
7	-0.0036 + 0.0012 i	0.0777 + 0.0319 i	0.0000 - 0.0000 i

cross symbols and the dotted curve, respectively. Note that the analytical solutions are obtained from Eq. (5.7) while the numerical solutions from Eq. (4.63) (see section 4.6). For the range of flow shear studied here very good agreement between the two solutions is found. In Figure 6.11 we have also illustrated how the aforementioned asymmetry in the growth rate spectrum affects the reconstructed global mode structures. For $\gamma_E = 0$ the structure is already tilted, but increasing flow shear in the negative direction acts to re-align the mode radially and for a critical value of flow shear $\gamma_E^m = -0.0047$, the effect of the profile variation is completely compensated, allowing an isolated mode again to form with largest growth rate, $\gamma =$Max$[\gamma_0(x_s, p)]$. This is as we expect from our analysis above. For the coefficients presented in Table 6.6 we have $f(0) = \sum_k S_k = -0.58894 + i0.23036$ and $R(0) = \sum_k R_k = -1.45931 - i6.69606$. Substituting this into Eq. (6.24) provides $\gamma_E^m = -0.0046$, which is in excellent agreement with the above numerical result. Note also that at this value of γ_E the mode is radially shifted slightly relative to $x_s = 0$ with a growth rate of $\gamma = 0.137$, which is $\sim 10\%$ higher than the growth rate for zero flow shear ($\gamma = 0.118$). This is a shifted isolated mode, and the radial shift can be calculated from Eq. (6.22) which provides $x_{0,r} = 0.0017$, while the corresponding numerical solution is $x_m \approx 0.0018$ and again we have good agreement between these two solutions. We note that increasing flow shear even further, beyond the critical value, tilts the mode structure in the opposite direction and lowers its linear growth rate again. These results, obtained purely from solutions of GS2 and the higher order theory, are in good qualitative agreement with global calculations

of linear electrostatic ITG modes presented in Ref [12]. Direct comparison of our flow shear results with the global simulations performed in Ref [12] is complicated as we employ a toroidal flow, while the simulations of Ref [12] employ an $\mathbf{E} \times \mathbf{B}$ flow, which is almost poloidal. Nevertheless, if parallel flows have a negligible impact, the two can be related by a geometric factor. We can factor out this geometric factor by considering the ratio of the flow shear which maximises the growth rate to the value required to stabilise the mode. Our result of ≈ -0.40 is then in excellent agreement with that of Ref [12], which is ≈ -0.39.

To summarise, for realistic and experimentally relevant cases where we take the profile variations into account, we do not in general expect to find isolated modes. Isolated modes can form only in special radial locations where the equilibrium profiles produce a stationary point in $\Omega_0(x_s, p)$. However, making adjustments to one equilibrium profile while the others are fixed, can produce the required stationary point and lead to the onset of the isolated mode, as arises in the above example for a critical toroidal flow shear equal to γ_E^m. It is also important to mention that, our results show that the isolated mode tends towards the general mode as linear profiles are introduced (e.g. the flow shear plots of Figure 6.10 and Figure 6.11), with reducing growth rates and poloidal shifting of the mode off the mid-plane as the flow is increased. However, as seen in Figure 6.11, the mode is fully stabilised for a flow shear of ≈ 0.008, and at this stage it is still far from a general mode which would be located at the top or bottom of the plasma. For the equilibrium that we have considered here the general modes are expected to be stable. Therefore, we have not included these in our simulations.

6.3 Effect of Shaping: Modified CYCLONE Base Case

One of the main obstacles in MCF research is to understand the turbulent transport of both heat and particles and seek a way to reduce its effect. Although substantial progress has been made, there are still some unsolved issues remaining. One of the

important issues is the influence of the magnetic flux surface shape. In this section, we employ the so-called Miller equilibrium model and investigate the effect of shaping on the electrostatic ITG modes in tokamaks.

We have seen from the previous section that the set of equilibrium parameters corresponding to the CYCLONE base case leads to weakly unstable global modes and, due to some numerical issues associated with the marginally unstable modes, it was challenging to explore the impact of non-circular magnetic flux surfaces for these parameters. To overcome this issue we have modified the equilibrium profile a/L_T in Eq. (6.15) and replaced it with the following one

$$\frac{a}{L_T} = 5.0 + 2.54\cosh^{-2}(\frac{x_s}{0.208}) \tag{6.25}$$

This in turn leads to strongly driven global modes which then allowed us to investigate a series of magnetic configurations with varying elongation $0.8 \leq \bar{\kappa} \leq 1.2$ and triangularity $-0.2 \leq \bar{\delta} \leq 0.2$. With this modification, performing the local ballooning analysis for the circular magnetic flux surface with $\bar{\kappa} = 1.0$ and $\bar{\delta} = 0.0$, the most unstable local mode is found at $k_y\rho_{ci} = 0.68$ and this corresponds to $n = 46$. For this most unstable mode, we have then performed our global analysis, considering only the isolated mode that arises with a flat η_i profile. Thus, only a/L_T and a/L_n vary with x_s and other equilibrium profiles are held constant at their values represented by the dashed lines in Figure 6.5[6].

Figure 6.12 shows the influence of shaping on the global growth rate γ. The numerical and analytical solutions correspond to squares and crosses, respectively. The global mode structures in the poloidal cross-section are also plotted for four of the shapes. These shapes are obtained from the Miller flux surface approach which is given by the following analytical formula [113]:

$$\begin{aligned} R(r,\theta) &= R_0(r) + r\cos[\theta + \bar{\delta}\sin\theta] \\ Z(r,\theta) &= \bar{\kappa} r \sin\theta \end{aligned} \tag{6.26}$$

[6]The model coefficients that we have used in this section, which are obtained from the fit of $\Omega_0(x_s, p)$ to the model in Eq. (6.5), are all presented in Appendix A. Note also that the numerical solutions are obtained from Eq. (4.63) (see section 4.6) while the analytical solutions from Eq. (5.7)

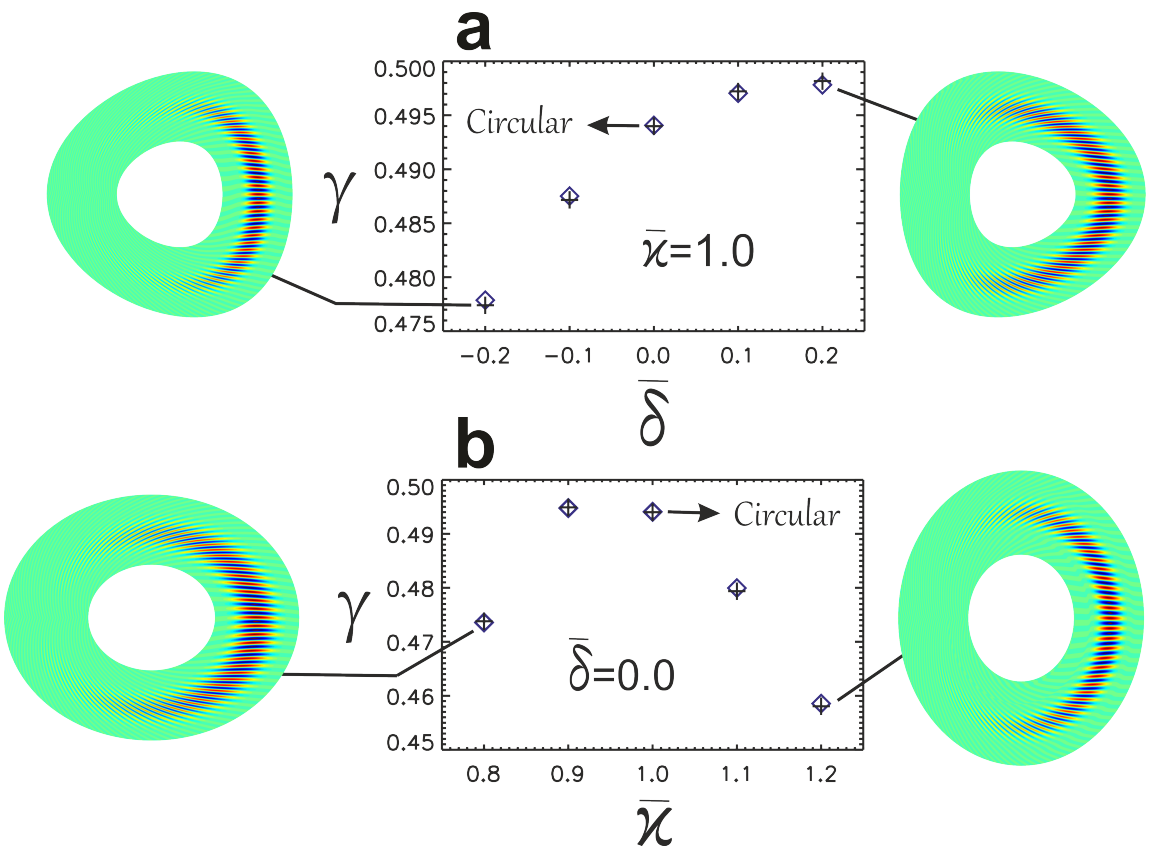

Figure 6.12: The global growth rate, γ, as a function of magnetic flux surface shaping. (a) presents the impact of triangularity on γ at fix elongation $\bar{\kappa} = 1.0$ while (b) shows the effect of elongation on γ at fixed triangularity $\bar{\delta} = 0.0$. The poloidal cross-section of the reconstructed global modes are also shown for four different configurations, namely for $(\bar{\kappa}, \bar{\delta}) = (1.0, -0.2)$, $(1.0, 0.2)$, $(0.80, 0.00)$ and $(1.2, 0.0)$, respectively. Note that the squares and crosses correspond to the numerical and analytic solutions, respectively.

where r and R_0 are minor and major radii of the toroidal flux surface, respectively. Note that the modes are radially peaked at $x_s = 0$ and the green shaded regions represent the simulation domain which is extended from $x_s = -0.10$ to $x_s = 0.10$. Keeping $\bar{\kappa} = 1.0$ constant and changing $\bar{\delta}$ (see Figure 6.12 - a), we find that the mode becomes more unstable as $\bar{\delta}$ increases. The effect of configurations with $\bar{\delta} < 0.0$ and $\bar{\delta} > 0.0$ are stabilising and destabilising, respectively, compared to circular magnetic flux surfaces. This favourable effect of negative triangularity captured in our simulations is very important and even though the physics is different, the trend here is similar to that presented in Ref [33] (see their figure 7) in which they have investigated the effect of shaping on the electron heat transport in TCV L-mode plasmas. Our understanding is that for $\bar{\delta} < 0$ the global mode is poloidaly extended over a bad curvature region which is smaller compared to the case with $\bar{\delta} > 0$.

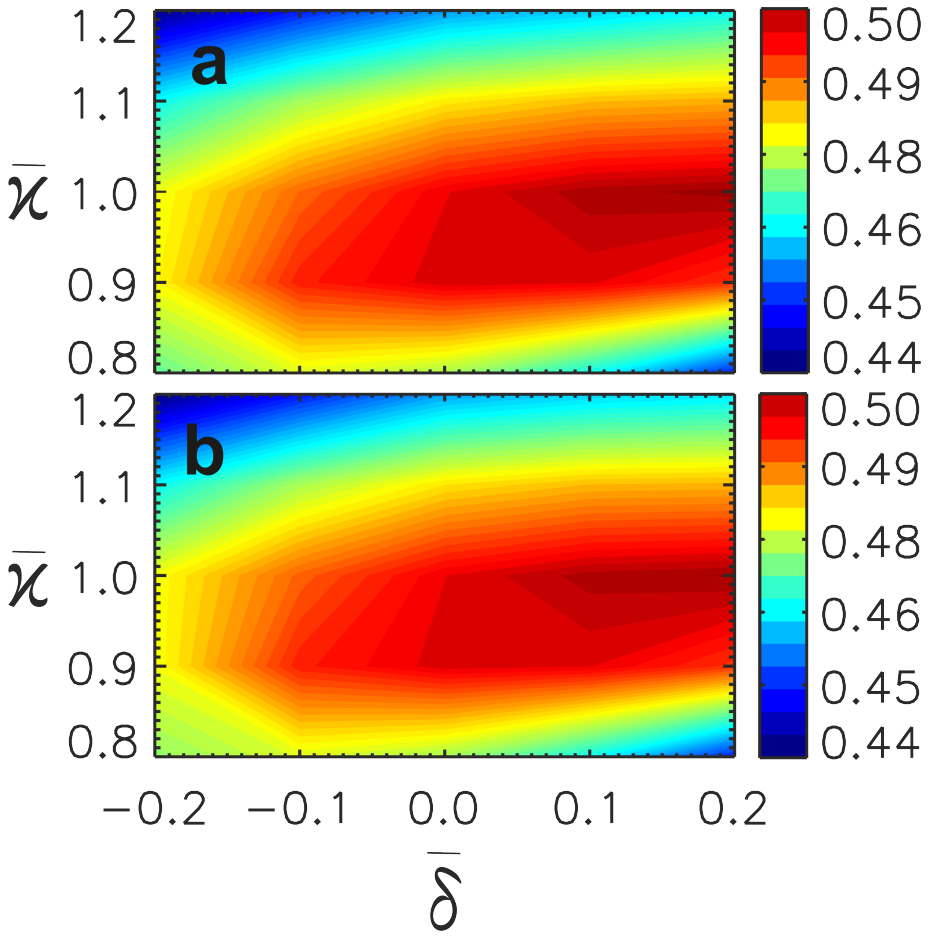

Figure 6.13: The contour plot of the global growth rate γ as function of $\bar{\kappa}$ and $\bar{\delta}$. (a) presents the numerical solutions and (b) shows the associated analytical solutions.

Turning to the effect of elongation, we keep $\bar{\delta} = 0.0$ constant and change $\bar{\kappa}$ (see Figure 6.12 - b). We find that the vertical elongation with $\bar{\kappa} > 1.0$ is stabilising. This trend is similar to the effect of vertical elongation on the linear gyrokinetic ITG growth rates found in [37, figure 1 and 38, figure 3] for the same value of $\bar{\delta} = 0$. A similar trend has been also reported for the edge turbulent electron transport in tokamaks [39] (see their figure 3). Moreover, for horizontal elongation with $\bar{\kappa} < 1.0$ the effect is initially weakly destabilising at $\bar{\kappa} = 0.9$, but below this value at $\bar{\kappa} = 0.8$ the mode again becomes less unstable compared to $\bar{\kappa} = 1.0$.

The combined effects of both elongation $0.8 \leq \bar{\kappa} \leq 1.2$ and triangularity $-0.2 \leq \bar{\delta} \leq 0.2$ have also been investigated. Figure 6.13 shows both numerical (a) and analytical (b) values for the global growth rate γ as function of $\bar{\kappa}$ and $\bar{\delta}$. As can be seen, for the parameter regime studied here, the most unstable mode corresponds to the configuration with $\bar{\kappa} = 1.00$ and $\bar{\delta} = 0.2$. The maximum value of growth

rate shifts slightly towards the lower values of $\bar{\kappa}$ as $\bar{\delta}$ decreases. This indicates that whether the effect of $\bar{\kappa}$ ($\bar{\delta}$) is stabilising or not depends on the value of $\bar{\delta}$ ($\bar{\kappa}$). We can also see that, for the parameters with vertical elongations, i.e. $\bar{\kappa} > 1.0$, the mode becomes more stable as $\bar{\delta}$ decreases. However, for the horizontal elongation, i.e. $\bar{\kappa} < 1.0$, this trend is gradually reversed and the most unstable mode is found at some intermediate values of $\bar{\delta}$, until eventually for $\bar{\kappa} = 0.8$ the effect is reversed; here the most stable mode corresponds to the region with $\bar{\delta} > 0$ rather than $\bar{\delta} < 0$. This reversed trend of the stabilising effects of positive triangularity has also been observed, for example, for H-mode discharges in both JET and AUG tokamaks [34], where the confinement improves with increasing positive triangularity. In addition, as we increase the effect of shaping towards the blue regions on the contour plots, corresponding to the vertical elongation $\bar{\kappa} > 1.0$ with $\bar{\delta} < 0$ and horizontal elongation $\bar{\kappa} < 1.0$ with $\bar{\delta} > 0$, we can see that the mode is stabilised compared to the configuration with circular flux surfaces and the least unstable mode is found at $\bar{\kappa} = 1.20$ and $\bar{\delta} = -0.2$. Finally, our finding here points to the fact that the magnetic flux surface shaping can be either stabilising or destabilising, and the values of $\bar{\kappa}$ and $\bar{\delta}$ can be optimised to provide a favorable stabilising effects on the underlying linear microinstabilities, with a corresponding reduction in the associated turbulent transport.

6.4 Summary and Conclusion

In this chapter a local gyrokinetic code, GS2, has been used to investigate the global properties of a linear electrostatic ITG mode in tokamak plasmas. Simulations presented here are divided into two parts. First, a so-called $s-\alpha$ equilibrium model has been employed in which circular magnetic flux surfaces with high aspect ratio has been assumed. Here we have used a set of equilibrium parameters which is strongly unstable, such that we are able to identify both isolated and general modes, which are radially confined close to the centre of our simulation domain. The effect of equilibrium variations other than the η_i profile were excluded. We found that the local mode frequency $\Omega_0(x_s, p)$ is stationary for a case with a quadratic η_i variation

and this is a special case that leads to a highly unstable isolated mode that usually balloons on the outboard mid-plane. In contrast, using a linear η_i profile, $\Omega_0(x_s, p)$ does not have stationary points, which in turn generates a relatively less unstable general mode that peaks on the top of the plasma.

Furthermore, in our second step, in order to benchmark against global gyrokinetic simulations, we have studied the CYCLONE base case and employed the so-called Miller equilibrium model with circular magnetic flux surfaces. Here, again, we started with a radially peaked profile for the mode drive centred about $x_s = 0$, and held other equilibrium profiles constant. This again provides an isolated mode. We have also investigated the effect of other equilibrium profiles as well as the rotational flow shear that was introduced through a Doppler shift in the local frequency $\Omega_0(x_s, p)$ such that $\Omega_0(x_s, p) \rightarrow \Omega_0(x_s, p) - nq'\gamma_E x_s$. For a set of parameters that generate an isolated mode, we found that the growth rate spectrum as a function of flow shear is symmetric about $\gamma_E = 0$. Taking the effect of the other equilibrium profiles into account leads to a mode that shifts away from the outboard mid-plane with reduced growth rate compared to the isolated modes. The profile variation introduces asymmetry into the spectrum of the growth rate as a function of flow shear. For a critical value of flow shear, i.e. $\gamma_E = \gamma_E^m$, we recapture an isolated mode even with arbitrary profiles, which is in good qualitative agreement with global gyrokinetic calculations presented in Ref [12]. Moreover, we have also derived an analytic theory to calculate the value of the critical flow shear for which the growth rate has a maximum, and this is found to be in excellent agreement with the numerical solutions. In addition to the above results, we have presented some initial results about the effect of shaping on the global properties of the ITG modes. Here, we have only considered the highly unstable isolated modes and found that the shapes of the magnetic flux surfaces, controlled via elongation $\bar{\kappa}$ and triangularity $\bar{\delta}$, can be either stabilising or destabilising.

In the following chapter we summarise the work presented in this thesis and present the plans for further future research.

Chapter 7

Summary, Conclusion and Future Work

The dominant transport mechanism in magnetically confined plasmas for both heat and particles is due to the turbulent fluctuations in the plasma parameters. These fluctuations are believed to originate from microinstabilities, especially low frequency drift modes. These fine scale instabilities, driven by free energy in the confined plasma associated with density and temperature gradients, can be a serious problem for effective confinement. Therefore, it is important to study, for example, the effect of possible magnetic configurations and plasma conditions and determine relevant criteria that could help control the instabilities and even to suppress or eliminate them completely. Theoretical investigation of turbulent transport associated with microinstabilities is usually performed via numerical simulations of the gyrokinetic equation. There are two main approaches, namely global and local. The former one takes into account the effect of the radial variation of the equilibrium profiles, but at relatively high computational cost. In contrast, the local approach exploits the separation between the equilibrium scale length and the characteristic radial size of the instability to simplify the problem to the local system.

This thesis is devoted to improving our understanding of the impact of the global

effects on linear microinstabilities. In this work, instead of using a direct global solution, we have reconstructed the 2D global mode structure and the global growth rate for linear electrostatic ITG modes, using local solutions from a gyrokinetic code (GS2) and higher order ballooning theory. There are two main advantages of using local results to build up global mode structures:

1. They are computationally less intensive than full global simulations, largely because the calculations of $\Omega_0(x_s, p)$ are trivially parallellised across the x_s and p meshes.

2. They allow one to probe the physics behind the global mode structures in more detail.

Our focus has been more on the latter, comparing with global simulations in the literature to interpret, for example, why modes do not always sit at the outboard mid-plane. The greater efficiency is a benefit, but it would be difficult to quantify without running equivalent global and flux tube simulations side by side for a range of parameters. This is a significant piece of work that we have not considered in this thesis, but it is likely to be useful to consider in the future.

Our approach has provided additional insight into the physics of global simulations of linear microinstabilities in tokamak plasmas. We began by extending the analytic theory of 2D ballooning modes in tokamaks beyond the two special limits of isolated and general modes previously considered in the literature. The former, which often sit on the outboard mid-plane, only occurs for a particular set of equilibrium parameters for which $\Omega_0(x_s, p)$ is stationary at some radial point. On the other hand, for the general mode $\Omega_0(x_s, p)$ is not stationary and this leads to a mode that either sits on the top or bottom of the plasmas with reduced growth rate compared to the isolated mode. The theoretical extensions developed in this work can account for a global mode that sits anywhere in the poloidal plane (generalised modes in our terminology). This is a quite important and profound theory and can basically improve our understanding of the microinstabilities for realistic experimental regimes.

For experimentally relevant equilibria the magnetic configurations do not, in general, have circular cross-section and one typically also needs to take the effect of the radial variations of the equilibrium profiles into account. This in turn might lead to a generalised type of modes rather than the above mentioned isolated or general modes. The theory can also provide explanations for the mechanisms behind both radial and poloidal symmetry breaking with respect to $x_s = 0$ and $\theta = 0$, respectively. We found that the imaginary components of the ballooning phase angle p_0 and the radial parameter x_0 result in radial and poloidal asymmetries, respectively.

It is important to mention that the approach and analysis that has been used in this thesis only works in linear regimes. Nevertheless, the transport associated with microturbulence is frequently modelled successfully using quasi-linear theory, which is based on the assumption that the saturated turbulence continues to resemble the linear modes. Linear theory of microinstabilities underlies other widely used models where the limiting of steep gradients can be associated with the onset of particular linear instabilities: e.g. the EPED model of the tokamak H-mode pedestal infers marginal stability of the kinetic ballooning mode. Our global linear calculations are of value because they improve on the local description of the linear modes, shedding light on the physics underlying the results of global simulations. Even though, the linear modes must be nonlinearly saturated/broken up by zonal flows in the turbulent state, the initial linear instability frequency and mode structure remain of interest.

While the method and techniques that have been implemented here were previously described and used in [5], this thesis (i) improves on the description of the method, (ii) makes the rather significant advance of demonstrating that the approach can be used with a state-of-the-art local gyrokinetic code (GS2), and (iii) has allowed us to benchmark this new method against global GK simulations in [12]. As a first illustration of using the method with GS2 we have chosen the simple and familiar example of electrostatic ITG instabilities in the $s-\alpha$ equilibrium, assuming that the electron response is adiabatic. Here, our first investigations used radial profiles for the mode drive, η_i, that were peaked and symmetric about $x_s = 0$, and we held all

other equilibrium profiles constant; this results in the local complex mode frequency, $\Omega_0(x_s, p)$, having a stationary point at $x_s = 0$. This condition produces a special class of mode, known as the "isolated mode", that peaks at the outboard mid-plane with a large growth rate, $\gamma \sim \text{Max}[\gamma_0(x_s, p)]$. These results are in very good qualitative agreement with the simplified fluid model of ITG modes presented in Ref [5]. In addition, introducing a linearly varying radial η_i profile removes the stationary point from $\Omega_0(x_s, p)$ and leads to a general mode that sits close to the top of the plasma and does not preserve either the radial or the poloidal symmetries.

Furthermore, we have also investigated the circular CYCLONE base case equilibrium, which has allowed us to benchmark our calculations against results from global gyrokinetic simulations that were presented in [12] for the same equilibrium. In addition to the radial profile for the mode drive that was peaked and symmetric about $x_s = 0$, we have introduced a radial variation into other equilibrium profiles. This leads to a shift in radial position of the stationary points in both local frequency, ω_0, and growth rate, γ_0, with respect to each other. In this case, the reconstructed global mode becomes less unstable and shifts poloidally away from the outboard mid-plane. Toroidal flow shear, introduced as a Doppler shift in the real frequency, also influences the global mode. Starting from the conditions of an isolated mode, with drive profiles peaked and symmetric about $x_s = 0$ and with no other profile variations, adding a constant flow shear is always found to be stabilising. When other profile variations are included, flow shear can be destabilising when the flow shear counteracts the tilting of the mode structure at the outboard mid-plane that is induced by the other profile variations. This results in an asymmetry in the growth rate as a function of flow shear about $\gamma_E = 0$, which is in qualitative agreement with previous global gyrokinetic calculations [12]. Moreover, flow shear is also found to shift the mode radially. For a critical flow shear (or a critical toroidal mode number for a given flow shear – see Eq. (6.24)) the isolated mode can exist even with arbitrary profiles. In our final step, using the Miller equilibrium model, we have presented some initial results on the effects of the magnetic flux surface shapes and for convenience we have limited ourselves to highly unstable isolated modes. The

shaping effects were controlled via the elongation $\bar{\kappa}$ and triangularity $\bar{\delta}$. For our parameters, we found that the combined effects of $\bar{\kappa}$ and $\bar{\delta}$ can be both stabilising or destabilising depending on the conditions.

Finally, it is worth mentioning that the methodology utilised in this thesis is truly general and can be applied to investigate instabilities for experimentally relevant tokamak equilibria, incorporating electromagnetic effects, kinetic electrons and non-circular toroidal magnetic geometries. For example, the procedure exploited here is being used to explore the global properties of a particular type of microinstability called kinetic ballooning modes (KBMs). This is extremely topical and forms a current European research project to construct a new model for ELMs and the pedestal structure. For MAST pedestal parameters, KBMs are found to have $\Omega_0(x_s, p)$ with very strong p dependence, peaking very sharply about $p = 0$. This might indicate that the isolated KBM mode is highly unstable, but the general KBM mode is close to marginal. Moreover, in the relatively high collisionality regime of the MAST pedestal, KBMs were found to be locally unstable [114], but close to marginal, while in a lower collisionality JET case it is locally strongly stable [115, 116]. A key question is whether the associated global modes are stable. We have seen in this thesis that the global effects are, in general, stabilising. If the local result is close to marginal stability (or even stable) then incorporating global effects is likely to result in stability, which would be inconsistent with EPED model. Work is ongoing to extend our study to explore this in the future. Furthermore, it is important to note that our procedure is robust, requiring that the magnetic shear length is not much larger than the equilibrium scale length, such that the equilibrium quantities vary slowly across rational surfaces, and only works in linear regimes. It will be interesting to consider whether a non-linear approach can be developed based on this method, but this will be challenging and it is not clear yet how to achieve this. We also note that whilst the computational approach to calculating the global structure from local simulations has significant advantages over a direct global simulation, there are some technical difficulties that can arise. For example, using the initial value GS2 code, there is a spectrum of linear modes at a particular n, x_s and p; as p and x_s are varied

it is necessary to track a single branch, which can be challenging for some equilibrium parameters where different branches cross one another. To address this, one might filter the result, by using a starting point closer to the eigenmode of interest, which one can identify by using the eigenmode of the previous p/x_s point as initial guess for the next. Despite these difficulties we have demonstrated that this approach is a powerful tool for studying global physics which offers benefits in both computation and interpretation.

Appendices

A Shaping Effect-Isolated Modes: The Model Coefficients

The model coefficients, f_k and R_k, with twelve Fourier modes for the shaping effect, with varying elongation $\bar{\kappa}$ and triangularity $\bar{\delta}$, presented in section 6.3. These coefficients are obtained from the fit using the parametrisation given in Eq. (6.5). The real and imaginary components contribute to the real frequency, ω_0, and growth rate, γ_0, respectively. Here, $S_k = 0$ for all k as only pure isolated modes are considered.

Table 1: $\bar{\kappa} = 0.80$ and $\bar{\delta} = -0.20$.

k	f_k	R_k
0	0.68309082+0.042677016 i	-2.0554813-1.4755869 i
1	0.10114897+0.042677016 i	3.3363627-1.4755869 i
2	0.095072343+0.087128198 i	-1.7957588-1.3800766 i
3	0.06752043+0.03132025 i	0.73010457+0.53626528 i
4	0.03295838+0.00328530 i	-0.82296302-0.41029634 i
5	-0.00329566+0.00661760 i	0.39154485+0.17307158 i
6	0.0012446598+0.0091394702 i	-0.012336610-0.041714520 i
7	-0.00357769+0.00202733	-0.37247055-0.15798101 i
8	-0.00497097+0.00325872 i	0.77433010+0.29724648 i
9	-0.00083070-0.00008747 i	-1.0786408-0.43488034 i
10	-0.00371363+0.00078696 i	1.3341999+0.53024498 i
11	-0.00006952-0.00084135 i	-1.4461732-0.58712975 i

Table 2: $\bar{\kappa} = 0.80$ and $\bar{\delta} = -0.10$.

k	f_k	R_k
0	0.67893964+0.050847068 i	-1.1645625-1.1818178 i
1	0.10240479+0.30233751 i	1.7098600-1.4107264 i
2	0.09090867+0.09471214 i	-0.28474462-0.78493390 i
3	0.06554877+0.02621109 i	-0.40056665+0.04278513 i
4	0.02800509-0.00109717 i	-0.04388113+0.00802085 i
5	0.00275931+0.00242268 i	-0.01907365-0.02344083 i
6	0.00090366+0.00555991 i	-0.04627431+0.00862854 i
7	0.00024663+0.00197121 i	0.01157460+0.00297086 i
8	-0.00135111+0.00222066 i	0.00268747+0.00297086 i
9	-0.00105377+0.00096174 i	-0.03899579-0.00589229 i
10	-0.00005943+0.00096174 i	0.05001108-0.00440295 i
11	-0.00126510-0.00014104 i	-0.04499669-0.01141441 i

Table 3: $\bar{\kappa} = 0.80$ and $\bar{\delta} = 0.00$.

k	f_k	R_k
0	0.67584453+0.05838062 i	-1.1214270-1.2156466 i
1	0.10341179+0.30346486 i	1.7020352-1.4653336 i
2	0.08747687+0.09985999 i	-0.20166826-0.75346542 i
3	0.06327799+0.01755421 i	-0.43201937+0.04589801 i
4	0.02911570-0.00618468 i	-0.05922889+0.06552281 i
5	0.00676393-0.00184823 i	-0.04253470-0.02637668 i
6	0.00350407+0.00403779 i	-0.07661257+0.01064867 i
7	0.00294472+0.00260984 i	0.02136977-0.01010066 i
8	0.00032567+0.00173006 i	-0.03414125-0.00129801 i
9	0.00006626+0.00219463 i	-0.02207919-0.00189223 i
10	0.00058054+0.00118589 i	0.03046667-0.01108000 i
11	-0.00094082+0.00049878 i	-0.050533620.00874585 i

Table 4: $\bar{\kappa} = 0.80$ and $\bar{\delta} = 0.10$.

k	f_k	R_k
0	0.67470750+0.064352179 i	-1.0977440-1.2664329 i
1	0.10362821+0.30354918 i	1.7141457-1.4756864 i
2	0.08435286+0.10192469 i	-0.12833931-0.71242124 i
3	0.06287021+0.00802377 i	-0.49779220+0.02816935 i
4	0.03208551-0.01166903 i	-0.06456055+0.15043588 i
5	0.01094396-0.00438198 i	-0.07635908-0.06058080 i
6	0.00557810+0.00323495 i	-0.09408417+0.00478311 i
7	0.00438400+0.00298395 i	0.03262861+0.03418313 i
8	0.00199229+0.00150662 i	-0.06975095-0.05182336 i
9	0.00062650+0.00254634 i	-0.00510611+0.03251567 i
10	0.00125574+0.00158540 i	0.01731460-0.00969928 i
11	-0.00011656+0.00087893 i	-0.06674908-0.04376952 i

Table 5: $\bar{\kappa} = 0.80$ and $\bar{\delta} = 0.20$.

k	f_k	R_k
0	0.67412582+0.06867411 i	-1.0473479-1.2715934 i
1	0.10401295+0.30355645 i	1.6854257-1.5314451 i
2	0.08154999+0.10137871 i	-0.07029064-0.65689425 i
3	0.06412347-0.00220004 i	-0.51379718+0.06250245 i
4	0.03629996-0.01723659 i	-0.15925530+0.15688144 i
5	0.01427110-0.00586003 i	-0.04320473-0.04641969 i
6	0.00695540+0.00275007 i	-0.10833086-0.00387205 i
7	0.00561013+0.00277709 i	-0.01623776+0.03044762 i
8	0.00314847+0.00120472 i	-0.01305499-0.02962231 i
9	0.00151051+0.00232561 i	-0.05482246+0.01780875 i
10	0.00213858+0.00191099 i	0.00710175-0.00524589 i
11	0.00056788+0.00126758 i	-0.02552410-0.03325254 i

Table 6: $\bar{\kappa} = 0.90$ and $\bar{\delta} = -0.20$.

k	f_k	R_k
0	0.57364600+0.07130641 i	2.8342775-1.9676974 i
1	0.10684759+0.27951523 i	1.3115367-0.49432044 i
2	0.08094551+0.09310512 i	0.36341384-0.76442895 i
3	0.03966512+0.03135422 i	0.91333516+0.08761602 i
4	0.00310504+0.01022116 i	0.80480919-0.26142543 i
5	-0.00684855+0.00745449 i	0.14774214+0.10796674 i
6	-0.00699813+0.00203064 i	0.22114699+0.20451131 i
7	-0.00531951-0.00021748 i	0.00212702+0.15201002 i
8	-0.00284577-0.00256050 i	-0.05963106+0.11742257 i
9	-0.00115923-0.00199294 i	-0.10645356+0.10096874 i
10	0.00083397-0.00239535 i	-0.05823940-0.01915222 i
11	0.00055644-0.00109508 i	-0.13038081-0.01672778 i

Table 7: $\bar{\kappa} = 0.90$ and $\bar{\delta} = -0.10$.

k	f_k	R_k
0	0.60196824+0.06588277 i	-0.81682027-1.1827237 i
1	0.10158109+0.28689052 i	1.4814265-1.3401863 i
2	0.08172810+0.10060787 i	-0.21350495-0.71927214 i
3	0.04859927+0.03038195 i	-0.22526818-0.01215104 i
4	0.01289562+0.00647971 i	0.04110096+0.02219467 i
5	-0.00122628+0.00598444 i	-0.00792490-0.05175593 i
6	-0.00235547+0.00362824 i	-0.02416009+0.03097903 i
7	-0.00284275+0.00187776 i	0.03235759+0.00204170 i
8	-0.00189041+0.00014377 i	-0.02289855-0.02924280 i
9	-0.00177650+0.00008548 i	0.00005323+0.03679472 i
10	-0.00013090-0.0007260 i	0.01761269-0.03779095 i
11	-0.00085916-0.0007655 i	-0.02951724+0.01246694 i

Table 8: $\bar{\kappa} = 0.90$ and $\bar{\delta} = 0.00$.

k	f_k	R_k
0	0.59709057+0.06637358 i	-0.79032121-1.1832297 i
1	0.09802457+0.28547121 i	1.4798583-1.3649035 i
2	0.07552045+0.10758639 i	-0.08538693-0.70920170 i
3	0.04786383+0.02736105 i	-0.25700539-0.02552909 i
4	0.01745254+0.00385149 i	0.00202824+0.06332597 i
5	0.00315306+0.00398245 i	-0.01571181-0.04844439 i
6	0.00076713+0.00415569 i	-0.05816854+0.01596669 i
7	-0.00058078+0.00292219 i	0.01814994+0.00982183 i
8	-0.00088413+0.00167780 i	-0.02351918-0.03500065 i
9	-0.00139590+0.00125908 i	-0.01749711+0.01861665 i
10	-0.00054350-0.00054350 i	0.02222734-0.02244055 i
11	-0.00104530-0.00012575 i	-0.02925464-0.01325887 i

Table 9: $\bar{\kappa} = 0.90$ and $\bar{\delta} = 0.10$.

k	f_k	R_k
0	0.59416726+0.06651830 i	-0.77745213-1.1833859 i
1	0.09560810+0.28371681 i	1.4862405-1.3850933 i
2	0.06982965+0.11218707 i	0.02956159-0.68794431 i
3	0.04769710+0.02405940 i	-0.28649381-0.03524398 i
4	0.02158127+0.00103142 i	-0.04530747+0.09942274 i
5	0.00724954+0.00252467 i	-0.02038018-0.04524776 i
6	0.00351177+0.00446482 i	-0.08495573-0.00174498 i
7	0.00128321+0.00385370 i	-0.00302255+0.02052571 i
8	0.00012819+0.00270849 i	-0.01584547-0.04235147 i
9	-0.00093946+0.00213882 i	-0.03497603+0.00649764 i
10	-0.00052298+0.00139157 i	0.01751035-0.01113255 i
11	-0.00100069+0.00055675 i	-0.02044590-0.03107717 i

Table 10: $\bar{\kappa} = 0.90$ and $\bar{\delta} = 0.20$.

k	f_k	R_k
0	0.59301558+0.06518668 i	-0.85384253-1.2882959 i
1	0.09275267+0.28089023 i	1.6519458-1.5361811 i
2	0.06450078+0.11563429 i	0.15870691-0.72842568 i
3	0.04827834+0.02006130 i	-0.36438741-0.03671710 i
4	0.02656793-0.00136722 i	-0.09682354+0.12211292 i
5	0.01127394+0.00204690 i	-0.02566529-0.04106594 i
6	0.00554228+0.00507229 i	-0.10946482-0.01841179 i
7	0.00279603+0.00467458 i	-0.02886808+0.02767046 i
8	0.00105755+0.00346033 i	-0.01193420-0.03836110 i
9	-0.00045517+0.00291987 i	-0.04908395-0.01036785 i
10	-0.00033347+0.00220288 i	0.00180247-0.00165773 i
11	-0.00087781+0.00128968 i	-0.01313105-0.04036707 i

Table 11: $\bar{\kappa} = 1.00$ and $\bar{\delta} = -0.20$.

k	f_k	R_k
0	0.54920060+0.07648522 i	-0.58492016-1.1576665 i
1	0.10829748+0.27411081 i	1.2648883-1.3102113 i
2	0.07620979+0.09324556 i	-0.26832825-0.61208598 i
3	0.03206187+0.03097919 i	-0.05475149-0.00390135 i
4	-0.00163564+0.01156682 i	0.09796883-0.04764725 i
5	-0.00792710+0.00650804 i	0.03053605-0.01791133 i
6	-0.00827229+0.00079542 i	0.03307587+0.03799815 i
7	-0.00503783-0.00123866 i	0.04277371+0.00233198 i
8	-0.00255637-0.00337049 i	-0.02141669+0.01673760 i
9	-0.00029529-0.00243892 i	0.01817408+0.02716148 i
10	0.00125859-0.00242919 i	-0.01917576-0.01126388 i
11	0.00121090-0.00077086 i	-0.00842067+0.02284728 i

Table 12: $\bar{\kappa} = 1.00$ and $\bar{\delta} = -0.10$.

k	f_k	R_k
0	0.54215064+0.07383058 i	-1.5769914-1.4567166 i
1	0.10204435+0.27190204 i	1.5804775-1.5827751 i
2	0.07010139+0.10196138 i	-0.14403172-0.78234367 i
3	0.03286441+0.03287973 i	-0.11570256-0.03814616 i
4	0.00307721+0.01175473 i	0.09081553+0.00168397 i
5	-0.00462597+0.00650920 i	0.01611046+-0.04113959 i
6	-0.00582617+0.00217108 i	-0.00580035+0.04453802 i
7	-0.00422202+0.00042790 i	0.04283299-0.00644119 i
8	-0.00246869-0.00163567 i	-0.03553981-0.00722991 i
9	-0.00132951-0.00140336 i	0.01931608+0.02636926 i
10	0.00027754-0.00170434 i	-0.00376019-0.02883817 i
11	0.00021560-0.00108886 i	-0.01111862+0.01962562 i

Table 13: $\bar{\kappa} = 1.00$ and $\bar{\delta} = 0.00$.

k	f_k	R_k
0	0.53583345+0.06967184 i	-0.56447467-1.1338439 i
1	0.09702579+0.26836327 i	1.2949608-1.2939132 i
2	0.06395216+0.10939624 i	0.00526190-0.64009955 i
3	0.03399172+0.03363123 i	-0.13104653-0.04892770 i
4	0.00803476+0.01149309 i	0.04200016+0.03580184 i
5	-0.00117162+0.00713908 i	0.00301616+-0.04354944 i
6	-0.00335087+0.00385418 i	-0.03975030+0.01808688 i
7	-0.00352990+0.00217540 i	0.02367670+0.00346569 i
8	-0.00248025+0.00014328 i	-0.01978643-0.03268625 i
9	-0.00216969-0.00045805 i	-0.00483928+0.01546880 i
10	-0.00074532-0.00098057 i	0.01867079-0.02242693 i
11	-0.00057812-0.00117006 i	-0.01322231-0.00482972 i

Table 14: $\bar{\kappa} = 1.00$ and $\bar{\delta} = 0.10$.

k	f_k	R_k
0	0.53234397+0.06518217 i	-0.56977839-1.1174672 i
1	0.09280987+0.26371427 i	1.3034203-1.2872696 i
2	0.05795526+0.11559553 i	0.13737919-0.63981117 i
3	0.03481970+0.03389782 i	-0.16688040-0.06243597 i
4	0.01262512+0.01084043 i	0.00217934+0.06516132 i
5	0.00243009+0.00772217 i	-0.00206252-0.04400970 i
6	-0.00086329+0.00540898 i	-0.06886601-0.00353278 i
7	-0.00254681+0.00386039 i	0.00313953+0.01002802 i
8	-0.00231843+0.00189445 i	-0.01192955-0.04762429 i
9	-0.00263974+0.00064545 i	-0.02253565-0.00149919 i
10	-0.00165102-0.00009497 i	0.02354811-0.017013508 i
11	-0.00130228-0.00082263 i	-0.00568808-0.02566074 i

Table 15: $\bar{\kappa} = 1.00$ and $\bar{\delta} = 0.20$.

k	f_k	R_k
0	0.53090087+0.05983713 i	-0.59037057-1.0943654 i
1	0.08986900+0.25844299 i	1.3149640-1.2875424 i
2	0.05261136+0.11965455 i	0.25754998-0.63411303 i
3	0.03553700+0.03393565 i	-0.19787660-0.06978570 i
4	0.01694613+0.01112699 i	-0.03305754+0.07946528 i
5	0.00564013+0.00897689 i	-0.00573833-0.03769001 i
6	0.00086200+0.00720957 i	-0.088218710.01760196 i
7	-0.00177529+0.00541017 i	-0.02152585+0.01053451 i
8	-0.00233940+0.00338654 i	-0.00950625-0.05196743 i
9	-0.00310664+0.00174368 i	-0.03311383-0.02035621 i
10	-0.00248698+0.00065248 i	0.01651141-0.01527036 i
11	-0.00206579-0.00041068 i	0.00377008-0.03898771 i

Table 16: $\bar{\kappa} = 1.10$ and $\bar{\delta} = -0.20$.

k	f_k	R_k
0	0.50158508+0.08322103 i	-0.39778798-1.1389426 i
1	0.11050266+0.26146493 i	1.0937941-1.2795177 i
2	0.06305430+0.09106918 i	-0.17443713-0.51604046 i
3	0.01646901+0.03111112 i	0.05267837-0.02426131 i
4	-0.00837373+0.01260441 i	0.11204100-0.03469267 i
5	-0.01083539+0.00296142 i	0.04629589+0.00643403 i
6	-0.00908825-0.00152455 i	0.04218090+0.05019216 i
7	-0.00378305-0.00404714 i	0.02101623+0.00788376 i
8	-0.00081114-0.00435897 i	-0.02247707+0.03580977 i
9	0.00167400-0.00275982 i	0.00266747+0.01026806 i
10	0.00246402-0.00143021 i	-0.02924233-0.00090125 i
11	0.00193363+0.00047637 i	-0.00468014+0.00200412 i

Table 17: $\bar{\kappa} = 1.10$ and $\bar{\delta} = -0.10$.

k	f_k	R_k
0	0.49394616+0.07750607 i	-0.40894496-1.1211521 i
1	0.10311735+0.25782615 i	1.1230906-1.2545795 i
2	0.05834331+0.10046936 i	-0.04929348-0.55311365 i
3	0.01931302+0.03436812 i	0.000735390.04044874 i
4	-0.00383490+0.01436990 i	0.09563084-0.00687048 i
5	-0.00827840+0.00508397 i	0.02552339-0.01970363 i
6	-0.00821311+0.00039794 i	0.01410776+0.04330575 i
7	-0.00464206-0.00199093 i	0.02941864-0.00383443 i
8	-0.00202577-0.00351373 i	-0.02343603+0.01111322 i
9	-0.00005860-0.00267528 i	0.01297885+0.01646187 i
10	0.00154986-0.00208726 i	-0.01099703-0.01067769 i
11	0.00142509-0.00074704 i	-0.00599526+0.01318723 i

Table 18: $\bar{\kappa} = 1.10$ and $\bar{\delta} = 0.00$.

k	f_k	R_k
0	0.48800082+0.07041183 i	-0.47756400-1.1144484 i
1	0.09710822+0.25276349 i	1.1579438-1.2444070 i
2	0.05313754+0.10889924 i	0.08138731-0.58447546 i
3	0.02179016+0.03714963 i	-0.04953151-0.05961755 i
4	0.00049883+0.01599147 i	0.07287902+0.01931331 i
5	-0.00559032+0.00767030 i	0.01609931-0.04077122 i
6	-0.00713940+0.00259955 i	-0.01737909+0.02551554 i
7	-0.00547950+0.00016261 i	0.03219740-0.00398771 i
8	-0.00322769-0.00228573 i	-0.01833295-0.01841520 i
9	-0.00183475-0.00248930 i	0.00893033+0.01729848 i
10	0.00027436-0.00238963 i	0.01174394-0.01656898 i
11	0.00075979-0.00181879 i	-0.00761870+0.00752775 i

Table 19: $\bar{\kappa} = 1.10$ and $\bar{\delta} = 0.10$.

k	f_k	R_k
0	0.48375451+0.06208485 i	-0.43050608-1.0608961 i
1	0.09282680+0.24591603 i	1.1517870-1.2029898 i
2	0.04809278+0.11535711 i	0.20254326-0.58787152 i
3	0.02369131+0.04025968 i	-0.08504971-0.07614989 i
4	0.00458575+0.01787607 i	0.03764584+0.03885374 i
5	-0.00309363+0.01045284 i	0.01157210-0.04603044 i
6	-0.00605163+0.00508712 i	-0.04663345+0.00223477 i
7	-0.00619323+0.00224253 i	0.01759140-0.00010198 i
8	-0.00443253-0.00073741 i	-0.00861352-0.04118309 i
9	-0.00343738-0.00211484 i	-0.00238907+0.00403696 i
10	-0.00128389-0.00254991 i	0.02914919-0.01506421 i
11	-0.00013349-0.00268195 i	0.00431334-0.00898841 i

Table 20: $\bar{\kappa} = 1.10$ and $\bar{\delta} = 0.20$.

k	f_k	R_k
0	0.48250488 + 0.05400098 i	-0.46601972-1.03117980 i
1	0.09015626 + 0.23907075 i	1.14601910 -1.19138230 i
2	0.04338279 + 0.12118213 i	0.31862749 -0.59621880 i
3	0.02463542 + 0.04317015 i	-0.11507688-0.08729447 i
4	0.00791044 + 0.01980512 i	0.00065834 +0.05217681 i
5	-0.00093305+ 0.01331432 i	0.01471385 -0.04028228 i
6	-0.00525144+0.007647228 i	-0.05926982-0.01436183 i
7	-0.00680151+0.003987887 i	0.00395562 +0.00619534 i
8	-0.00566844+0.000540155 i	0.01025577 -0.04911688 i
9	-0.00499132-0.001843332 i	-0.00246420-0.01522543 i
10	-0.00302894-0.002892220 i	0.03940932 -0.01402472 i
11	-0.00136737-0.003493643 i	0.02371301 -0.02726136 i

Table 21: $\bar{\kappa} = 1.20$ and $\bar{\delta} = -0.20$.

k	f_k	R_k
0	0.45765811+0.08466596 i	0.38378365-0.87758218 i
1	0.11260236+0.24735578 i	0.77846688-1.0167712 i
2	0.04991837+0.08703062 i	-0.07054082-0.34952899 i
3	0.00463918+0.03012197 i	0.10702962-0.02546904 i
4	-0.01225506+0.01110224 i	0.09741840-0.00577455 i
5	-0.01270576-0.00039937 i	0.05152567+0.02877147 i
6	-0.00793063-0.00374401 i	0.03036897+0.04936514 i
7	-0.00200827-0.00581434 i	-0.00523270+0.01976254 i
8	0.00136514-0.00437805 i	-0.02394581+0.02969699 i
9	0.00320046-0.00200565 i	-0.01819113-0.00055244 i
10	0.00295222+0.00006881 i	-0.02202125-0.00656254 i
11	0.00166184+0.00178172 i	-0.00330469-0.01423263 i

Table 22: $\bar{\kappa} = 1.20$ and $\bar{\delta} = -0.10$.

k	f_k	R_k
0	0.45135680+0.07746869 i	0.30747649-0.87286184 i
1	0.10468762+0.24356349 i	0.82333280-1.0068211 i
2	0.04692888+0.09682253 i	0.01367682-0.39178065 i
3	0.00832415+0.03469223 i	0.05824972-0.03873910 i
4	-0.00863030+0.01452375 i	0.09127168-0.00171464 i
5	-0.01136033+0.00262406 i	0.03432300+0.00339957 i
6	-0.00910157-0.00188737 i	0.02556237+0.04199897 i
7	-0.00404376-0.00453818 i	0.01251001+0.00797132 i
8	-0.00067495-0.00487517 i	-0.01733708+0.02231205 i
9	0.00181142-0.00305972 i	-0.00231126+0.00928301 i
10	0.00290008-0.00150544 i	-0.01793693-0.00349197 i
11	0.00231041+0.00053336 i	-0.00738612+0.00022071 i

Table 23: $\bar{\kappa} = 1.20$ and $\bar{\delta} = 0.00$.

k	f_k	R_k
0	0.44848861+0.06913138 i	-0.29989568-1.0525205 i
1	0.09792792+0.23852962 i	1.0126560-1.1621228 i
2	0.04306391+0.10646038 i	0.13279173-0.51358283 i
3	0.01117208+0.03934990 i	0.01086411-0.06388957 i
4	-0.00562935+0.01811797 i	0.09316910+0.00582331 i
5	-0.00987723+0.00648480 i	0.02442170-0.02751769 i
6	-0.00990538+0.00043114 i	0.00803632+0.03420706 i
7	-0.00617456-0.00279780 i	0.02992002-0.00041335 i
8	-0.00270964-0.00497654 i	-0.01384184+0.00662822 i
9	-0.00010270-0.00426576 i	0.01194124+0.02014165 i
10	0.00227731-0.00323384 i	-0.00099889-0.00388767 i
11	0.00253924-0.00145289 i	-0.00673898+0.01275323 i

Table 24: $\bar{\kappa} = 1.20$ and $\bar{\delta} = 0.10$.

k	f_k	R_k
0	0.54207359+0.07018493 i	-1.9566178-0.70824433
1	0.16299503+0.25860727 i	1.7629234-2.1106117 i
2	-0.05946903+0.11136536 i	2.3282440-0.44794162 i
3	-0.09263188+0.01318097 i	-1.6334974+1.0398760 i
4	-0.03501446+0.00165250 i	-0.22702845-0.50932270 i
5	0.01923667+0.00076926 i	1.4387224+0.060140406 i
6	0.02572709+0.01448085 i	-0.25345868-0.16851772 i
7	0.00170531+0.01171258 i	-0.87362612+0.12951789 i
8	-0.00630028-0.00158848 i	0.15934858+0.18245285 i
9	0.00091826-0.00328335 i	0.77745966-0.53939143 i
10	0.00726971-0.00873729 i	-0.21971203+0.30942040 i
11	0.00461637-0.00009001 i	-0.71917686-0.04351483 i

Table 25: $\bar{\kappa} = 1.20$ and $\bar{\delta} = 0.20$.

k	f_k	R_k
0	0.55307287+0.06313760 i	-0.64110188-1.6848641 i
1	0.16175416+0.26456763 i	0.86014798-0.95202373 i
2	-0.07998028+0.12331589 i	0.45634331-0.19244083 i
3	-0.08808530+0.00058320 i	0.19458346+0.12894088 i
4	-0.02432487-0.00140464 i	0.28390001+0.25703508 i
5	0.01055687+0.00518220 i	-0.03765351-0.55356523 i
6	0.01565620+0.01166997 i	-0.02768630+0.49402597 i
7	0.00528172+0.01357402 i	-0.05900644-0.29141453 i
8	0.00018655-0.00390116 i	0.02647444-0.01344938 i
9	-0.00535825+0.00094461 i	0.17151819+0.20666680 i
10	-0.00193757-0.00587756 i	-0.10087706-0.49189440 i
11	0.01119458-0.00457094 i	-0.07175891+0.51818779 i

Lists of Symbols and Abbreviations

$\bar{T}$	Electron to Ion Temperature Ratio
$\bar{x}_s$	A Shifted Radial Coordinate which is related to x_s according to $\bar{x}_s \rightarrow x_s + x_m$
χ	A Complex Parameter that controls the Localisation of $A(p)$ in p Space as well as $\tilde{\phi}(x_s, \theta)$ in x_s Space
δ_b	Width of a Banana Orbit
Δ_p	The Width of $A(p)$ in p Space
Δ_r	Distance between Rational Surfaces
Δ_x	The Radial Width of the Reconstructed Global Mode $\tilde{\phi}(x_s, \theta)$ in x_s Space
ϵ	Inverse Aspect Ratio
ϵ_0	Electric Permeability of Free Space
η	Extended Ballooning Angle Coordinate along the Magnetic Field Lines
η_i	The Drive for ITG Modes which is defined as a Ratio of Density to Temperature Scale Length, i.e. $\eta_i = L_n/L_T$
Γ	The Specific Heat Ratio
γ	Global Growth Rate
γ_0	Local Growth Rate
γ_E	Related to the Rotational Flow Shear Ω_φ according to $\gamma_E = d\Omega_\varphi/dq$
γ_E^m	A Critical Value of Flow Shear that Maximises the Global Growth Rate γ for a Given Set of Plasma Equilibrium Profiles
$\hat{A}$	Incorporates the Slow Variation Part of the Global Electrostatic Perturbations $\tilde{\phi}(\psi, \eta)$ in the the WKB Expansion Method
$\hat{F}$	Incorporates the Slow Variation Part of the Global Electrostatic Perturbations $\tilde{\phi}(\psi, \theta)$ in the the WKB Expansion Method
$\hat{q}$	Local Safety Factor
$\hat{S}$	Eikonal Function

$\hat{s}$	Magnetic Shear
$\hat{Y}$	Toroidal Angle Independent Part of the Eikonal Function $\hat{S}$
$\lambda_\perp$	Wave Length perpendicular to the Magnetic Field Lines
λ_D	Debye Length
$\ln \Lambda$	Coulomb Logarithm Factor
μ	Magnetic Moment
μ_0	Magnetic Permeability of Free Space
ν_{ei}	Electron-Ion Collisional Frequency
ν_{ie}	Ion-Electron Collisional Frequency
ν_{ii}	Ion-Ion Collisional Frequency
Ω	Global Complex Mode Frequency
ω	Global Real Frequency
Ω_0	Local Complex Mode Frequency
ω_0	Local Real Frequency
$\omega_{\star e}^n$	Electron Density Diamagnetic Drift Frequency
$\omega_{\star i}^T$	Ion Temperature Diamagnetic Frequency
$\omega_\star^P$	Pressure Diamagnetic Frequency
Ω_φ	Rotational Flow Shear
ω_{ce}	Electron Cyclotron Frequency
ω_{ci}	Ion Cyclotron Frequency
ω_c	Cyclotron Frequency
ω_s	Ion Sound Frequency
ψ	Poloidal Flux within a Magnetic Surface
q'	Radial Derivative of the Safety Factor at $x_s = 0$
ρ	Charge Density
ρ_{ce}	Electron Gyroradius
ρ_{ci}	Ion Gyroradius
ρ_c	Gyro or Larmor Radius
τ_{ei}	Electron-Ion Collision Mean Free Time
τ_E	Plasma Confinement Time
τ_{ie}	Ion-Electron Collision Mean Free Time
τ_{ii}	Ion-Ion Collision Mean Free Time

θ	Poloidal Angle
$\tilde{\mathcal{L}}$	Electromagnetic Field Perturbation
$\tilde{\phi}$	Electrostatic Global Mode Structure
$\tilde{f}$	Fluctuating Distribution Function
$\tilde{G}$	Fluctuating Physical Quantities
$\tilde{h}$	Non-adiabatic Part of the Fluctuating Distribution Function
$\tilde{n}_e$	Electron Fluctuating Density
$\tilde{n}_i$	Ion Fluctuating Density
$\underline{\hat{b}}$	Unit Vector along The Magnetic Field Lines
$\underline{\hat{e}}_\psi$	Radial Unit Vector
$\underline{\hat{e}}_\theta$	Poloidal Unit Vector
$\underline{\hat{e}}_\varphi$	Toroidal Unit Vector
$\underline{\nabla}$	Gradient Operator
$\underline{\nabla}_\perp$	Gradient Operator perpendicular to the Magnetic Field Lines
$\underline{\nabla}_r$	Gradient Operator in Spatial Space
$\underline{\nabla}_v$	Gradient Operator in Velocity Space
$\underline{\tilde{B}}$	Fluctuating Magnetic Field
$\underline{\tilde{V}}_e$	Fluctuating Electron Fluid Velocity
$\underline{\tilde{V}}_i$	Fluctuating Ion Fluid Velocity
$\underline{a}$	Acceleration
$\underline{B}$	Magnetic Field
$\underline{B}_0$	Equilibrium Magnetic Field
$\underline{D}$	Electric Displacement Field
$\underline{E}$	Electric Field
$\underline{E}_\perp$	Component of $\underline{E}$ perpendicular to the Magnetic Field Lines
$\underline{F}$	Lorentz Force
$\underline{F}_\perp$	Component of $\underline{F}$ perpendicular to the Magnetic Field Lines
$\underline{J}$	Current Density
$\underline{k}$	Wave Vector
$\underline{r}$	Position Vector
$\underline{R}_c$	Guiding Centre Position Vector
$\underline{U}$	Guiding Centre Velocity

$\underline{U}_D$	Guiding Centre Particle Drift
$\underline{V}$	Fluid Velocity
$\underline{v}$	Particle Velocity
$\underline{v}_{\nabla B}$	Magnetic Gradient Drift Velocity
$\underline{v}_{\perp}$	Component of $\underline{v}$ perpendicular to the Magnetic Field Lines
$\underline{v}_{cr}$	Magnetic Curvature Drift Velocity
$\underline{v}_{E\times B}$	$\underline{E} \times \underline{B}$ Drift Velocity
$\underline{V}_e$	Electron Fluid Velocity
$\underline{V}_i$	Ion Fluid Velocity
φ	Toroidal Angle
ξ	Local Mode Structure
$A(p)$	The Envelope Function that determines the Radial Structure for the Reconstructed Global Mode $\tilde{\phi}(x_s, \theta)$
c	Speed of Light
$C(f)$	Collision Operator
$d\ell$	Incremental Distance along the Magnetic Field Lines
$d\ell_\theta$	Incremental Distance along the Poloidal Direction
$d\ell_\varphi$	Incremental Distance along the Toroidal Direction
D_b	Neoclassical Diffusion Coefficient
D_{cl}	Classical Diffusion Coefficient
dl	Differential Line Element
dV	Differential Volume Element
dv	Volume Element in Velocity Space
E_n	Energy
$f(0)$	Coefficient of the Zeroth Order Term in the Taylor Expansion of $f(p)$ about $p = 0$
$f(p)$	Coefficient of the Zeroth Order Term in the Taylor Expansion of the Local Complex Mode Frequency $\Omega_0(x_s, p)$ about $x_s = 0$
$f(p_0)$	Coefficient of the Zeroth Order Term in the Taylor Expansion of $f(p)$ about $p = p_0$
$f''(0)$	Coefficient of the Second Order Term in the Taylor Expansion of $f(p)$ about $p = 0$
$f''(p_0)$	Coefficient of the Second Order Term in the Taylor Expansion of $f(p)$ about $p = p_0$

$f'(0)$	Coefficient of the First Order Term in the Taylor Expansion of $f(p)$ about $p = 0$
$f'(p_0)$	Coefficient of the First Order Term in the Taylor Expansion of $f(p)$ about $p = p_0$
F_0	Equilibrium Distribution Function
f_e	Electron Distribution Function
f_i	Ion Distribution Function
f_k	Coefficients in the Fourier Expansion $f(p) = \sum_k^{N_k} f_k \cos kp$
f_t	Fraction of Trapped Particles
G	Represents the Physical Quantities
G_0	Represents the Equilibrium Part of the Physical Quantity G
g_N	Webber-Hermite Polynomial of Degree N
H_N	Hermite Polynomial of Degree N
I	Identity Matrix
J	Jacobian
$k_\perp$	Wave Vector perpendicular to the Magnetic Field Lines
k_B	Boltzmann Constant
$k_y\rho_{ci}$	Normalised Binormal Wave number
keV	Kilo-Electron Volt
L	Equilibrium Scale Length
L_n	Equilibrium Density Scale Length
L_T	Equilibrium Temperature Scale Length
M	Mass
M_e	Electron Mass
M_i	Ion Mass
MeV	Mega Electron Volt
n	Toroidal Mode Number
n_0	Plasma Equilibrium Density
n_e	Electron Density
n_i	Ion Density
N_k	Number of the Fourier Coefficients Retained in the Expansion $\Omega_0(x_s, p) = \sum_k^{N_k} \left[f_k \cos kp + x_s S_k \cos kp + x_s^2 R_k \cos kp \right]$
n_p	Plasma Density

n_{ref}	Plasma Density on a Rational Surface at $x_s = 0$
p	Ballooning Angle Coordinate
p_0	The Complex Ballooning Phase Angle
P_e	Electron Pressure
P_i	Ion Pressure
Q	Square Complex Non-symmetric almost Tridiagonal Matrix
q	Global Safety Factor
q_0	Safety Factor at $x_s = 0$
q_e	Electron Charge
q_i	Ion Charge
q_j	Electric Charge
R	Major Radius Coordinate
r	Minor Radius of the Toroidal Flux Surface
$R(0)$	Coefficient of the Zeroth Order Term in the Taylor Expansion of $R(p)$ about $p = 0$
$R(p)$	Coefficient of the Second Order Term in the Taylor Expansion of the Local Complex Mode Frequency $\Omega_0(x_s, p)$ about $x_s = 0$
$R(p_0)$	Coefficient of the Zeroth Order Term in the Taylor Expansion of $R(p)$ about $p = p_0$
$R''(0)$	Coefficient of the Second Order Term in the Taylor Expansion of $R(p)$ about $p = 0$
$R''(p_0)$	Coefficient of the Second Order Term in the Taylor Expansion of $R(p)$ about $p = p_0$
$R'(0)$	Coefficient of the First Order Term in the Taylor Expansion of $R(p)$ about $p = 0$
$R'(p_0)$	Coefficient of the First Order Term in the Taylor Expansion of $R(p)$ about $p = p_0$
R_0	Major Radius of the Toroidal Flux Surface
R_k	Coefficients in the Fourier Expansion $R(p) = \sum_k^{N_k} R_k \cos kp$
R_{nl}	Non-linear Component of The Gyrokinetic Equation
$S(0)$	Coefficient of the Zeroth Order Term in the Taylor Expansion of $S(p)$ about $p = 0$
$S(p)$	Coefficient of the First Order Term in the Taylor Expansion of the Local Complex Mode Frequency $\Omega_0(x_s, p)$ about $x_s = 0$
$S(p_0)$	Coefficient of the Zeroth Order Term in the Taylor Expansion of $S(p)$ about $p = p_0$

$S''(0)$	Coefficient of the Second Order Term in the Taylor Expansion of $S(p)$ about $p = 0$
$S''(p_0)$	Coefficient of the Second Order Term in the Taylor Expansion of $S(p)$ about $p = p_0$
$S'(0)$	Coefficient of the First Order Term in the Taylor Expansion of $S(p)$ about $p = 0$
$S'(p_0)$	Coefficient of the First Order Term in the Taylor Expansion of $S(p)$ about $p = p_0$
S_k	Coefficients in the Fourier Expansion $S(p) = \sum_k^{N_k} S_k \cos kp$
T	Plasma Temperature
t	Time
T_e	Electron Temperature
T_i	Ion Temperature
T_{ref}	Plasma Temperature on a Rational Surface at $x_s = 0$
$V_{\star e}$	Electric Diamagnetic Drift Speed
V_s	Ion Sound Speed
v_{th}	Thermal Speed
x_0	Complex Radial Parameter
x_m	Determines the Physical Radial Shift of the Reconstructed Global Mode Structures $\tilde{\phi}(x_s, \theta)$ with Respect to $x_s = 0$
x_s	Measures Distance from a Reference Rational Surface at $x_s = 0$
${}^6L_i$	Lithium
${}^0_{-1}e$	Electron
${}^0_0\nu_e$	Electron-Neutrino
${}^2_1H$	Deuterium
${}^{56}_{26}F_e$	Iron
${}^3_2H$	Tritium
${}^4_2H$	Helium
${}^{238}_{91}U$	Uranium
1D	One Dimensional
2D	Two Dimensional
AUG	ASDEX Upgrade
DEMO	DEMOnstration Power Plant
ECRH	Electron Cyclotron Resonance Heating

ECRH	Neutral Beam Injection
H-Mode	High Confinement Mode
ICF	Inertial Confinement Fusion
ICRH	Ion Cyclotron Resonance Heating
ITER	International Thermonuclear Experimental Reactor
ITG	Ion Temperature Gradient Mode
JET	Joint European Torus
L-Mode	Low Confinement Mode
MAST	Mega Amp Spherical Tokamak
MCF	Magnetic Confinement Fusion
TCV	Tokamak Configuration Variable
WKB	Wentzel Kramers Brillouin

References

[1] J. D. Lawson. **Some Criteria for a power producing thermonuclear reactor**. *proceeding of the physical society*, **6**(B70), 1957. 21

[2] John Wesson. *Tokamaks*. Claredndon Press, Oxford, third edition, 2004. 21, 22, 31, 38, 42, 44, 45

[3] ITER Physics Basis. **Chapter 1: Overview and summary**. *Nucl. Fusion*, **39**:2137–2638, 1999. 22

[4] W. Horton. **Drift waves and transport**. *Rev. Mod. Phys.*, **71**(3):1–8, April 1999. 22, 45, 47

[5] D. Dickinson, C. M. Roach, J. M. Skipp, and H. R. Wilson. **Structure of micro-instabilities in tokamak plasmas: Stiff transport or plasma eruptions?** *Phys. Plasmas*, **21**(010702):1–4, January 2014. 22, 23, 61, 78, 81, 85, 117, 125, 126, 138, 139, 147, 154, 171, 172

[6] J. W. Connor and T. J. Martin. **Rotation shear and drift wave stability**. *Plasma Phys. Control. Fusion*, **49**:1497–1507, 2007. 126, 127

[7] P. W. Terry. **Suppression of turbulence and transport by sheared flow**. *Rev. Mod. Phys.*, **72**:109–165, January 2000. 126

[8] Y. Kishimoto. *et al.* **Toroidal mode structure in weak and reversed magnetic shear plasmas and its role in the internal transport barrier**. *Plasma Phys. Control. Fusion*, **41**(3A), 1999. 126

[9] C. M. Roach. *et al.* **Gyrokinetic simulations of spherical tokamaks**. *Plasma Phys. Control. Fusion*, **51**(124020):1–11, 2009.

[10] H. Biglari, P. H. Diamond, and P. W. Terry. **Influence of sheared poloidal rotation on edge turbulence**. *Phys. Fludis B*, **2**(1):1–4, 1990.

[11] R. E. Waltz, G. D. Kerbel, and J. Milovich. **Toroidal gyroLandau fluid model turbulence simulations in a nonlinear ballooning mode representation with radial modes**. *Phys. Plasmas*, **1**:2229–2244, 1994. 22, 126

[12] P. Hill, S. Saarelma, B. McMillan, A. Peeters, and E. Verwichte. **Perpendicular wavenumber dependence of the linear stability of global ion temperature gradient modes on $E \times B$ flows**. *Plasma Phys. Control. Fusion*, **54**:1–8, May 2012. 22, 24, 56, 127, 139, 148, 149, 155, 156, 160, 162, 167, 171, 172

[13] P. A. Abdoul, D. Dickinson, C. M. Roach, and H. R. Wilson. **Using a local gyrokinetic code to study global ion temperature gradient modes in tokamaks**. *Plasma Phys. Control. Fusion*, **57**(6):065004, 10 April 2015. 22, 24, 56, 61, 95, 127

[14] G. M. Staebler, J. E. Kinsey, and R. E. Waltz. **A theory-based transport model with comprehensive physics**. *Phys. Plasmas*, **51**:055909, November 2007. 22

[15] P. H. Rutherford and E. A. Frieman. **Drift Instabilities in General Magnetic Field Configurations**. *Phys. Fluids*, **11**(8):569–585, 1968. 22, 57, 74

[16] J. B. Taylor and R. J. Hastie. **Stability of General Plasma Equilibria-I Formal Theory**. *Plasma Phys.*, **10**:479–494, 1968. 57

[17] E. A. Frieman and L. Chen. **Nonlinear Gyrokinetic Equations for Low-frequency Electromagnetic Waves in General Plasma Equilibria**. *Phys. Fluids*, **25**:502–508, 1982. 22, 57, 59, 74

[18] J. W. Connor, J. B. Taylor, and H. R. Wilson. **Shear Damping of Drift Waves in Toroidal Plasmas**. *Phys. Rev. Lett.*, **70**(12):1803–1805, March 1993. 23, 78, 81, 85, 147

[19] J. B. Taylor, H. R. Wilson, and J. W. Connor. **Structure of short wavelength drift modes and transport in a toroidal plasma**. *Plasma Phys. Control. Fusion*, **38**(8):2543–250, 1996. 23, 60, 78, 82, 85, 139, 154

[20] R. L. Dewar. **Spectrum of the ballooning Schrdinger equation**. *Plasma Phys. Control. Fusion*, **39**:453–470, 1997. 60, 127, 154

[21] M. Kotschenreuther, G. Rewoldt, and W. M. Tang. **Comparison of initial value and eigenvalue codes for kinetic toroidal plasma instabilities**. *comput. phys. commun.*, **88**:128–140, 1995. 23, 61, 74

[22] W. Dorland, F. Jenko, M. Kotshenreuther, and B.N. Rogers. **Electron Temperature Gradient Turbulence**. *Phys. Rev. Lett.*, **85**:5579, 2000. 23, 61, 74

[23] J. W. Connor, R. J. Hastie, and J. B. Taylor. **Shear, Periodicity, and Plasma Ballooning Modes**. *Phys. Rev. Lett.*, **40**:396–399, 1978. 23, 78, 139, 140

[24] J. W. Connor, R. J. Hastie, and J. B. Taylor. **High Mode Number Stability of an Axisymmetric Toroidal Plasma**. In *proceeding of the Royal Society of London A, Mathematical and Physical Sciences*, **365**, pages 1–17, Feb. 19 1979. 23, 60, 63, 71, 78

[25] T. Xie, Y. Z. Zhang, S. M. Mahajan, and A.K. Wang. **Ballooning theory of the second kind−two dimensional tokamak modes**. *Phys. Plasmas*, **19**(072105):1–13, 2012. 23, 74, 78, 81, 85

[26] F. Romanelli and F. Zonca. **The radial structure of the ion temperature gradient driven mode**. *Phys. Fluids B*, **5**(11):4081–4089, 1993. 23, 52, 74

[27] Y. Camenen, Y. Idomura, S. Jolliet, and A. G. Peeters. **Consequences of profile shearing on toroidal momentum transport**. *Nucl. Fusion*, **51**:1–11, May 2011. 24, 95, 98, 148, 155

[28] H. S. Xie and Y. Xiao. **Unconventional Ballooning Structures for Toroidal Drift Waves**. *arXiv:1503.04440*, 2015. 24, 102, 107, 113, 148

[29] A. Bottino et al. **Simulation of global electrostatic microinstabilities in ASDEX Upgrade Discharges**. *Phys. Plasmas*, **11**:198–2006, 2004. 24, 148

[30] A. G. Peeters. *et al.* **Overview of toroidal momentum transport**. *Nucl. Fusion*, **51**(9):094027, 31 August 2011. 24, 95, 148

[31] P. H. Diamond. *et al.* **An overview of intrinsic torque and momentum transport bifurcations in toroidal plasmas**. *Nucl. Fusion*, **53**(10):104019, 26 September 2013.

[32] Felix I. Parra and Michael Barnes. **Intrinsic rotation in tokamaks: theory**. *Plasma Phys. Control. Fusion*, **57**:045002, 5 March 2015. 24, 95, 148

[33] Y. Camenen. *et al.* **Impact of plasma triangularity and collisionality on electron heat transport in TCV L-mode plasmas**. *Nucl. Fusion*, **47**:510516, June 2007. 24, 164

[34] A. Kallenbach. *et al.* **Scaling of the pedestal density in type-I ELMy H-mode discharges and the impact of upper and lower triangularity in JET and ASDEX Upgrade**. *Nucl. Fusion*, **42**:1184–1192, July 2002. 24, 166

[35] S. Yu Medvedev. *et al.* **Beta Limits and Edge Stability for Negative Tringularity Plasmas in the TCV Tokamak.** *35th EPS Conference on Plasma Physics*, **32D**, Hersonissos, 9-13 June 2008. 24

[36] J. Anderson, H. Nordman, and J. Weiland. **Effects of non-circular tokamak geometry on the ion-temperature-gradient driven modes**. *Plasma Phys. Control. Fusion*, **42**:545–555, February 2000. 24

[37] J. E. Kinsey, R. E. Waltz, and J. Candy. **The effect of plasma shaping on turbulent transport and $E \times B$ shear quenching in nonlinear gyrokinetic simulations.** *Phys. Plasmas*, **14**(012306), October 2007. 165

[38] E. A. Belli, G. A. Hamett, and W. Dorland. **Effects of plasma shaping on nonlinear gyrokinetic turbulence**. *Phys. Plasmas*, **15**(092303):1–11, September 2008. 24, 165

[39] A. Kendl and Bruce D. Scott. **Flux-surface shaping effects on tokamak edge turbulence and flows**. *Phys. Plasmas*, **13**(012504), January 2006. 24, 165

[40] Peter Atkins. *The Laws of Thermodynamics: A Very Short Introduction*. Oxford University Press, Great Clarendon Street, Oxford ox26DP, 2010. 28

[41] Francis F. Chen. *An Indispensable Truth: How Fusion Power Can Save the Planet*. Springer Science+Business Media, LLC 2011, New York, 2011. 28

[42] Mark Maslin. *Global Warming: A Very Short Introduction*. Oxford University Press, Great Clarendon Street, Oxford ox26DP, 2004. 28

[43] **World energy consumption**. `http://commons.wikimedia.org/wiki/File:World_energy_consumption.svg`. [Accessed : 03/07/15]. 29

[44] **Fission and fusion reactions**. `http://www.21stcentech.com/energy-update-fusion-reaction-progress-report/`. [Accessed : 03/07/15]. 30

[45] **Nucleon Binding Energy**. `http://scienceblogs.com/startswithabang/2013/11/13/binding-energy-nuclear-physics-and-radiation-poisoning/`. [Accessed : 03/07/15]. 30

[46] Maxwell Irvine. *Nuclear Power: A Very Short Introduction*. Oxford University Press, Great Clarendon Street, Oxford ox26DP, 2011. 31

[47] Daniel Clery. *A piece of the Sun: The Quest for Fusion Energy*. Overlook Press, 2013. 31

[48] Andreas Dinklage. *et al. Lecture Notes in Physics, Plasma Physics, Confinement, Transport and Collective Effects*. Springer, Berlin Heidelberg, 2005. 31

[49] J. L. Basdevant, J. Rich, and M. Spiro. *Fundamentals In Nuclear Physics*. Springer Science and Business Media, New York, third edition, 2005. 31

[50] **Fusion reaction rate as function of temperature**. `http://en.wikipedia.org/wiki/Nuclear_fusion`. [Accessed : 03/07/15]. 33

[51] Hans-Steph Bosch. *et al. Summer University for Plasma Physics*. EURATOM-ASSOCIATION, D-85748 Garching, Germany, September 27 - October 1 2004. 33

[52] Leslie C. Woods. *Theory of Tokamak Transport: New Aspects for Nuclear Fusion Reactor Design*. Wiley-VCH, Weinheim, 2006. 42

[53] B. B. Ayushin. *et al.* **Study of Plasma Heating in Discharges with Neutral Beam Injection in the Globus-M Spherical Tokamaks**. *Plasma Phys. Rep.*, **34**:81–94, 2008. 33

[54] E. H. Holt and R. E. Haskell. *Foundations of Plasma Dynamics*. Plenum Press, Macmillan Company, 1965. 35

[55] Francis F. Chen. *Plasma Phys. Control. Fusion*. Plenum Press, New York, 1984. 35, 38, 42, 47, 66

[56] R. A. Cairns. *Plasma Physics*. Blackie and Son Limited, Glasgow G64 2NZ, third edition, 1985.

[57] R. O. Dendy. *PLASMA DYNAMICS*. Claredndon Press, Oxford, third edition, 1990. 35

[58] T. J. Dolan. *Fusion Research*. Pergamon Press, New York, 1982. 38, 39

[59] M. Wakatani. *Stellarators and Heliotron Devices*. Oxford Univ. Press, New York, third edition, 1998. 38, 39, 44

[60] R. Weynants. **Fusion Machines**. *Fusion Science and Technology*, **41**(2):49–55, 2000. 38

[61] **The stellarator Wendelstein 7-X**. `http://en.wikipedia.org/wiki/Wendelstein_7-X`. [Accessed : 03/07/15]. 39

[62] K. Nishikawa and M. Wakatani. *Plasma Physics: Basic Theory with Fusion Applications*. Springer, Heidelberg, third edition, 2000. 41, 42

[63] F. L. Hinton and R. D. Hazeltine. **Theory of plasma transport in toroidal confinement systems**. *Rev. Mod. Phys.*, **48**(2), April 1976. 41, 42

[64] Roscoe B. White. *The theory of Toroidally Confined Plasmas*. Imperial College Press, Princeton, second edition, 2001. 42

[65] M. N. Rosenbluth, W. M. MacDonald, and D. L. Judd. **Fokker-Plank Equation for an Inverse-Square Force**. *Phys. Rev*, **107**(1):1–6, 1957. 42

[66] J. Crank. *The mathematics of diffusion*, chapter 11. Clarendon Press, Oxford University Press, Ely House, London W.I, 1975. 43

[67] **The Random Walk - The Physics of Diffusion**. `http://www.pas.rochester.edu/~stte/phy104-F00/n9/notes-9a.html`. [Accessed : 03/07/15]. 43

[68] G. P Thomson and M. Blackman. **British patent 817 681, "Improvements in Gas Discharge Apparatus for Producing Thermonuclear Reactions"**. *In M. G. Haines , Plasma Phys. Contrl. Fusion*, **38**:643, January 1996. 43

[69] Per Helander and Dieter J. Sigmar. *Collisional transport in magnetized plasmas*. Cambridge University Press, The Pitt Building. Trumpington Street, Cambridge, United Kingdom, 2002. 44

[70] F. Wagner and U. Stroth. **Transport in toroidal devices-the experimentalist's view**. *Plasma Phys. Control. Fusion*, **35**(10):1321–1371, 1993. 44

[71] Ulrich Stroth. **A comparative study of transport in stellarators and tokamaks**. *Plasma Phys. Control. Fusion*, **40**:9–74, November 1998. 44

[72] W. M. Tang. **Microstability Theory in Tokamaks**. *Nucl. Fusion*, **18**(8):1089–1160, 1978. 44, 45, 47

[73] J. W. Connor and H. R. Wilson. **Survey of theories of anomalous transport**. *Plasma Phys. Control. Fusion*, **36**:719–795, 1994. 45, 47

[74] D. L. Brower. *et al.* **Observation of a high-density ion mode in tokamak microturbulence**. *Phys. Rev. Lett.*, **59**(48), 6 July 1987. 52

[75] S. C. Cowley, R. M. Kulsrud, and R. Sudan. **Considerations of ion-temperature-gradient-driven turbulence**. *Phys. Fluids B*, **3**:2767, 02 June 1991. 52

[76] R. D. Hazeltine and J. D. Meiss. *Plasma confinement*. Dover Publications, 2003. 54

[77] J. J. Ramos. **General expression of the gyroviscous force**. *Phys. Plasmas*, **12**(112301), 2 November 2005. 54

[78] L. Pearlstein and H. Berk. **Universal Eigenmode in a Strongly Sheared Magnetic Field**. *Phys. Rev. Lett.*, **23**:220, 1969. 55

[79] J. B. Taylor. **Does magnetic shear stabilize drift waves?** In *booktitle*, **6** of *in Proceedings Of The Sixth International Conference On Plasma Physics And Controlled Nuclear Fusion Research*, pages 323–329, Vienna, 1977. 55, 68

[80] J. W. Connor, R. J. Hastie, and J. B Taylor. **Stability of toroidal plasmas: the influence of magnetic shear, periodicity and rotation**. *Plasma Phys. Control. Fusion*, **46**:B1–B11, November 2004. 56, 100

[81] D. Dickinson. *Effects of profiles on microinstabilities in tokamaks*. PhD thesis, University of York/Physics department/YPI, 2012. 56, 74, 81, 91, 139

[82] A. J. Brizard and T. S. Hahem. **Foundations of Nonlinear Gyrokinetic Theory**. *Rev. Mod. Phys., American Physical Social Society*, **79**:421–468, 2007. 57

[83] T. M. Antonsen and B. Lane. **Kinetic Equations for low Frequency Instabilities in Inhomogeneous Plasmas**. *Phys. Fluids, AIP*, **23**:1205–1214, 1980. 57

[84] W.M. Tang J.B. Catto and D.E. Baldwin. **Generelized Gyro-kinetics**. *Plasma Phys.*, **23**:639–650, 1981. 57

[85] F. Pegoraro and T.J. Schep. **Low frequency modes with high toroidal mode numbers: A general formulation**. *Phys. Fluids*, **24**:478–497, 1981. 63

[86] W. A. Newcomb R. D. Hazeltine. **Inversion of the ballooning transformation**. *Phys. Fluid B*, **2**(7):7–10, 1990.

[87] Y. Z. Zhang and S. M. Mahajan. **On Broken Ballooning Symmetry**. *Phys. Lett A*, **157**(2,3):133–136, July 1991. 63, 74

[88] J. D. Callen W. D. D'haeseleer, W. N. G. Hitchon and J. L. Shohet. *Flux Coordinates and Magnetic Field Structure*, chapter 11. Spriner, Berlin, Heidelberg, New York, London, Paris, Tokyo, hong Kong, Barcelona, 1991. 64

[89] George Schmidt. *Physics of High Temperature Plasmas*. Academic Press, New York, second edition, 1979. 66

[90] Dwight R. Nicholson. *Introduction to Plasma Theory*. John Wiley & Sons, New York, 1983. 66

[91] K. V. Roberts and J. B. Taylor. **Gravitational Resistive Instability of an Incompressible Plasma in a Sheared Magnetic Field**. *Phys. Fluids*, **8**:315–322, 1965. 67

[92] Jeffrey P. Freidberg. *Plasma Physics and Fusion energy*. Cambridge University Press, 2008. 70

[93] Richard L. Burden and J. Douglas Faires. *Numerical Analysis*. Brooks/Cole Publishing Company, Pacific Grove, California 93950, 1997. 78

[94] H. Kneser. *Funktionentheorie*. Vandenhoeck and Ruprecht Göttingen, 1958. 80

[95] R. Remmert. *Theory of Complex Functions*. Springer-Verlag, 1991. 80

[96] **Gauss integral with complex analysis**. `http://math.stackexchange.com/questions/34767/int-infty-infty-e-x2-dx-with-complex-analysis`. [Accessed : 03/07/15]. 80

[97] KEITH CONRAD. **THE GAUSSIAN INTEGRAL**. `http://www.math.uconn.edu/~kconrad/blurbs/analysis/gaussianintegral.pdf`. [Accessed : 03/07/15]. 80

[98] S. Briguglio, F. Romanelli, C. M. Bishop, J. W. Connor, and R. J. Hastie. **Stability of toroidicity-induced drift waves in divertor tokamaks**. *Phys. Fluids B*, **7**:1449–1458, July 1989. 87

[99] Y. Z. Zhang, S. M. Mahajan, and X. D. Zhang. **Two dimensional aspects of toroidal drift waves in the ballooning representation**. *Phys. Fluids B*, **4**(9):2729–2732, Septemebr 1992. 87

[100] R. Courant and D. Hilbert. *Methods of Mathematical Physics*, **I**. Wiley-Interscience, 1966. 104

[101] W. W. Bell. *Special Functions for Scientists and Engineers*. Dover Publications, Inc., New York, third edition, 1996. 104

[102] U. Stroth, P. Manz, and M. Ramisch. **On the interaction of turbulence and flows in toroidal plasmas**. *Plasma Phys. Control. Fusion*, **53**(024006):1–14, January 2011. 126

[103] S. P. Hirshman. **The ambipolarity paradox in toroidal diffusion, revisited**. *Nucl. Fusion*, **18**(917), March 1978. 126, 157

[104] R. C. Morris, M. G. Haines, and R. J. Hastie. **The neoclassical theory of poloidal flow damping in a tokamak**. *Phys. Plasmas*, **3**(4513), 1996. 126, 157

[105] P. J. Catto, M. N. Rosenbluth, and C. S. Liu. **Parallel velocity shear instabilities in an inhomogeneous plasma with a sheared magnetic field**. *Phys. Fluids*, **16**:1719–1729, 1973. 126

[106] S. L. Newton, S. C. Cowley, and N. F. Loureiro. **Understanding the effect of sheared flow on microinstabilities**. *Plasma Phys. Control. Fusion*, **52**(125001), 2010. 126

[107] X. Lapillonne *et al*. **Clarifications to the limitations of the $s - \alpha$ equilibrium model for gyrokinetic computations of turbulence**. *Phys. Plasmas*, **16**(032308):1–9, 2009. 139, 140, 149

[108] R. L. Miller. *et al.* **Noncircular, finite aspect ratio, local equilibrium model**. *Phys. Plasmas*, **5**(4):973–978, 1998. 139

[109] A. M. Dimits. *et al.* **Comparisons and physics basis of tokamak transport models and turbulence simulations**. *Phys. Plasmas*, **7**(3):969–983, 2000. 149

[110] G. L. Falchetto. *et al.* **The European turbulence code benchmarking effort: turbulence driven by thermal gradients in magnetically confined plasmas**. *Plasma Phys. Control. Fusion*, **50**(9):124015, 2008. 149

[111] Peter A. Hill. *The effect of toroidal flows on the stability of ITGs in MAST*. PhD thesis, The University of Warwick, 2012. 155

[112] Mykhaylo Reshko. *Gyrokinetic Simulations of the Effects of Equilibrium $E \times B$ Flow Shear on Microinstabilities and Transport in Tokamaks*. PhD thesis, The University of York, 2009. 157

[113] A. Burckel, O. Sauter, C. Angioni, J. CAndy, E. Fable, and X. Lapillonne. **On the effects of the equilibrium model in gyrokinetic simulations: from $s - \alpha$ to diverted MHD equilibrium**. *Journal of Physics*, **260**(012006), July 2010. 163

[114] D. Dickinson, C. M. Roach, S. Saarelma, R. Scannell, and H. R Krik, A. Wilson. **Kinetic Instabilities that Limit βin the Edge of a Tokamak Plasma: Picture of an H-Mode Pedestal**. *Phys. Rev. Lett.*, **108**:135002, March 2012. 173

[115] S. Saarelma. *et al.* **MHD and gyro-kinetic stability of JET pedestals**. *Nucl. Fusion*, **53**(123012):1–9, January 2013. 173

[116] C. M. Roach. *et al.* **Gyrokinetic Instabilities near an Evolving Tokamak H-mode Pedestal.** *In proceeding of 24th IAEA Fusion Energy Conference, San Diego*, pages (TH/5–1), 2012. 173